



HAL
open science

Réalisation de jonctions tunnel ferroélectriques pour la mise en œuvre de synapses artificielles

Greta Segantini

► **To cite this version:**

Greta Segantini. Réalisation de jonctions tunnel ferroélectriques pour la mise en œuvre de synapses artificielles. Autre. Ecole Centrale de Lyon, 2023. Français. NNT : 2023ECDL0007 . tel-04117435

HAL Id: tel-04117435

<https://theses.hal.science/tel-04117435>

Submitted on 5 Jun 2023

HAL is a multi-disciplinary open access archive for the deposit and dissemination of scientific research documents, whether they are published or not. The documents may come from teaching and research institutions in France or abroad, or from public or private research centers.

L'archive ouverte pluridisciplinaire **HAL**, est destinée au dépôt et à la diffusion de documents scientifiques de niveau recherche, publiés ou non, émanant des établissements d'enseignement et de recherche français ou étrangers, des laboratoires publics ou privés.

N° d'ordre NNT : 2023ECDL0007

Thèse de doctorat de l'Université de Lyon

opérée au sein de l'École Centrale de Lyon
en cotutelle internationale avec le Royal Melbourne Institute of
Technology

École Doctorale N°34: Matériaux

Spécialité de doctorat : Matériaux

Soutenance publique le 31 janvier 2023, par

Greta Segantini

Fabrication of Ferroelectric Tunnel Junctions for the Implementation of Artificial Synapses

Devant le jury composé de :

Alain Sylvestre,	Professeur, G2Elab Université Grenoble Alpes,	Président, Rapporteur
Laurence Méchin,	Directrice de recherche CNRS, GREYC Caen,	Rapporteuse
Catherine Dubourdieu,	Professeur, Freie Universität Berlin,	Examinatrice
José Pedro Basto Silva,	Chargé de recherche, UMinho,	Examineur
Ingrid Cañero Infante,	Chargé de recherche CNRS, INSA Lyon,	Examinatrice
Bertrand Vilquin,	Maître de conférences, ECL,	Directeur de thèse
Damien Deleruyelle,	Professeur, INSA Lyon,	Co-directeur de thèse
Sharath Sriram,	Professeur, RMIT Melbourne,	Co-directeur de thèse
Laurent Grenouillet,	Ingénieur R&D, CEA LETI,	Invité
Pedro Rojo Romeo,	Maître de conférences, ECL,	Invité

Aknowledgements

First, I would like to thank the jury, Alain Sylvestre, Laurence Méchin, Catherine Dubourdieu, José Pedro Basto Silva, Ingrid Cañero Infante, and Laurent Grenouillet to have accepted to examine my work.

Afterwards, I would like to deeply thank my supervisors at INL and RMIT University: Bertrand Vilquin, Damien Deleruyelle, and Pedro Rojo Romeo to have introduced me to the field of ferroelectrics and for their support throughout the thesis, Sharath Sriram and Shruti Nirantar, from the FMM group, for their warm welcome at RMIT University, their time, and valuable advice.

Also, I would like to acknowledge the ECLAUSion COFUND, directed by Christian Grillet and Arnan Mitchell, and the PhD students, sponsored by this program, with whom I shared my journey at INL and RMIT University: Ana Maria, Harris, Panteha, Kokou, Marko, Iulia, Marina, Mohab, and Georgii. I would like to acknowledge the projects 3eFERRO and ALPhFA as well, thanks to which I had the opportunity to participate in conferences and events related to the PhD, and to travel to Melbourne.

A big thanks to the members of the Ferro-Team: Bertrand, Pedro, Damien, Jordan, Ingrid, Benoît, Rabei, Sara, Swayam, and Nicolas. Thanks to Benoît, who shared with me this project since the beginning, for his work on the electrical characterisations.

A special thanks to Ingrid for the insightful scientific discussions and support for experiments and data analysis. Moreover, I would like to thank Matthieu for the time he dedicated to my research and his precious advice.

I want to express my gratitude to the people of the team "Hétéroépitaxie et Nanostructures", administrative and technical staff of INL, and to Edwin, Matt, and Billy of the RMMF facility at RMIT University.

Thanks to all the PhD students and post-docs at INL with whom I shared coffee breaks and after-works, in particular to Paule, Antonin, Oleh, Martina, and Gaukhar. Furthermore, I would like to thank Suvankar to have welcomed me on the first day at RMIT University and helped me with the organisation of the experiments.

Finally, this achievement would not have been possible without my family, friends, and Pierre, who have always supported and motivated me in every choice I made.

Contents

Aknowledgements	i
List of Tables	vii
List of Figures	ix
Acronyms	xvii
Abstract	xxi
Résumé	xxiii
Introduction	1
I Ferroelectricity and ICT Applications	5
I.1 Electric Polarisation	5
I.1.1 Polarisation for Deformation	6
I.1.2 Orientational Polarisation	6
I.2 Ferroelectricity	7
I.2.1 Landau Devonshire Theory	8
I.2.2 Ferroelectric Domains	9
I.2.3 Polarisation switching	11
I.2.4 Antiferroelectricity	12
I.2.5 Phonon Contribution to Ferroelectricity	13
I.2.6 Factors that Affect Ferroelectric Properties	14
I.3 Ferroelectric Materials	17
I.3.1 Perovskites	17
I.3.2 Hafnium Oxide	18
I.4 Ferroelectric Non-volatile Memory Devices	24
I.4.1 Ferroelectric Random Access Memory	24

I.4.2	Ferroelectric Field Effect Transistor	25
I.4.3	Negative Capacitance Field Effect Transistor	27
I.4.4	Ferroelectric Tunnel Junctions	28
I.4.5	Ferroelectric Tunnel Junctions: State of the Art	32
I.5	Neuromorphic Devices	34
I.5.1	Mechanisms and Materials for Neuromorphic Devices	34
I.5.2	Artificial Synapses	44
I.5.3	Artificial Neurons	46
I.6	FTJs for Neuromorphic Computing	48
I.6.1	FTJs Industrial Requisites for Neuromorphic Applications	50
I.7	Conclusion of the Chapter	51
II	Experimental Techniques	53
II.1	Sputtering Techniques	54
II.1.1	Physical Mechanism	54
II.1.2	Magnetron Sputtering: Set Up and Operation Modes	56
II.1.3	Equipment Used for Experiments	58
II.2	UV Photolithography	58
II.3	Fabrication Process of Capacitors	59
II.4	Rapid Thermal Annealing	60
II.5	Characterisation Techniques: Structural, Physical, and Chemical Char- acterisation	62
II.5.1	X-Ray Diffraction	62
II.5.2	Glancing Incidence X-ray Diffraction	63
II.5.3	X-Ray Reflectometry	64
II.5.4	Transmission Electron Microscopy	65
II.5.5	Atomic Force Microscopy	71
II.5.6	Rutherford Backscattering Spectrometry	72
II.6	Characterisation Techniques: Electrical Characterisation	74
II.6.1	Current vs Voltage Measurements	75
II.6.2	Capacitance vs Voltage Measurements	76
II.6.3	Polarisation vs Voltage Measurements: Hysteresis Cycle	78
II.6.4	Endurance Test	81
II.7	Conclusion of the Chapter	81

III HZO Thin Films-Based Devices: Synthesis and Applications	83
III.1 HZO Thin Films: State of the Art	83
III.1.1 Deposition Techniques of HZO Thin Films	84
III.1.2 Impact of Annealing Conditions	85
III.1.3 Oxygen Vacancies	86
III.1.4 Formation of Dead Layers	87
III.2 Synthesis of the Reference Structure	88
III.2.1 Fabrication Process	88
III.2.2 Post-Metallisation Annealing	89
III.2.3 Characteristics of the Reference Structure	90
III.3 Structural Characterisations	93
III.3.1 XRR Measurements	93
III.3.2 GI-XRD Analysis	94
III.3.3 RBS Analysis	97
III.3.4 AFM Analysis	98
III.3.5 TEM and HR-TEM Analysis	99
III.4 Electrical Characterisations	101
III.4.1 PUND	101
III.4.2 Current Transport Mechanisms in the Reference Structure .	104
III.5 Furnace Annealing	106
III.6 Scaling Down the HZO Thickness	108
III.7 Conclusion of the Chapter	109
IV Reduction of HZO Thickness and Impact of the Bottom Electrode	111
IV.1 Analysis of the Effect of Thickness Reduction	111
IV.1.1 Structural Characterisations: GI-XRD and HR-TEM	112
IV.1.2 Electrical Characterisations	116
IV.2 Bottom Electrode: State of the Art	121
IV.3 Investigated Structures	122
IV.3.1 Structural Characterisation: GI-XRD	123
IV.3.2 Electrical Characterisation: PUND	126
IV.4 Thickness of TiN Bottom Electrode	128
IV.5 Conclusion of the Chapter	129

V Synthesis and Optimisation of Ultra-Thin HZO-based Ferroelectric Tunnel Junctions	131
V.1 Ultra-Thin Interfacial Layers: State of the Art	131
V.2 Ultra-Thin Interfacial Layers: Experimental Results	132
V.3 Titanium Interfacial Layer	133
V.3.1 Structural Characterisations: GI-XRD, and EELS	133
V.3.2 Electrical Characterisation: PUND	137
V.4 Aluminium Interfacial Layer	141
V.5 Tungsten Electrodes	142
V.5.1 Electrical Characterisations: PUND and I-V Measurements .	143
V.5.2 Structural Characterisations: GI-XRD, EELS, and HR-TEM . .	145
V.6 Summary of the Ferroelectric Performances of the Analysed Samples	152
V.7 Conclusion of the Chapter	152
VI Advanced Applications of HZO-based Thin Films: Perspectives	155
VI.1 In-memory Computing	155
VI.1.1 Brain-inspired In-memory Computing	157
VI.1.2 Ferroelectric Memristors for Brain-inspired Computing . . .	160
VI.2 Crossbar Architecture	161
VI.3 Multi-state Programming	164
VI.4 Study of HZO Optical Properties for Optoelectronic Applications . .	166
VI.5 Conclusion of the Chapter	168
Conclusion and Perspectives	171
Annex A: Scientific Communications Throughout the Thesis	175
Annex B: GI-XRD Fitting Procedure	179
Annex C: Samples with Ti Interfacial layer Inserted at the Top Interface and Different HZO Thickness	181
Annex D: Ti Interfacial Layer at the Bottom Electrode/HZO Interface	185
Annex E: XPS Analysis of the HZO/Top Electrode Interface	189
Bibliography	193

List of Tables

1	Acronyms	xvii
I.1	Phases of HfO ₂	21
I.2	Examples of dopant materials used for HfO ₂	22
I.3	State of the art of FTJs and HZO-based FTJs performances.	50
III.1	Film growth, annealing, and capacitor fabrication conditions.	90
III.2	Current transport mechanisms in ferroelectric capacitors.	105
IV.1	Average o-phase out-of-plane crystallite size for different HZO thicknesses.	116
IV.2	Value of ϵ_r for different HZO thicknesses.	120
IV.3	Average out-of-plane o-phase crystallite size of a 12 nm-thick HZO layer deposited on different bottom electrodes.	124
IV.4	Thermal expansion coefficients (TECs) of HZO and of different bottom electrodes.	126
V.1	State of art: thin-HZO-based structure with the addition of the interfacial layers	132
V.2	Growth conditions of the interfacial layers.	133
V.3	Values of endurance, in number of cycles, and $2P_r$, in $\mu\text{C}\cdot\text{cm}^{-2}$, in pristine state, after $\sim 10^5$ cycles, and at breakdown of samples 0, 1, 2, and 3.	139
V.4	Values of the remanent polarisation and endurance for structures with Al interfacial layer.	141
V.5	Average o-phase out-of-plane crystallite size of the studied structures.	147
V.6	Summary of the ferroelectric performances of the analysed samples with a 6 nm-thick HZO layer.	152

C1	Average out-of-plane o-phase crystallite size of HZO for different thicknesses and Ti interfacial layer deposited at the top interface.	182
C2	Remanent polarisation and endurance of samples with different HZO thicknesses, and with a 3 nm- and 1 nm-thick Ti interfacial layer at the top interface.	183
D1	Average out-of-plane o-phase crystallite size of HZO with different thicknesses and a Ti interfacial layer at the bottom interface.	186

List of Figures

I.1	Free energy <i>versus</i> polarisation for the second-order and the first-order phase transitions.	10
I.2	Ferroelectric hysteresis loop: polarisation <i>versus</i> electric field. .	11
I.3	a) Schematic of the antiferroelectric phase transition. b) Schematic of the ferroelectric phase transition.	12
I.4	Example of the P - E characteristic of antiferroelectric materials. .	13
I.5	a) Evolution of the polarisation as a function of the applied voltage cycles. Wake-up and fatigue states, and the value of the endurance are highlighted. b) Retention. c) Imprint that implies a right or left shift of the hysteresis loop.	17
I.6	Schematic of the perovskite BTO unit cell.	18
I.7	Phase diagram of Hf-O.	19
I.8	Six crystal structures of HfO ₂	20
I.9	$P - V$ curves and $C - V$ curves of HfO ₂ -ZrO ₂ -based capacitors at room temperature, for different Zr content.	23
I.10	a) Architecture of a 1T-1C memory cell. b) Readout operation of a FRAM, P - V loop.	25
I.11	Operation principle of a FeFET.	26
I.12	P - V characteristic of a negative capacitance-based device.	28
I.13	Modulation of a rectangular potential barrier due to polarisation charges in a FTJ.	30
I.14	Schematic illustration of the switching process and I - V curves of simple binary anion-migration-based devices.	37
I.15	Schematic illustration of the change of the oxide thickness in a redox reaction in non-filamentary type devices.	38
I.16	Schematic of the ionic dynamic during the negative SET process in ion-migration-based devices.	38

I.17	Configurations demonstrating the atomic rearrangements during the phase transition in PCM, with and without pre-structural ordering.	39
I.18	Spintronic-based neuromorphic devices.	40
I.19	Metal-insulator transition-based devices.	41
I.20	Photo-tunable mechanism-based devices.	43
I.21	Electrolyte-gated mechanism-based devices.	43
I.22	Electronic-based devices.	44
I.23	Schematic of the working principle of a synaptic junction. . . .	45
I.24	Illustration of a neuron. Science Photo Library - KTSDESIGN/Getty Images	47
II.1	Schematic of the structure of a sample synthesised in this work.	53
II.2	Schematic representation of a sputtering chamber.	55
II.3	Schematic of the magnetron sputtering configuration.	56
II.4	Magnetron sputtering system available at INL: AC-450 by Alliance Concept.	59
II.5	Reversal photolithography procedure for the deposition of top electrodes and top contacts.	60
II.6	Photo-mask used during the UV photolithography for the fabrication of capacitors.	61
II.7	a) Structure of a finished sample. b) Optical image of a portion of the sample surface, where the pattern of capacitors is visible.	61
II.8	Illustration of the Bragg's law.	63
II.9	$2\theta/\omega$ configuration of a Smartlab Rigaku Diffractometer.	64
II.10	Diffractometer by Rigaku available at INL.	65
II.11	Oscillation pattern obtained by means of XRR.	66
II.12	Schematic of a TEM microscope equipped with the STEM mode.	68
II.13	TEM microscope JEOL JEM-200F used for HR-TEM experiments.	69
II.14	TEM microscope JEM-ARM200F NeoARM by JEOL used for EELS and HR-STEM experiments.	70
II.15	Schematic of AFM technique.	71
II.16	Park NX10 AFM.	72
II.17	Representation of large-angle scattering.	73

II.18	Schematic of a Van de Graaff accelerator.	74
II.19	Agilent 4156B semiconductor parameter analyser.	76
II.20	Voltage waveform used to acquire I - V characteristics.	76
II.21	Typical curve that represents the logarithm of the current density vs the applied electric field of a ferroelectric-based device.	76
II.22	Dielectric permittivity ϵ_r as a function of the electric field for a ferroelectric material.	77
II.23	HP 4284A Precision LCR meter.	77
II.24	C - V curve typical of ferroelectric materials	78
II.25	Schema of the circuit used to measure the polarisation as a function of the applied voltage.	79
II.26	PUND pulse train.	80
III.1	Schema of the fabrication process of the reference structure.	89
III.2	Schematic of the reference structure.	91
III.3	Schematic of the TiN oxidation process proposed by Esaka.	93
III.4	XRR measurements.	94
III.5	GI-XRD pattern of the reference structure taken over a 2θ range 15° - 100°	96
III.6	GI-XRD pattern and fit of the reference structure.	96
III.7	GI-XRD pattern and fit of the reference structure with the difference between the two.	97
III.8	RBS spectrum of the reference structure.	98
III.9	AFM images of the surface of the reference structure. a) Before RTA procedure. b) After RTA procedure.	98
III.10	TEM images at low magnification.	99
III.11	HR-TEM image of the reference structure.	100
III.12	a) HR-TEM image of the reference structure. Highlighted in blue, the area over which the FFT was performed. b) FFT of the area highlighted in blue in a). Inset: magnified view of the area highlighted in blue together with the o-HZO unit cell in the $[uvw]=[01-1]$ zone axis.	101

III.13	a) P - V curve of the reference structure after 10^3 cycles. The hysteresis loop in blue accounts only for the current contributions recorded for pulses P and N , thus the leakage current contributions are not subtracted. The hysteresis loop in red corresponds to the application of the PUND correction, thus only ferroelectric effects are considered (section II.6.3) b) Evolution of P_r as a function of voltage cycles.	103
III.14	Endurance test, showing the evolution of the P_r as a function of the number of applied voltage cycles.	104
III.15	PN, UD, PN-UD currents as a function of time.	104
III.16	ϵ_r of the reference structure as a function of voltage.	105
III.17	a) J/V curves of the reference sample at different temperatures. b) Fit of the experimental results according to the Poole-Frenkel conduction mechanism.	106
III.18	On the left a photo of a sample annealed at 450°C , on the right of a sample annealed at 600°C	107
III.19	Furnace Annealing	107
III.20	P - V curve of: a) sample 1, extracted after 10^3 cycles. b) Sample 2, extracted after 10^3 cycles.	108
III.21	Endurance test of: a) sample 1. b) Sample 2.	108
IV.1	GI-XRD patterns for different HZO thickness.	113
IV.2	HR-TEM measures of a thin HZO film.	114
IV.3	GI-XRD pattern for different HZO thicknesses with the difference between the experimental data and the fit.	116
IV.4	Crystallite size vs HZO thickness.	117
IV.5	P - V curves for different HZO thickness.	118
IV.6	Endurance tests of samples with different HZO thickness	119
IV.7	I - V curves in semi-log scale, for applied voltage ± 1.5 V, of samples $n^+\text{Si}(100)/\text{TiN}/\text{HZO}/\text{TiN}/\text{Ti}/\text{Pt}$ with: HZO ~ 12 nm, HZO ~ 8 nm, HZO ~ 7 nm, and HZO ~ 6 nm.	120
IV.8	C - V measurements, for applied voltage of ± 3.5 V, of samples $n^+\text{Si}(100)/\text{TiN}/\text{HZO}/\text{TiN}/\text{Ti}/\text{Pt}$ with: HZO ~ 12 nm, HZO ~ 8 nm, HZO ~ 7 nm, and HZO ~ 6 nm.	121

IV.9	Schematics of the analysed samples with different bottom electrodes.	123
IV.10	Superimposed GI-XRD patterns of samples with different bottom electrodes.	124
IV.11	GI-XRD patterns with fit and difference between fit and experimental data of HZO deposited on different bottom electrodes. .	125
IV.12	<i>P-V</i> curves of 12 nm-thick HZO deposited on different bottom electrodes.	127
IV.13	Endurance test of 12 nm-thick HZO deposited on different bottom electrodes.	128
V.1	Schematic of the structure of the samples with and without Ti interfacial layer.	133
V.2	GI-XRD patterns of samples with and without Ti interfacial layer.	134
V.3	STEM-EELS analysis of sample 0. a) EELS spectra acquired across the TE/HZO interface. Each spectrum is the average of 81 spectra projected horizontally along the interface, and is shifted vertically for clarity. The HAADF image acquired simultaneously is shown in inset. A spectrum image dataset of 16×81 pixels was acquired with a step size of 3.9 \AA , over an area of $\sim 6.3 \times 32 \text{ nm}^2$. b), c), d) Display over a narrower energy range of the N-K, Ti-L _{2,3} , and O-K edges, respectively.	136
V.4	STEM-EELS analysis of sample 2. a) EELS spectra acquired across the TE/HZO interface. Each spectrum is the average of 81 spectra projected horizontally along the interface, and is shifted vertically for clarity. The HAADF image acquired simultaneously is shown in inset. A spectrum image dataset of 16×81 pixels was acquired with a step size of 3.9 \AA , over an area of $\sim 6.3 \times 32 \text{ nm}^2$. b), c), d) Display over a narrower energy range of the N-K, Ti-L _{2,3} , and O-K edges, respectively.	137
V.5	Electrical characterisation of samples 0, 1, 2, and 3: <i>P-V</i> curves taken on woken up capacitors after $\sim 10^5$ cycles.	138

V.6	Electrical characterisation of samples 0, 1, 2, and 3: endurance tests. Circles are drawn at the number of cycles at which the PUND measure was extracted, black stars indicate the breakdown point.	139
V.7	Schematic of the studied samples.	142
V.8	<i>P-E</i> measurements of the four samples: TiN/HZO/TiN extracted at 10^5 cycles, TiN/HZO/W extracted at 10^4 cycles, W/HZO/TiN extracted at 10^5 cycles, and W/HZO/W extracted at 10^4 cycles. .	143
V.9	Endurance tests performed on samples: TiN/HZO/TiN, TiN/HZO/W, W/HZO/TiN, and W/HZO/W. Circles are drawn at the number of cycles at which the PUND measure was extracted (where the P_r was at the maximum), black stars indicate the breakdown point.	144
V.10	<i>I-V</i> curves and ON/OFF ratio of n^+ Si/W/HZO/W/Ti/Pt sample	145
V.11	GI-XRD patterns and fits of samples with W electrodes.	146
V.12	EELS analysis of structures with TiN, and W electrodes.	150
V.13	HR-TEM analysis of structures with TiN and W electrodes.	151
VI.1	Von-Neumann vs in-memory computing.	156
VI.2	The three generations of neural networks.	158
VI.3	Schematic of DNN working principle.	159
VI.4	Schematic of the crossbar architecture.	162
VI.5	Images taken by optical microscope that show details of: a) a series of memristors. b)A single memristor. c) A Crossbar array.	163
VI.6	Image taken by optical microscope of a crossbar sample.	163
VI.7	Demonstration of multi-state programming of the polarisation .	165
VI.8	Switching of the polarisation as a function of the number of writing pulses and of the writing voltage	165
VI.9	Demonstration of a potentiation/depression characteristic measured on one of the here synthesised devices.	166
VI.10	Refractive index and extinction coefficient obtained with ellipsometry on a p^+ Si/HZO samples.	167
VI.11	VEELS spectrum of orthorhombic HZO.	168

C1	GI-XRD patterns and fits of samples with Ti interfacial layer at the top interface.	182
C2	<i>P-V</i> measures of samples with Ti interfacial layer at the top interface.	183
C3	Endurance test of samples with Ti interfacial layer at the top interface.	184
D1	Schematic of the structure $n^+Si(100)/TiN/Ti/HZO/TiN/Ti/Pt$, with Ti interfacial layer deposited at the bottom interface. . . .	185
D2	GI-XRD patterns and fits of samples with Ti interfacial layer at bottom interface.	186
D3	<i>P-V</i> measures of samples with Ti interfacial layer at bottom interface.	187
D4	Endurance test of samples with Ti interfacial layer at the bottom interface.	188
D5	Average out-of-plane <i>o</i> -phase crystallite size vs HZO thickness for samples without Ti interlayer, with Ti at top interface, and with Ti at bottom interface.	188
E1	Scheme of an experiment of photoemission spectroscopy.	190
E2	Inelastic mean free path as a function of the kinetic energy of electrons, and scheme of the generation process of a photoelectron.	191
E3	Scheme of an hemispherical electron energy analyser.	191
E4	Kratos AXIS Supra XPS.	192
E5	a) Hf XPS peaks of sample $n^+Si/TiN/HZO/TiN$, with TiN top electrode ~ 2 nm, b) Hf XPS peaks of sample $n^+Si/TiN/HZO/TiN$, with TiN top electrode ~ 2 nm, and Ti interlayer ~ 2 nm.	192

Acronyms

Table 1: Acronyms

Acronym	Meaning
FTJ	Ferroelectric tunnel junction
CMOS	Complementary-metal-oxide-semiconductor
HZO	Hafnium zirconium oxide
P, E, ϵ	Polarisation, electric field, dielectric permittivity
BTO	Barium titanate
PZT	Lead zirconate titanate
BFO	Bismuth ferrite
FRAM	Ferroelectric random access memory
FeFET	Ferroelectric field-effect transistor
NC	Negative capacitance
TER	Tunnel electroresistance ratio
ANN	Artificial neural network
HRS	High resistance state
LRS	Low resistance state
PCM	Phase change material

Continued on next page

Table 1: Acronyms (Continued)

Acronym	Meaning
MTJ	Magnetic tunnel junction
TMR	Tunnel magnetoresistance ratio
MIT	Metal-insulator transition
LTP	Long-term potentiation
LTD	Long-term depression
STP	Short-term potentiation
STD	Short-term depression
STPD	Synaptic time-dependent plasticity
DC	Direct current
RF	Radio frequency
UV	Ultra-violet
RTA	Rapid thermal annealing
XRD	X-ray diffraction
GI-XRD	Glancing-incidence X-ray diffraction
XRR	X-ray reflectometry
TEM	Transmission electron microscopy
HR-TEM	High-resolution transmission electron microscopy
STEM	Scanning transmission electron microscopy
EELS	Electron energy-loss spectroscopy
HAADF	High-angle annular dark field
AFM	Atomic force microscopy
RBS	Rutherford backscattering spectrometry
XPS	X-ray photoelectron spectroscopy
PUND	Positive-up-negative-down
ALD	Atomic layer deposition

Continued on next page

Table 1: Acronyms (Continued)

Acronym	Meaning
PE-ALD	Plasma-enhanced atomic layer deposition
PLD	Pulsed laser deposition
OV	Oxygen vacancy
PMA	Post-metallisation annealing
FWHM	Full width at half maximum
BE	Bottom electrode
TE	Top electrode
MFIM	Metal-ferroelectric-insulator-metal
ELNES	Energy-loss near-edge structure
AI	Artificial intelligence
DNN	Deep neural network
SNN	Spike neural network
MVM	Matrix-vector multiplication
V-EELS	Valence electron energy-loss spectroscopy
DFT	Density functional theory
PES	Photoemission or photoelectron spectroscopy

Abstract

Ferroelectric materials are ideal candidates for the realisation of memristors, thanks to the non-volatile resistance states and fast resistance switching. Ferroelectric memristors are studied as memory units for the fabrication of dense memory arrays to implement hardware neuromorphic networks. This architecture would satisfy the requests of high process speed of large amount of data and low power consumption. The latter are the limits of the modern Von-Neumann architecture, which is experiencing the so-called memory bottleneck. Among ferroelectric materials, hafnium zirconium oxide (HZO) is characterised by robust ferroelectricity at a nanometric thickness and is compatible with the complementary-metal-oxide-semiconductor (CMOS) technology, thus industrially transferable. The objectives of this work are the realisation and optimisation of HZO-based ferroelectric tunnel junction (FTJ) memristors for the implementation of memory arrays, using the crossbar integration method. One of the major challenges associated to the use of HZO is the degradation of the ferroelectric properties when its thickness is reduced to very few nanometers. Throughout the thesis, different approaches to increase the scalability of HZO without compromising its ferroelectricity are explored. Structural, physical, and chemical properties of HZO-based heterostructures are investigated by means of spectroscopic techniques and electrical characterisations are performed to evaluate their ferroelectric behaviour. The correlation between the structural properties of HZO and of electrode/oxide interfaces, and the ferroelectric performances is highlighted and used for the optimisation of ultra-thin HZO-based devices for neuromorphic applications.

Résumé

Les matériaux ferroélectriques sont des candidats idéaux pour la réalisation de memristors grâce aux états de résistance non volatils et à la commutation rapide de la résistance. Les memristors ferroélectriques sont étudiés comme unités de mémoire pour la fabrication de réseaux de mémoire denses afin de mettre en œuvre des réseaux neuromorphiques artificiels. Cette architecture répondrait aux exigences d'une vitesse de traitement élevée d'une grande quantité de données et d'une faible consommation d'énergie. Ces dernières sont les limites de l'architecture Von-Neumann moderne, qui connaît le fameux goulot d'étranglement de la mémoire. Parmi les matériaux ferroélectriques, l'oxyde de hafnium et de zirconium (HZO) se caractérise par une ferroélectricité robuste à une épaisseur nanométrique et est compatible avec la technologie des semi-conducteurs à oxyde métallique complémentaire (CMOS), ce qui permet un transfert industriel. L'objectif de ce travail est la réalisation et l'optimisation de memristors à jonction tunnel ferroélectrique (FTJ) à base de HZO pour la mise en œuvre de matrices de mémoire, en utilisant la méthode d'intégration crossbar. L'un des défis majeurs associés à l'utilisation du HZO est lié à la dégradation de ses propriétés ferroélectriques lorsque son épaisseur est réduite à quelques nanomètres. Tout au long de la thèse, différentes approches visant à réduire la taille du HZO sans compromettre sa ferroélectricité sont explorées. Les propriétés structurelles, physiques et chimiques des hétérostructures à base de HZO sont étudiées au moyen de techniques spectroscopiques et des caractérisations électriques sont réalisées pour évaluer leurs propriétés ferroélectriques. La corrélation

entre les propriétés structurelles du HZO et des interfaces électrode/oxyde et les performances ferroélectriques est mise en évidence et utilisée pour l'optimisation des dispositifs ultra-minces à base de HZO pour les applications neuromorphiques.

Introduction

The end of Moore's law has challenged the research to find solutions to the quest of increase of scalability and reduction of power consumption that characterises the modern semiconductor industry. The Von-Neumann hardware architecture is failing in keeping up with growingly diffused power-hungry technologies, such as artificial intelligence systems. Limitations in terms of the process speed and energy consumption of the Von-Neumann architecture created the need for novel approaches beyond the traditional silicon-based technologies. Two examples, which have been extensively studied in the recent years, are quantum computing and neuromorphic computing. Quantum computing performs computational tasks exploiting the phenomena of quantum mechanics, while neuromorphic computing takes inspiration from the working mechanisms of networks of biological neurons and synapses. Both these approaches guarantee faster operation speed and potentially demand a lower energy cost compared to modern computers. Despite few successful demonstrations at a laboratory level and for specific tasks, quantum and neuromorphic computers remain far from commercialisation. To reduce the size of this gap, research in this field has been increasingly focused on studying materials, integration processes, and algorithms to optimise these technologies for a future vast scale commercialisation.

The development of an artificial neuromorphic system requires the control over a large number of aspects, such as suitable materials to fabricate the memory components, efficient ways for their integration, circuit design, and development of computational algorithms that can reproduce synaptic functionalities. Each of

these aspects need be optimised to obtain a complete functioning system.

A promising component for the realisation of memory arrays for brain-inspired computing is the memristor, theorised in 1971 by Leon Chua in Berkely. The word "memristor" comes from the merge of two words "memory" and "resistor", as it has memory of the past applied voltage or flowing current. The memristor is defined as a two terminal non-volatile memory device based on a resistance switching mechanisms. Over the years, various materials and physical mechanisms, which provide resistance switching have been investigated. Among them, ferroelectric materials were shown to be extremely suitable for the realisation of memristors, thanks to their multiple non-volatile resistance states, which offer the possibility of analog storage of information. During the second half of the past century, various non-volatile ferroelectric-based memory devices have been proposed and studied. However, until recently, ferroelectric materials used for the implementation of these devices were mainly perovskites, which are not compatible with the complementary-metal-oxide-semiconductor (CMOS) platforms.

The discovery of ferroelectricity in doped-hafnium oxide in 2011 by Böscke paved the path towards the integration of ferroelectric-based memory devices into CMOS industry. Ferroelectric memristors can be organised in specific hardware architectures, such as crossbar, that allow the synthesis of dense memory arrays. In a first time, this would increase the hardware scalability, through the fabrication of a more compact memory unit, while the calculations can be performed at the periphery by the CMOS circuitry. In a second time, the crossbar matrices, thanks to their non-volatility and low-power programmability, could be used directly to perform calculations without the necessity of an external process unit. This is the concept of in-memory computing, which completely eliminates latency and overcomes power issues related to the transfer of large amount of data between memory and process units. A major issue linked to the fabrication of the aforementioned memory arrays is the device-to-device variability of the memory components, which greatly compromises performances of the system.

This work focuses on the fabrication and optimisation of ferroelectric capacitors for the synthesis of ferroelectric tunnel junction (FTJ) memristors for neuromorphic applications. The material used as ferroelectric layer is the CMOS-compatible hafnium zirconium oxide (HZO). I investigated the synthesised devices from a structural, physical, chemical, and electrical point of view. I highlighted the as-

pects that influence ferroelectricity in ultra-thin HZO films and the issues related to its scalability that need to be overcome for the development of FTJs, which could be used to emulate the behaviour of biological synapses.

The manuscript is divided as follows:

- **Chapter 1: Ferroelectricity and ICT Applications**

Firstly, it describes from a theoretical point of view the concepts of electric polarisation and ferroelectricity, together with the relevant parameters that have to be considered for technological applications. Secondly, it introduces the ferroelectric materials and the main ferroelectric-based memory devices. Finally, it gives an overview of the neuromorphic systems for the emulation of biological neurons and synapses.

- **Chapter 2: Experimental Techniques**

It describes in detail the experimental techniques used for the fabrication of samples and for their structural, chemical, physical, and electrical characterisations.

- **Chapter 3: HZO Thin Film-Based Devices: Synthesis and Applications**

Firstly, it gives an overview on the techniques used for the synthesis of ferroelectric thin films, on FTJs state of the art, and on the requisites for their commercialisation. Secondly, it reports in detail the fabrication conditions, used materials, and structural and electrical characterisations of the heterostructure that was taken as a reference for this work.

- **Chapter 4: Reduction of HZO Thickness and Impact of the Bottom Electrode**

The first part is dedicated to a study, from the structural and electrical point of view, of devices characterised by decreasing HZO thickness. The second part is devoted to the investigation of different materials used as bottom electrodes, with the aim of optimising the HZO ferroelectric properties.

- **Chapter 5: Synthesis and Optimisation of Ultra-Thin HZO-Based Ferroelectric Tunnel Junctions**

It reports two successful approaches for the synthesis of ultra-thin HZO layers with enhanced ferroelectricity. The structural and electrical properties of the specimens are analysed, with a special focus on the role played by the

electrode/HZO interfaces on the ferroelectric performances of 6 nm-thick HZO-based stacks. Finally, a FTJ device is presented.

- **Chapter 6: Advanced Applications of HZO-Based Thin Films: Perspectives**

Firstly, it gives an introduction to in-memory and brain-inspired computing. The crossbar fabrication method is described and a crossbar sample fabricated during the thesis is presented. Secondly, it introduces a test protocol for the multi-state programming of the polarisation of HZO-based devices. Finally, preliminary results on the investigation of HZO optical properties are presented. These are studied from an experimental and theoretical point of view, to explore the possibility to use HZO for optoelectronic applications.

Ferroelectricity and ICT Applications

The first chapter of the manuscript is divided in three main sections. The first one recalls the concepts of electric polarisation and ferroelectricity. The second one is devoted to the presentation of ferroelectric materials, with a special focus on hafnium zirconium oxide (HZO). Finally, the third one is focused on ferroelectric-based non-volatile memory devices and neuromorphic systems.

I.1 Electric Polarisation

A system made by two fixed point charges, which are separated by a distance δr and have equal absolute value and opposite sign, is called electric dipole (\vec{p}). When an external electric field is applied to a dielectric material, its charges gain an average non-zero electric dipole ($\langle\vec{p}\rangle$) oriented in the direction of the field and proportional to it. The phenomenon for which a dielectric, subjected to an electric field, gains a dipole moment is called electric polarisation and it can be identified by the macroscopic polarisation vector \vec{P} , which is defined as electric dipole moment per unit volume:

$$\vec{P} = \frac{dN\langle\vec{p}\rangle}{dV} \quad (\text{I.1})$$

Where N is the number of charges of the dielectric in the unit volume V . The

electric polarisation can be classified in two main contributions: polarisation for deformation and orientational polarisation.

I.1.1 Polarisation for Deformation

Let us consider an atom, composed by the nucleus with a positive charge Ze and the electronic cloud, spherically distributed around the nucleus. When a local electric field is applied, the electronic cloud undergoes a deformation and it gains a dipole moment \bar{p} . The nucleus experiences a force $f = Ze\bar{E}$ and the center of gravity of the electronic cloud a force $-f = -Ze\bar{E}$. Consequently, the nucleus, heavier than the electronic cloud, is subjected to a displacement \bar{r} (in the direction of the field) with respect to the center of gravity of the electronic cloud and, since they have opposite charge, they attract with a force \bar{f}' . The equilibrium condition is satisfied when $|\bar{f}'| = |f|$. Since \bar{r} is proportional to the applied electric field, also the electric dipole ($\bar{p} = Ze\bar{r}$) is proportional to it, according to the equation:

$$\bar{p} = \alpha_d \bar{E} \quad (\text{I.2})$$

where α_d is called electronic polarisability.

I.1.2 Orientational Polarisation

A major part of polyatomic molecules is characterised by an asymmetric spatial distribution and, consequently, by an intrinsic dipole moment (\bar{p}_0) independent from the presence of an external electric field. However, it manifests only when an electric field is applied. Indeed, molecules are randomly oriented and the mean value of the dielectric dipole ($\langle \bar{p}_0 \rangle$) is equal to zero, but, when an electric field is applied, the dipoles align in the direction of field and give rise to a non-zero dipole moment. $\langle \bar{p}_0 \rangle$ as a function of \bar{E} can be written as:

$$\langle \bar{p} \rangle = \alpha_0 \bar{E}, \alpha_0 = \frac{p_0^2}{3KT} \quad (\text{I.3})$$

Where K is the Boltzmann constant and T the temperature. Differently from the polarisation for deformation, where the dipole moment of each molecule is proportional to \bar{E} , here it is its mean value to be proportional to \bar{E} . For high values of \bar{E} , $\langle \bar{p}_0 \rangle$ reaches a saturation regime, where all the molecules are aligned

along the field, and it ceases to be proportional to \bar{E} .

Certain dielectric materials present a permanent spontaneous polarisation P_s , which means that the electric polarisation is different from zero in the absence of an external electric field. In this cases the electric polarisation can be expressed as:

$$P = \epsilon_0 \chi E + P_s \quad (\text{I.4})$$

Where ϵ_0 is the vacuum dielectric constant and χ is the electric susceptibility. For this class of materials, the polarisation as a function of \bar{E} follows an hysteresis loop, which is discussed in more details later in the chapter. Ferroelectric materials are characterised by an hysteretic behaviour.

I.2 Ferroelectricity

Ferroelectric crystals exhibit a non-zero value of the spontaneous polarisation even in absence of an external stimulus. They possess at least two equilibrium orientations of the spontaneous polarisation vector that switches between one another upon the application of an electric field. Ferroelectricity exists uniquely in materials with a lattice that lacks an inversion centre, thus ferroelectric properties are detected only in non-centrosymmetric crystals. Most ferroelectric materials are characterised by a transition temperature, called Curie temperature, identified by T_c , at which they are subjected to a structural phase transition. They typically transit from a high-temperature non-ferroelectric or paraelectric phase into a low-temperature ferroelectric phase, with a lower symmetry than the former one. The dielectric permittivity (ϵ) follows the Curie-Weiss law, according to which it decreases as the temperature increases above the Curie point.

$$\epsilon = \epsilon_0 + \frac{C}{T - T_0} \approx \frac{C}{T - T_0} \quad (\text{I.5})$$

Where C is the Curie constant and $T_0 (\leq T_c)$ the Curie-Weiss temperature.

I.2.1 Landau Devonshire Theory

The transition into the ferroelectric phase can be a first order phase transition or a second order phase transition. The former case is associated to a discontinuity of the value of polarisation at the Curie temperature, while, in the latter case, the polarisation goes to zero without a discontinuous change as the temperature increases. Through thermodynamic calculations, it is possible to describe the behaviour of a ferroelectric crystal by considering the expansion of the Landau free energy as a function of the polarisation P . If the one-dimension case is considered, i.e. long uniform rod, the free energy density F can be expanded as:

$$F(P; T; E) = -EP + g_0 + \frac{1}{2}g_2P^2 + \frac{1}{4}g_4P^4 + \frac{1}{6}g_6P^6 + \dots \quad (\text{I.6})$$

where the g_n coefficients are temperature dependent. Odd terms do not appear in the series expansion if the unpolarised crystal is centro-symmetric. At the thermal equilibrium, the value of the polarisation satisfies the relation $\frac{\partial F}{\partial P} = 0$, consequently, P is obtained by solving the equation:

$$\frac{\partial F}{\partial P} = -E + g_2P + g_4P^3 + g_6P^5 + \dots \quad (\text{I.7})$$

The transition into the ferroelectric phase implies that the coefficient g_2 in eq. I.6 becomes zero for a certain temperature, called T_0 .

$$g_2 = \gamma(T - T_0) \quad (\text{I.8})$$

where γ is a positive constant and T_0 is equal or lower than the Curie temperature T_c . The phase transition is of the first order whether g_4 is negative, while it is of second order if g_4 is positive. In a first order transition, the negative value of g_4 forces the coefficient g_6 to be taken into account, in order to prevent F to go to $-\infty$. The equilibrium condition, when the applied electric field is zero, is given by:

$$\gamma(T - T_0)P_s - |g_4| P_s^3 + g_6P_s^5 = 0 \quad (\text{I.9})$$

To satisfy the previous equation, either $P_s = 0$, or

$$\gamma(T - T_0)P_s - |g_4| P_s^2 + g_6P_s^4 = 0 \quad (\text{I.10})$$

It derives that there are two stable minima for the free energy F , which correspond to the two found solutions. On the contrary, when the transition is of second order, g_4 is positive, thus g_6 can be neglected. When $E=0$, the value of the polarisation is obtained by solving the equation:

$$\gamma(T - T_0)P_s - g_4P_s^3 = 0 \quad (\text{I.11})$$

which is solved for $P_s=0$ or for $P_s^2 = (\gamma/g_4)^{1/2}(T - T_0)^{1/2}$. Since g_4 is positive and γ is chosen to be positive, the only possible solution is found for $T < T_0$, with T_0 Curie temperature. The minimum of the Landau free energy at zero applied field is at $|P_s| = (\gamma/g_4)^{1/2}(T_0 - T)^{1/2}$. Figure I.1 shows the temperature dependent free energy vs polarisation for the first order and the second order phase transitions.

I.2.2 Ferroelectric Domains

The spontaneous polarisation, P_s , of a ferroelectric material is usually not aligned along the same direction throughout the whole crystal. Ferroelectric domains form to minimise the electrostatic energy associated to the depolarising field, discussed in section I.2.6, and elastic energy derived from the mechanical stress that follows the paraelectric-ferroelectric transition. At the Curie point, the onset of the spontaneous polarisation leads to the formation of a surface charge, which is responsible for the creation of the depolarising field (E_d). This is oriented opposite to the spontaneous polarisation and it generates whenever the latter is not homogeneous. Since E_d can take considerably high values (of the order of MV/m), the formation of a single ferroelectric domain is energetically unfavourable, and, to minimise its electrostatic energy, ferroelectric materials split into multiples domains with oppositely oriented polarisation. Regions that separate adjacent ferroelectric domains are called domain walls and can be identified as ferroelectric and ferroelastic. Ferroelectric domain walls have a different orientation with respect to the spontaneous polarisation vector, while, ferroelastic ones differ in orientation from the spontaneous strain tensor. Domain walls that separate regions where the polarisation is antiparallel to P_s are called 180° walls and the ones that divide domains with perpendicular polarisation are called 90° walls. 180° walls are purely ferroelectric, 90° are both ferroelectric and ferroelastic, since they differ in orientation from the polarisation vector and from the spontaneous strain tensor.

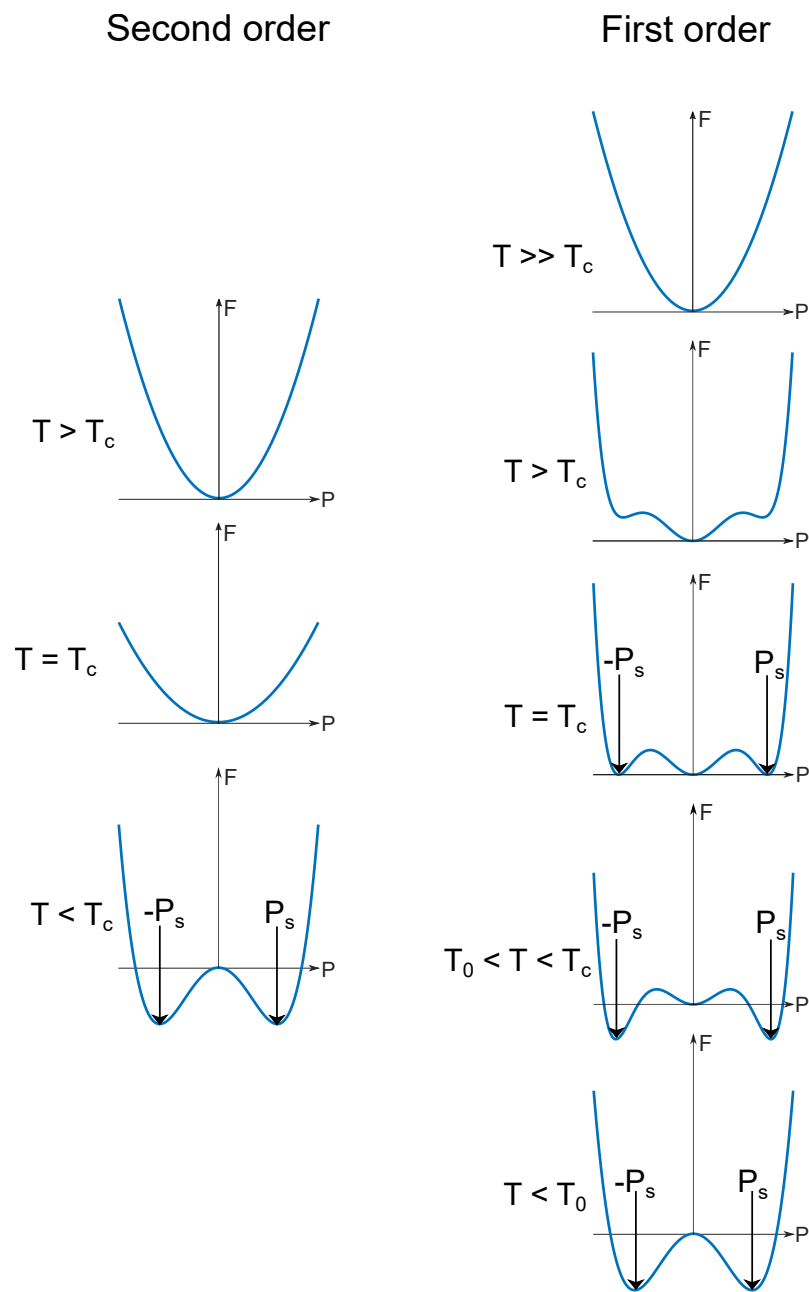


Figure I.1: Free energy *versus* polarisation for the second-order and the first-order phase transitions.

Ceramic and polycrystalline ferroelectrics are generally split in many domains due to the complex elastic and electric boundary conditions at each crystalline grain. If the spontaneous polarisation vector of each domain is randomly distributed, the result is a zero net polarisation. However, polycrystalline ferroelectric materials can be brought into a polar state by the so-called poling process, which consists on applying a strong electric field that is responsible for the re-orientation of the domains along the field. The polarisation at zero applied electric field is called remanent polarisation (P_r).

I.2.3 Polarisation switching

The most relevant feature of ferroelectric materials is the reversal of the polarisation upon the application of an electric field (polarisation switching mechanism). The re-orientation of domains by the electric field is responsible for the occurrence of the ferroelectric hysteresis loop, in figure I.2. For small values of E , P rises linearly with the amplitude of the applied field. In this regime, E is not strong enough to switch domains with an unfavourable polarisation direction. Large values of E trigger the switching of P in the direction of E itself, and P response becomes strongly non linear. Once the domains are all aligned in the direction of E , P turns back to be linear. A decrease of the applied electric field brings to a back-switching of some domains, but, when it reaches zero, P still registers a positive value. In order to bring P to zero, E has to be reversed. A negative increase of the latter leads to new alignment of dipoles and, eventually, the saturation is reached. To complete the cycle, E is then reduced once more to zero. The value of the field at which $P=0$ is called coercive field (E_c).

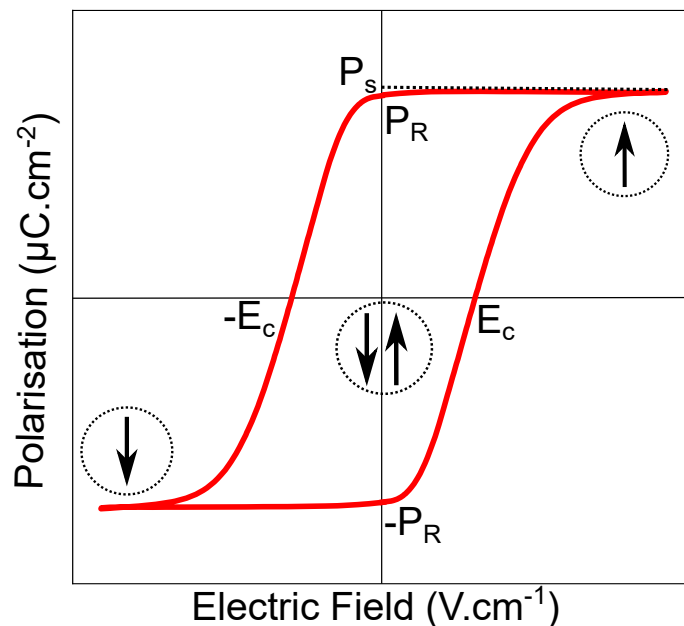


Figure I.2: Ferroelectric hysteresis loop: polarisation *versus* electric field.

In the ideal case, the hysteresis loop is symmetric, $P_r = -P_r$ and $E_c = -E_c$, however, many parameters as defects, thickness of film, mechanical stress, preparation conditions, and thermal treatment might affect its shape.

The polarisation reversal is not uniquely associated to a single mechanism, but it is due to many factors, such as the growth of existing anti-parallel domains, the

domain walls motion, and the nucleation and growth of new anti-parallel domains [1]. The presence of imperfections and defects is responsible for the inhibition of domain walls motion and it interferes with the polarisation switching mechanism. Defects, such as oxygen vacancies or electrons trapped in domain wall areas, are said to pin or clamp the domains, preventing their switching.

I.2.4 Antiferroelectricity

The antiferroelectricity was firstly discovered in the perovskite lead zirconate (PbZrO_3) in 1950 by Shirane *et al.* [2] and by Sawaguchi *et al.* [3] in two independent publications. Antiferroelectricity can be described as the ability to induce a phase transition between an antiferroelectric phase to a ferroelectric phase, with different physical properties. In an antiferroelectric crystal, the spontaneous polarisation of two neighbouring cell points in opposite directions, resulting in a zero net polarisation. However, if an external electric field is applied, the electric dipole moments begin to align along the direction of the field and, starting from a certain value of $E > 0$, an hysteresis loop forms. Figures I.3 and I.4 show a schematic of antiferroelectric and ferroelectric phase transitions, and the P - E curve that characterises antiferroelectrics. The same trend is obtained for $E < 0$. As ferroelectric materials, also antiferroelectrics are characterised by a Curie temperature, above which they cease to be antiferroelectric.

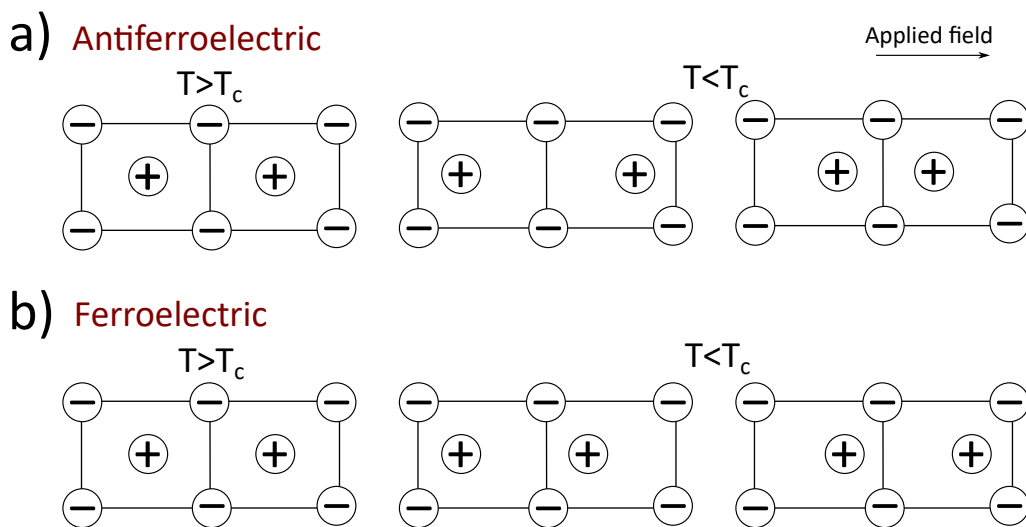


Figure I.3: a) Schematic of the antiferroelectric phase transition. b) Schematic of the ferroelectric phase transition.

Antiferroelectric materials are of interest for certain technological applications,

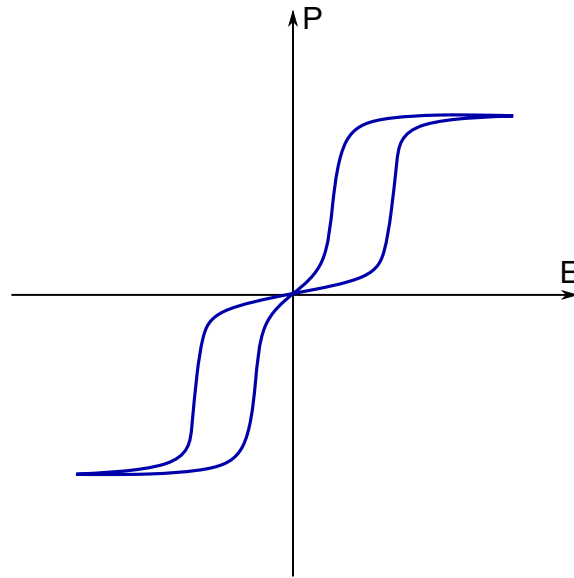


Figure I.4: Example of the P - E characteristic of antiferroelectric materials.

for instance, super capacitors and high energy storage devices [4], [5]. However, reasons why antiferroelectricity manifests have not been fully comprehended since its discovery. More recently, a study by Tagantsev *et al.* [6] demonstrated that origin of antiferroelectric state in PbZrO_3 , which is considered the archetype of antiferroelectric materials, is related to a single ferroelectric instability that allows the system into the antiferroelectric phase.

I.2.5 Phonon Contribution to Ferroelectricity

In order to better understand local mechanisms of the phase formation, it is worthy to mention the contribution of the phonons to ferroelectricity. Ferroelectric polarisation originates from an unbalance of positive and negative charges inside the crystal, which are responsible for a non-zero dipole moment at no applied electric field. When the temperature is different from absolute zero, atoms in the crystal vibrates at a certain frequency around their equilibrium position. The latter vibrations are described by phonon modes, which are described by phonon dispersion spectra that characterise a certain material. The local displacement of atoms, which is responsible for the development of ferroelectricity, is called soft mode and can be considered as a wave in the crystal. Below the Curie temperature T_c , the wavelength of the optical soft mode increases, becoming infinite in case of an infinite crystal. The material is then in the polar phase. Above T_c , the frequency of the soft mode is too high to align the dielectric dipoles, resulting in

the paraelectric phase. It is straightforward that, in order to sustain the ferroelectric soft mode, it is necessary the presence of multiple unit cells. Consequently, a minimum number of the latter is necessary to stabilise ferroelectricity, which can be ultimately considered as the collective response of multiple unit cells. This constraint imposes an obvious limit to the scalability of ferroelectric materials, which is known as intrinsic size effect and which, and, in the case of a semi-infinite crystal, is revealed by a computational research to be three unit cells [7]. Ferroelectric properties are strongly influenced by the size of the ferroelectric and changes of the latter are known as scaling effects. They can be identified as a decrease of the remanent polarisation, a decrease of the dielectric permittivity, a rise of the coercive field, and a suppression of the phase transition temperature. Furthermore, thin ferroelectric films are affected by the strain induced by electrodes and more defects with respect to their bulk counterpart [8], since they are often synthesised at lower temperature. The interfaces with electrodes may also influence the ferroelectric properties, due to the formation of interfacial layers that do not possess the same properties of the bulk. The role of the electrodes and interface properties will be extensively discussed in chapters IV and V. Finally, the screening of the polarisation charges becomes more and more important as thin films are concerned, since even a metallic electrode is not sufficient to entirely screen the spontaneous polarisation charges. More difficult task is for conductive nitride and oxides electrodes [9].

Nevertheless, nowadays the size reduction of ferroelectric devices is of great importance for technological applications. This means that the optimisation of the ferroelectric properties of thin films is crucial and it must be achieved through the optimisation of the fabrication conditions, synthesis techniques, and materials used as electrodes.

I.2.6 Factors that Affect Ferroelectric Properties

In this section, some of the conditions that could impact the ferroelectricity are analysed. The properties of a non-ideal ferroelectric are strongly influenced by micro-structure, defects, compositional inhomogeneity, external field, and domain wall displacement.

Depolarising Field

The depolarising field, mentioned in section I.2.2, is generated by uncompensated charges [10] associated to a dielectric layer (often identified as dead layer) at the ferroelectric/electrode interfaces. Its effect translates in a tilt of the hysteresis loop, which indicates the presence of a low-dielectric constant layer in series with the ferroelectric. The depolarising field associated with a dielectric layer can be identified as $E_d = -Pd/\epsilon_d t$, where ϵ_d and d are the permittivity and the thickness of the dielectric layer, t is the thickness of the ferroelectric, and P is the polarisation [11]. If the condition $d \ll t$ is satisfied, the total electric field E_f across the ferroelectric is given by the expression:

$$E_f = E - \frac{Pd}{\epsilon_d t} \quad (\text{I.12})$$

With E being the applied field. The tilt of the hysteresis loop, considered as the slope of the hysteresis at the coercive field E_c , can be described by the equation:

$$\left(\frac{\partial E}{\partial P}\right)_{E_c} - \left(\frac{\partial E_f}{\partial P}\right)_{E_c} = \frac{d}{\epsilon_d t} \quad (\text{I.13})$$

For a perfectly squared hysteresis loop $\left(\frac{\partial E_f}{\partial P}\right)_{E_c} = 0$, so the tilt enhances as the ratio d/t increases, since slope of measured loop is $d/\epsilon_d t$.

Fatigue, Wake-up Effect, Endurance, Retention, and Imprint

Other contributions, which are linked to the ferroelectric behaviour of ferroelectric materials and that are of interests for technological applications are listed below [11]. Figure I.5 shows the effect of the latter on the performances of a ferroelectric-based device. Some of these aspects will be discussed more extensively in the following chapters.

- **Fatigue**

The ferroelectric fatigue, which is defined as a loss of switchable remanent polarisation as a function of the number of bipolar switching cycles, is generated by defects. In particular, the elements that are responsible for the occurrence of this phenomenon are: the presence of surface layers [12], domain walls pinning by defects in the wall regions [13], charge trapping

and charge injection [14], clamping of the polarisation switching by volume defects [15], suppression of nucleation of oppositely oriented domains at the surface [16], damages at the ferroelectric/electrodes interfaces [17], and oxygen vacancies [18]. It is worthy to provide more details on the role of oxygen vacancies on the ferroelectric fatigue. In the literature, several models are based on the observation that oxygen vacancies accumulate at the ferroelectric/electrode interfaces during the cycling process [19]. This results in oxygen deficient regions in the bulk, which partially screens the ferroelectric film from the applied field, resulting in a polarisation loss [20]. According to this hypothesis, the fatigue is attributed to pinning of domain walls by the generated oxygen vacancies that are responsible for a high injection of electronic charges from the electrodes. Consequently, a small number of oxygen vacancies would reduce injection of charges, thus limiting the domain wall pinning and lowering the fatigue.

- **Wake-up Effect**

The wake-up refers to an increase of the ferroelectric remanent polarisation, P_r , as a function of voltage cycling. Multiple factors contribute to the wake-up effect, which is reported in perovskites as well as in fluorite-structure-based ferroelectrics.

- **Endurance**

The endurance is the capability of a device to retain a given level of polarisation as a function of the accumulated rewriting cycles.

- **Retention**

The retention is the capability of device to retain a given level of polarisation after a given period from the write operation.

- **Imprint**

The imprint is the tendency of a ferroelectric material to develop a preferential state, once it has been forced to that state over a prolonged period of time. The consequence of the imprint is that the device might not be able to maintain a different state for a significantly long time, possibly causing data loss [21],[22].

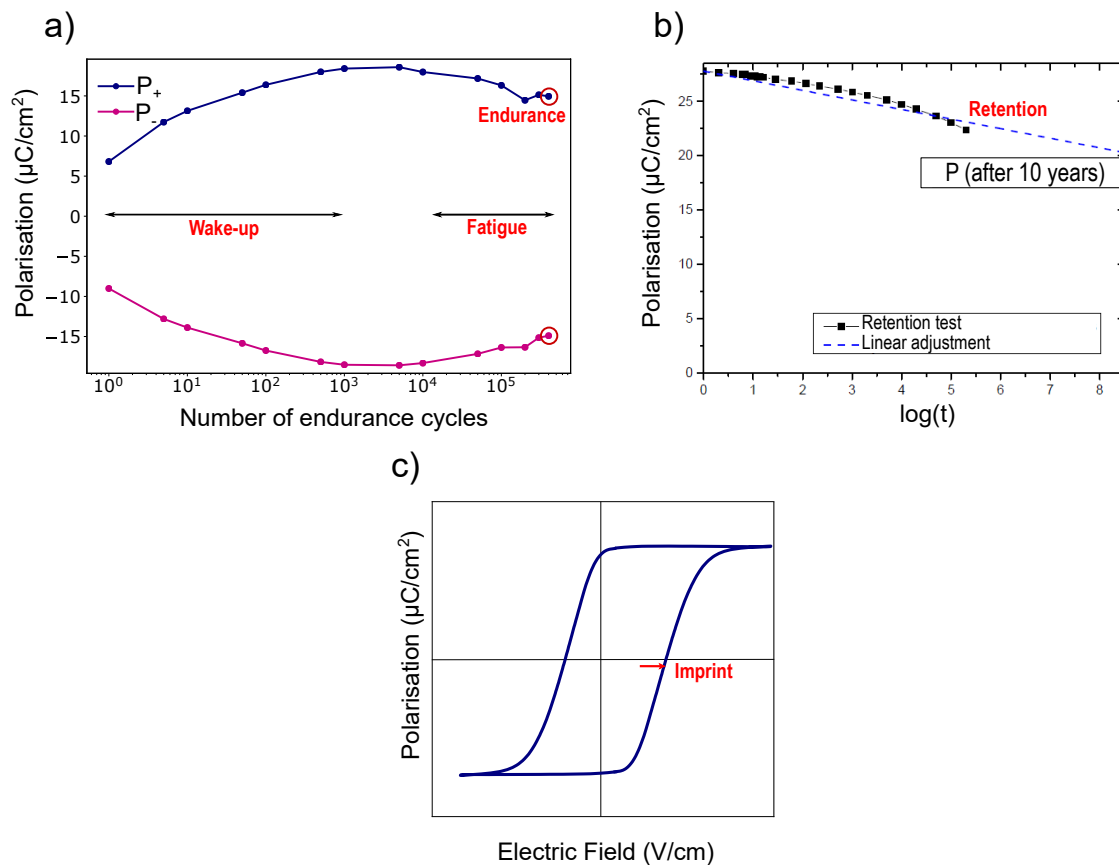


Figure I.5: a) Evolution of the polarisation as a function of the applied voltage cycles. Wake-up and fatigue states, and the value of the endurance are highlighted. b) Retention. c) Imprint that implies a right or left shift of the hysteresis loop.

I.3 Ferroelectric Materials

I.3.1 Perovskites

A well-known and extensively investigated class of ferroelectric materials is perovskite oxides [23]. They are identified by the general formula ABO_3 , where A and B represent the electropositive elements forming cations, which transfer electrons to oxygen. For these materials, the ferroelectricity is associated to a displacement of the B-site ion between the two stable states described in section I.2.1. Figure I.6 shows the schematic of a unit cell of the perovskite BaTiO_3 (BTO).

The most famous and used perovskites are: $\text{Pb}(\text{Zr},\text{Ti})\text{O}_3$ (PZT), BTO, and BiFeO_3 (BFO). Thanks to their robust ferroelectricity, perovskites have been considered promising for many kind of applications in the electronic industry, of particular interest is their use for ferroelectric memory devices. However, these oxides are characterised by important limitations, especially associated to their in-

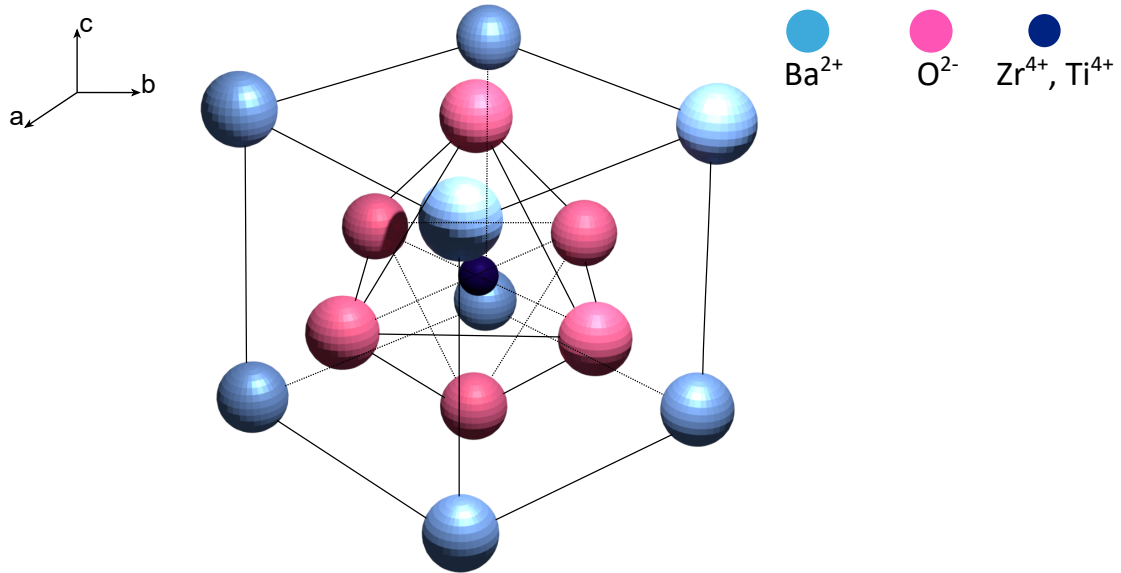


Figure I.6: Schematic of the perovskite BTO unit cell.

tegration into the silicon-based industry [24]. For instance, most of them have a crystallisation temperature that exceeds 600 °C, which is in contrast with the constraints imposed by CMOS process in back-end-of-line (BEOL) that requires annealing temperatures below 450°C [25]. Because of these reasons, research has been focused on studying new materials that could overcome these limits.

I.3.2 Hafnium Oxide

The turning point came with the discovery of ferroelectricity in silicon-doped hafnium oxide (HfO_2) in 2011 by Böске *et al.* [26], [27]. Hafnium oxide, HfO_2 , is a fluorite-crystal-structure oxide that, prior to the discovery of its ferroelectric properties, had been extensively used in micro- and nano-electronic applications as high-dielectric constant (high-k) gate material. For the latter applications, amorphous HfO_2 is preferred to crystalline HfO_2 , because the presence of grain boundaries promotes leakage currents [28]. Since the discovery of ferroelectricity, research on HfO_2 has attracted great interest, in particular for the implementation of non-volatile memory devices that are discussed in section I.4.

The phase diagram of bulk HfO_2 , figure I.7, is characterised by three stable centro-symmetric phases, which are the monoclinic phase (m-phase), the cubic phase (c-phase), and the tetragonal phase (t-phase), and by three unstable orthorhombic phases, to one of which ferroelectricity is associated. At room temperature, the most stable phase is the monoclinic that is characterised by the space

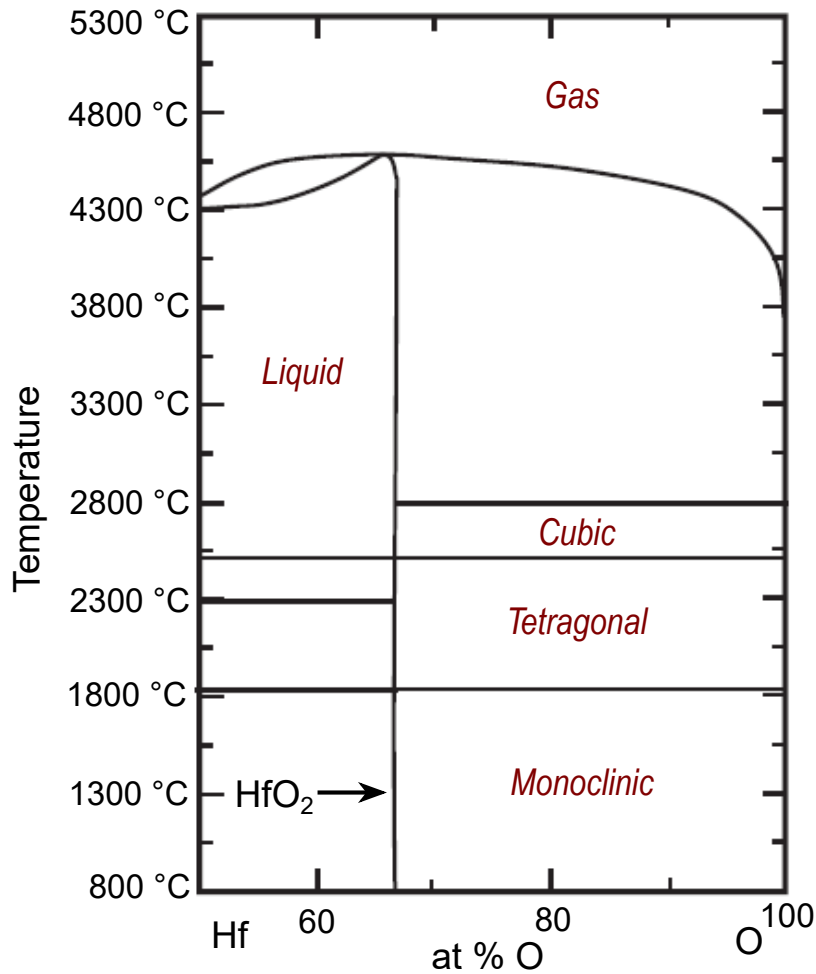


Figure I.7: Phase diagram of Hf-O. Reprinted from "Ferroelectricity in Doped Hafnium Oxide Materials Properties and Devices" [29].

group $P2_1/c$, and which consist of a sevenfold oxygen coordination around the Hf^{4+} ions with four O^{-2} at the base of the cube, an O^{-2} ion at the upper corner, and two O^{-2} at the mid point of the cube [30]. Beside the monoclinic phase, other two centro-symmetric crystal structures, stable at high temperature and high pressure, had been reported. These are the tetragonal phase, space group PA_2/nmc [31], and the cubic phase, space group $Fm\bar{3}m$ [31]. The phase transformations from the monoclinic to the tetragonal and cubic phases occurs above 1700°C and 2600°C, respectively [30][32]. The phase transition from the monoclinic to the tetragonal phase is a martensitic transformation, which occur over a finite temperature range. In addition to centro-symmetric phases, various orthorhombic phases exist: orthorhombic I phase (o-phase, space group $Pca2_1$), orthorhombic II phase (o-II phase, space group $Pnma$), and polar orthorhombic III phase (f-phase, space group $Pca2_1$). The phase transition from the m-phase to the o-phase is observed at a compressive pressure of about 4-12 GPa in bulk [33]. The oII-phase is obtained

at very high compressive pressure, around 20 GPa [33]. Finally, the f-phase forms from the m-phase under asymmetric stress conditions [34] or from the t-phase through a martensitic transformation during cooling. However, f-phase formation has only been observed in thin films and not in bulk. It is a metastable phase that exists in the range of thickness of ~ 10 nm and can only be stabilised under anisotropic strain conditions [35]. Figure I.8 (A-F) reports unit cells of centrosymmetric and non-centrosymmetric phases of HfO₂. Table I.1 summarises the phases of HfO₂, their symmetry group, and the unit cell parameters [35]. In the remainder of the manuscript the polar orthorhombic or ferroelectric phase is identified by f-phase or o-phase.

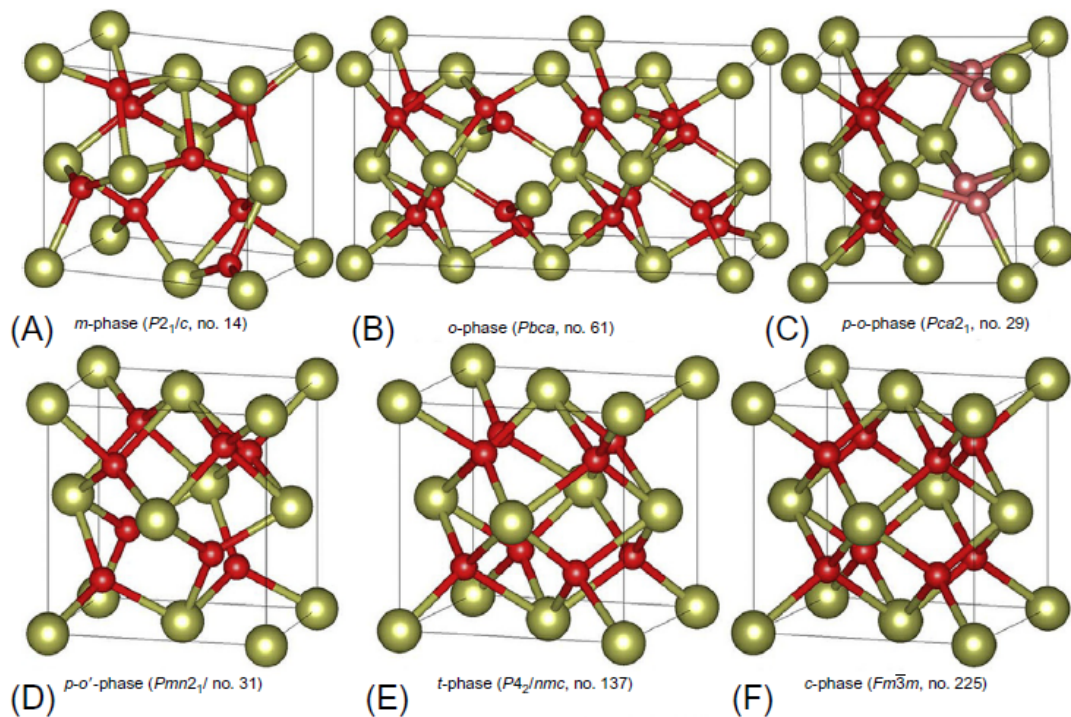


Figure I.8: Six crystal structures of HfO₂. Reprinted from "Ferroelectricity in Doped Hafnium Oxide Materials Properties and Devices" [29].

Dielectric Properties of Hafnium Oxide

Ferroelectricity in HfO₂ was discovered in the frame of the development of thin films for memory applications, which require high quality crystal structures. As mentioned before, HfO₂ has been widely investigated as high-k gate material, because of its high dielectric constant (k) and large band-gap (5.6 eV). Prior to HfO₂, other materials had been exploited as gates, such as SiO₂, which, however, is characterised by a small dielectric constant (~ 4), and perovskites that have a

Table I.1: Phases of HfO₂.

Phase	Phase acronym	Space group Nr.	H-M notation	Unit cell parameter
Monoclinic phase	m-phase	14	P2 ₁ /c	$a=5.15 \text{ \AA}(x), b=5.20 \text{ \AA}(y), c=5.32 \text{ \AA}(z)$
Tetragonal phase	t-phase	137	P4 ₂ /nmc	$a=c=5.09 \text{ \AA}, b=5.18 \text{ \AA}$
Cubic phase	c-phase	225	Fm3m	$a=b=c=5.12 \text{ \AA}$
Orthorhombic I phase	o-phase	61	Pbca	$a=2 \times 5.04 \text{ \AA}, b=5.09 \text{ \AA}, c=5.26 \text{ \AA}$
Orthorhombic II phase	oII-phase	62	Pnma	$a=3.334 \text{ \AA}, b=5.556 \text{ \AA}, c=6.505 \text{ \AA}$
Orthorhombic III phase	f-phase	29	Pca2 ₁	$a=5.07 \text{ \AA}, b=5.26 \text{ \AA}, c=5.08 \text{ \AA}$

large dielectric constants, but small bandgaps (3-5 eV). A computational study by Zhao and Vanderbilt [36] revealed that values of k for monoclinic, tetragonal, and cubic phases of HfO₂ are 16, 70, and 29 respectively.

Materials Used as Dopants for Hafnium Oxide

To better understand some of the characteristics of the dopant materials compatible with HfO₂, it is worthy to recall few rules [37] that are useful to suggest different metal oxide (M_xO_y with M metal cation) compound combinations that could form a continuous solid solution. These are:

- The atomic radius of the solute and the solvent must be no more than $\approx 15\%$ different
- The crystal structure of each of the oxides must be similar
- Each of the M ions must have the same valency
- The formation of a new phase can limit the solid solubility

The first dopant that was used in the demonstration of ferroelectricity in HfO₂ was Si [26]. The latter was reported to play two important roles, such as to increase the crystallisation temperature of Si:HfO₂, favouring a controlled crystallisation after the deposition of a top electrode, and to reduce the stability of the monoclinic phase. Afterwards, systematic experimental and theoretical studies on

the effects of various dopants were performed, in order to optimise the ferroelectric performances of HfO₂-based compounds, which are strongly correlated to the amount of orthorhombic phase [38–40]. Findings showed a dependence of the remanent polarisation on the ionic radius of the dopant, in particular, large dopants (in a certain range [38]) induce a higher remanent polarisation with respect to small ones. However, other parameters were shown to affect the ferroelectricity of doped HfO₂, i.e. doping concentration and growth method [39], leading to quantitative differences in the ferroelectric performances. Table I.2 lists several materials used as dopants for the synthesis of ferroelectric HfO₂ thin films.

Table I.2: Examples of dopant materials used for HfO₂.

Dopants	Reference
Si	[26]
Zr	[27]
Y	[41], [42]
Al	[43]
Gd	[44], [45]
Sr	[46]
La	[47]
Zr	[27]
Sm	[48]
St	[38]
Mg	[38]
Ba	[38]
Co	[38]
Ni	[38]
Ga	[38]
In	[38]

It is worthy to mention that ferroelectric behaviour was demonstrated also in undoped HfO₂ thin layers [49, 50].

Zirconium-doped Hafnium Oxide

Zirconium oxide (ZrO₂) was investigated as dopant due to its structural and chemical similarity to HfO₂. Its use as dopant results in the formation of a continuous

monoclinic and fluorite-type solid solution [30, 51]. Moreover, it was shown in literature that for Zr-doped HfO_2 thin films of several nanometres, the phase transition temperature from monoclinic to tetragonal phase is significantly reduced [30, 51–53]. The latter aspect is of great interest, because this phase transition is accompanied by the development of ferroelectricity. A study conducted by Müller *et al.* [54] reported the composition- and temperature-dependent ferroelectric phase transition, covering the full mixing range of HfO_2 - ZrO_2 thin films. The investigation of structural properties was mainly conducted by glancing incidence X-ray diffraction (GI-XRD) and revealed a composition-dependent tetragonal to orthorhombic to monoclinic phase transition in HfO_2 - ZrO_2 thin films, starting from Zr-rich solid solutions. A non-centrosymmetric polar phase, to which ferroelectricity is associated, was stabilised at room temperature. The results of this study showed an evolution from the paraelectric HfO_2 to the ferroelectric HfO_2 - ZrO_2 to the anti-ferroelectric ZrO_2 . Figure I.9 reports the P - V and C - V curves of HfO_2 - ZrO_2 -based capacitors for different Zr content.

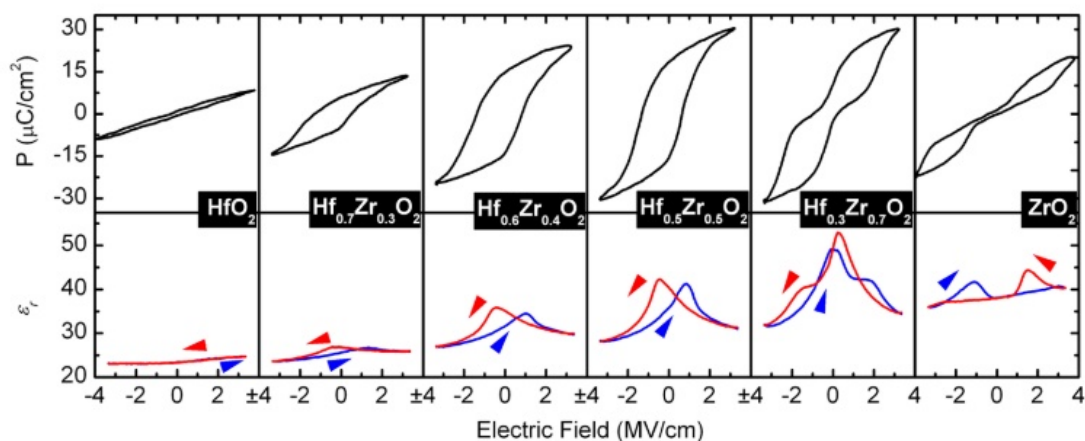


Figure I.9: $P - V$ curves and $C - V$ curves of HfO_2 - ZrO_2 -based capacitors at room temperature, for different Zr content. The curves show an evolution from the paraelectric HfO_2 to the ferroelectric HfO_2 - ZrO_2 to the antiferroelectric ZrO_2 . Reprinted from Müller *et al.*, "Ferroelectricity in Simple Binary ZrO_2 and HfO_2 ", Nano lett. 2012, 12, 4318-4323.

This suggests that Hf-rich samples are characterised by a predominantly monoclinic structure, while Zr-rich samples crystallise in a tetragonal phase. Ultimately, the ferroelectric properties observed in HfO_2 - ZrO_2 thin films are the result of the phase transition from the tetragonal to the polar orthorhombic phase during cooling. Many works have shown that the 1:1 Hf:Zr substitution compound is of particular interest for its high value of the remanent polarisation [54, 55]. Finally,

in 2018 Wei *et al.* [56] reported the stabilisation of a ferroelectric rhombohedral phase (r-phase) of space group $R3m$ in epitaxial $\text{Hf}_{0.5}\text{Zr}_{0.5}\text{O}_2$. The formation of the r-phase implies the growth of highly oriented cubic phase crystallites, which can be synthesised during the epitaxial growth. Thanks to epitaxial strain, the crystallites can be deformed into a rhombohedral polar structure.

Because of its high value of remanent polarisation and low crystallisation temperature [27], in this work $\text{Hf}_{0.5}\text{Zr}_{0.5}\text{O}_2$ was used as ferroelectric material for the synthesis of ferroelectric capacitors and ferroelectric tunnel junctions.

I.4 Ferroelectric Non-volatile Memory Devices

Ferroelectric materials have been considered very promising for non-volatile memory applications, in particular the advantages that they offer are related to low energy and high operation speed. In this section some examples of non-volatile ferroelectric-based memory devices are presented, with a special focus on ferroelectric tunnel junctions (FTJs).

I.4.1 Ferroelectric Random Access Memory

The concept of ferroelectric random access memory (FRAM) was firstly proposed by Dudley Allen Buck, a researcher at MIT, who used BTO as ferroelectric material [57]. The development of FRAMs began in the late 1980s and their commercialisation based on PZT took place at the beginning of the 1990s. However, both perovskites, BTO and PZT, suffer from issues related to the scaling of the layer thickness and compatibility with the CMOS process [58]. The working principle of FRAMs is based on the Landau theory of the phase transition, discussed in section I.2.1, for which, below the Curie temperature, two stable states of polarisation exist: $-P_r$ and P_r , which represents logic-low "0" and logic-high "1", respectively. The architecture of a FRAM memory cell is similar to the one of a dynamic random access memory, except for the use of the ferroelectric material, instead of the dielectric to achieve the non-volatility. In a FRAM cell, the storage ferroelectric capacitor is connected in series to a transistor in 1 Transistor - 1 Capacitor architecture. During the write operation of a "1" or "0", the word line is pulsed to enable the access to the storage capacitor, while during read operation, a voltage

is applied to the plate line and the word line is simultaneously pulsed. Since the read operation is destructive, a further rewriting step is required to bring back the memory cell in the initial state. Figure I.10 illustrates the working principle of a FRAM.

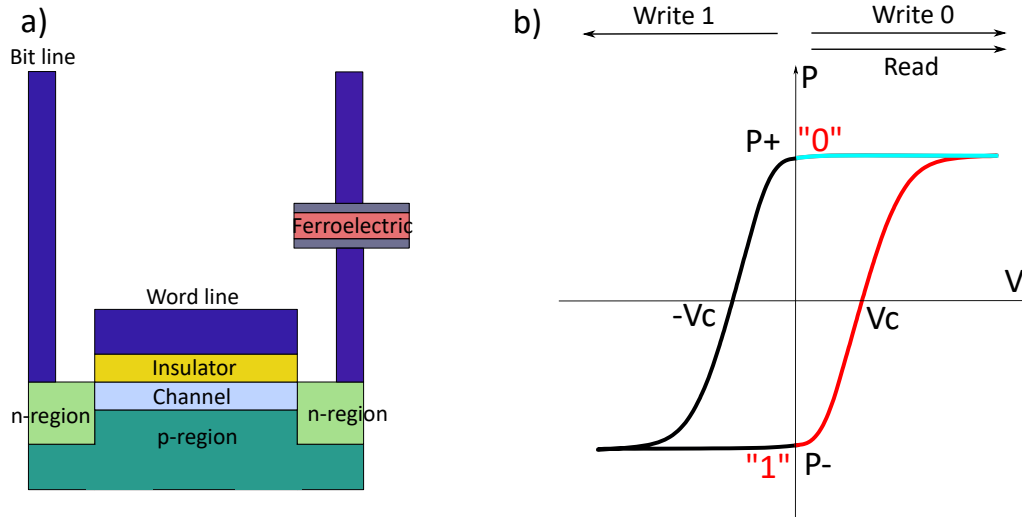


Figure I.10: a) Architecture of a 1T-1C memory cell. b) Readout operation of a FRAM, P - V loop.

Hafnium Oxide-Based FRAM

Because of the scalability issues and the high crystallisation temperature, the synthesis of PZT-based FRAM was not pursued, but the discovery of ferroelectricity in CMOS-compatible hafnia-based compounds retrieved the interest for ferroelectric memory devices. Contrary to perovskites, which limit the FRAM to a planar structure [59], HfO_2 -based ferroelectrics can be integrated in 3D capacitors. Moreover, they are characterised by a value of remanent polarisation similar to the one of PZT and by a larger coercive field, which results in a longer retention time. Because of the existence of ferroelectricity in HfO_2 -based thin films, HfO_2 -based FRAMs are eligible for scaling and integration in capacitors structures with high aspect ratio. Nevertheless, work has still to be done to improve their endurance and reliability.

I.4.2 Ferroelectric Field Effect Transistor

Ferroelectric field effect transistors (FeFET) can be related to conventional metal-oxide-semiconductor FETs, where the insulating layer is replaced by the ferroelec-

tric material in a metal-ferroelectric-insulator structure. A buffer layer is often inserted between the semiconductor substrate and the ferroelectric, in order to facilitate the growth of the latter onto the silicon substrate. To write the logic-high "1" or logic-low "0", a tension (V_g), higher than coercive voltage (V_c) of the ferroelectric, is applied to the gate. When $V_g > V_c$, the logic value "1" is written, when $V_g < -V_c$, the logic value "0" is written, figure I.11. The read operation is performed by applying a tension $-V_c < V_g < V_c$, in order to not write any bit at the same time as the reading process. The read current depends on resistance state of the channel, which increases or decreases as a function of the ferroelectric polarisation state. The performances of a FeFET are evaluated according to the so-called memory window (equation I.14), which can be defined as the difference between the voltage necessary to induce the polarisation state associated to the logic "1" and the one associated to the logic "0".

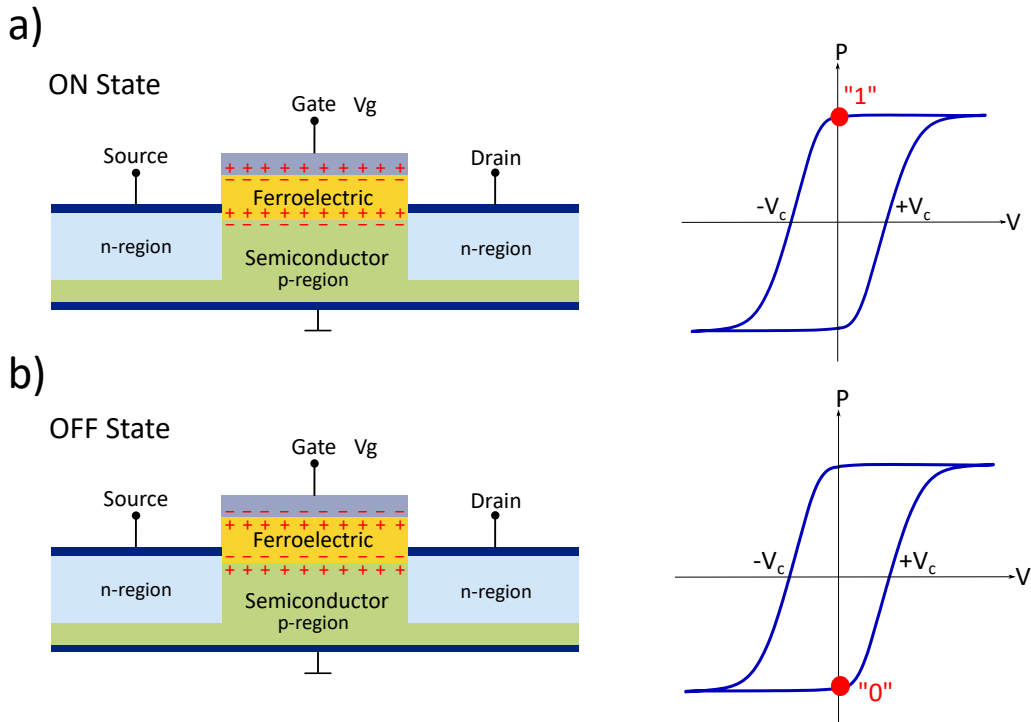


Figure I.11: Operation principle of a FeFET. a) On the left, the FeFET in the "ON" state, on the right the corresponding state in the hysteresis loop. b) On the left the FeFET in the "OFF" state, on the right the corresponding state in the hysteresis loop.

$$MW = |V_{th}("1")| - |V_{th}("0")| \quad (I.14)$$

Equation I.14 can also be rewritten as a function of the flat-band voltage, V_{FB} :

$$MW = V_{FB+} - V_{FB-} = 2E_c t_{FE} = \Delta V_{FB} \quad (I.15)$$

Where E_c is the coercive field of the ferroelectric and t_{FE} its thickness.

Hafnium Oxide-Based FeFET

Perovskite-based FeFETs experienced the same issues as FRAM systems, but FeFETs based on HfO_2 are considered promising candidates for embedded non-volatile memory devices, thanks to their high coercive field that enables their scalability and improves the data retention. However, a drawback of the use of HfO_2 is linked with the presence of defects, especially at the substrate/electrode interface, which cause low endurance and data losses [60, 61].

I.4.3 Negative Capacitance Field Effect Transistor

The concept of negative capacitance (NC) was first proposed by Salahuddin and Datta in 2008 [62]. The idea was to use a ferroelectric layer as a gate insulator in a FET and then stabilise it in a negative capacitance state below a critical thickness of the film. In the latter state, the ferroelectric would be completely depolarised and it would not show any hysteretic behaviour of the polarisation, figure I.12. This state enables an amplification of the surface potential of the semiconductor with respect to the gate voltage, meaning that the sub-threshold swing of this NCFET could be lower than the fundamental Boltzmann limit, $\ln(10)k_b T/e$ (k_b Boltzmann constant, T temperature, e elementary charge) [63]. The interest of this aspect is associated to a reduction of the supply voltage and so of the power consumption, which increases exponentially for decreasing dimensions of the device, if the Boltzmann limit is not overcome. As far as negative capacitance effects are concerned, it is important to make a distinction between two experimental findings that have a different physical origin and characteristics: transient NC effect and stabilised NC effect. The transient NC effect [64] can be measured during the polarisation switching and is accompanied by a P - E hysteresis, which might not be of use in low-power logic transistors. In this case small-signal voltage amplification is not possible [62]. The stabilised NC effect does not show any hysteresis and could allow small-signal voltage amplification. Even though they would be ideal

for the implementation of devices based on stabilised NC effect, only transient NC effect was demonstrated in HfO₂-based ferroelectrics [65].

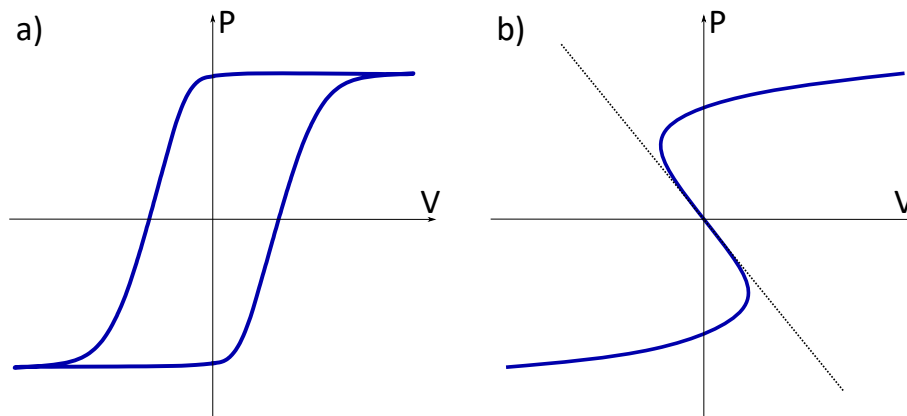


Figure I.12: a) P - V characteristic of ferroelectric-based devices. b) P - V characteristic of negative capacitance-based devices.

I.4.4 Ferroelectric Tunnel Junctions

This section gives an exhaustive presentation of the ferroelectric tunnel junction (FTJ) device, object of this thesis, including the physical principle on which it is based and an overview on the state of the art. FTJs, which consist in a three-layer structure where two electrodes sandwich an ultra-thin ferroelectric film, have been the subject of an intense research for their promising application in nanoelectronic [66]. The concept of FTJ was first proposed by Esaki *et al.* [67] in 1971, pointing out the possibility of a change in the tunnel resistance thanks to the polarisation reversal. The polarisation of a ferroelectric layer, pointing towards an electrode or the other, can be switched by the application of an external voltage across the barrier. However, experimental studies on FTJs were neglected for few decades, due to the belief that ferroelectricity would not be possible below a critical thickness required for electrons to tunnel. More recently, thanks to improvements of available experimental techniques, such as growth conditions and advanced characterisation tools, FTJs regained the interest of the scientific community, as ferroelectricity is being demonstrated in thinner and thinner layers [68].

Physical Mechanism

The physical mechanism on which FTJs rely on is the tunnel electroresistance effect (TER): the reversal of spontaneous polarisation of the tunnel barrier modifies

the internal electric field, which alters the potential profile inside the barrier. The resulting resistance change is written as:

$$TER = \frac{R_{P \rightarrow} - R_{P \leftarrow}}{R_{P \leftarrow}} \times 100\%. \quad (\text{I.16})$$

The polarisation charges present at the surface of the ferroelectric, depending on their sign, attract or repel electrons over a short distance (few nm for metals, tens of nm for semiconductors) inside the electrodes. The distance over which the electrons screen the polarisation charges, screening length, is defined by the Thomas-Fermi theory and it is a function of the electron density at the Fermi level. However, the screening distance strongly depends on the physical properties of the ferroelectric/electrode interface and can be rather different from the prediction of the Thomas-Fermi model [69]. This is particularly true for semiconductor electrodes, where imperfect screening of the polarisation charges is responsible for an additional electrostatic potential at the interface, which is proportional to the screening length and modifies the tunnel barrier profile. For a better insight, let us first consider a rectangular potential barrier (same barrier heights on both sides). The effect of the polarisation charges is to produce an asymmetry of the electronic potential profile, and, once the polarisation is reversed by an external voltage, the asymmetry is also reversed. Since the tunnel probability depends exponentially on the barrier height, the resistance of the junction depends on the polarisation direction, figure I.13.

One of the main consequences of this principle is that the asymmetry of the structure is a fundamental requirement to modulate the current transmission across the ferroelectric barrier. That does not necessarily mean that the electrodes must be made of different materials, since this asymmetry can rise also from factors, such as defects or different interface terminations.

Electronic Tunnelling Mechanisms

The electronic conduction across the ferroelectric layer in FTJs should mainly depend on the following transport mechanisms:

- **Direct Tunnelling**

Direct tunnelling is a quantum-mechanical phenomenon, which occurs below a certain thickness of few nanometers. The electrons can flow from one

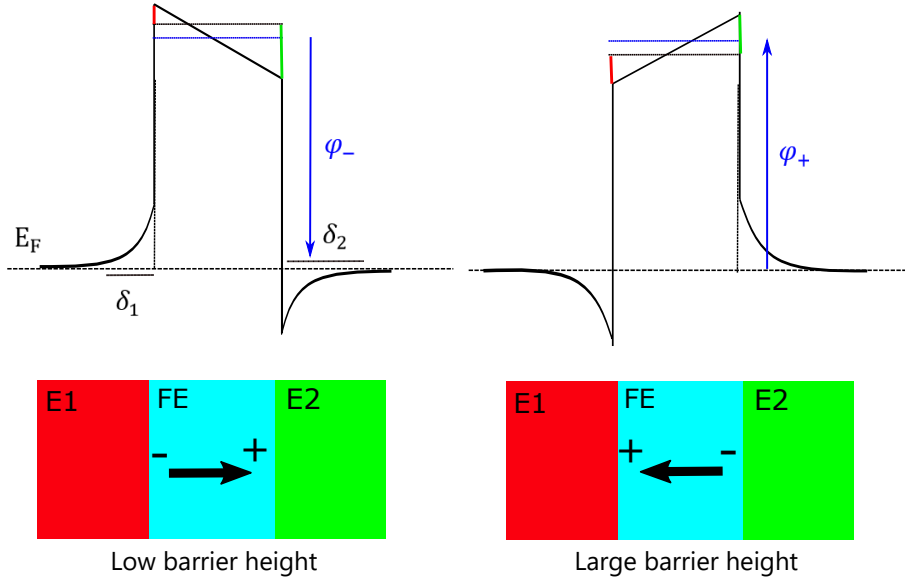


Figure I.13: Modulation of a rectangular potential barrier due to polarisation charges in a FTJ. δ_1 and δ_2 are the screening lengths of electrode 1 and electrode 2, ϕ_+ is the high barrier height, and ϕ_- is the low barrier height.

electrode through the other, even though the ferroelectric layer is insulating by definition. Direct tunnelling dominates at low voltages and exponentially decreases as the barrier thickness increases. The equation of the current density for direct tunnelling is:

$$j_{DT}(V) = C \frac{\exp\left[\alpha(V) \left\{ \left(\phi_{B,2} - \frac{eV}{2} \right)^{3/2} - \left(\phi_{B,1} + \frac{eV}{2} \right)^{3/2} \right\}\right]}{\alpha(V)^2 \left[\left(\phi_{B,2} - \frac{eV}{2} \right)^{1/2} - \left(\phi_{B,1} + \frac{eV}{2} \right)^{1/2} \right]^2} \times \sinh \left[\frac{3eV}{4} \alpha(V) \left\{ \left(\phi_{B,2} - \frac{eV}{2} \right)^{1/2} - \left(\phi_{B,1} + \frac{eV}{2} \right)^{1/2} \right\} \right] \quad (\text{I.17})$$

Where C is a constant that depends on the effective mass (m^*) of the tunnelling electrons, and alpha a constant that depends on the same effective mass and on the potential barriers $\phi_{B,1}$ and $\phi_{B,2}$.

- **Fowler-Nordheim Tunnelling**

Fowler-Nordheim tunnelling is prominent at high voltages. This mechanism rises when the voltage at the ferroelectric/electrode interface exceeds the height of the potential barrier. This happens because part of the energy profile of the potential barrier in the ferroelectric lies below the Fermi level of the electrode. This phenomenon has been described as cold field electrons

emission from a metal into vacuum. The equation of the current density for Fowler-Nordheim tunnelling is:

$$j_{FNT}(E) = C \frac{e^3}{16\pi^2 \hbar m^* \phi_B} E^2 \exp \left[-\frac{4\sqrt{2m_e m^*} \phi_B^{3/2}}{3\hbar e} \frac{1}{E} \right] \quad (\text{I.18})$$

Where ϕ_B is the potential barrier.

- **Thermionic or Schottky Emission**

At high temperatures, the electrons have a finite possibility to overcome the potential barrier by thermal excitation. The thermionic emission mechanism dominates at large ferroelectric thickness and it is described by the equation:

$$j_{TI}(E) = A^* T^2 \exp \left[-\frac{1}{k_B T} \left(\phi_B - \sqrt{\frac{e^3 E}{4\pi \epsilon_0 \epsilon_r}} \right) \right] \quad (\text{I.19})$$

Where A^* is the Richardson constant and ϵ_r is the relative permittivity of the ferroelectric.

- **Poole-Frenkel Emission**

It is very similar to the Schottky emission, but the conduction occurs between trap states in the ferroelectric. The thermal excitation allows the trapped electrons to be promoted in the conduction band of the ferroelectric, and the application of an electric field further enhances the probability of the latter transition by lowering the Coulomb potential of those electrons. The Poole-Frenkel emission is dominant at high temperature and high electric field, and the most relevant parameter which characterises it is the trap depth. It is described by the equation:

$$j_{PF}(E) = q\mu N_C E \exp \left[\frac{-q \left(\phi_T - \sqrt{qE/\pi\epsilon_r\epsilon_0} \right)}{k_b T} \right] \quad (\text{I.20})$$

Where μ is the electron mobility, N_C is the density of states in the conduction band, and ϕ_T the trap depth. In the case where the electronic transport is dominated by the Poole-Frenkel emission, the trend of $\ln(j/E)$ as a function of \sqrt{E} is linear, and the trap depth can be extracted from the intercept at the origin.

Even though the features of each transport mechanism can be identified through voltage and temperature dependencies of the electronic current, the separation between different mechanisms is hard to define. It depends on various parameters, such as dielectric constant, screening distance, interface barrier height, and effective mass of the electrons.

I.4.5 Ferroelectric Tunnel Junctions: State of the Art

Perovskites-Based Ferroelectric Tunnel Junctions

Ferroelectric tunnel junctions (FTJs) are extremely promising components for non-volatile memory applications, because they offer the possibility to increase the device scalability for its integration into dense memory arrays [66]. A detailed description of FTJs and their physical principle are given in sections I.4.4 and I.4.4. This paragraph is devoted to the presentation of FTJ devices and their evolution during the past few decades. A first demonstration of TER ratio in a FTJ-like structure dates back to 2003, when Rodriguez Contreras *et al.* [70] measured an ON/OFF ratio (ratio between the current in low resistance state and high resistance state) of 4 at room temperature in a Pt/PZT/SrRuO₃ structure. Lately, however, they concluded that the resistive switching was most likely due to ion movement rather than ferroelectric polarisation reversal [71]. First demonstration of resistive switching due to the reversal of the ferroelectric polarisation was given by Gajek *et al.* [72] in 2007. The structure they presented was a La_{0.1}Bi_{0.9}MnO₃-based multiferroic junction. They were able to differentiate between magnetic and ferroelectric contributions to the resistance variation, measuring a TER of 5% at room temperature. Afterwards, in 2009, two groups, Garcia *et al.* [73] and Gruverman *et al.* [74], published the first proper results of TER ratio in a BTO-based structure. They reported an ON/OFF ratio of 750 and 80, respectively. The first FTJ was synthesised by Pantel *et al.* [75], who showed an ON/OFF ratio superior to 1500 at room temperature in a La_{0.7}Sr_{0.3}MnO₃/Pb(Zr_{0.2}Ti_{0.8})O₃/Cu FTJ. In 2019, Wang *et al.* [76] found that, by modulating the thickness of BTO in a Pt/BTO/LaNiO₃ stack, the ON/OFF ratio increased of two orders of magnitude. Subsequently, the research on FTJs rapidly grew with various combination of electrodes and ferroelectric materials being published, with a particular interest for BTO. The highest difference in resistance was obtained by Xi *et al.* [77] and

again improved by Li *et al.* [78] in a Pt/BTO/Nb:SrTiO₃ structure, where it was 6×10^6 and 5.1×10^7 respectively at room temperature. A further relevant result was obtained by Chanthbouala *et al.* [79], who exploited the partial switching of domains in Au/Co/BTO/LSMO/NGO stack to demonstrate memristive and multi-state behaviour in FTJs. Beside BTO, other excellent candidates for the synthesis of FTJs were PZT and BFO, as well as other exotic materials. In 2013, Yoon *et al.* [80] reached an ON/OFF ratio of 10^7 , using Ag cation migration through a Ag/PZT/LSMO FTJ for synaptic learning mechanisms. In 2016, Bruno *et al.* [81] reported an ON/OFF ratio of 10^4 in a Pt/Co/BFO/LNO stack.

HZO-Based Ferroelectric Tunnel Junctions

As already explained in section I.3, perovskite-based FTJs share a major issue related to the too high deposition and/or annealing temperatures required to crystallise the ferroelectric phase. For this reason, HfO₂-based ferroelectrics became increasingly attractive, although perovskites allow ferroelectricity at lower thicknesses and a considerably higher ON/OFF ratio, with respect to HfO₂-based compounds [66, 82]. However, the latter ones are compatible with the thermal budget required by the CMOS process. In 2017, Ambriz Vargas *et al.* [83] firstly reported a HZO-based FTJ with a Pt/HZO/Pt structure and a ON/OFF ratio of 20. They attributed the measured ON/OFF ratio to direct tunnelling. A year later, Goh and Jeon [84] studied the impact of different bottom electrodes on HZO ferroelectric performances, using titanium nitride (TiN) as top electrode. They found a TER of 30 when germanium (Ge) was used as bottom electrode. The high TER value was ascribed to a depletion region in the Ge semiconductor, which acted as an additional barrier to the tunnel one. In 2019, Yoon *et al.* [85] studied the variation of the TER ratio in Pt/HZO/TiN FTJs depending on HZO thickness, showing that the main mechanism responsible for the TER effect was direct tunnelling. In 2020, Goh *et al.* [86] reported a TER ratio of 16 and synaptic behaviour in ultra-thin HZO-based FTJ. Sulzbach *et al.* showed a TER ratio of 450 % and 210 %, attributed to ferroelectric switching, in a Pt/HZO/LSMO structure with 4.6 nm-thick and 2 nm-thick epitaxial HZO, respectively [87, 88]. Finally, Jiao *et al.* [89] obtained an ON/OFF ratio of 800 in a Pt/HZO/Nb:SrTiO₃ FTJ. In this case as well, the HZO was grown by epitaxy and the ON/OFF ratio was attributed to direct

tunnelling. More recently, other strategies have been explored to improve the ferroelectric properties of Zr doped-HfO₂, such as the use of ultra-thin oxide layers placed at the interface between the electrodes and HZO. The latter solution will be investigated in chapter V.

I.5 Neuromorphic Devices

The request of miniaturisation and increase of capacity of the modern semiconductor technology asks for new computation paradigms and efficient architectures that can satisfy these demands. Indeed, the Von Neumann architecture is reaching its limits in terms of operation speed and energy consumption [90]. A possible solution to this problem is the implementation of a novel hardware architecture that takes inspiration from the biological networks of neuron and synapses in the brain. The branch of research that is devoted to this task is called neuromorphic engineering and its goal is to realise artificial neuromorphic networks (ANNs) composed by two fundamental units: artificial neuron and synapse. Aim of ANNs is to process large amount of information in parallel, as the brain does, substantially increasing the operation speed and reducing the energy cost. A brief description of the operation principle of ANNs is given in Chapter VI. So far, the most promising method for the implementation of this kind of architectures is the use of the memristor, an electronic component theorised in 1971 in Berkeley by Leon Chua [91]. Memristors thanks to their multiple states of resistance have been considered the best approach for emulating synaptic plasticity mechanisms [92]. Up to date, multiple memristive devices based on different materials and physical principles have been demonstrated. This section provides an overview of various neuromorphic devices other than ferroelectric-based ones, which are the focus of this work. Finally, a brief description of the biology of neurons and synapses will be given.

I.5.1 Mechanisms and Materials for Neuromorphic Devices

Emerging neuromorphic devices can be classified according to their operation principle into nine categories:

- Ferroelectric devices

- Anion migration based devices
- Metal ion migration based devices
- Phase change devices
- Magnetic devices
- Metal-insulator-transition (MIT) based devices
- Photo-tunable devices
- Electrolyte-gated devices
- Purely electronic devices

These have been widely investigated and used for neuromorphic applications and for other machine learning tasks, thanks to their ability to realise some of the functions typical of biological neurons and synapses. More details on this topic can be found in the review by Zhu *et al.* [93].

Anion Migration-Based Devices

The anion migration-based devices rely on a measurable change in material properties, i.e. resistance, induced by the migration of anions inside the material when an external stimulus is applied, such as an electric field or a temperature gradient [94],[95]. Depending on the material structure during and after application of the external stimulus, anion migration-based devices can be classified into filamentary type and non-filamentary type.

Filamentary Type

Filamentary type devices consist on a metal/insulator/metal sandwich structure. When an external voltage is applied to the anode, the conductivity of the insulating layer significantly changes. Such a change in resistance can be sustained even in absence of voltage and it makes these kind of structures suitable for memory devices, i.e. resistive random access memories [96]. The working principle of filamentary type-devices is based on: forming or SET process, to initiate the device from the original state to the low resistance state (LRS), and a RESET step, to switch back the device from LRS to high resistance state (HRS), figure I.14. The electronic conduction inside the insulating layer is rather complex and it results

in the combination of three electrode-limited conduction mechanisms: Schottky emission, Fowler-Nordheim tunnelling, and direct tunnelling and six bulk-limited: Poole-Frenkel emission, ohmic conduction, space-charge-limited conduction, ionic conduction, hopping conduction, and trap-assisted tunnelling. During the SET step, the application of an external high electric field knocks the oxygen atoms out of the lattice of the insulating layer, which drift towards the anode and leave oxygen vacancies near the cathode. These form a conductive filament that connects the two electrodes, resulting in a resistance switch from HRS to LRS. The RESET process, represented by the rupture of the conductive filament, is not unique. A possible way to implement it could be the application of an inverse voltage pulse with respect to the SET, which triggers an opposite ion migration. The insulating layer of metal-insulator-metal structure, employed as a building block for memristor-based artificial synapses, can be made of different materials, such as metal oxides, two-dimension transition metal dichalcogenides (TDMC), perovskites, and organic materials.

Non-Filamentary Type

To face the issues related to the stochastic nature of formation and rupture of the filament in filamentary-type devices, research focused on more reliable non-filamentary-type ones. As part of the latter category, it is worthy to mention devices based on interfacial reactions, i.e. redox. They occur at the electrode/oxide interfaces, leading to a variation of the oxide layer thickness and, consequently, to the creation of multiple states of resistance [97], figure I.15. The redox reaction is uniform along the interface, ensuring a higher reliability compared to the stochastic filament formation process. An increase in the device conductivity is induced by the application of a positive voltage, which triggers the redox reaction. The reverse process is obtained by applying a negative voltage. A further way to achieve the resistive switching in non-filamentary type devices is by anion migration through grain boundaries, which can be observed in 2D materials [98].

Metal-Ion Migration-Based Devices

The metal-ion migration devices are based on a metal/electrolyte/metal structure and the resistive switching is realised by migration of metal ions and formation of a metallic conductive filament between the anode and the cathode, figure I.16.

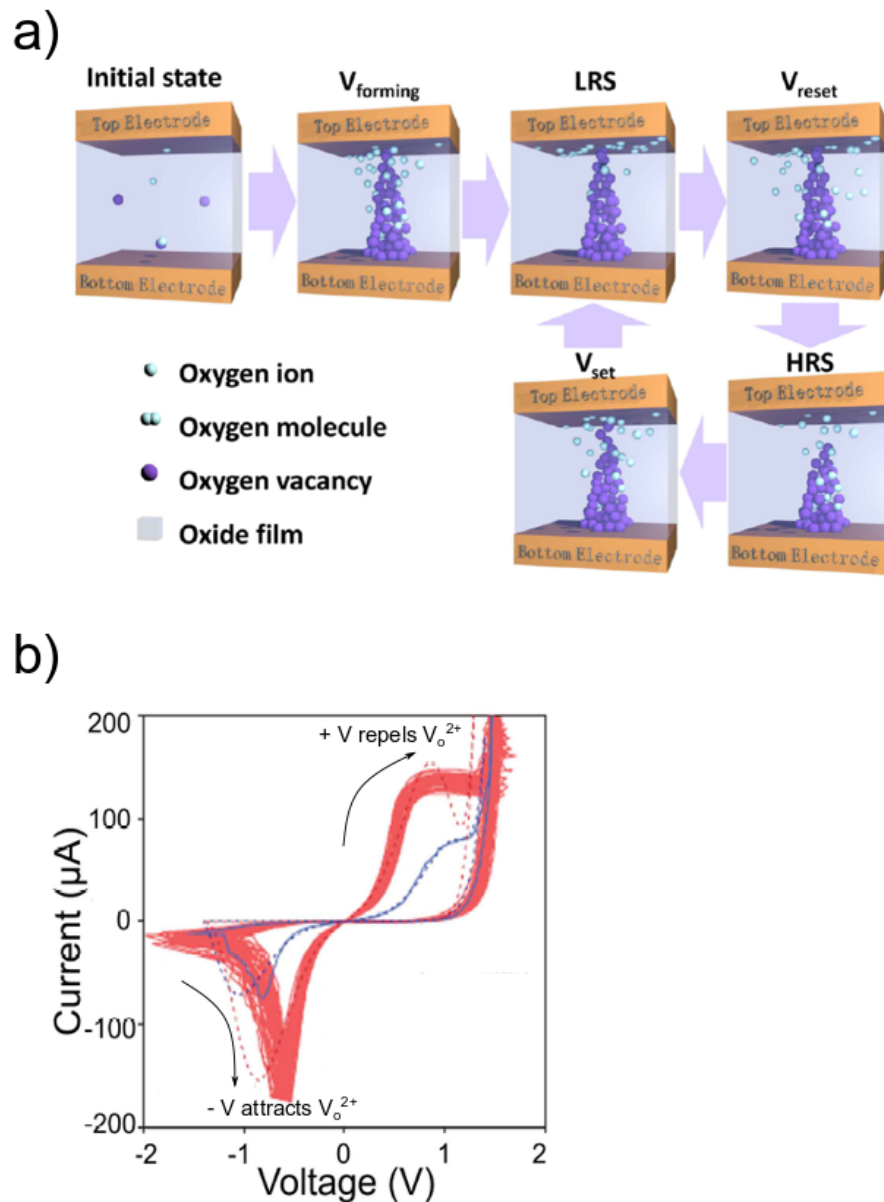


Figure I.14: a) Schematic illustration of the switching process in simple binary anion-migration-based devices. b) Switching I - V curves that represent multiple resistive states of the device. Reprinted from J. Zhu et al. "A Comprehensive review on emerging artificial neuromorphic devices" Applied Physics Reviews (2020) [93].

Also called "electrochemical metallisation cells" (ECM) [99], since they base their operation on redox reactions, these devices are promising for neuromorphic applications thanks to their ultra-low operation voltage, high ON/OFF ratio, and potential for large scale integration. The general working principle consists of: a forming process to incorporate the metal ions into the electrolyte layer -the anode undergoes an oxidation that turns the active metal atoms into ions-, a SET step that ensures the ion migration, thus formation of conductive filament, and a RESET process to dissolve the filament. The main conduction mechanisms in metal-ion-migration-based devices are ohmic and space charge limited conduction

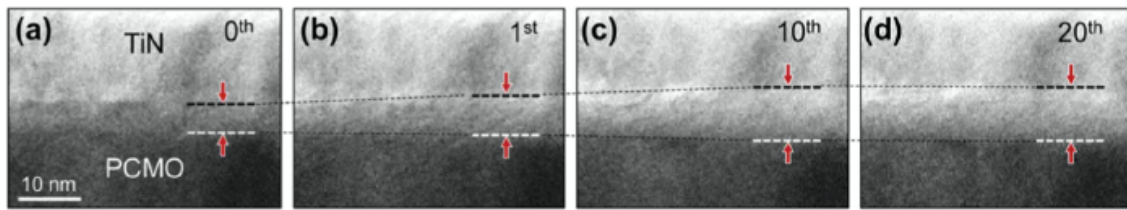


Figure I.15: Schematic illustration of the change of the oxide thickness in a redox reaction in non-filamentary type devices. a)-d) Snapshot TEM images showing the evolution of the TiO_xN_y layer at TiN/PCMO interface. The thickness of the a- TiO_xN_y layer is marked by red arrows. Reprinted from J. Zhu et al. "A Comprehensive review on emerging artificial neuromorphic devices" Applied Physics Reviews(2020) [93].

(SCLC) [100].

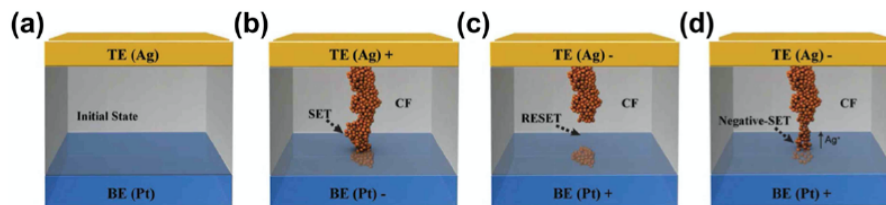


Figure I.16: Schematic of ionic dynamic during the negative SET process. a) Initial state. b) The conductive filament formed after SET process. c) Rupture of the conductive filament after the RESET process, the filament is not fully dissolved and parts of it remains inside the bottom electrode. d) Ag atoms inside the BE, when a negative voltage continuously applied on the anode. Reprinted from J. Zhu et al. "A Comprehensive review on emerging artificial neuromorphic devices" Applied Physics Reviews (2020) [93].

Phase Change Materials-Based Devices

Characterised by a good stability and potential to be integrated with a high density and in a very large scale, phase change material (PCM)-based devices constitute the most mature technology in terms of neuromorphic design and few kinds have been already commercialised [101, 102]. PCM devices are characterised by a high-resistance state (HRS) and a low-resistance state (LRS), and the SET and RESET processes rely on the PCM crystallisation and amorphisation. The SET step is realised by the application of a low and wide voltage pulse, which promotes the crystallisation of the material and so the change from HRS to LRS. The RESET process is based on the application of a high and short voltage pulse that melts part of the PCM, which, by cooling down very quickly, forms an amorphous region. The latter is characterised by a lower electron density that brings to a resistive

transition from LRS to HRS, figure I.17. In PCM systems, the control of the degree of disorder of the crystal structure enables multiple resistance states for the storage of information [103, 104]. Ge₂Sb₂Te₅ (GST) based-devices were considered for brain-inspired computing [105], thanks to their good stability and capability of scaling and integration. The main issues for the use of PCMs are low switching speed and high energy consumption.

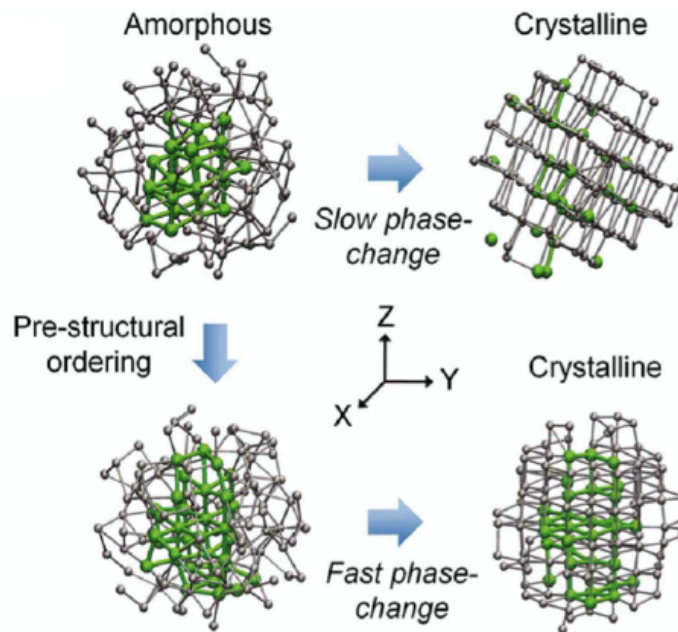


Figure I.17: Model configurations demonstrating the atomic rearrangements during the phase transition in PCM, with and without pre-structural ordering. Reprinted from J. Zhu et al. "A Comprehensive review on emerging artificial neuromorphic devices" *Applied Physics Reviews* (2020) [93].

Magnetic Mechanisms-Based Devices

Spintronic devices have been developed and used since the end on the nineties for artificial neuromorphic systems thanks to their extreme precision, fast switching speed, and low energy cost [106]. An example of these type of systems is the spin-transfer torque magnetic tunnel junction (MTJ) device [107]. A MJT, based on the principle of the spin transfer torque [108], consists of two ferromagnetic layers separated by a paraelectric insulating tunnel layer. The resistance depends on the spin orientation of the two ferromagnets. The LRS corresponds to the parallel orientation and the HRS to the antiparallel one. Tunnel magnetoresistance ratio (TMR), similarly to TER ratio for FTJ, is defined by:

$$TMR = \frac{R_{AP} - R_P}{R_P} \times 100\% \quad (I.21)$$

In the LRS, electrons with a certain spin orientation can easily tunnel through the barrier, since the filled states in band structure of one contact matches to the empty states for the same spin orientation of the other. Further ways to implement the magnetic switching are the spin-orbit torque, based on the spin-orbit coupling for the manipulation of spins, and the domain-wall-motion, which exploit the control of magnetic domain walls. These kind of devices have opened a wide range of possibilities for the implementation of neural and synaptic functionalities [109, 110]. Figure I.18 shows the working principle of few magnetic mechanisms-based devices.

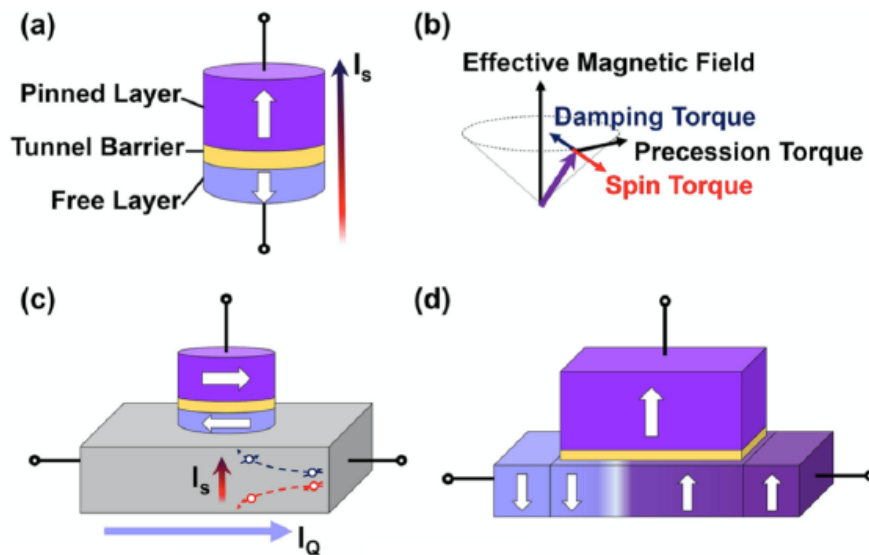


Figure I.18: a) Vertical spin-valve. b) The magnetisation dynamic evolves under the influence of a damping torque, precession torque, and spin-torque, due to an input spin current. c) Spin-orbit torque. d) Schematics of domain wall motion-based devices. Reprinted from J. Zhu et al. "A Comprehensive review on emerging artificial neuromorphic devices" *Applied Physics Reviews* (2020) [93].

Metal-Insulator-Transition-Based Devices

The metal-insulator transition (MIT) is a phenomenon that characterises many transition metal oxides with a partially filled d -band, which behave as insulators despite the expectation to be metallic. In these systems, the transformation of the electron states from itinerant to localised can be led by several mechanisms, for instance the Mott transition [111]. An example of the resistive switching in these kind of systems is the thermally induced MIT, where the LRS is generated by the creation of granular conductive filaments, upon an electronic avalanche breakdown. The process can be reversed by means of Joule heating. Figure I.19 shows an example of a material that undergo a MIT.

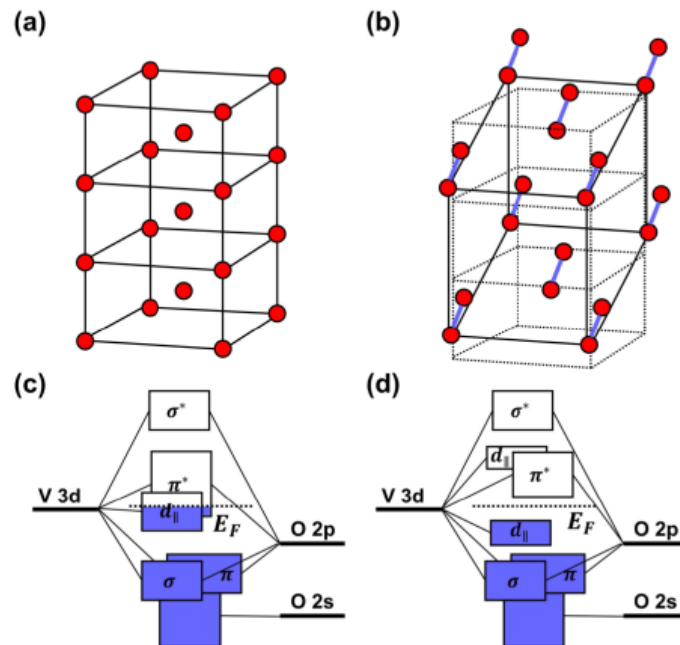


Figure I.19: Vanadium sublattice of the: a) tetragonal (metallic), b) monoclinic crystal structure of VO₂. c) Schematic band structure of the undistorted metallic phase of VO₂. d) Schematic of the altered band structure, upon transition, of the distorted insulating phase of VO₂. Reprinted from J. Zhu et al. "A Comprehensive review on emerging artificial neuromorphic devices" Applied Physics Reviews (2020) [93].

Photo-tunable Mechanisms-Based Devices

Similarity between biological neurons and synapses, and optoelectronic devices has brought to the investigation of photonic systems for neuromorphic applications [112]. Up to now, there are three main mechanisms on which photo-tunable devices rely on: photo-generated carriers, structural change of materials, tuning of optical cavities with waveguides. The main advantages of photo-tunable mechanisms-based systems are a high transmission speed and energy efficiency, while the major drawback is their integration in small scale. Two examples of the operation mechanisms of photonic neuromorphic devices are reported below.

- **Trapping**

The conductivity is controlled by photo-generated carriers. Photons, generated by photo stimuli, create electron-hole pairs inside the device. The carriers migrate into the trap sites, switching the device to state "1". The RESET step is obtained by applying a negative voltage to the anode, so that the trapped carriers are released and the conductance can switch back to the original state. The most suitable candidates for the construction of such photo-tunable devices are oxide materials with intrinsic traps or metal/oxide hetero-junctions with interface traps, figure I.20.

- **Phase Change Material Assisted**

They rely on the phase change of specific materials due to the heat generated by absorption of photons. The grade of crystallisation corresponds to a different refractive index, which can change in a wide range depending on the crystallisation rate. Hence the state of device can be defined by its optical transmission. Neuronal and synaptic behaviour has already been demonstrated for this systems [113], which are characterised by an extremely energy efficient modulation enabled by light-matter interaction.

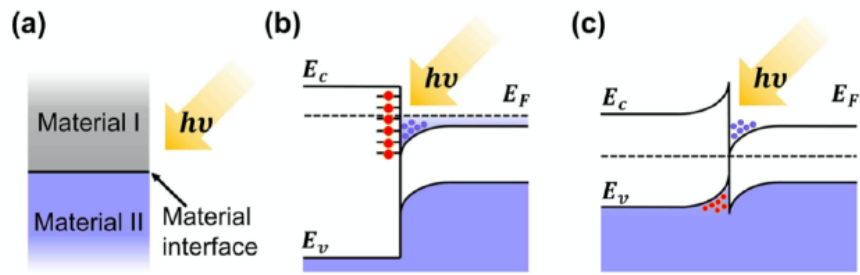


Figure I.20: Schematics of: a) heterojunction for optical applications. b) Band diagram at oxide/semiconductor interface with interface charges. c) Band diagram at a semiconductor interface. Reprinted from J. Zhu et al. "A Comprehensive review on emerging artificial neuromorphic devices" Applied Physics Reviews (2020) [93].

Electrolyte-Gated Mechanisms-Based Devices

As an example of electrolyte-gated devices, the resistance change based on the formation of an electric double layer (EDL) [114] is described, figure I.21. A constant gate voltage or a low-frequency gate pulse drive ions with positive charge in the electrolyte towards the interface with the channel material, leading to an accumulation of cations. Due to electrostatics, the latter induces a thin layer of electron near the surface of the channel material, which form, with the cations, an ultra-thin capacitor (figure I.21b). The ion-induced electron layer acts as a conductive path and changes the conductance of the channel material. The main advantage of this method is the creation of a very intense electric field (≈ 10 MV/cm) that leads to a decrease of the device operation voltage. Finally, once the external voltage is switched off, the accumulated ions quickly diffuse back inside the electrolyte and the system goes back to the original state. An example of an electrolyte-gated synaptic transistor is given by Ling *et al.* [115].

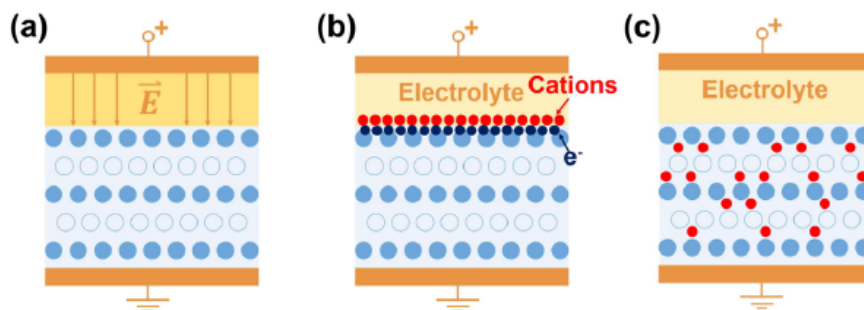


Figure I.21: Schematics of: a) Electric control. b) Formation of the electrical double layer. c) Intercalation. Reprinted from J. Zhu et al. "A Comprehensive review on emerging artificial neuromorphic devices" Applied Physics Reviews (2020) [93].

Electronic-Based Devices

Purely electronic systems have been object of research in this field thanks to their stability, fast rate response, and CMOS compatibility. They rely on three main mechanisms: I. Trapping and de-trapping mechanism, figure I.22, which is based on a transistor-like structure and uses traps in the dielectric layer to control the device conductance (the LRS corresponds to filled traps) [116]. II. Quantum dots, which rely on the change of the quantised conductance caused by the formation of atomic-scale conductive filaments [117]. III. Field-effect electron transport, in which the conventional working principle of FETs is improved in various ways to achieve better performances for the implementation of neuromorphic devices [118].

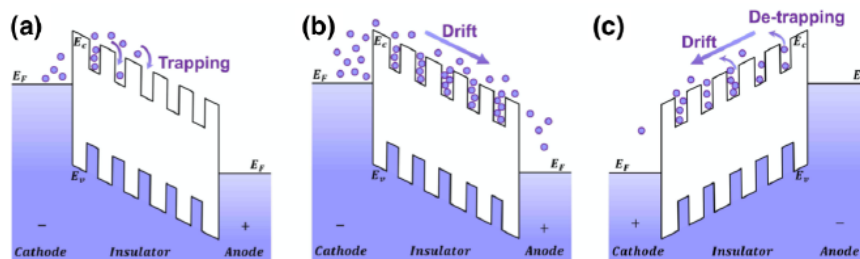


Figure I.22: Schematic of the band diagram during the: a) set process. b) Reset process. c) LRS conduction process. Reprinted from J. Zhu et al. "A Comprehensive review on emerging artificial neuromorphic devices" Applied Physics Reviews (2020) [93].

I.5.2 Artificial Synapses

The similarity between the behaviour of memristive devices and biological synapses makes them able to emulate various synaptic plasticities. Synaptic plasticity is defined as an activity-dependent modification of the strength (or efficacy) of the synaptic transmission that controls the communication between neurons, figure I.23. Examples of synaptic plasticities are: long-term potentiation and depression (LTP/LTD), short-term potentiation and depression (STP/STD), and spike-timing dependent plasticity (STDP). A brief description of LTP/LTD, STP/STD, and STDP mechanisms is provided below.

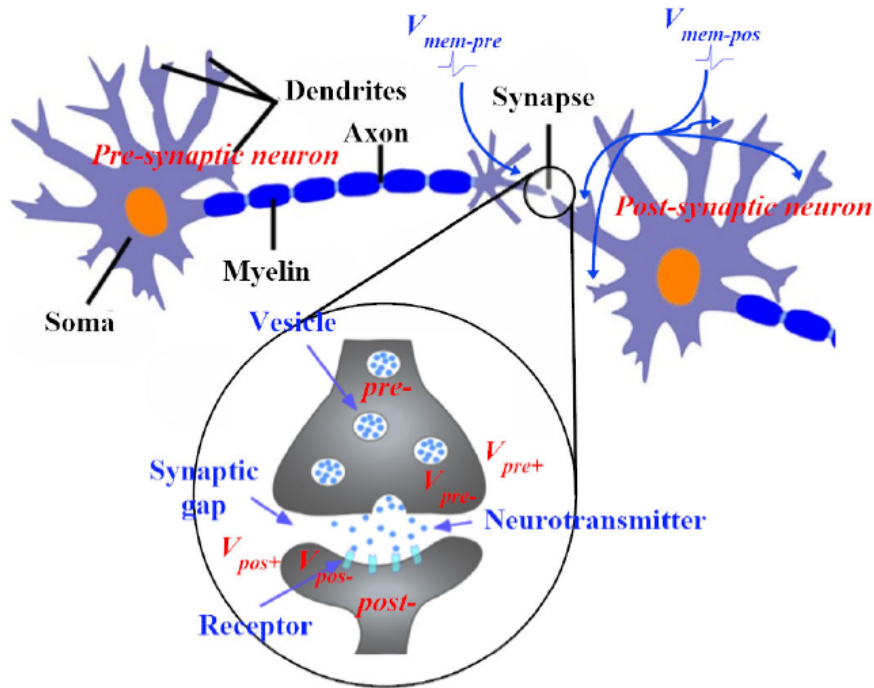


Figure I.23: Schematic of the working principle of a synaptic junction. *Reprinted from Mohan et al., "Neuromorphic Low-Power Inference on Memristive Crossbars With On-Chip Offset Calibration", IEEE Access, 2021 [119].*

Synaptic Plasticity Mechanisms

- **Long-Term Potentiation and Depression**

The long-term potentiation (LTP) and depression (LTD) identifies an increase and decrease, respectively, in the synaptic efficacy and it is thought to be related to the learning memory functions. The basic requirement to implement the synaptic long-term plasticity is that the connection strength, which is represented by a change in the resistance of the synaptic device, can be controlled by an external stimulus and it is non-volatile. The same requirement concerns electronic synapses in ANNs, where the synaptic weights that connect two neurons need to be regularly adjusted. The main issues for the implementation of long-term plasticity are linked to a non-linear behaviour of memristive devices, as in case of filamentary-type ones, which generates a lack of correspondence between the current and the number of applied programming pluses.

- **Short-Term Potentiation and Depression**

The short-term plasticity represents a temporary potentiation/depression of the neural connections. Contrarily to the long-term one, which can last even

days, the short-term potentiation/depression has a maximum duration of tens of minutes and is likely related to the spatio-temporal information processes in biological neural systems. This mechanism exploits the volatility of memristors, for instance, the instability of the conductive filament.

- **Spike-Timing Dependent Plasticity**

STDP is the capability of a synapse to increase or decrease exponentially its connecting strength depending on the delay time between the pre- and post-synaptic pulses. The pre-synaptic spike is the impulse send by a neuron called pre-synaptic neuron, the post-synaptic one is the impulse that the post-synaptic neuron receives by the synapse. In particular, the synaptic strength varies according to the time at which pre- and post- spikes occur. The STDP mechanism can be implemented in ANNs by designing the width, the number, and the voltage amplitude of the programming pulses.

I.5.3 Artificial Neurons

A critical aspect to account for in the development of neuromorphic architectures is the implementation of artificial neurons at a hardware level. The basic components of a biological neuron are: the cell body, the axons, the nerve fibres that conduct the electrical pulses, and the dendrites that propagate the electrochemical stimulations from other neurons to the cell body (figure I.24). The information, encoded as a spike, is received by the body cell as a change in its voltage potential and, once the latter achieved a certain threshold, the body cell generates an action potential that transmits the information through the axon. Based on this process, the basic requirement for an artificial neuron is to achieve the potential accumulation process and the spike generation functions. Depending on the applications, artificial neurons can be classified as: I. bio-mimetic, the design of which is inspired by the functionalities of the biological neurons. II. Mathematical, which do not consider the biology, but only the way the neurons perform calculations. III. Neurons for specific networks, the characteristics of which vary according to the application. An example of the latter category is the oscillation neurons for oscillatory neural networks, inspired by the oscillatory behaviour of some parts of the brain [120]. To implement artificial neurons, the same devices and physical mechanisms listed at the beginning of section I.5.1 are considered.

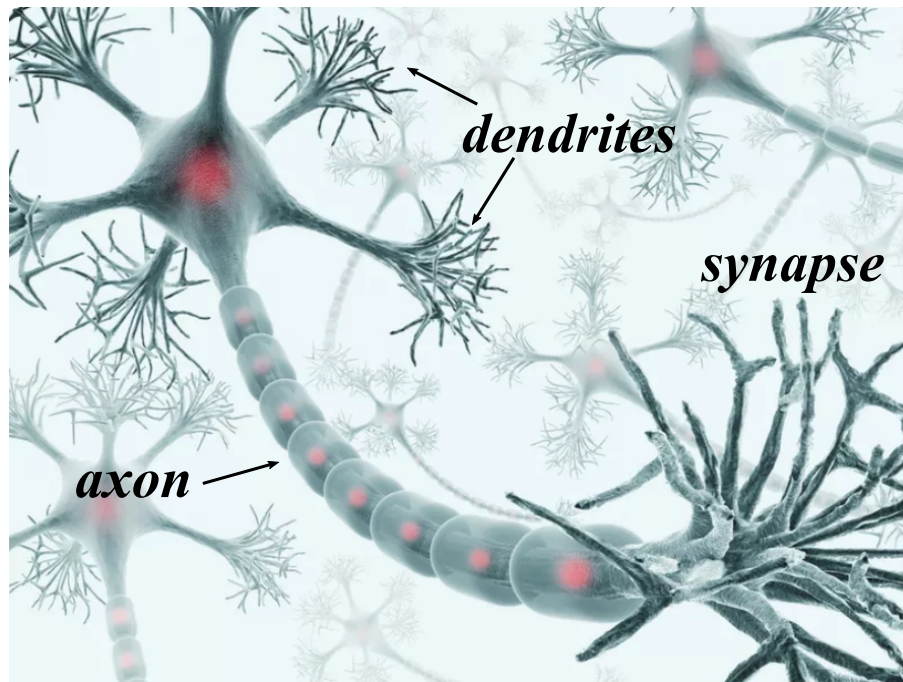


Figure I.24: Illustration of a neuron. Science Photo Library - KTSDESIGN/Getty Images

In conclusion, for the development of an artificial neuromorphic system it is important to consider not only the single device, but also the general picture that includes other types of tasks to implement, such as the reproduction of central nervous system. In order to reproduce its functionalities, various learning methods have been proposed, i.e. supervised learning, unsupervised learning and reinforcement learning [121–123]. It is worthy to mention that these functions can be implemented through the crossbar integration of memory components [124]. This architecture, which is described in chapter VI, allows the synthesis of dense matrices of devices, high operation speed, and scaling of the system dimensions. Neuromorphic devices have been object of an intensive research for more than a decade and some of them have already been commercialised. Nevertheless, there are still some issues to overcome, for instance, the stochasticity of filament formation in filament-based devices and the complex synthesis of MTJ in spintronic-based devices. These concerns oriented the researches towards the use of other more reliable devices, such as ferroelectric-based ones [125]. However, at a hardware level, the complications are linked to the linearity and symmetry issues that rise from the implementation of synaptic plasticity. The ultimate challenges are the development of new fabrication methods, algorithms, and efficient ways of integration of these devices for the realisation of functioning neuromorphic net-

works.

I.6 Ferroelectric Tunnel Junctions for Neuromorphic Computing

Ferroelectric-based devices represent a promising solution for the implementation of artificial neurons and synapses for the realisation of ANNs and, over the past few years, research has been increasingly focused on demonstrating synaptic plasticity mechanisms in ferroelectric-based structures. This paragraph elucidates the operating principle of FTJs for neuromorphic applications and gives an insight on the current state of these devices. To begin, a brief recall on the structure and the physical mechanism of FTJs. A FTJ is a two terminal device, where the ferroelectric layer is sandwiched between two electrodes. The application of an external voltage promotes the polarisation switching and a modulation of the potential profile, which leads to the generation of a high and a low resistance states. The change of the polarisation state, thus the variation of the device resistance, is used to store the information. The read operation can be non-destructive, if the applied electric field is lower than the coercive field (E_c). The switching, which alters the polarisation state, is extremely high energy-efficient compared to other resistive switching mechanisms, such as PCM-based, or spin-transfer torque-based. Switching currents below the nA [126] and a write energy per bit of 500 aJ were demonstrated [127]. This features made FTJs the most power-efficient switching devices [128]. Beside the non-volatile behaviour, FTJs allow analog switching, which opens the possibility of storing multiple weights in the same device, thus increasing the density of the networks. Analog switching is achieved by controlling the polarisation state of the ferroelectric domains by voltage pulses. A different voltage amplitude and pulse time lead to a different portion of switched domains and, by consequence, to different resistance states of the device [129]. To simplify the circuitry for the implementation of CMOS technology, a train of identical pulses should be applied in order to change the polarisation state. However, if non-identical pulses are used to change the resistance, it is necessary to know the previous state of the device in order to apply the correct programming pulse. This generates two main disadvantages: a more complex circuit and an increased la-

tency before the following programming operation. A possible solution to these issues is represented by the use of the accumulative switching behaviour, which involves the gradual change of the device state by the integration of the effect of multiple pulses, sum of which is lower than E_c . As far as concerns the synaptic learning capability of FTJs, the learning algorithms that were demonstrated so far are mostly Hebbian, among which the most common is STDP, section I.5.2. In the literature, an accuracy of 96 % for pattern classification in FTJ-based synapses trained with STDP algorithms, is reported [130]. More details on this topic can be found in the review paper by Covi *et al.* [131]. A further relevant feature that characterises FTJs is their extremely fast response time. The switching time of a FTJ is of the order of nanoseconds, hence it could allow the processing of events that occurs almost simultaneously in time, for instance, biological STDP. By spike-engineering, the plastic behaviour of artificial synapses can be tuned to reproduce several learning mechanisms [132]. At last, another important aspect to consider is the possibility of 3D integration of FTJs, which is crucial for parallel and dense neuromorphic systems. To conclude the section, a brief overview on the state of art of HZO-based FTJ for the emulation of synaptic functionalities is given. In 2018, Chen *et al.* [133] published their results on a HZO-based FTJ for hardware neuromorphic network implementation, which exhibited high integration density. However, the endurance and the ON/OFF ratio were rather low, 3 and 10^3 , respectively. In 2020, Max *et al.* [129] demonstrated the long term potentiation/depression and STDP behaviour in a HZO-based FTJ synapse, showing an ON/OFF ratio of 10. In 2021, Luo *et al.* [134] fabricated a HZO-based FTJ for the realisation of a FTJ crossbar array, found to be a promising candidate for neuro-inspired computing. In 2022, Zhu *et al.* [135] presented a capacitive artificial synapse that could be trained to reconstruct incomplete images. Nevertheless, many aspects have still to be improved for these devices to reach maturity. In particular, FTJ structures have to be optimised in terms of high remanent polarisation, high endurance, and good retention. The research, in this increasingly explored field, is still focused in finding the optimal fabrication conditions and facing the challenges of device integration to make this technology industrially transferable.

I.6.1 FTJs Industrial Requisites for Neuromorphic Applications

As conclusion to the first part of the chapter, it is important to mention the constraints that neuromorphic memories, in particular FTJs, have to meet in order to be commercialised. International Roadmap for Design and Systems (IRDS) provided a range of values for some of the most important parameters that define neuromorphic memories. These indications are based on the restrictions imposed by the CMOS industry and on the necessity to equalise the biological processes of the brain [136]. According to IRDS, the device lateral dimension should not exceed 10 nm, the energy consumption for each programming event should be limited to 10 pJ, the programming speed should be below 10 ns/switch, the operation voltage should not surpass 1 V, the minimum value for ON/OFF ratio should be 10^6 , and 10 years for the retention, finally, the endurance should reach at least 10^9 cycles. Table I.3 reports the state of art of values for the above mentioned parameters obtained for FTJs and HZO-based FTJs.

Table I.3: State of the art of FTJs and HZO-based FTJs performances.

Performances	FTJ	Reference	HZO-FTJ	Reference
Dimensions	20 nm	[137]	60 nm	[133]
Energetic Consumption	0.1 pJ	[138]	1.8 pJ/spike	[133]
Speed	0.6 ns	[127]	100 ns	[133]
ON/OFF ratio	5×10^7	[78]	180	[139]
Operation Voltage	1.5 V	[140]	2.5 V	[139]
Retention	10 y	[84]	10 y	[84]
Endurance	2×10^7	[141]	2×10^7	[141]

Although some of the indications are respected, there are few parameters as dimensions, operation voltage, and endurance that still need to be optimised.

I.7 Conclusion of the Chapter

The beginning of the chapter was dedicated to an introduction of the physical concepts at the basis of ferroelectricity. In a first place, the notion of electric polarisation was presented, followed by a detailed discussion on the ferroelectricity and the phenomena that impact it. In a second place, ferroelectric materials were introduced, with a special focus on HZO.

HZO is a promising material for non-volatile memory applications and compatible with the CMOS technology. Eventually, the last part of the chapter gave an overview on non-volatile memory devices based on ferroelectric HZO, in particular on FTJs that are the devices that this work aims to develop, and on various neuromorphic systems.

The objectives of this thesis are:

- Synthesis of ultra-thin HZO layers to implement ferroelectric tunnel junctions. One of challenges related to use of HZO is its scalability below 8 nm, where ferroelectricity significantly degrades.
- Engineering of ultra-thin HZO-based stacks and optimisation of their ferroelectric performances. The aim is to develop high-quality thin layers characterised by robust ferroelectric properties, which include maximisation of endurance, minimisation of wake-up, and achievement of a large ON/OFF ratio for FTJ devices. To do so, several aspects have to be considered to optimise the device structure and performances, i.e. the choice of the electrode material, and the interface properties, the effect of which is dominant at low thickness of the ferroelectric. The latter points are discussed in chapters IV and V.
- Realisation of crossbar arrays and emulation of synaptic plasticity using the synthesised structures. The ultimate goal of this PhD project would be to contribute to the development of reliable and scalable HZO-based devices for artificial neuromorphic networks, using industrially transferable methods.

CHAPTER II

Experimental Techniques

This chapter is dedicated to the fabrication process and experimental techniques employed for the synthesis and characterisation of the specimens presented in chapters III, IV, and V. Figure II.1 gives a schematic of the structure of the samples realised in this work. The first part of the chapter describes the steps of the sample fabrication. Firstly, sputtering is used for the growth of the HZO layer, electrodes, and top conductive layer, secondly, UV photolithography is employed to obtain the capacitive patterns, and finally, an annealing process is performed to crystallise the HZO film. The second part of the chapter illustrates the techniques used for structural, chemical, and physical characterisations of the specimens. To conclude, the third part provides a description of the protocols used for their electrical characterisations.

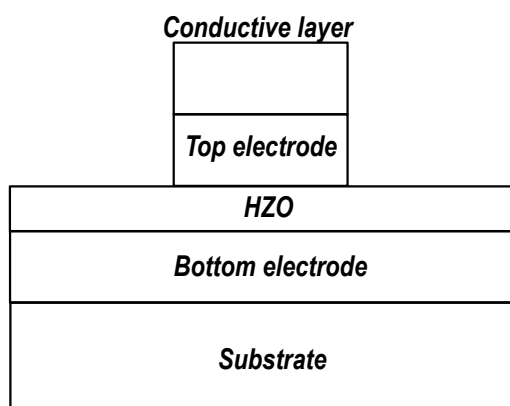


Figure II.1: Schematic of the structure of a sample synthesised in this work.

II.1 Sputtering Techniques

Sputtering is a physical vapour deposition technique used to produce coatings in a vacuum environment. Among the different types of sputtering processes, magnetron is of particular interest for technological applications in the microelectronic industry. It is an ionic sputtering method where high-energy ions strike on a solid target, knocking-off surface atoms. In cathodic sputtering, including magnetron, ions are derived from a plasma, formed in a low-pressure gas between two electrodes. Magnetron sputtering emerged in the mid-seventies to overcome the limitations related to the low deposition rate of cathodic sputtering. It is considered a high-rate vacuum coating technique extremely efficient for the deposition of metals, alloys, and compound up to 5 μm . Other than high deposition rate, magnetron sputtering has further advantages, such as the synthesis of high-purity films, the high adhesion of the films, the easy deposition of metals, alloys, and compounds, a very good coverage of small surface features, an excellent uniformity on large-area samples, and the room temperature and carbon-free deposition.

II.1.1 Physical Mechanism

In sputtering, molecules or atoms of a target, made of the material that is intended to be used as coating, are ejected from the surface by the bombardment of high-energy particles. In cathodic sputtering these particles are positive ions generated by an electrical discharge in the gas used to induce the plasma. The ejected atoms form the coating directly on the substrate. A vacuum environment is required in order to guarantee ions with a sufficient high energy, adequate mean free path, and low collision rate. The operation pressure must be 10^{-2} mbar or lower. The plasma is generated by a direct-current (DC) or a radio-frequency (RF) power supply. At stable conditions, the electrons are emitted by the cathode and accelerated towards the anode, when they have an energy sufficient to ionise the atoms of the gas, a glow, characteristic of its electronic transition, appears. The created positive ions are then accelerated towards the cathode, and, once they have impinged on its surface, secondary electrons and sputtered atoms are produced. Also the secondary electrons are accelerated and capable to ionise other atoms of gas, so that the process is able to sustain itself. Figure II.2 reports a schematic represen-

tation of a sputtering chamber. For pressures lower than 10^{-2} mbar the process stops, as the plasma extinguishes. Indeed, at this pressure, the mean free path of the sputtered atoms is too little to ensure a proper coating of the substrate. Magnetron sputtering is designed to overcome these constraints, by guaranteeing a more efficient ionisation at low pressures.

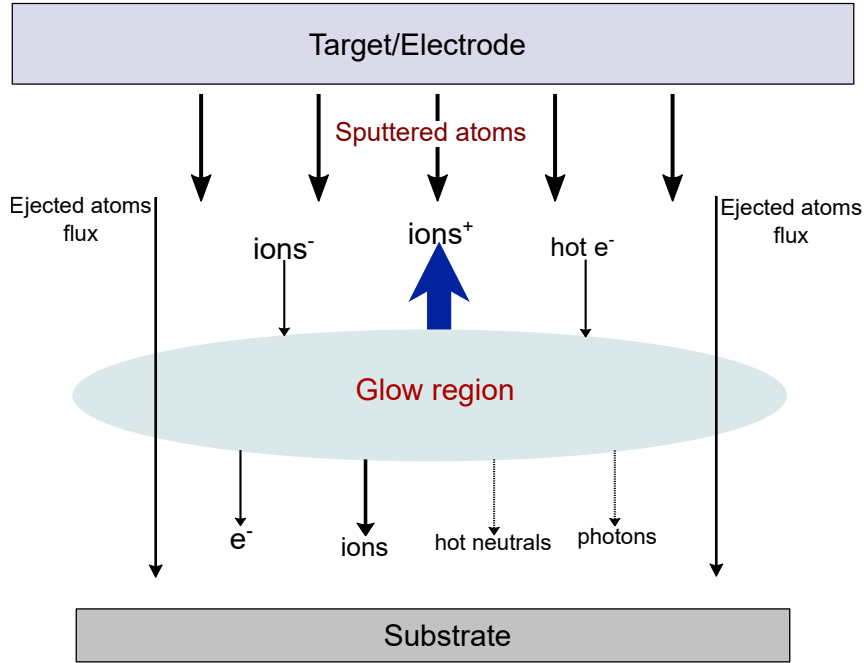


Figure II.2: Schematic representation of a sputtering chamber.

The most important parameter that characterises the sputtering process is the sputtering yields S , eq. II.1, defined as the number of atoms or molecules ejected from a target surface per incident ion. S is a measure of the efficiency of the process.

$$S = \frac{\bar{E}}{E_t} \left\{ 1 + \left(\frac{\ln \bar{E} / E_b}{\ln 2} \right) \right\} \sigma_0 n_A \quad (\text{II.1})$$

From equation II.1, it is possible to establish that S is proportional to the following terms:

- Number of atoms displaced towards the surface per primary collision: $\frac{\bar{E}}{2E_t}$, where \bar{E} is the mean energy of the struck target atom and E_t is the threshold energy required to displace an atom. The factor 2 indicates that only half of the displaced atoms moves toward the surface.
- Number of atomic layers that contribute to sputtering. The number of collisions necessary to slow down an atom from the initial energy \bar{E} to the

surface binding energy E_b is: $N = \frac{\ln \bar{E}/E_b}{\ln 2}$.

- Number of target atoms per unit area, n_A .
- Cross section σ_0 .

II.1.2 Magnetron Sputtering: Set Up and Operation Modes

A magnetron source consists on the application of a specially shaped magnetic field to a sputtering target, so that the cathode surface is immersed in a magnetic field that traps the emitted electrons. In this way the primary and secondary electrons are confined by magnetic field in the region of cathode, rising their chances to produce a higher number of ionisation events. This latter phenomenon has as a consequence a high ion current impinging on the target. To achieve an efficient electron trap, permanent magnets are used with a field strength of 20 mT or more. Figure II.3 shows the configuration of a magnetron source.

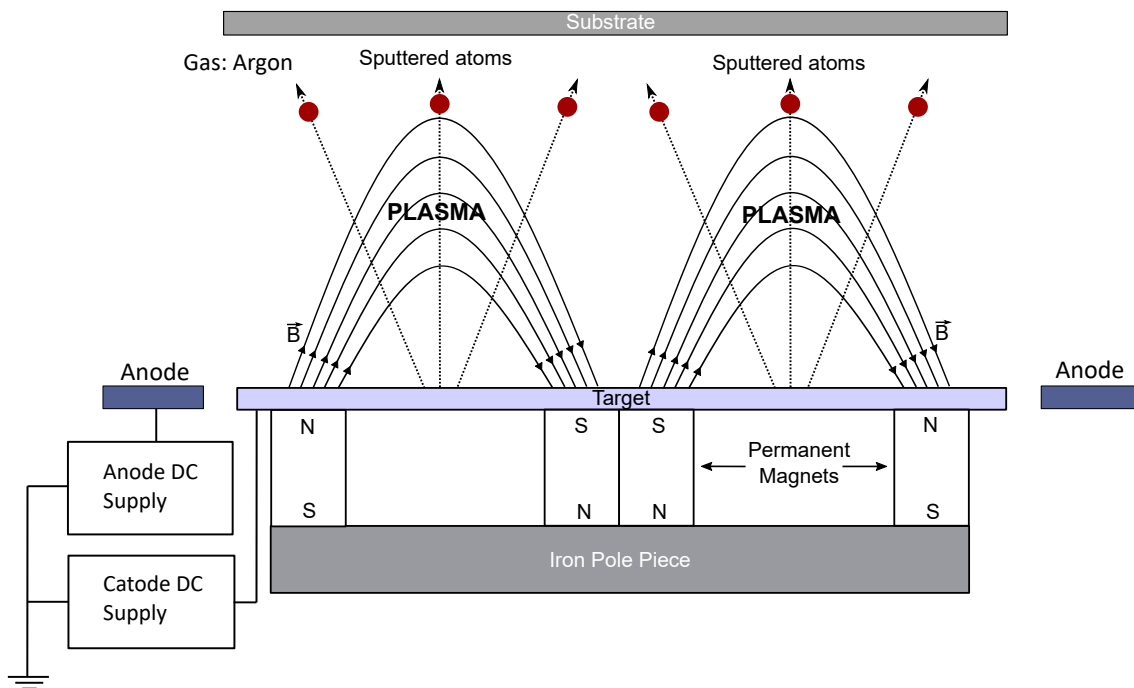


Figure II.3: Schematic of the magnetron sputtering configuration.

DC Magnetron Sputtering

The DC magnetron sputtering is the least expensive and simplest sputtering technique, thanks to the easy manufacturing of the DC power supplies. Its design guarantees high deposition speed and makes it suitable for high-production-rate

processes. The DC magnetron sputtering is mainly used for the deposition of metals for microelectronic applications, where film uniformity, compositional control, and step coverage are required. It does not work with insulating targets, since no current can flow through them.

RF Magnetron Sputtering

RF magnetron sputtering was developed to sputter insulating targets, by using an alternate current at a high frequency. When an AC signal lower than 50 kHz is applied to the electrodes, the DC sputtering conditions prevail and they behave alternately as cathode and anode. On the contrary, above 50 kHz, the electrons that oscillates in plasma (glow region) are able to sustain the discharge, because they have enough energy to create ionising collisions. This would reduce the need for secondary electrons. Moreover, RF voltages make possible to sputter any material independently from its resistivity, since it can be coupled through any kind of impedance. Typically the range of frequencies employed for the RF sputtering is 5 to 30 MHz, but the most common one is 13.56 MHz. The advantages of the RF sputtering over the DC one are: the diffusion of the plasma throughout the whole chamber, rather than being confined in the region around the cathode, and the possibility of sustaining a plasma at low pressure, resulting in a low collision-rate and in a more efficient deposition. Examples of RF sputtering applications are the synthesis of superconductive films, hard coatings, and dielectric films for optics. Nevertheless, the deposition rates of the RF sputtering are generally lower with respect to the DC one.

Reactive Magnetron Sputtering

In reactive magnetron sputtering, thin films of compounds are deposited on the substrates by sputtering of metallic targets in the presence of a reactive gas, which is usually mixed with the inert working gas (Ar). The most common compounds deposited by means of reactive sputtering are:

- Oxides
- Nitrides
- Sulfides

- Carbides
- Oxynitrides and Oxycarbides

The resulting sputtered films can be: solid solution alloys of the metal target doped with the reactive element, compounds, or mixtures of the two. Moreover, by controlling the flow rate of the reactive gas, it is possible to control the stoichiometry of the deposited film. However, a drawback of this technique is the "poisoning" of target by atoms of reactive gas.

Pre-sputtering

Pre-sputtering or conditioning is a necessary step to perform when a target is first pumped down into the sputtering chamber. In this phase, the contaminants present on the surface of the targets are removed and deposited onto the shutters, placed between the target and the substrate.

II.1.3 Equipment Used for Experiments

Magnetron sputtering system was used for the synthesis of the HZO layer, electrodes, and top electrical contact. The set up used for the growth of samples presented in this work consisted of: a deposition chamber, a lock-down chamber, a RF generator, a DC generator, four target holders of 4 inch, situated above substrate holder (3 inch), and connections with gas lines of Ar, N₂, O₂, H₂, and Ar/O₂. The distance between the target and the substrate was 8 cm.

II.2 UV Photolithography

The UV photolithography is a technique used to pattern the surface of samples to obtain circuit components at the nanoscale. In this work, UV photolithography with a negative mask was employed to fabricate the top electrodes and the top electrical contacts. The first step of the photolithographic process consists on the application of a photoresist (or resist) on the surface of the sample that is then irradiated by the UV light. The resist can be positive, negative, or reversal. If a positive resist is used, once the sample is exposed to UV radiation, any portion of it touched by the light dissolves in the resist developer and the obtained pattern



Figure II.4: Magnetron sputtering system available at INL: AC-450 by Alliance Concept.

resembles the one on the photo-mask. When a negative resist is employed, the parts exposed to the UV radiation become insoluble in the developer and resultant pattern is the inverse of the one on the photo-mask. Eventually, the reversal resist, used in this work, consists on a positive resist, which after a further treatment that includes a second exposition and annealing, behaves as a negative resist. The advantage of such a resist is related to the fact that its sidewalls form an undercut profile, which avoids damages to the adjacent electrodes during the development step. Furthermore, this process allows local depositions by "lift-off" procedure. The resist used in this work was the AZ5214, the developer the MIF726, and the lift-off procedure was performed in acetone. Figure II.5 describes step by step the UV photolithography process [142].

II.3 Fabrication Process of Capacitors

The samples described in this thesis were synthesised following the procedure here illustrated. N-doped silicon substrates, doped with P atoms and with a resistivity $> 200 \Omega/\text{cm}$, were initially cleaned by acetone and ethanol, and freed from the native oxide by a buffer oxide etching process (BOE). The bottom electrode and the HZO were deposited without breaking the vacuum and on the full surface of

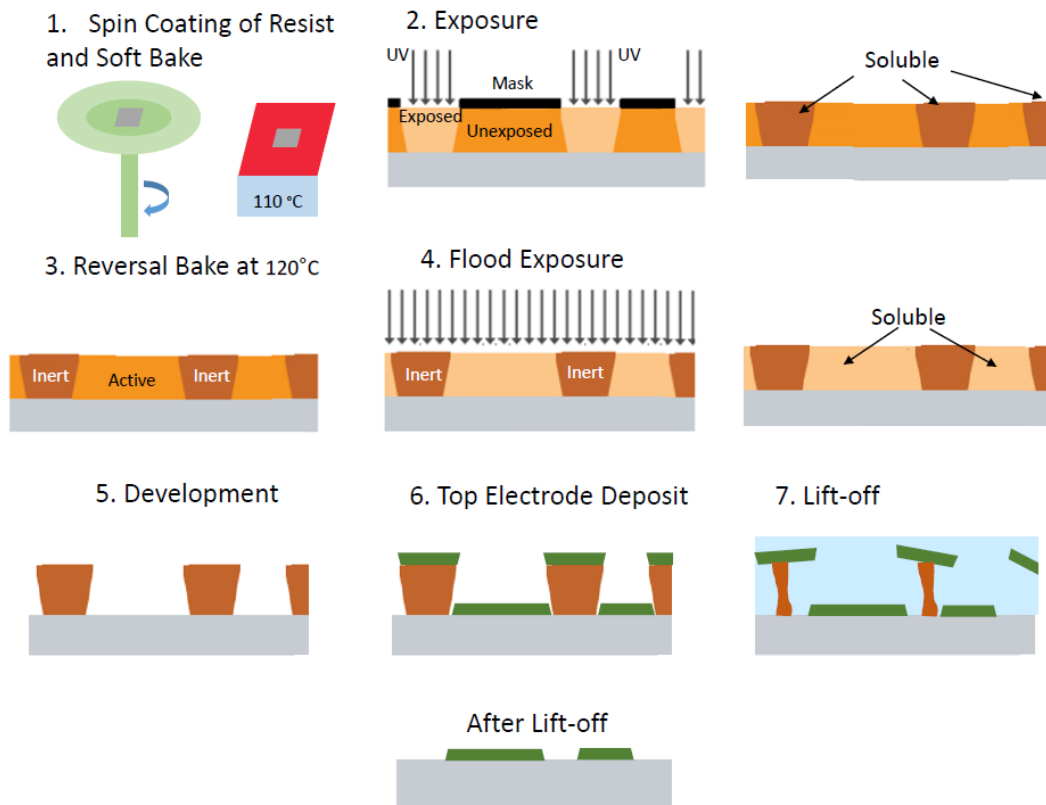


Figure II.5: Reversal photolithography procedure for the deposition of top electrodes and top contacts.

the sample by magnetron sputtering at room temperature. The deposition conditions and process are explained in chapter III. Prior to the top electrode and top electrical contact deposition, the UV photolithography was performed, using the mask depicted in figure II.6.

The top electrodes and top electrical contacts were deposited by magnetron sputtering, and, finally, the lift-off was performed to obtain the pattern of capacitors. The structure of a finished sample is represented in figure II.7, together with optical image of a portion of the sample surface.

II.4 Rapid Thermal Annealing

The rapid thermal annealing (RTA) is a semiconductor manufacturing process, which allows to rapidly heat samples in a short period of time, usually few minutes, in order to modify their chemical and structural properties. Rapid heating process is performed by high-intensity lamps controlled by a pyrometer and thermocouples that measure the temperature of the samples. The cooling step has to

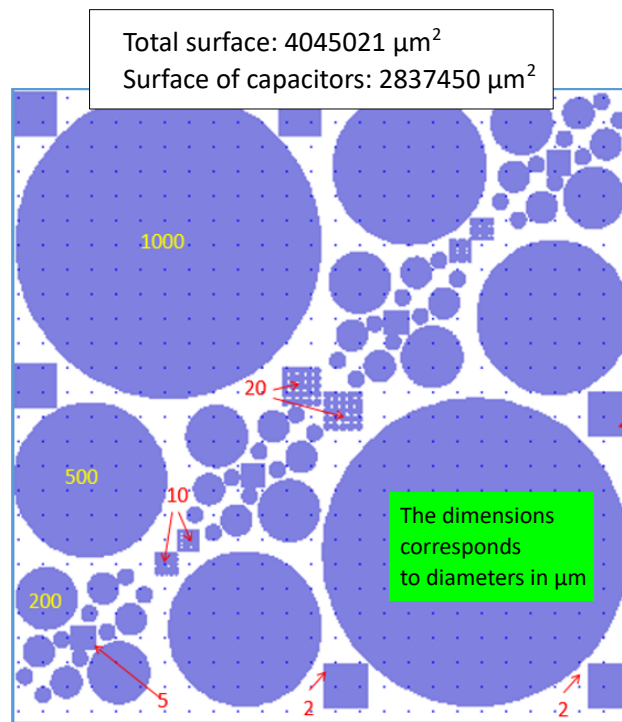


Figure II.6: Photo-mask used during the UV photolithography for the fabrication of capacitors.

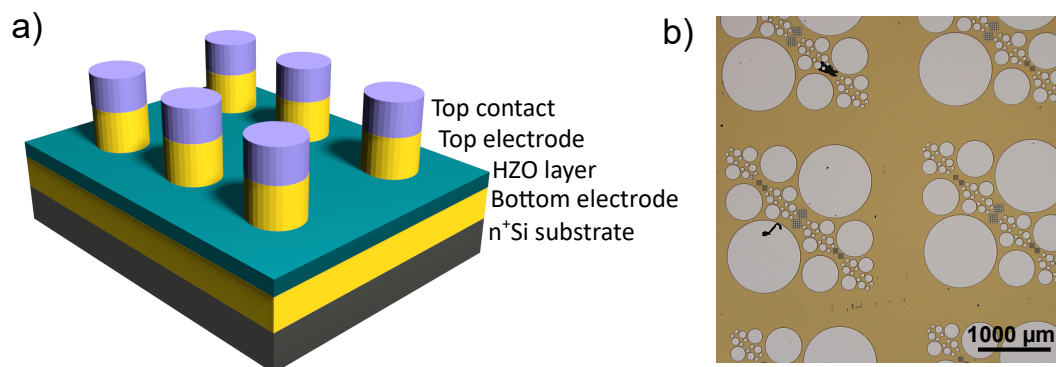


Figure II.7: a) Structure of a finished sample. b) Optical image of a portion of the sample surface, where the pattern of capacitors is visible.

be perfectly controlled in order to avoid damages to the sample. The RTA annealing was fundamental to achieve specific structural properties for the specimens presented in this work. It was performed using a RTA furnace JetStar 100SR by JIPELEC in a N_2 atmosphere.

II.5 Characterisation Techniques: Structural, Physical, and Chemical Characterisation

II.5.1 X-Ray Diffraction

X-ray diffraction is a powerful and non-destructive technique for the structural characterisation of crystalline materials. It provides information on several parameters such as, the crystal structure, the crystal phase, the crystallographic orientation, the grain size, the strain, and the crystal defects. It relies on the constructive interference of monochromatic X-rays and a crystalline sample. The X-rays are used because their wavelength is of the same order of magnitude of the distance between the atoms in a lattice. In this section the physical principle of XRD and its applications are illustrated, together with a description of the XRD equipment used for the experiments.

Physical Principle

Diffraction is defined as any deviation from geometrical optics that is caused by the obstruction of a wave front of light. For instance, it occurs when a light beam is scattered by a periodic lattice with a long-range order and generates constructive interference at specific angles. In a periodic crystal lattice, the electrons of the atoms coherently scatter the radiation and the scattering strength is directly proportional to the number of electrons around each atom. Each diffraction pattern is unique of the crystal structure of a material and materials that are not crystalline over a long-range, such as amorphous ones or glass, do not produce any diffraction pattern.

Bragg's Law

In 1913, the physicists W.H. Bragg and his son W.L. Bragg derived an equation, eq. II.2, to explain how the cleavage faces of crystals reflect the X-rays at certain angles. Figure II.8 illustrates the Bragg's law.

$$n\lambda = 2d\sin\theta \quad (\text{II.2})$$

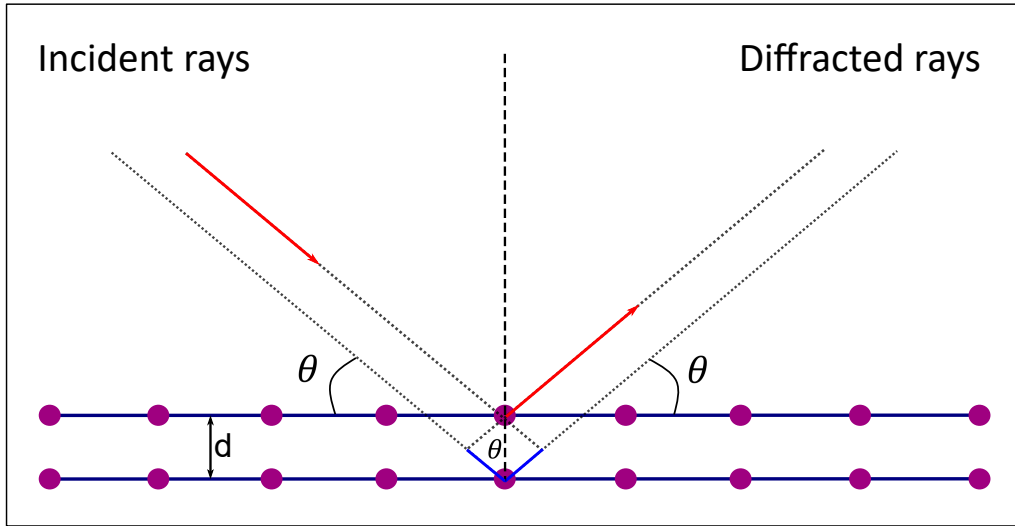


Figure II.8: Illustration of the Bragg's law.

where n is an integer, λ the X-ray wavelength, d the distance between two crystalline planes, identified by the Miller indexes hkl , and θ the incidence angle of light beam on the sample surface. The Bragg's law is used to obtain the angle at which the constructive interference from X-rays, scattered by parallel planes, generates the diffraction peaks. Since in most of the cases λ is fixed, a family of planes will produce a diffraction peak only at a specific angle 2θ . The intensity of the diffraction peaks is determined by the arrangement of the atoms in the crystal and it is proportional to the squared modulus of the structure factor F_{hkl} , according to the relation:

$$I_{hkl} = |F_{hkl}|^2 \quad (\text{II.3})$$

The structure factor sums the results of the scattering from all the atoms inside the unit cell to obtain a diffraction peak from the (hkl) planes of atoms.

$$F_{hkl} = \sum_{j=1}^m N_j f_j \exp[2\pi i (hx_j + ky_j + lz_j)] \quad (\text{II.4})$$

where m is the number of atoms in the unit cell and N_j is the fraction of every equivalent position that is occupied by an atom j .

II.5.2 Glancing Incidence X-ray Diffraction

Structural study of the specimens presented in this thesis was performed by glancing-incidence X-ray diffraction (GI-XRD). GI-XRD is a surface selective tech-

nique useful for the structural characterisation of thin films. It is based on the fact that, at X-rays energy, most of the materials are characterised by a refractive index approximatively equal to 1, so the total external reflection from the surface is possible at small enough incidence angles. In these conditions, the substrate is mostly invisible to the X-rays and only an evanescent wave penetrates and scatters from it. As a consequence, the X-rays intensity is maximum in the region of the surface. The GI-XRD technique in the configuration $2\theta/\omega$, figure II.9, was used. The latter consists on moving the mechanical arms, where source and detector are placed, to permanently obtain $\theta=\omega$, where ω is incidence angle and θ diffraction one. Initially, $\omega=\omega_c$ with ω_c being the measured critical angle.

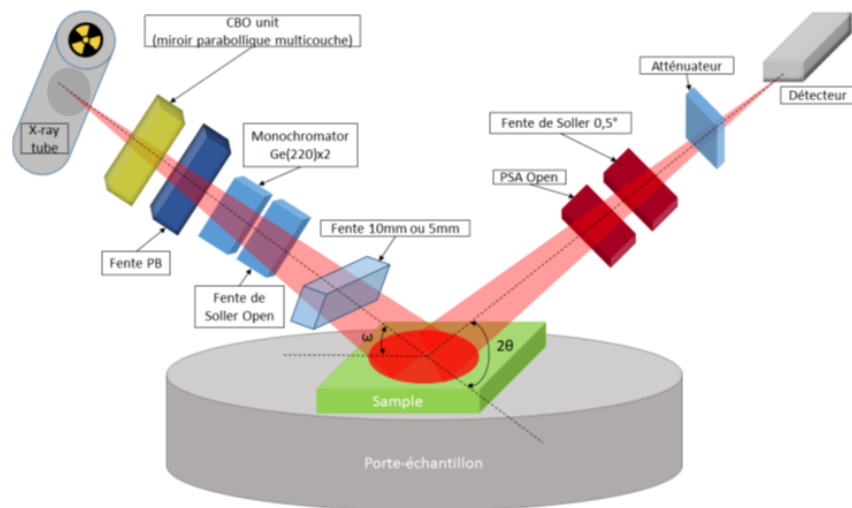


Figure II.9: $2\theta/\omega$ configuration of a Smartlab Rigaku Diffractometer [143].

Diffractometer

A X-ray diffractometer is composed by a X-ray generator, a sample holder, and a X-ray detector. The diffractometer used for the experiments was a five-circle goniometer Smartlab Rigaku, equipped with a 9 kW copper rotating anode, and shown in figure II.10.

II.5.3 X-Ray Reflectometry

X-ray reflectometry (XRR) is a technique used to determine the thickness, density, and roughness of a single layer or a multilayer structure, which can be crystalline



Figure II.10: Diffractometer by Rigaku available at INL.

or amorphous. This technique is performed in a $2\theta/\omega$ configuration. When the X-rays impinge on the flat surface of the sample, if angle of incidence ω is lower than ω_c , the X-rays are totally reflected. While, if $\omega > \omega_c$, the radiation penetrates in the sample and the reflectivity suddenly decreases. A rough surface is responsible for a sharper decrease in reflectivity. In the case of a multilayer structure with different electronic density, the X-rays reflected at the interface between layers and the ones reflected at free surface of the film interfere and generate an oscillation pattern. These oscillation are called Kiessig fringes. From the periodicity of the oscillations it is possible to deduce the thickness of films, while from the angular dependency of the amplitude of the oscillation patterns, information on the surface and on the interfaces are obtained. Figure II.11 reports an example of an oscillation patter obtained by XRR and the parameters of interest that can be extracted.

II.5.4 Transmission Electron Microscopy

Transmission electron microscopy is a technique of primary importance in the characterisation of microstructural properties of materials. It exploits an electron beam that, focused on a microscopic region of sample, gives a diffraction pattern. The "Diffraction contrast" mode can be used to take images of defects, dislocations,

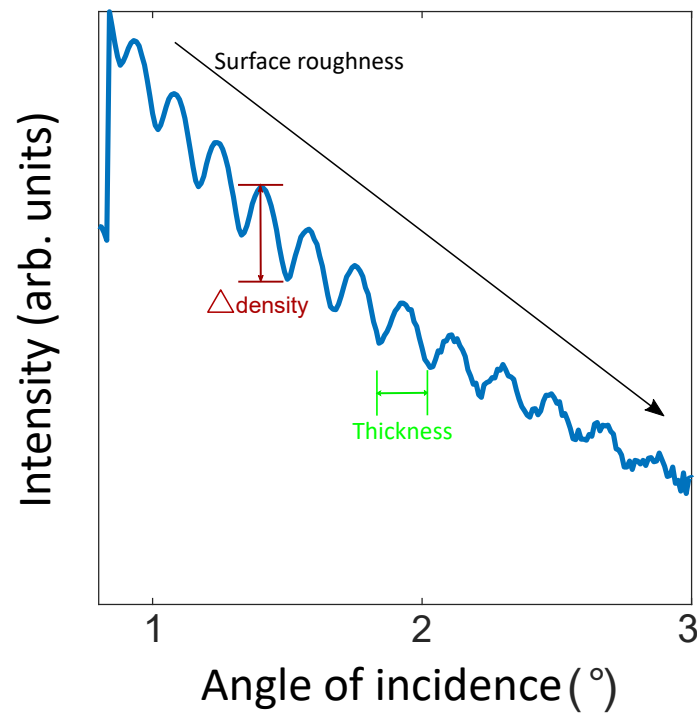


Figure II.11: Oscillation pattern obtained by means of XRR. In evidence the parameters of interest that can be extracted from the oscillations.

and interfaces, by measuring the variation of the intensity of electron diffraction in thin specimens. High-resolution transmission electron microscopy allows to obtain atomically resolved images, with information on the crystal structure and the lattice parameter. A further method, named "high-angle annular dark-field imaging", is used to obtain high-resolution images. In this case, electron nanobeams impinge on the sample and electrons are scattered at high-angles to minimise the interference. Beside the diffraction and spatial imaging, TEM technique is used to acquire information on the chemical properties of specimens, through electronic excitations of atoms, generated by high-energy electrons. This latter configuration is called "Analytical TEM" and it divides in two types of spectrometry:

- **Energy-dispersive X-ray spectrometry (EDS)**

A X-ray spectrum is acquired from small regions of the sample illuminated by a focused electron beam. The characteristic X-rays from the chemical elements are used to determine the concentration of the chemical species.

- **Electron energy-loss spectrometry (EELS)**

The energy losses of electrons are measured once the high-energy electrons have crossed the specimen. Information on the structure and local chemistry are obtained from the features of EELS spectra, caused by the core electron

and plasmon excitations.

A further mode in which TEM can operate is scanning transmission electron microscopy (STEM), where a narrow (≈ 10 Angstrom) and focused electron beam scans in a raster pattern the surface of the specimen. In synchronisation with the scan, various data from the sample are acquired, such as emitted X-rays, secondary electrons, and backscattered electrons. The transmitted electrons are collected by a detector placed at the bottom of the microscope column. The STEM mode is of interest for spectroscopy work, since it provides a sort of "chemical-map" of the sample. An annular dark-field detector can be used in STEM mode for high-angle annular dark-field imaging.

To conclude the main operation modes of a TEM microscope are listed below:

- Conventional imaging (bright-field and dark-field TEM)
- Electron diffraction (selected area electron diffraction SAD)
- Convergent-beam electron diffraction (CBED)
- Phase-contrast imaging (high-resolution TEM, HRTEM)
- *Z*-contrast imaging
- Energy-dispersive X-ray spectroscopy (EDS)
- Electron energy-loss spectroscopy

Figure II.12 show a schematic of a TEM microscope that include the STEM functionality.

In this work, mainly HR-TEM and EELS were used to analyse the microstructure and the chemical properties of the specimens presented in chapters III, IV, and V. A more detailed explanation of the latter operation modes is given below.

High-Resolution TEM

High-resolution (HR) TEM microscopy allows to obtain atomically resolved TEM images. An HR-TEM pattern is generated by the interference of an electron wave function with itself after being diffracted from the specimen. In order to better understand HR-TEM images, the Fourier transform method is used. The wave

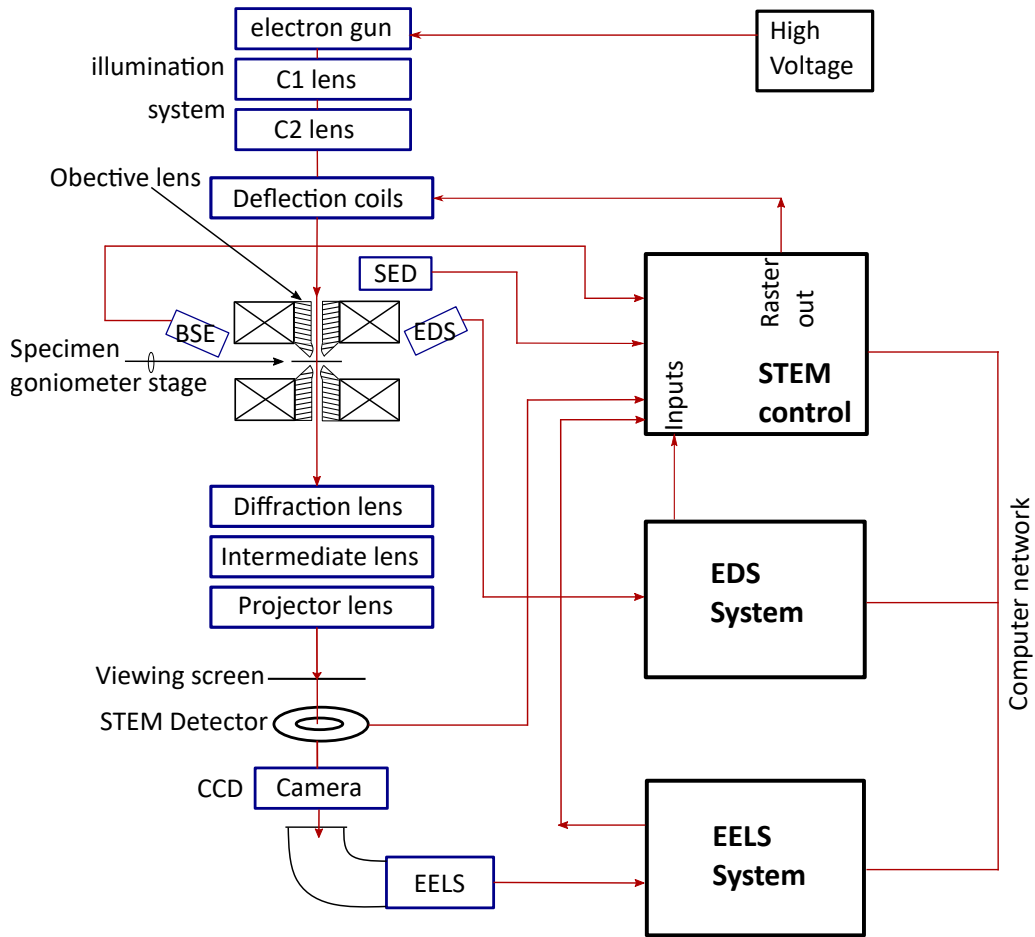


Figure II.12: Schematic of a TEM microscope equipped with the STEM mode.

function of the diffracted electrons, $\psi(\bar{\Delta}k)$, is the Fourier transform of the scattering factor distribution $f(\mathbf{r})$ in the material, which follows the atoms arrangement. $\bar{\Delta}k$ is the diffraction vector. The Fourier transform of the arrangement of atoms in the specimen in the real space is:

$$\psi(\bar{\Delta}k) = F[f(\mathbf{r})] \quad (\text{II.5})$$

and

$$f(\mathbf{r}) = F^{-1}[\psi(\bar{\Delta}k)] \quad (\text{II.6})$$

The explicit forms of the forward and inverse Fourier transforms are:

$$\psi(\bar{\Delta}k) = \frac{1}{\sqrt{2\pi}} \int_{-\infty}^{+\infty} f(\mathbf{r}) e^{-\bar{\Delta}k \cdot \mathbf{r}} d^3\mathbf{r} \quad (\text{II.7})$$

and

$$f(\mathbf{r}) = \frac{1}{\sqrt{2\pi}} \int_{-\infty}^{+\infty} \psi(\bar{\Delta}k) e^{+\bar{\Delta}k \cdot \mathbf{r}} d^3 \bar{\Delta}k \quad (\text{II.8})$$

Evidently to obtain full spatial details, the Fourier transform has to be performed considering as limits for $\bar{\Delta}k$ $-\infty$ and $+\infty$. Since the latter condition cannot be satisfied, the limits of $\bar{\Delta}k$ are imposed by the objective aperture in the back focal plane of objective lens. For instance, an image formed with a small range of $\bar{\Delta}k$ shows only long range spatial features. Consequently, for an objective aperture that selects a range δk , smallest spatial feature in the image has a size δx , where:

$$\delta x \approx \frac{2\pi}{\delta k} \quad (\text{II.9})$$

δk is the reciprocal lattice vector or separation in reciprocal space of two first diffraction spots from the transmitted beam. In order to resolve the atomic arrangement, the aperture needs to span over a range $\delta k \approx 2\pi/d$, with d being the distance between atoms. In scanning mode (HR-STEM), the microscope lenses create a focused electron beam, which is scanned across sample surface and the signal is collected point-by-point, allowing higher contrast.

HR-TEM data were collected at RMIT Microscopy and Microanalysis Facility (RMMF) at RMIT University, with a JEOL JEM-200F microscope, figure II.13.



Figure II.13: TEM microscope JEOL JEM-200F used for HR-TEM experiments.

Electron-Energy Loss Spectroscopy

Once the electrons have traversed the TEM sample, a part of them lost its energy to core or plasmon excitations, so the energy at which they reach the detector is

lower than the initial one. The EELS spectrometer measures the energy spectrum of these losses. The spectrometer includes a magnetic sector used to disperse electrons according to their energy, for instance, electrons of the same energy are bent by Lorentz force into arcs of equal curvature. The spectrometer can be of two types: serial or parallel. In a serial spectrometer, a slit is placed on the focal plane of the magnetic sector and a scintillation counter is mounted after the slit. Only the intensity corresponding to the electrons bent at an angle that allows them to enter the slit is recorded. The range of energy losses is selected by varying the intensity of the magnetic field. A parallel spectrometer covers the focal plane of the magnetic sector with a scintillator and a position-sensitive photon detector, for instance a photodiode array. The post-field lenses magnify the energy dispersion before the electron reaches the scintillator. Nowadays, the best EELS spectrometers can reach a energy resolution of 0.1 eV.

The EELS data presented in this work were collected at the "Consortium Lyon Saint-Etienne de microscopy (CLYM)", using a JEM-ARM200F NeoARM microscope by JEOL, in figure II.14, and at RMIT Microscopy and Microanalysis Facility (RMMF) at RMIT University with a JEOL JEM-200F microscope, in figure II.13.



Figure II.14: TEM microscope JEM-ARM200F NeoARM by JEOL used for EELS and HR-STEM experiments.

II.5.5 Atomic Force Microscopy

Atomic force microscopy (AFM) is part of the scanning probe microscopy techniques characterised by a resolution below the nanometer. It is used to probe the morphology of a surface and its magnetic properties. An AFM measurement consists on a cantilever equipped with a sharp tip, which serves as a probe, that is used to scan the surface of the specimens. Once the probe approaches the sample, the forces between the latter and surface lead to a deflection of cantilever measured by a laser beam. Figure II.15 shows a schematic of an AFM measurement. A feedback mechanism is employed to adjust the distance between probe and sample, in order to maintain constant the force between the two. The probe tip is mounted on a piezoelectric system that allows to scan the surface along x, y, and z directions. An AFM microscope can operate in three modes: static, dynamic (or tapping), and non-contact. In static mode, the scanning tip is kept in contact with the surface of the specimen. In this case, the tip exerts a repulsive force on the surface, which can result in the application of a rather high pressure that might damage the sample. In dynamic mode, the cantilever oscillates close to its resonance frequency, and it "taps" on the surface of the sample in an intermittent manner. Finally, in non-contact mode, the tip vibrates at its resonance frequency close to the sample and without touching it. The forces that generate between tip and surface are attractive. This latter method is commonly used to scan soft surfaces.

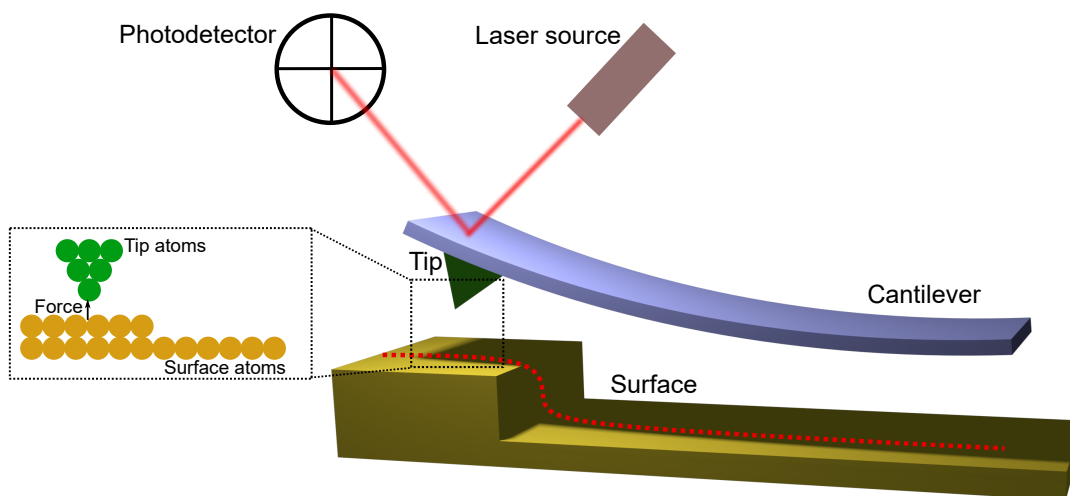


Figure II.15: Schematic of AFM technique.

AFM images were acquired at INL by means of a Park NX10 AFM, in figure

II.16.



Figure II.16: Park NX10 AFM.

II.5.6 Rutherford Backscattering Spectrometry

RBS technique is a thin-films analysis technique used to investigate the structure and composition of materials. It relies on the elastic scattering of α particles of few MeV emitted by a radioactive source. The first experimental evidence of such phenomenon refers to the well-known Rutherford's experiments in 1909. In this case the α particles had an energy of 5 MeV and target was a 0.6 μm -thick gold foil. By using the scintillation method, the scattering pattern was obtained on a fluorescent screen. This scattering phenomenon was attributed to the repulsive Coulomb interaction between α particles and atomic nuclei. From 1950 Rutherford scattering began to be used as a surface analysis technique, under the name of Rutherford Backscattering Spectrometry (RBS).

Physical Principle

The most important parameter to define is the kinematic factor K , which is the ratio between the initial energy (E_0) of the incident ions and the energy they have after the scattering event. Figure II.17 represents the large-angle scattering phenomenon.

The expression of the kinematic factor K is given by:

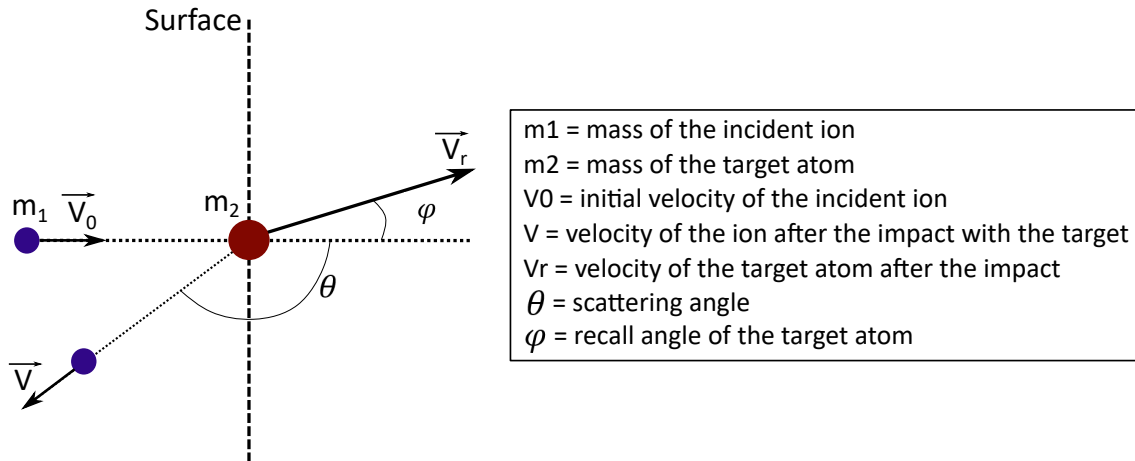


Figure II.17: Representation of large-angle scattering.

$$K = \left[\frac{m_1 \cos \theta + \sqrt{m_2^2 - m_1^2 \sin^2 \theta}}{m_1 + m_2} \right]^2 \quad (\text{II.10})$$

With m_1 , E_0 , and θ fixed, K is unique function of m_2 . This means that, from the measure of energy of the scattered ions, it is possible to determine the atomic mass of the atoms of sample surface. From the evolution of the kinematic factor as a function of atomic mass of target atoms it is possible to conclude that:

- For a given incident ion, the selectivity of the RBS analysis, which is its capability to discriminate between two species with similar atomic numbers, is improved for lower values of m_2 .
- For a given atomic species of the target, the selectivity increases as m_1 increases.
- The selectivity decreases as the diffusion angle, θ , decreases. It can be considered constant for values of θ between 150° and 180° .

RBS Experimental Equipment

The experimental equipment used to perform the RBS analysis consists of:

- An accelerator, which, through the application of a high voltage (1-4 MV), accelerates the ions (for instance H^+ , He^+). The ions are produced by a source where the plasma is generated by means of a RF power supply.
- A mass spectrometer, which sorts ions according to their mass/charge ratio and allows only the ones characterised by the correct ratio.

- Electromagnetic lenses used to focus the ion beam. The flux is typically 10^{13} ions. $\text{cm}^{-2}.\text{s}^{-1}$.
- A chamber that contains the sample to be analysed and the detectors for scattered ions. The chamber is kept under vacuum at a pressure of $\approx 10^{-6}$ mbar. The vacuum is generated by a pumping system, usually a turbo-molecular pump.

The experiments were performed using ${}^4\text{He}^+$ ions of 2 MeV energy delivered by the 2 MV Van de Graaff accelerator, in figure II.18, of the SAFIR platform located at Paris Institute of Nanosciences.

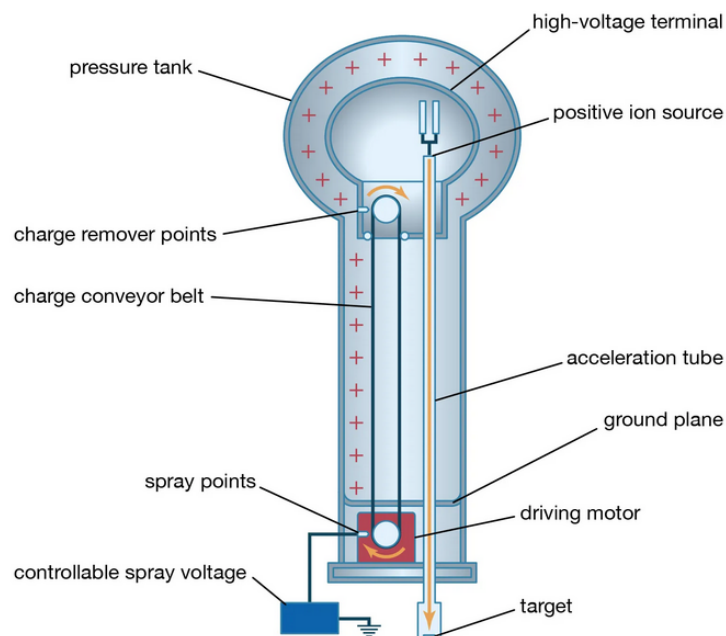


Figure II.18: Schematic of a Van de Graaff accelerator used for RBS analysis. Reprinted from: <https://www.britannica.com/science/electricity/Conductors-insulators-and-semiconductors>.

II.6 Characterisation Techniques: Electrical Characterisation

The electrical characterisations of the synthesised samples were performed at the micro-scale by means of different techniques, which gave information about the electrical properties of the specimens. The measurements that were performed are: current vs voltage measurements, capacitance vs voltage measurements, and

polarisation vs voltage measurements, by means of the positive-up-negative-down (PUND) technique. The electrical characterisation were carried out by means of a manual probe station, where the samples were kept in a closed environment and the electrical contact was made with two tungsten-tip probes. The voltage was applied by contacting the top electrical contact of each device with one probe, while the other was kept on the common bottom electrode. I - V , C - V , and P - V curves were acquired on a single capacitor structure, where the Pt layer was used as electrical contact, reference to the structure in figure II.7.

II.6.1 Current vs Voltage Measurements

The measure of the leakage current is a fundamental parameter for the characterisation of ferroelectric-based devices. This aspect is treated in the following with a special focus on the importance of this mechanism for FTJs. The largest part of technological applications, for instance ferroelectric random access memory, require the leakage current to be minimised [144]. Indeed, the latter is responsible for the fragility of ferroelectric materials, which is among the causes that provoke an early electrical breakdown [145], [146]. On the contrary, for the synthesis of FTJs, the leakage current becomes an important parameter to take into account for the maximisation of TER ratio, introduced in section I.4.4. I - V characteristics were acquired by means of a *Agilent 4156B Semiconductor parameter analyser*, in figure II.19, and the measure was performed by the application of a step-shaped voltage waveform, represented in figure II.20, from 0 to $V_{max}/-V_{max}$, in this work the used delay time (t_d) was ≈ 0 [142]. The current response was then recorded by applying a voltage of the same shape, in order to avoid the response generated by the back-switching of ferroelectric domains. Figure II.21 [142] shows an example of the characteristic curve of the leakage current of a ferroelectric capacitor. An insight on the nature of leakage current can be extrapolated by fitting experimental curves with charge transport mechanisms that occur inside a ferroelectric, section III.4.2, to find the dominant one.



Figure II.19: Agilent 4156B semiconductor parameter analyser.

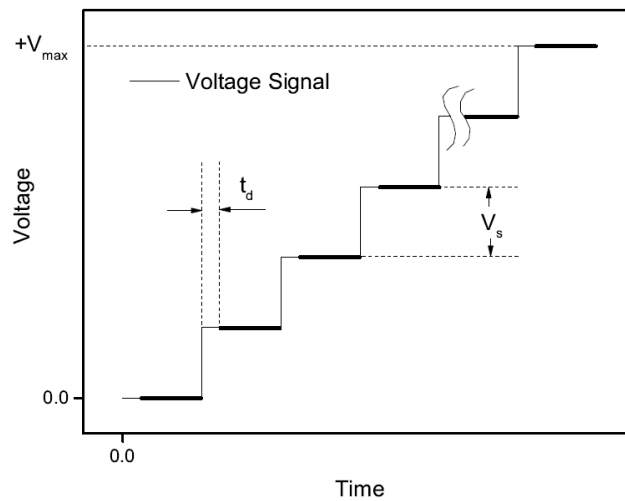


Figure II.20: Voltage waveform used to acquire *I-V* characteristics.

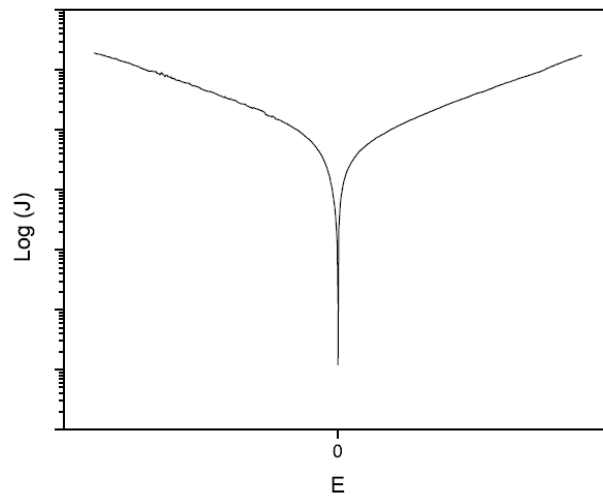


Figure II.21: Typical curve that represents the logarithm of the current density vs the applied electric field of a ferroelectric-based device.

II.6.2 Capacitance vs Voltage Measurements

Ferroelectric materials are characterised by a non-linear dielectric permittivity ϵ_r , which varies according to the applied field, temperature, and frequency. In the

case of an ideal ferroelectric, ϵ_r as a function of frequency shows two peaks approximately in correspondence of the the coercive field, $\pm E_c$, figure II.22 [142].

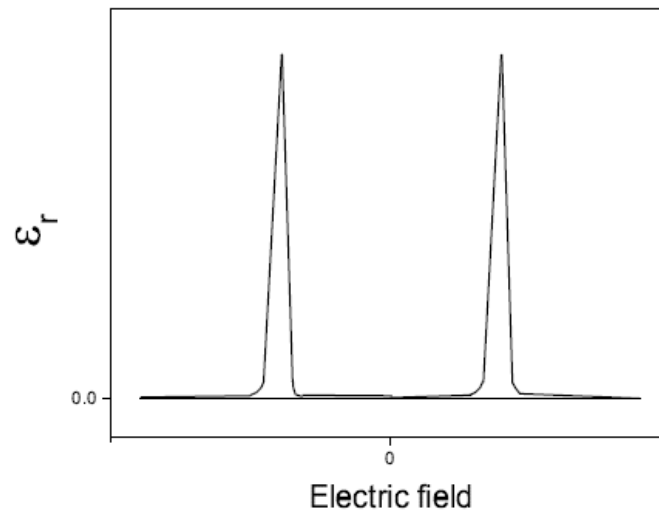


Figure II.22: Dielectric permittivity ϵ_r as a function of the electric field for a ferroelectric material.

The explanation for this trending refers to the fact that, during polarisation switching, small changes in the electric field are responsible for a sharp increase of the dielectric permittivity [147]. For high quality ferroelectric films, the height of the peaks can exceed 5000 [148]. However, as previously mentioned, the peak value of ϵ_r depends on the frequency and, as it increases, the latter reaches a constant limiting value. This result is explained by the dipole movements, indeed, as frequency increases the response of the domains to changes in the electric field is delayed and the charge accumulation at the metal/ferroelectric interface diminishes [149]. The set up used to perform C - V measurements was a *HP 4284A Precision LCR meter*, in figure II.23.



Figure II.23: HP 4284A Precision LCR meter.

A bias DC voltage, with a waveform similar to the signal in figure II.20, was applied to the ferroelectric and a small AC signal was used to measure the ca-

capacitance [142]. The experimental curve obtained from a C - V measurement of a ferroelectric device resembles the one in figure II.24. The curve is composed by a linear part (in green) independent from the frequency and voltage, a non-linear part (in red) with two peaks, due to the ferroelectric switching behaviour of the material, and a further linear part (in blue) which corresponds to the paraelectric contribution. The latter refers to those dipoles that displace under the action of the electric field and that regain the original position once the field is removed.

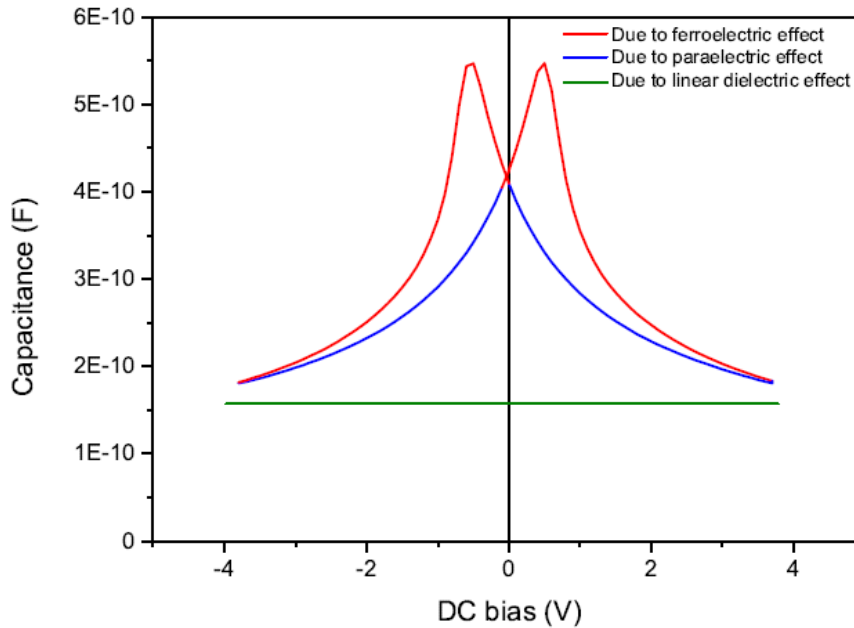


Figure II.24: C - V curve typical of ferroelectric materials

II.6.3 Polarisation vs Voltage Measurements: Hysteresis Cycle

The experimental set up employed to measure the polarisation as a function of the applied voltage consisted in a *NF WF1966 2-channel* generator, a *Nicolet INTEGRA-40* oscilloscope, and a *KEITHLEY 4200A-SCS* semiconductor parameter analyser. The generator sends specified train of voltage pulses and oscilloscope registers the current response, previously amplified by the signal amplifier. Figure II.25 outlines the circuit used for P - V curves acquisition.

The pulse train that was found optimal for the acquisition of the P - V characteristics was the PUND schema, which consists on a train of five triangular pulses with the same amplitude ($\pm V_{max}$) and rise and fall time (t_{rise} , t_{fall}), figure II.26 [143].

- **Pre-switch pulse:** it aligns the domains along one direction.

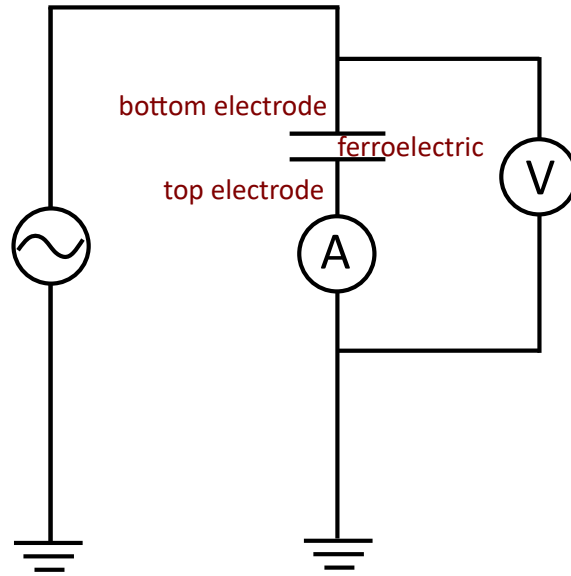


Figure II.25: Schema of the circuit used to measure the polarisation as a function of the applied voltage.

- **First positive pulse (P):** to switch domains upward, it includes other contributions due to domain motion and leakage current.
- **Second positive pulse (U):** to measure other contributions to the current, which are not due to the domain switching.
- **First negative pulse (N):** it switches domains downward, it includes other contributions due to the domains motion and leakage current in the opposite sense.
- **Second negative pulse (D):** as for the U pulse, it is used to measure other contributions to the current, which are not due to the domain switching.

By the integration of the current response recorded during each pulse of PUND train, the hysteresis loop is extracted according to the following equations:

$$\bar{D} = \epsilon_0 \bar{E} + \bar{P} = \epsilon_0 \epsilon_r \bar{E} \quad (\text{II.11})$$

where D is the displacement vector and ϵ_r relative dielectric constant. Recalling that the current is defined as dI/dt , it is possible to express the charge as a function of the displacement vector D , II.12:

$$Q = \int I \cdot dt = \int_s \bar{D} d\bar{S} \quad (\text{II.12})$$

Where $d\bar{S}$ is the δ surface crossed by current I in time δt .

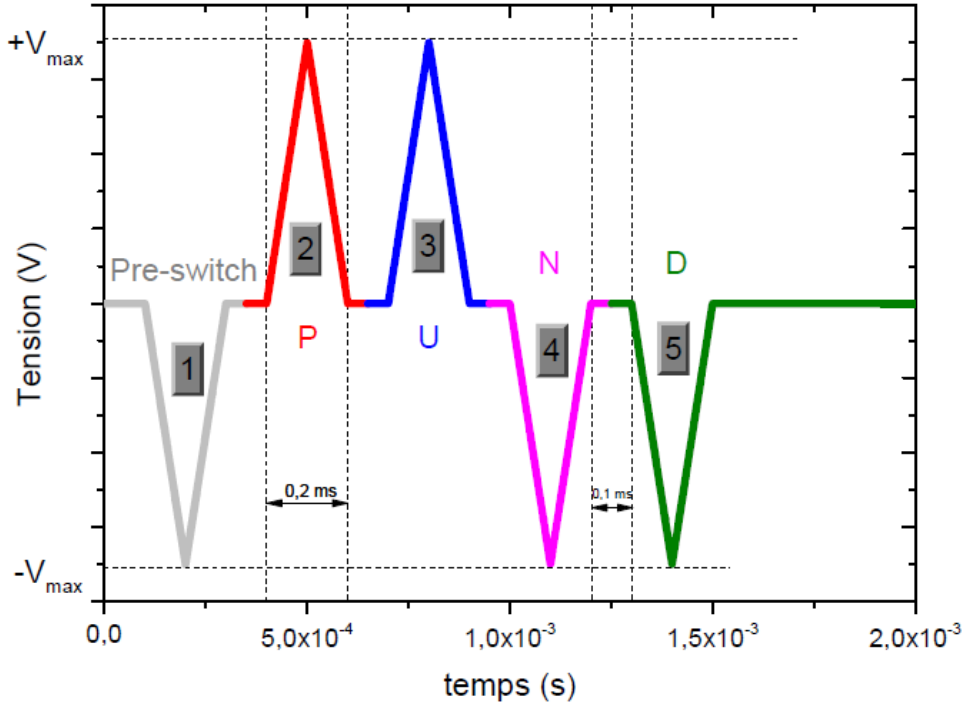


Figure II.26: PUND pulse train.

$$\bar{D} = \frac{1}{S} \int I dt \quad (\text{II.13})$$

For the case of pulses P and U :

$$\bar{D} = \frac{1}{S} \int_0^{t_{pulse}} I(P) - I(U) dt = \frac{1}{S} \left[\int_0^{t_{pulse}} I(P) dt \right] - \left[\int_0^{t_{pulse}} I(U) dt \right] \quad (\text{II.14})$$

$$\bar{D} = \bar{D}(P) - \bar{D}(U) \quad (\text{II.15})$$

From equation II.11, D can be expressed as a function of the polarisation.

$$\bar{D} = \epsilon_0 \bar{E} + \bar{P}(P) - [\epsilon_0 \bar{E} + \bar{P}(U)] \quad (\text{II.16})$$

$$\bar{D} = \bar{P}(P) - \bar{P}(U) \quad (\text{II.17})$$

As it was previously mentioned, the pulse P includes the current response due to the switching of ferroelectric domains and other current contributions, such as leakage, while the second upward pulse U only contributions due to leakage

currents. In the ideal case:

$$D_{PU} = P_{PU,ferroelectric} \quad (\text{II.18})$$

If the same procedure is repeated for the two negative pulses N and D , the obtained P - E hysteresis loop will only correspond to ferroelectric effects. On the contrary, if only the integral of current response of the pulses P and N is considered, the contributions due to leakage current would lead to a overestimated value of the remanent polarisation and the coercive field.

II.6.4 Endurance Test

The endurance test was performed by submitting the samples to multiple pulse trains until it reached the electrical breakdown. The samples underwent a procedure composed by two sequences: the "cycling" and the "measure". During the former, the properties of the samples evolved, this evolution was due to the present of defects in the ferroelectric layer (section I.2.6), while the aim of the latter was to extract the P - V hysteresis loop. The endurance test, as it is explained later, is often responsible for a change of material ferroelectric properties. The used sequence for the "measure" was PUND pulse train that was described in section II.26.

II.7 Conclusion of the Chapter

This chapter provided a description of the equipment employed for the synthesis and characterisation of the specimens made during the thesis. Sputtering, UV photolithography, and rapid thermal annealing were used for sample fabrication. The structural, physical, and chemical characterisations were performed by XRR, GI-XRD, TEM, HR-TEM, EELS, AFM, and RBS. Finally, I - V measurements, C - V measurements, and PUND were carried out to test the electrical properties of devices. In chapters III, IV, and V the experimental results acquired by means of the aforementioned techniques are presented.

CHAPTER III

HZO Thin Films-Based Devices: Synthesis and Applications

Chapter III is divided in two main sections. The first part is dedicated to the fabrication techniques used to grow thin HZO films for non-volatile memory applications and to the technological constrains related to their synthesis. The second section describes the fabrication process and the structural, physical, and electrical properties of the heterostructure taken as reference for this work.

III.1 HZO Thin Films: State of the Art

The growth technique used for the synthesis of HZO and the post-deposition annealing play a fundamental role in understanding the ferroelectric behaviour of thin films. Different techniques, such as atomic layer deposition (ALD), plasma-enhanced ALD (PE-ALD), sputtering, and pulsed laser deposition (PLD), have been reported in literature. The following paragraphs provide a brief analysis of each of the mentioned techniques and of the impact of post-deposition annealing temperature and conditions. As a conclusion for the first section, a description of technological issues and limitations related to the synthesis of HZO thin films is given.

III.1.1 Deposition Techniques of HZO Thin Films

Atomic Layer Deposition

Atomic layer deposition (ALD) is a thin film deposition technique that allows to reach atomic-scale control. Reactants (or precursors) of elements or alloys, which will constitute the thin film, are pulsed in a reactor, placed under vacuum, alternately and cycle-wise. H_2O is often used as reactant for the deposition of oxides. Precursors react with each other thanks to saturative surface reactions and sub-monolayers of material are deposited during each cycle. ALD is widely used for deposition of HfO_2 , ZrO_2 , and HZO films with robust ferroelectric properties [27, 54, 150–152].

Plasma-enhanced ALD

A variant of ALD is plasma enhanced ALD (PE-ALD). Here, a radio-frequency plasma facilitates the chemical reactions through the creation of reactive oxygen ions, allowing a lower processing temperature compared to ALD. In the literature, several works showed ferroelectric HfO_2 -based thin films realised by PE-ALD [153, 154].

Sputtering

Sputtering, as a method for the synthesis of HfO_2 -based films, has gained interest only in recent years. Indeed, before 2015, there were no example in the literature of HfO_2 -based thin films grown by sputtering. The use of this technique for the deposition of thin films presents several benefits compared to others methods. Sputtering is a low-cost process, it reduces risks of carbon contamination compared to ALD, it allows fast, room temperature, and large scale depositions, and it is reproducible. Furthermore, by sputtering, it is possible to grow high quality ferroelectric thin films [22, 83, 155–160]. Finally, it allows the control of many degrees of freedom, such as deposition pressure, temperature, and power.

Pulsed Laser Deposition

Pulsed laser deposition (PLD) is a powerful technique for the synthesis of monocrystalline thin films. It consists of a target holder and a substrate holder

placed in a vacuum chamber, a high-power laser beam is focused, through optical components, over the target that is vaporised and the thin film grown. The advantages of this technique are the ability to preserve the stoichiometry of compounds materials -the thin film has the same chemical composition of the target material- and capability to synthesise films with complex chemistry. On the contrary, a drawback of PLD is related to the time cost required for the deposition process. Examples of PLD for deposition of HfO₂-based thin films are reported in the literature [56, 87, 161–165]. As an example, Sulzbach *et al.* demonstrated ferroelectricity in epitaxial HZO layers down to 2 nm [88]. However, even though ultra-thin epitaxial ferroelectric films grown on matched substrates are often characterised by better electrical properties than the ones synthesised by other methods, up to now, there is no viable manner for the integration of such layers into dense networks for neuromorphic applications.

III.1.2 Impact of Annealing Conditions

The annealing process is crucial for the formation of the ferroelectric phase in HZO. The annealing method and the temperature heavily impact the performances of the final device. As mentioned in section I.3, the crystallisation temperature (450 °C) of the ferroelectric phase in HfO₂-based materials is compatible with the back-end-of-line integration process. Furthermore, the Hf_{0.5}Zr_{0.5}O₂ compound, through Hf:Zr 1:1 substitution, allows the lowest crystallisation temperature. The annealing process influences the electrical properties of HfO₂-based devices, including remanent polarisation, wake-up, and endurance. In the literature, several groups reported the impact of the annealing conditions on the device performances. Bouaziz *et al.* compared the electrical characteristics of samples annealed at different temperatures and showed that, at high annealing temperature (600 °C), the remanent polarisation increased, while, at low temperature (450 °C), samples showed higher endurance [159]. Kim *et al.* managed to suppress the leakage current and reduce the wake-up effect in HZO-based capacitors by annealing at 850 °C [166]. Finally, Jeon *et al.* compared the effect of high-pressure post-deposition annealing (HPPMA) at different temperatures with rapid thermal annealing (RTA). They showed a strong increase of the value of remanent polarisation for samples annealed by HPPMA at 550 °C and achieved a maximum

dielectric constant at 350 °C [167].

III.1.3 Oxygen Vacancies

Section I.2.6 of chapter I listed the main issues that influence the ferroelectric properties of HfO₂-based devices and more in general of ferroelectric materials. One of the major causes of such issues, which is of fundamental interest in this work, is the concentration of oxygen vacancies (OVs) in the HZO layer. OVs can be considered as point defects, which could be pre-existing in the film, generated during its synthesis process, or during electric field cycling. OVs were demonstrated to be responsible for the wake-up effect [168, 169] and for an early electrical breakdown. The movement of OVs has been exploited for resistive random access memory (RRAM). Indeed, the control of their displacement inside the ferroelectric film leads to a change in its resistance, through a filament formation process that is responsible for the occurrence of two states of resistance. When the filament is formed, the device is in a low resistance state, while the high resistance state is achieved after the rupture of the latter [170]. Nevertheless, OVs play different roles as other types of devices are concerned. For instance, for ferroelectric tunnel junctions, they constitute a crucial parameter for the control of the TER ratio, discussed in section I.4.4. In this case, the difference in flowing current between the low and the high resistance states has to be maximised, in order to increase TER ratio, and OVs act as trap states for electrons in the trap-assisted tunnel mechanism [171, 172]. Furthermore, several studies conducted by Mittmann *et al.* [173, 174] showed that, at very low HZO thickness (typically below 8 nm), OVs help the stabilisation of the ferroelectric phase, favouring the formation of the t-phase, which, through annealing, transforms into o-phase [45]. Moreover, it was shown by Schroeder *et al.* that OVs help reducing the annealing temperature for the formation of the f-phase in HfO₂-based compounds (reference to "*From fundamentals aspects of ferroelectricity to devices based on HfO₂-ferroelectrics*", IEEE FerroSchool Lyon 2022).

Depending on the employed fabrication technique, the concentration of OVs generated during the synthesis process of HfO₂-based films might vary. For instance, in ALD-manufactured thin films, the average concentration of OVs is usually higher compared to the other fabrication methods, because of the high oxygen rate used

during the deposition. For each synthesis and annealing techniques, different fabrication specifications allow a certain degree of control over the OV's concentration for the optimisation of the device ferroelectric properties [174–176].

III.1.4 Formation of Dead Layers

At the interface between the ferroelectric layer and the electrodes, it is common to observe the so-called dead layer. This is a dielectric layer that do not contribute to the polarisation reversal and which is responsible for the generation of a depolarising field that leads to a degradation of the ferroelectric properties [177]. Its effect is substantially to reduce the active thickness of the ferroelectric film, by decreasing the amount of the switching domains. The effect of the dead-layer becomes more evident when the thickness of the active layer is low. Interface engineering is of extreme importance to limit this phenomenon [178, 179]. Below a more detailed explanation of the link between the dead-layer and the depolarising field. If a ferroelectric capacitor is considered, the total capacitance can be expressed as:

$$C_T = \frac{C_{FE}C_{dl}}{C_{FE} + C_{dl}} = \frac{\epsilon_0\epsilon_{FE}\epsilon_{dl}}{\epsilon_{FE}d_{FE} + \epsilon_{dl}d_{dl}} \quad (\text{III.1})$$

Where C_{FE} is the capacitance of the ferroelectric layer, C_{dl} capacitance of the dead layer, and ϵ_{dl} dielectric permittivity of the dead layer. The voltage across the ferroelectric and the dead layer results in:

$$V = E_{FE}d_{FE} + E_{dl}d_{dl} \quad (\text{III.2})$$

With E_{dl} being the field across the dead layer, and E_{FE} the one across the ferroelectric. The displacement fields of the ferroelectric and the dead layer are equal to:

$$D_{FE} = \epsilon_0\epsilon_{FE}E_{FE} + P \quad (\text{III.3})$$

$$D_{dl} = \epsilon_0\epsilon_{FE}E_{dl} \quad (\text{III.4})$$

If short circuit conditions are considered ($V=0$), $D_{FE}=D_{int}$, the depolarising

field can be expressed as:

$$E_{dep} = \frac{-Pd_{dl}}{\epsilon_0(\epsilon_{FE}d_{dl} + \epsilon_{dl}d_{FE})} \quad (\text{III.5})$$

Meaning that the thicker the dead layer and the lower its dielectric permittivity, the higher the depolarisation field, which is also inversely proportional to the thickness of ferroelectric. The field across dead layer results in:

$$E_{dl} = \frac{Pd_{FE}}{\epsilon_0(\epsilon_{FE}d_{dl} + \epsilon_{dl}d_{FE})} \quad (\text{III.6})$$

When $\epsilon_{FE}/\epsilon_{dl} > 1$ and $d_{FE}/d_{dl} > 1$, charge injection occurs from the dead layer to the ferroelectric. This phenomenon was shown to be one of the causes of the imprint I.2.6.

III.2 Synthesis of the Reference Structure

III.2.1 Fabrication Process

n⁺Si(100) substrates were used for the growth of the stacks. Prior to the deposition of titanium nitride (TiN) bottom electrode, n-doped Si substrates were cleaned in acetone and ethanol and freed from the native oxide layer by a buffer oxide etching process. A pre-sputtering II.1.2 procedure was carried out to clean the surface of the Ti target from the TiO₂ contamination and to improve the vacuum in the deposition chamber down to 10⁻⁶ mbar. As bottom electrode, a 50 nm-thick TiN layer was grown by reactive magnetron sputtering from a Ti target at a pressure of 5 × 10⁻³ mbar, in a mixture of Ar:50 sccm and N₂:30 sccm. Without breaking the vacuum, 12 nm-thick HZO film was deposited on TiN bottom electrode by magnetron sputtering from a Hf_{0.5}Zr_{0.5}O₂ ceramic target at a pressure of 5 × 10⁻² mbar. Afterwards, UV photolithography was performed to obtain the electrical contacts. The top electrode consisted of a 50 nm-thick TiN layer, deposited in the same conditions as bottom one. Following the deposition of the top electrode, a protective conductive film made of few nm-thick Ti adhesive layer and a 50-nm thick Pt layer was grown. Once the last deposition step was completed, the sample underwent a lift-off procedure with acetone. Figure III.1 schematises the fabrication process of the reference structure. Prior to the growth of the stack,

the deposition speed of HZO, TiN, Ti, and Pt was calibrated, in order to ensure the deposition of the right thickness. The latter was checked by profilometer, inside the cleanroom facility, or, for synthesis of ultra-thin films, by X-ray reflectometry (XRR). The growth and the capacitors processing conditions are reported in table III.1. More details on the fabrication process of the reference structure can be found in the thesis work of J. Bouaziz [143].

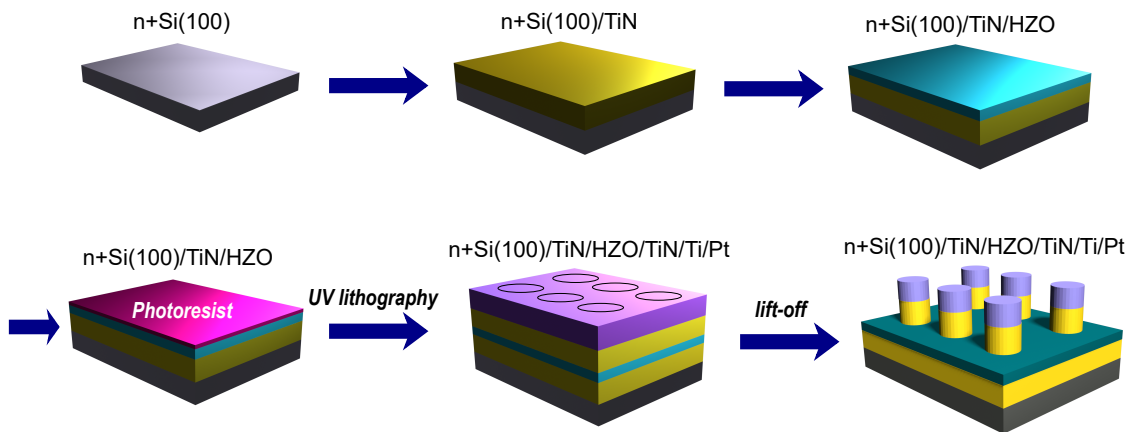


Figure III.1: Schema of the fabrication process of the reference structure.

III.2.2 Post-Metallisation Annealing

The last step of sample fabrication was the annealing, performed to obtain crystalline HZO. GI-XRD analysis revealed that, before the annealing process, HZO was amorphous. Annealing was carried out mostly by RTA and after the deposition of the top electrode and electrical contact (post-metallisation annealing (PMA)). RTA was carried out in a N_2 atmosphere for 30 seconds. As far as the temperature is concerned, the majority of the specimens were annealed at 450 °C, to respect the constraints imposed by the CMOS technology. However, samples annealed at 600 °C were tested for comparison. Another used annealing method was the tubular furnace annealing in a N_2 atmosphere and for 30 minutes. In this case as well, temperatures of 450 °C and 600 °C were tested. However, the furnace annealing required a higher thermal budget compared to the RTA. Experimental results obtained on samples annealed by RTA or tubular furnace are presented later in the chapter. Annealing conditions are reported in table III.1.

Table III.1: Film growth, annealing, and capacitor fabrication conditions.

Sputtering Process				
Target-substrate distance	8 cm			
Base pressure	$< 5 \times 10^{-7}$ mbar			
Ignition pressure	5×10^{-2} mbar			
Pre-sputtering of Ti				
Power (W)	290 W DC			
Time (min)	30 min			
Gas (sccm)	Ar 50 sccm			
Working pressure (mbar)	5×10^{-3} mbar			
Deposited elements	TiN	Hf _{0.3} Zr _{0.5} O ₂	Ti	Pt
Substrate	n ⁺ Si(100)	n ⁺ Si(100)/TiN	n ⁺ Si(100)/TiN/HZO	n ⁺ Si(100)/TiN/HZO/TiN
Target (purity)	Ti (99,995 %)	ZrO ₂ /HfO ₂ (50%/50%)	Ti(99,995 %)	Pt (99.95 %)
Target RF power/voltage (W/V)	300 W	100 W	100 W	137 V
Holder DC bias voltage (V)	60 V	None	None	None
Gas (sccm)	Ar 50 sccm; N ₂ 3 sccm	Ar 50 sccm	Ar 50 sccm	Ar 50 sccm
Working pressure (mbar)	5×10^{-3} mbar	5×10^{-2} mbar	5×10^{-2} mbar	5×10^{-3} mbar
Deposition rate	≈ 5 nm/min	≈ 4 nm/min	≈ 3.5 nm/min	≈ 17 nm/min
UV Lithography Conditions				
Photoresist	Positive AZ5214			
Exposure time (s)	5 s			
Flood exposure time (s)	25 s			
Power per units area (mW cm ⁻²)	20 mW cm ⁻² at 405 nm			
Rapid Thermal Annealing Conditions				
Temperature (°C)	450 °C/600 °C			
Atmosphere (1 atm)	N ₂			
Time (s)	30 s			
Ramp (°C/s)	9 °C/s			
Tubular Furnace Annealing Conditions				
Temperature (°C)	450 °C/600 °C			
Atmosphere (1 atm)	N ₂			
Time (s)	30 min			
Ramp (°C/min)	7 °C/min			

III.2.3 Characteristics of the Reference Structure

Thickness of the HZO layer

The thickness of HZO chosen to synthesise the reference structure was 12 nm. At this thickness, a robust ferroelectricity and reproducible results were obtained. A reference structure, figure III.2, fabricated according to previously mentioned conditions, was synthesised before the fabrication each batch of samples, in order to probe the quality of the HZO layer. Structural characterisations by XRR and GI-XRD, and electrical characterisation by PUND were performed on the reference sample to ensure the presence of the o-phase. Once the good quality of the structure was confirmed, other parameters were changed, such as the thickness of HZO film, the thickness of electrodes, and the material of electrodes.

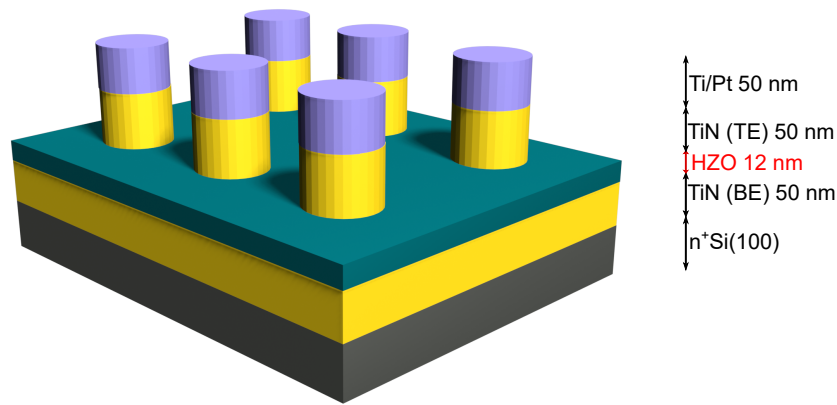


Figure III.2: Schematic of the reference structure.

Effect of the Top Electrode

The top electrode, TiN in the presented case (and for the most part of structures analysed in this work), plays a fundamental role in the o-phase formation in HZO during the post-annealing phase. Indeed, it exerts a mechanical confinement that inhibits the t-phase to m-phase transition, favouring the t-phase to o-phase one [180]. This phenomenon had been reported in the literature by several studies and it is known as "capping layer" effect. Ferroelectric properties of HZO can be modified by the in-plane strain induced by the top electrode, which promotes a phase transformation. The strength of the strain and its nature, tensile or compressive, depend on the thermal expansion coefficient (TEC) of the considered materials. Cao *et al.* [181] studied the effect of different top electrodes on the ferroelectric properties of a 10 nm-thick HZO-based capacitors. As TEC decreases, the tensile strain increases and the fraction of ferroelectric phase rises accordingly. Furthermore, it was shown by Lee *et al.* [182] that the capping layer increases the activation energy for the t- to m-phase transition, reducing its probability with respect to structures without top electrode. A significant number of works reported devices, in which TiN was used as top electrode, suggesting its efficiency as a capping layer. Although, it was demonstrated by Athle *et al.* [183] that texturing of the TiN film might considerably influence the ferroelectricity of HZO. For a majority of (002) texture, they observed a sharp degradation of the remanent polarisation, which increased up to $30 \mu\text{C}\cdot\text{cm}^{-2}$ for a majority of (111) texture. This result shows that the conditions in which samples are fabricated, in this case the deposition process of TiN top electrode, play a crucial role in the modulation of HZO ferroelectric properties. This was confirmed also by J. Bouaziz [143]. In

this work, the texture of TiN, which is polycrystalline, does not seem to affect HZO ferroelectricity. This could be due to multiple factors strictly related to the experimental conditions, such as, in case of magnetron sputtering, the composition of target, the RF power, the pressure, and the N₂ flow. The physical properties of TiN electrodes, grown in the same conditions as here reported, as a function of various parameters are extensively examined in the work of J. Bouaziz [143].

Titanium Nitride Electrodes

TiN was used as bottom and top electrodes for reference structures. There are multiple reasons behind this choice. First, rather practical, motivation is related to the fact that this type of capacitive stack was object of a previous PhD project at INL. It was extensively studied and optimised for non-volatile memory applications by J. Bouaziz [143]. In particular, in his work, Bouaziz investigated the physical properties of TiN depending on several factors, such as the sputtering power, the nitrogen flow, the deposition temperature, and the deposition pressure. Further reasons are related to the abundance of nitrogen and titanium in nature and to its physical characteristics. TiN is characterised by low resistivity, $\sim 3 \times 10^{-8} \Omega \cdot \text{m}^{-1}$ (measured by four probe method), which makes it a good conductor, is a hard material, and has a good adherence. The TiN synthesised by sputtering throughout this thesis was polycrystalline and it presented mainly (200) and (111) orientations.

Titanium Nitride Oxidation Mechanisms

The oxidation of TiN is a further relevant aspect to take into account for structural and electrical analysis of the reference structures and of samples that include TiN as electrode. TiN oxidation phenomenon has a remarkable impact on the microstructure of the TiN/HZO interface and it can influence the ferroelectricity of the HZO layer, also in relation to its thickness. This oxidation mechanism has been described by Esaka *et al.* [184], figure III.3. TiN shows an intermediate oxidation state of the form N_x-Ti-O_y. Ti-N bond is a mix between a covalent, metallic, and ionic bond, and, when Ti-O bond forms, the ionic bond Ti-N is strengthened. The consequence is a charge transfer from Ti to N atoms. TiN(O) might originate from the residual oxygen in the sputtering chamber or from the oxygen present in the

oxide target during HZO growth. Moreover, the presence of TiN(O) at the interface electrode/HZO can be associated to the oxygen redistribution that occurs during the annealing process. TiN(O) interfacial layer is revealed by compositional analysis by EELS, presented in chapter V, and it is confirmed in the in the works of Bouaziz *et al.* [22, 158, 159].

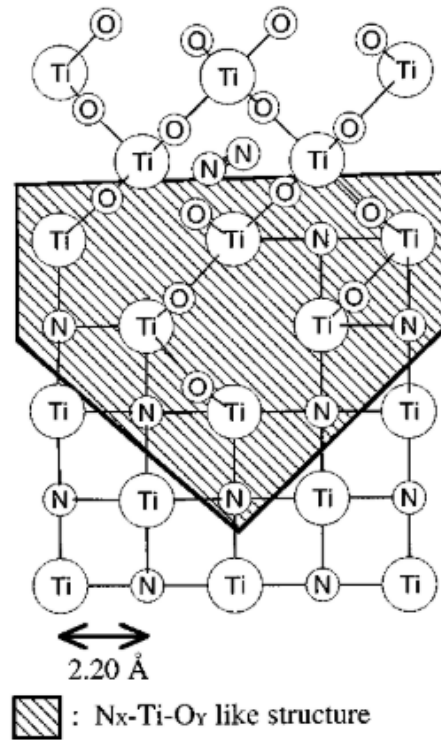


Figure III.3: Schema of the TiN oxidation process proposed by Esaka [184].

III.3 Structural Characterisations

III.3.1 XRR Measurements

The structural characterisations were carried out by means of X-ray reflectometry (XRR) and glancing-incidence X-ray diffraction (GI-XRD). Figure III.4 represents the XRR spectra of 50 nm-thick TiN layer deposited on n^+ Si(100), figure III.4a, of 12 nm-thick HZO layer on n^+ Si(100), figure III.4b, and of n^+ Si(100)/TiN/HZO, figure III.4c. XRR was performed prior to synthesis of the finished samples to check the thickness of deposited layers and calibrate deposition time of each used material. In figure III.4a, the number of oscillations reveals a rather thick deposited layer, which corresponds to the 50 nm-thick TiN electrode. On the con-

trary, broader oscillations in figure III.4b are characteristics of the 12 nm-thick HZO layer. Figure III.4c shows both the presence of TiN, denser oscillations, and HZO, broader oscillations.

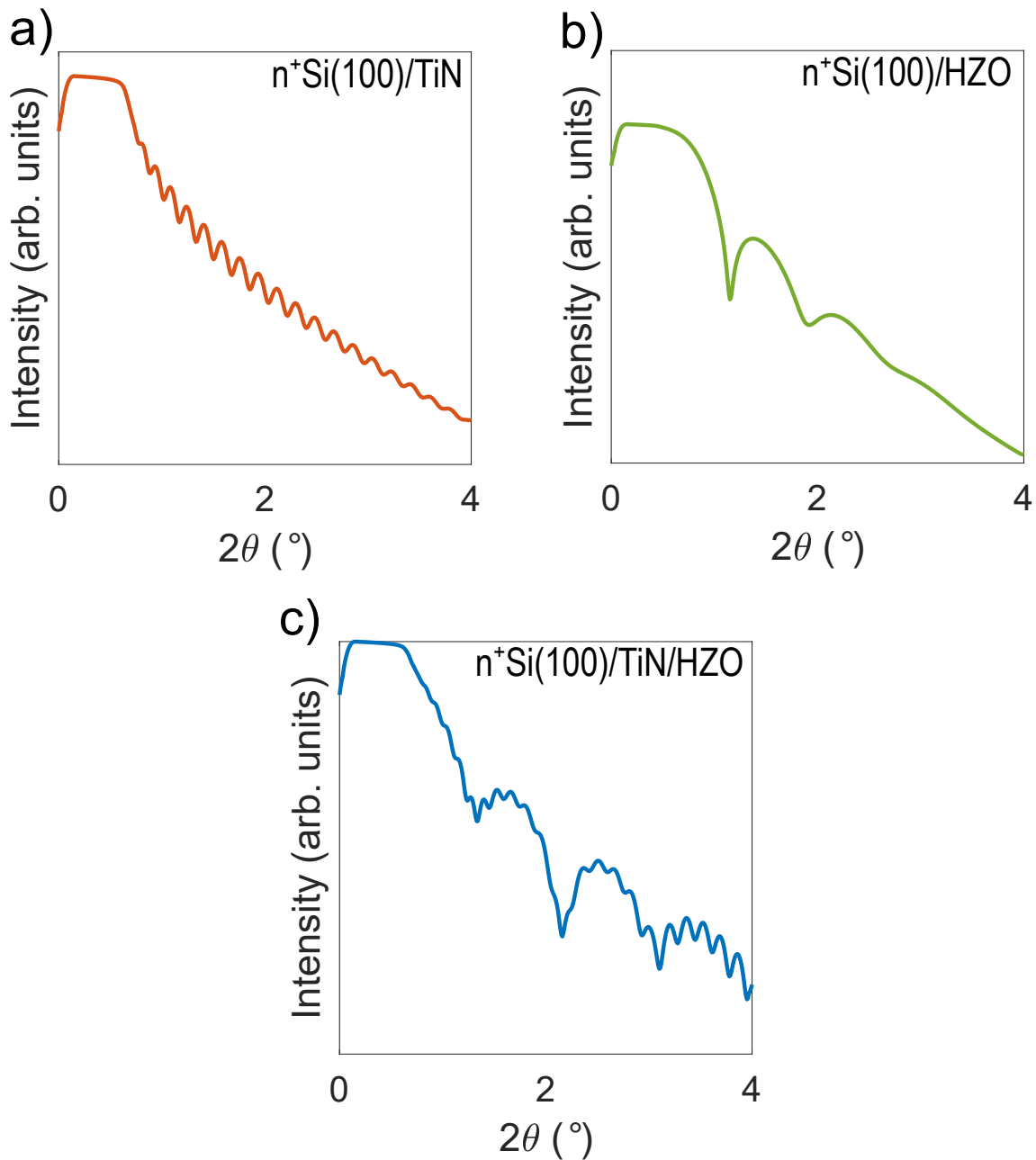


Figure III.4: XRR patterns acquired for: a) $n^+Si(100)/TiN$ with TiN 50 nm. b) $n^+Si(100)/HZO$ with HZO 12 nm. c) $n^+Si(100)/TiN/HZO$ with TiN 50 nm and HZO 12 nm.

III.3.2 GI-XRD Analysis

Crystalline phase of HZO was investigated by means of GI-XRD experiments. The latter allows to verify the presence of the f-phase. Figure III.5 shows GI-XRD

pattern of the reference structure, taken in the range of incidence angle (2θ) 15-100°. This angular range allows to identify the whole set of peaks associated to HZO, TiN, Pt, and Si substrate. For phase study of HZO, 2θ range of interest was between 25° and 45°. Figure III.6a reports GI-XRD pattern of reference structure with a label for each peak. The reference XRD patterns, used to label the peaks, are from ICDD01-97 083-0808 for HZO o-phase, ICDD00-034-0104 for HZO m-phase, ICDD00-038-1420 for TiN, and ICDD00-004-0802 for Pt. In figure III.6b, the red dotted line represents the experimental data and the straight blue line the fit. The fitting function is a pseudovoigt that accounts for Cu K alpha 1 and Cu K alpha 2 radiations, a description can be found in annex B VI.5. The position of the o-/t-peak at 30.5° corresponds to the (111) family of planes. Monoclinic components are detected at 28.4° (m-HZO(11-1)), at 31.6° (m-HZO(111)), and at 35.5° (m-HZO(200)). TiN peaks are identified at 36.6° (TiN(111)) and at 42.6° (TiN(200)), and a Pt peak at 39.8°. A further small Pt peak at $\sim 40.2^\circ$ is distinguishable and corresponds to the K alpha 2 radiation. The appearance of two peaks of Pt, of the Cu K alpha 1 and Cu K alpha 2 radiations, suggests that Pt is characterised by large crystallites. The result of fit of o-HZO(111) diffraction peak, at 30.5°, was considered for evaluation of the average out-of-plane crystallite size of o-HZO crystallites by means of Scherrer equation [185]:

$$D = \frac{K\lambda}{\beta \cos \frac{2\theta}{2}} \quad (\text{III.7})$$

Where $K=0.9$ is shape factor, $\lambda=0.154060$, β full width at half maximum (FWHM) of diffraction peak o-HZO(111) at 30.5°, extracted from the fit, and 2θ scattering angle of o-HZO(111) reflection. The average o-phase crystallite size in a 12 nm-thick HZO layer was found to be ~ 8.6 nm. Scherrer equation was also used to evaluate average out-of-plane crystallite size of the m-phase crystallites. FWHM of m-peak(11-1) at 28.6 ° was considered and D was found to be ~ 9 nm. From this analysis, it seems that average size of o-phase and m-phase crystallites is similar.

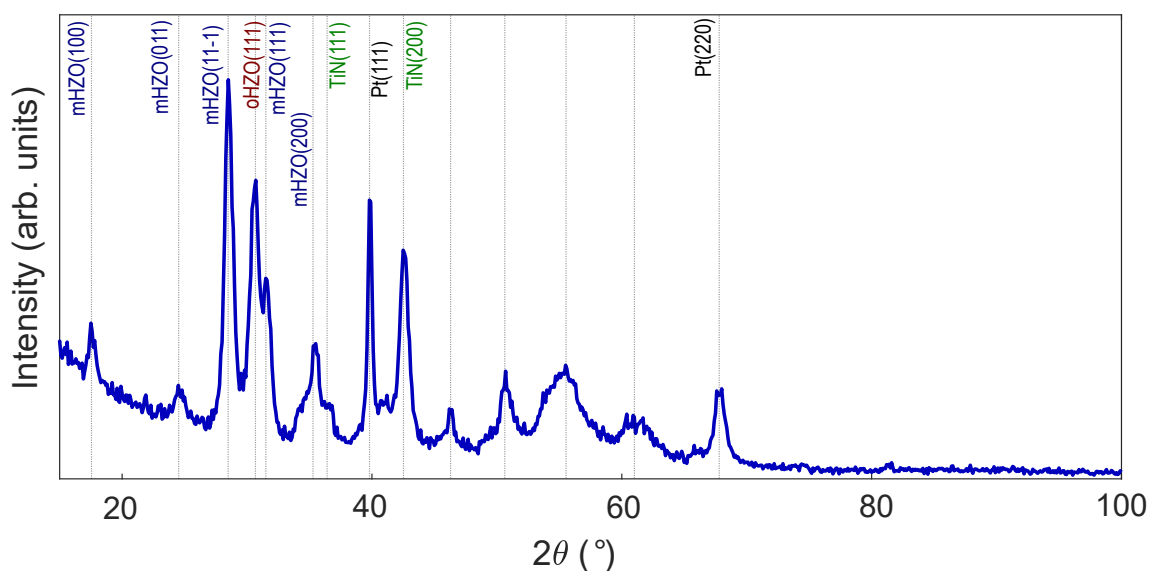


Figure III.5: GI-XRD pattern of the reference structure taken over a 2θ range 15°-100°.

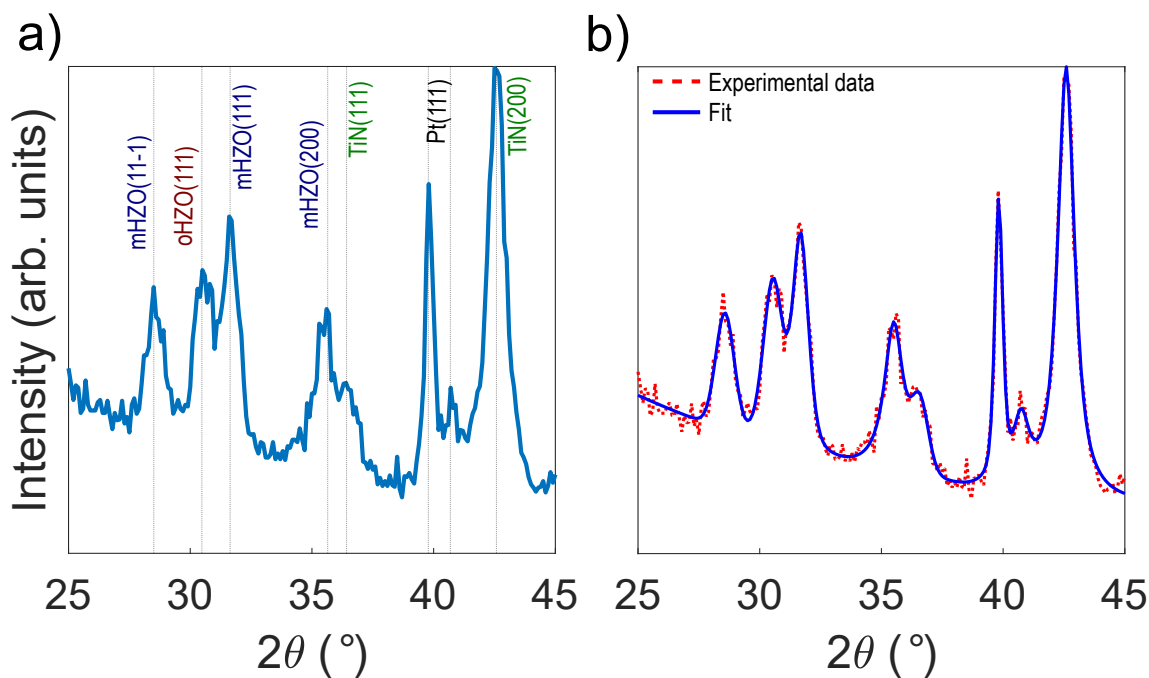


Figure III.6: a) GI-XRD pattern of the reference structure taken over a 2θ range 25°-45°. b) Fit performed using a pseudo-voigt function accounting for Cu K alpha 1 and Cu K alpha 2 radiations.

Figure III.7 reports the GI-XRD pattern of the reference structure and the fit, together with the difference between the two. The yellow line represents the result of the fit for the o-HZO(111) peak.

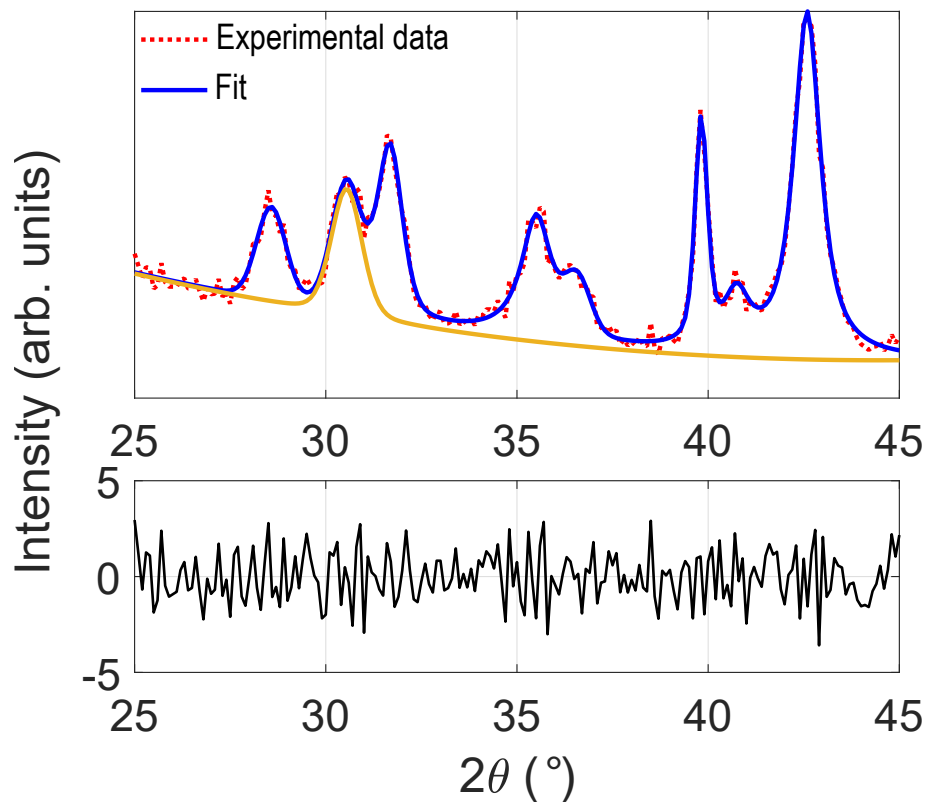


Figure III.7: GI-XRD pattern of the reference structure taken over 2θ range 25° - 45° . The dashed red line represents the experimental data, the straight blue line the fit. The yellow line represents the result of the fit, if only the pseudovoigt of the o-HZO(111) peak is considered. Below, the difference between the experimental data and the fit.

III.3.3 RBS Analysis

The stoichiometry of the reference structure was evaluated by RBS spectroscopy, figure III.8. The analysis was performed with $^4\text{He}^+$ ions of 2 MeV energy. Backscattered ions were detected with a 13 keV resolution implanted junction set at an angle of 165° with respect to the beam axis. RBS data confirmed the stoichiometry 1:1:4 for $\text{Hf}_{0.5}\text{Zr}_{0.5}\text{O}_2$ deposited by sputtering.

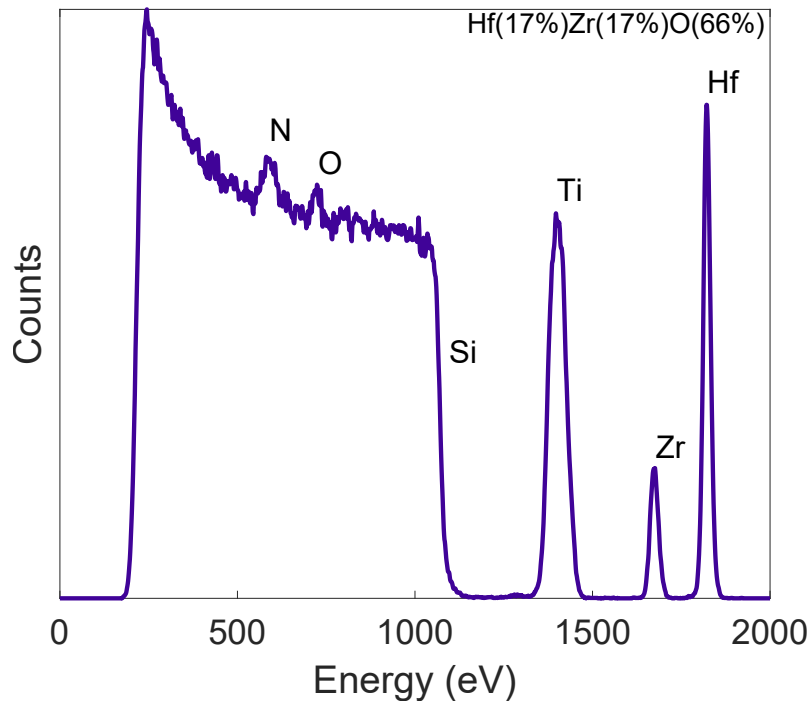


Figure III.8: RBS spectrum of the reference structure.

III.3.4 AFM Analysis

To study the surface morphology of HZO deposited on the TiN bottom electrode, AFM analysis was performed in tapping mode. Figure III.9 shows the surface of a 12 nm-thick HZO layer deposited on a 50 nm-thick TiN bottom electrode, before RTA (figure III.9a) and after (figure III.9b). The results indicate that the surface is rather flat, either before or after the annealing. Indeed, RMS roughness was measured to be ~ 0.42 nm and ~ 0.33 nm, respectively. The area over which the scan was performed was $2 \times 2 \mu\text{m}^2$.

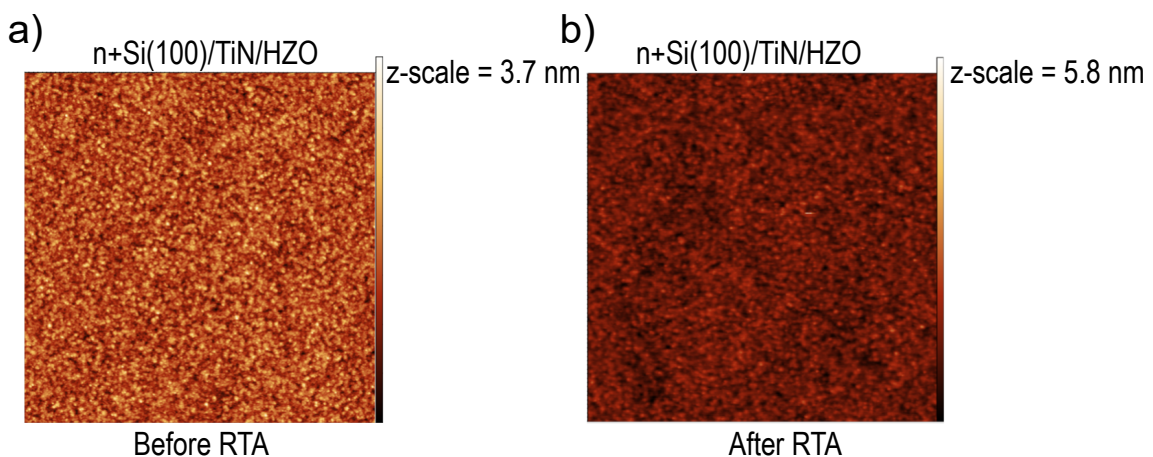


Figure III.9: AFM images of the surface of the reference structure. a) Before RTA procedure. b) After RTA procedure.

III.3.5 TEM and HR-TEM Analysis

TEM measurements were acquired to probe the morphological and structural properties of the HZO layer, and of the interfaces between the oxide and the electrodes. The TEM cross-section of the specimens was prepared by mechanical thinning followed by Ar^+ ion milling on a Gatan PIPS machine, with an acceleration voltage of 4 kV, and at a 6° incident angle. TEM analysis was performed at the National Institute of Material Physics in Romania, in the frame of the H2020 European project 3 ϵ FERRO. Figure III.10a shows low magnification TEM image of the reference sample, where it is noticeable the contrast of the 12 nm-thick HZO layer on the TiN bottom electrode. The electron diffraction pattern, in figure III.10b, was obtained on a selected area that includes the Si substrate and the deposited films.

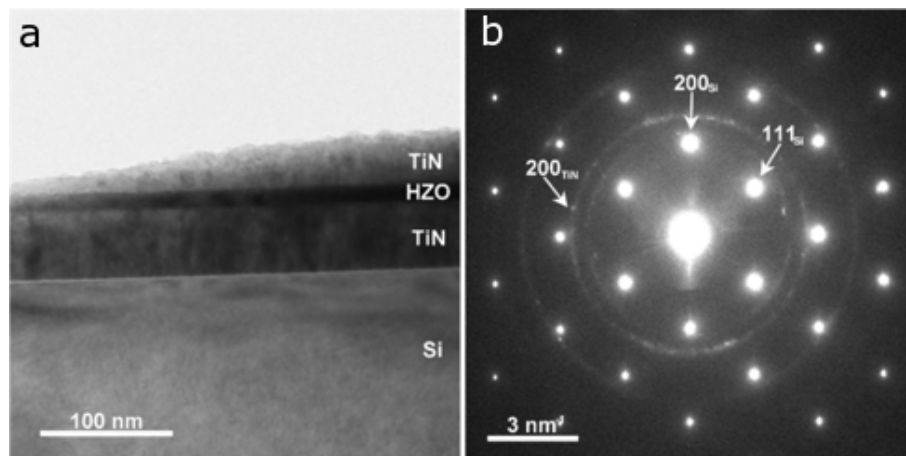


Figure III.10: a) TEM image at low magnification of the reference structure. b) SAED pattern performed on the TEM image at low magnification.

Figure III.11a reports HR-TEM image of reference structure, where it is possible to identify two different HZO crystallites corresponding to the o-phase and to the m-phase. Figure III.11b shows a magnified view of the two crystal structures. To determine the crystal structure of HZO, fast Fourier transform (FFT) on HR-TEM image was performed. FFT allowed to assign the two spots of the pattern in figure III.11c to o-HZO(111) planes and to m-HZO(111) planes. Obtained results suggest that there is a coexistence of o- and m- phase in HZO. Figure III.11d represents a mixed-color image obtained by filtering out all FFT intensities except HZO(111) peaks, to better highlight the spatial relationship between HZO crystallites with different structure.

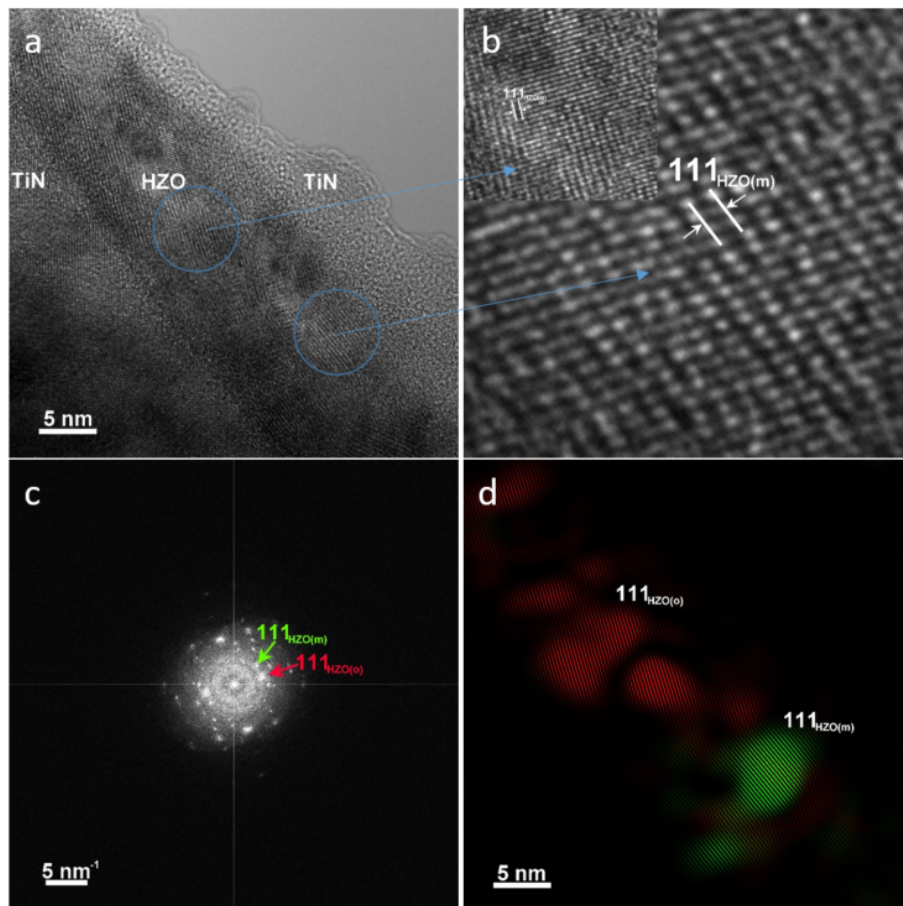


Figure III.11: a) HR-TEM image of the reference structure. b) Magnified view of HZO crystallites with different crystal structures, from the area marked by the two blue circles in a). c) FFT performed on a). d) Reconstructed image of the HZO crystallites using the two spots marked on c).

To have a better insight on the mixture of crystalline phases that characterise HZO layer, another area of the cross-section was analysed. Figure III.12a shows the HR-TEM image of reference sample, the area highlighted in blue was used to perform the FFT in figure III.12b. The inset in figure III.12b offers a magnified view of selected area, together with a schematic of the orthorhombic unit cell, simulated by the VESTA software in the $[uvw]=[01-1]$ zone axis. From the FFT image, it is possible to assign the spots to the (111), (-1-1-1), and (200) planes of the o-phase.

In conclusion, TEM and HR-TEM study revealed that the o-phase is dominant in a 12 nm-thick HZO layer and only isolated monoclinic crystallites are identified. However, some areas of the sample could not be analysed because they were not transparent to the electron beam. This analysis confirmed the coexistence of o-phase and m-phase crystallites that was already found by GI-XRD presented in section III.3.2.

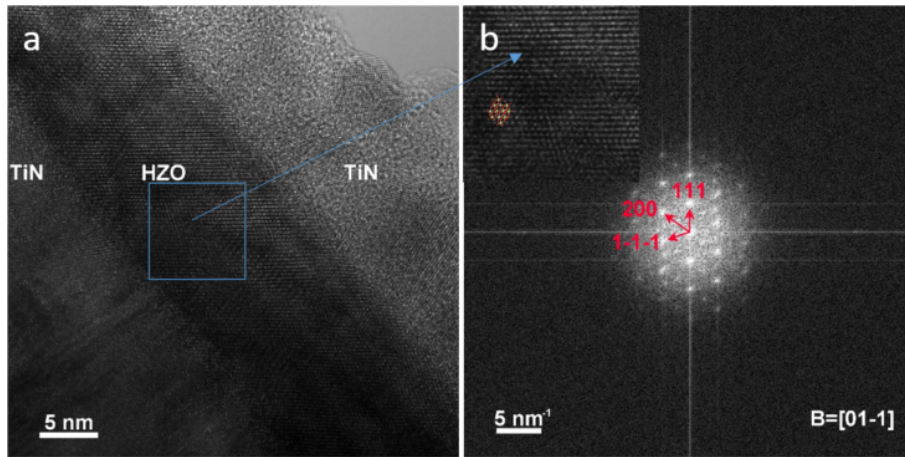


Figure III.12: a) HR-TEM image of the reference structure. Highlighted in blue, the area over which the FFT was performed. b) FFT of the area highlighted in blue in a). Inset: magnified view of the area highlighted in blue together with the o-HZO unit cell in the $[uvw]=[01-1]$ zone axis.

III.4 Electrical Characterisations

In order to validate the presence of the ferroelectric phase in the reference structure, electrical characterisations were performed. The specimens were analysed by PUND, I-V, and C-V measurements, as explained in chapter II.

III.4.1 PUND

The polarisation *vs* voltage P - V measurements were performed at room temperature on 20 μm -diameter capacitors. The set up employed for the electrical characterisation consisted in a manual probe station, where the samples were kept in a close environment and the electrical contact was made with two tungsten-tip probes. The voltage was applied by contacting the Pt contact of each device with one probe, while the other was kept on common bottom electrode. The protocol used for the voltage cycling consisted on the application of trapezoidal bipolar signals at a frequency of 2.5 kHz and a voltage amplitude between 2 V to 5 V, depending on samples, followed by a PUND sequence (section II.6.3) at the same frequency. The results presented in this section were obtained after 10^3 voltage cycles. Figure III.13a shows the P - V characteristic of the reference structure. The blue curve represents the $P(V)$ extracted from the PN sequence, while the red and yellow curves the $P(V)$ extracted from the PUND one. The latter, as explained in section II.6.3, is corrected by subtracting the contributions of the leakage and dis-

placement currents. Double remanent polarisation (P_r), considered as $2|P_{\pm}|$, was $\sim 26 \mu\text{C}/\text{cm}^2$, in line with the values reported in the literature [151, 155, 186–188]. It is noticeable, in figure III.13a, a slight right shift with respect to the 0 V of the hysteresis loop due to the imprint (section I.2.6). Since the reference structure was symmetric (bottom and top electrode are made of the same material), the imprint was probably due to a different surface reconstruction at the top and bottom interfaces, considering that the sample was exposed to air before the deposition of the top electrode [189–191]. A further reason for the presence of the imprint could be associated to electron de-trapping from oxygen vacancies, as Yuan *et al.* recently proposed [192]. The wake-up (figure III.13) effect is responsible for the increase of P_r as a function of applied voltage cycles.

Endurance tests were performed on pristine capacitors, usually until the electrical breakdown occurred. Figure III.14 shows evolution of P_- and P_+ as a function of the number of cycles. The initial increase of the P_r is associated to wake-up effect. The P_r reaches its maximum value after approximately 10^3 cycles, afterwards it slightly falls until electrical breakdown occurs at $\sim 5 \times 10^5$. As for the value of the $2P_r$, also the value of the endurance is similar to what can be found in the literature [159, 170]. Decrease of P_r is associated to a fatigue state, I.2.6, that precedes the electrical breakdown.

In figure III.15, the red curve corresponds to the PN current, which includes the switching, leakage, and displacement currents. The yellow curve represents the UD current, which groups the contributions of leakage and displacement current. Finally, the blue line corresponds to the signal obtained by subtracting UD from PN currents.

Further reference samples were characterised during this thesis and it was possible to conclude that a stack with 12 nm-thick HZO layer, which was synthesised in previously presented conditions, showed a robust ferroelectricity. The P_r oscillated in a range between 10 and $20 \mu\text{C}/\text{cm}^2$. In most of the analysed cases, the electrical breakdown occurred after 10^6 cycles, but some of the structure showed an endurance up to 10^8 cycles.

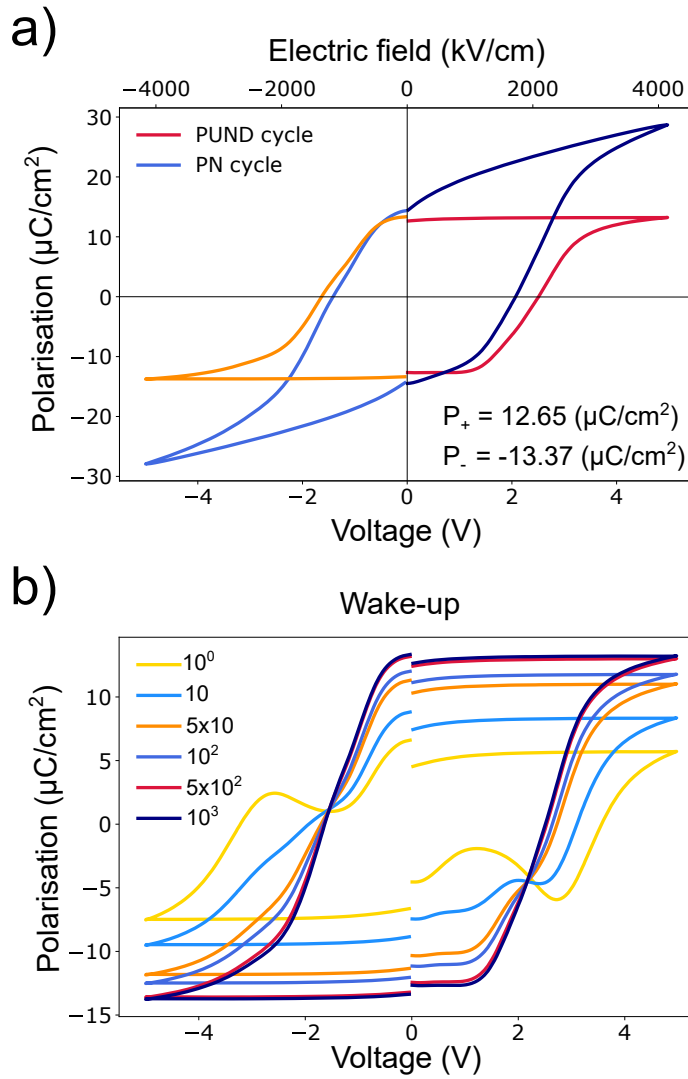


Figure III.13: a) P - V curve of the reference structure after 10^3 cycles. The hysteresis loop in blue accounts only for the current contributions recorded for pulses P and N , thus the leakage current contributions are not subtracted. The hysteresis loop in red corresponds to the application of the PUND correction, thus only ferroelectric effects are considered (section II.6.3) b) Evolution of P_r as a function of voltage cycles.

C-V Measurements

The values of the relative dielectric constant (ϵ_r) and capacitance (C) of HZO can be extracted from the equation:

$$\epsilon_r = \frac{C \times d}{\epsilon_0 \times A} \quad (\text{III.8})$$

where C is the maximum value of the capacitance, d the thickness of HZO layer, ϵ_0 the vacuum dielectric constant, and A the area of capacitor. Considering a circular capacitor with $10 \mu\text{m}$ radius and a HZO thickness of 12 nm , the maximum value of ϵ_r was ~ 38 , in accordance with the literature, for which the value of ϵ_r

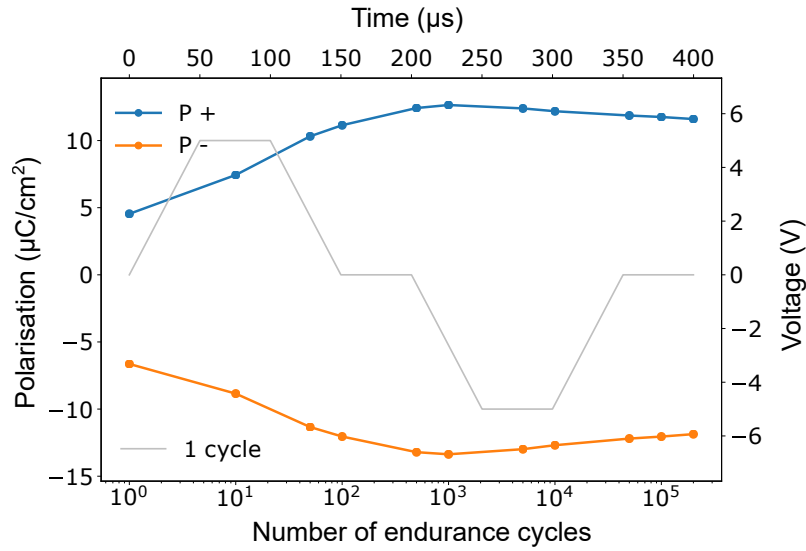


Figure III.14: Endurance test, showing the evolution of the P_r as a function of the number of applied voltage cycles.

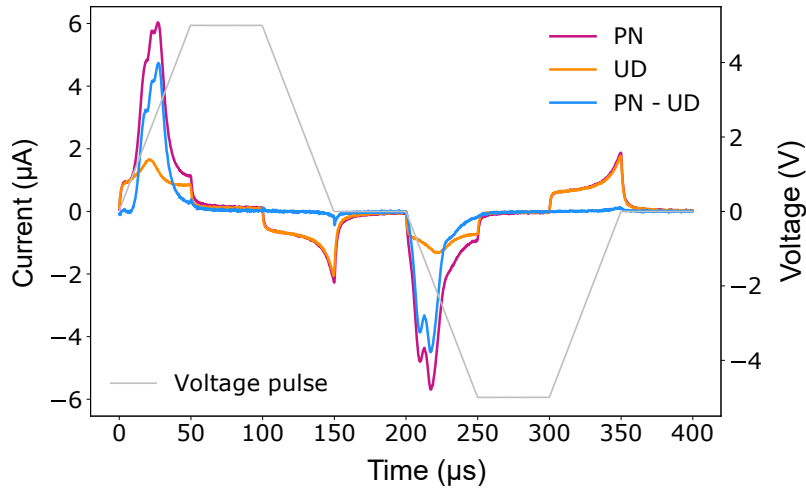


Figure III.15: PN, UD, PN-UD currents as a function of time.

for HZO is ~ 35 [158, 193, 194]. If the maximum value of ϵ_r is considered, figure III.16, C is found to be ~ 10 pF. ϵ_r is described by a butterfly-shaped curve, figure III.16, characteristic of ferroelectric materials.

III.4.2 Current Transport Mechanisms in the Reference Structure

To investigate which current transport mechanism was dominant in the reference structure, J/V measurements were performed. Prior to the presentation of the experimental results, table III.3 reminds which are the main conduction mechanisms that can characterise ferroelectric capacitors [142].

J/V plots were obtained at different temperatures, ranging from 4 K to 300

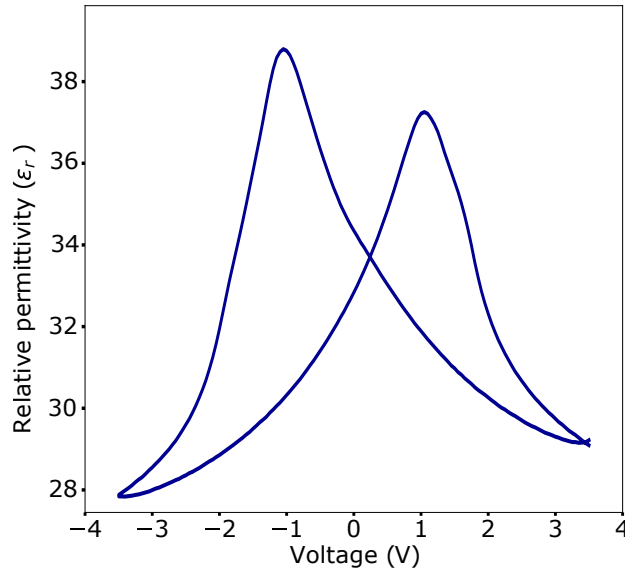
Figure III.16: ϵ_r of the reference structure as a function of voltage.

Table III.2: Current transport mechanisms in ferroelectric capacitors.

Mechanism	Equation	Dominated by
Schottky Emission	$j_{SE}(E) = A^*T^2 \exp\left[\frac{-q(\phi_B - \sqrt{qE/4\pi\epsilon_0\epsilon_r})}{k_bT}\right]$	Interface
Fowler-Nordheim Tunnelling	$j_{FNT}(E) = C \frac{e^3}{16\pi^2\hbar m^* \phi_B} E^2 \exp\left[-\frac{4\sqrt{2m_e m^*} \phi_B^{3/2}}{3\hbar e} \frac{E}{E}\right]$	Interface
Ohmic Conduction	$j_{OC} = E \exp\left(\frac{-\Delta E_{ac}}{k_bT}\right)$	Bulk
Thermionic Emission	$j_{TE}(E) = A^*T^2 \exp\left[-\frac{1}{k_B T} \left(\phi_B - \sqrt{\frac{e^3 E}{4\pi\epsilon_0\epsilon_r}}\right)\right]$	Bulk
Poole-Frenkel Emission	$j_{P-F}(E) \propto E \exp\left[\frac{-q(\phi_B - \sqrt{qE/\pi\epsilon_0\epsilon_r})}{k_bT}\right]$	Bulk
Space Charge Limited Current (SCLC)	$j_{SCLC} = A_0 \frac{V^n}{d^m}$	Bulk

A^* Richardson constant, ϕ_B ferroelectric/electrode barrier, ϵ_r relative permittivity of the ferroelectric, k_b Boltzmann constant, m^* effective mass, m_e mass of the electron, E_{ac} activation field of electrons, A_0 , m , and n are positive constants.

K. In figure III.17a, the significant reduction of current as a function of the temperature indicates that the thermionic emission plays an important role at high temperature. By fitting the experimental results with the different conduction mechanisms, it was found that the dominant one in reference structure was the Poole-Frenkel emission, figure III.17b, with an extracted trap depth of 0.21 eV. These results are in accordance to what is reported in the literature concerning the current conduction mechanisms in HfO_2/HZO -based capacitors [195, 196].

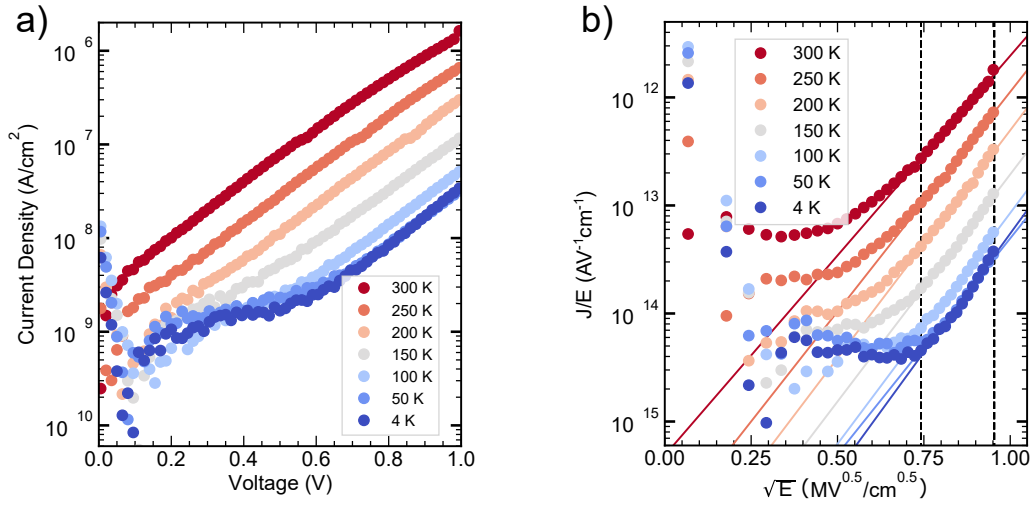
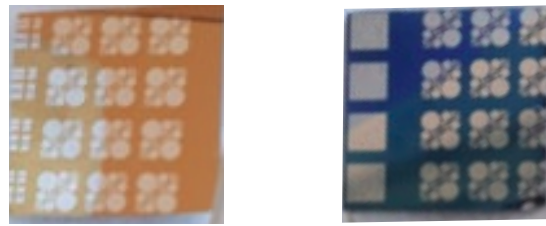


Figure III.17: a) J/V curves of the reference sample at different temperatures. b) Fit of the experimental results according to the Poole-Frenkel conduction mechanism.

III.5 Furnace Annealing

This section is dedicated to a rapid presentation of results of the structural and electrical characterisation of two reference samples annealed by tubular furnace annealing. The two presented stacks were prepared under the same conditions, but annealed at 450°C and 600°, respectively. They are called sample 1 and sample 2, for simplicity. Figure III.19a reports the GI-XRD pattern of sample 1, together with the fit, and figure III.19b the GI-XRD patterns sample 2 and corresponding fit. The average out-of-plane crystalline size of o-phase and m-phase crystallites of HZO was calculated by Sherrer equation III.7. Sample 1 was characterised by an average o-phase and m-phase crystalline size of ~ 8 nm and ~ 10 nm, respectively. For sample 2, they were ~ 11 nm and ~ 8 , respectively. Latter result suggests that a high annealing temperature promoted the formation of larger o-phase crystallites and smaller m-phase crystallites compared to low temperature. However, a high annealing temperature might also be responsible for the creation of structural defects that alter the bandgap of HZO, as the change of the color of the sample surface indicated in Figure III.18. It is important to mention that the GI-XRD analysis is qualitative, due to the slight different area of the samples and a different surface patter of capacitors. For this reason, the comparison of the intensity of the o-peak would not be meaningful.

The electrical characterisation shows that sample 1 is marked with a higher



Annealing at 450 °C Annealing at 600 °C

Figure III.18: On the left a photo of a sample annealed at 450 °C, on the right of a sample annealed at 600 °C.

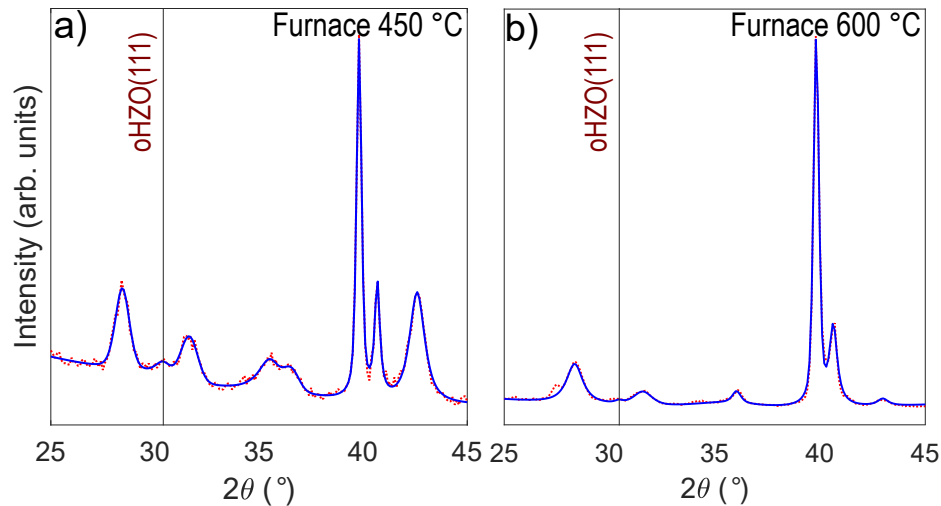


Figure III.19: a) GI-XRD pattern of the reference structure annealed by tubular furnace at a) 450°C. b) 600°C.

$2P_r$, of $\sim 39 \mu\text{C}/\text{cm}^2$, compared to sample 2, for which the $2P_r$ is $\sim 29 \mu\text{C}/\text{cm}^2$, figures III.20a and b. Both samples are characterised by imprint, slightly more evident in sample 1. The endurance test is shown in figures III.21a and b. The endurance of sample 1 is 5×10^5 cycles, slightly higher than the one of sample 2, for which the electrical breakdown occurs after 10^5 cycles. However, sample 2 is characterised by almost null wake-up, meaning that value of P_r does not change as a function of cycling. The latter is an extremely important feature for optimised ferroelectric-based devices.

If compared to the properties of the reference structure annealed by RTA, these results seem to be better either in terms of remanent polarisation or endurance. However, use of the tubular furnace as annealing method was not pursued along the thesis, because of a lack of reproducibility of results. The RTA process was found to be a more reliable technique to obtain structures characterised by robust ferroelectric properties and it required a lower thermal budget compared to the furnace.

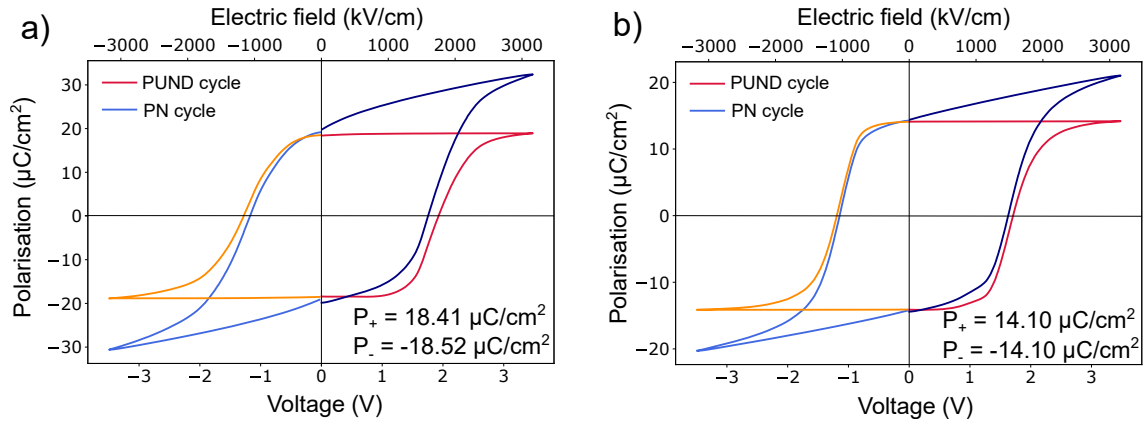


Figure III.20: P - V curve of: a) sample 1, extracted after 10^3 cycles. b) Sample 2, extracted after 10^3 cycles.

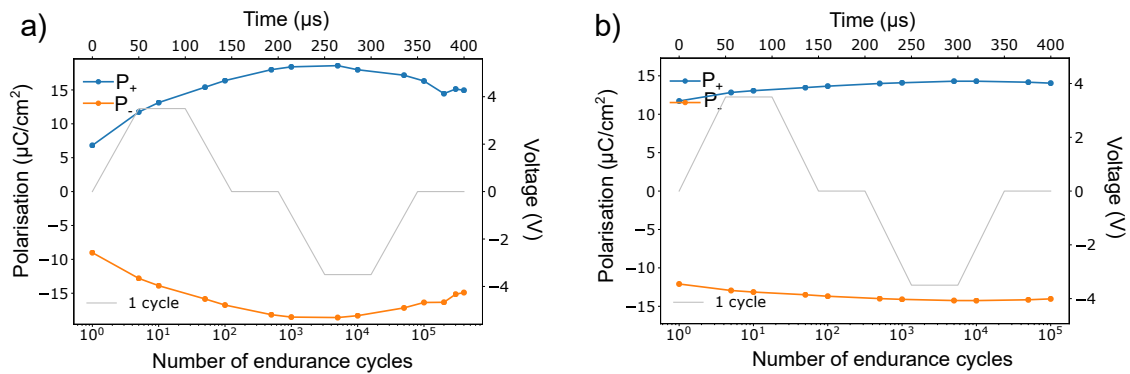


Figure III.21: Endurance test of: a) sample 1. b) Sample 2.

III.6 Scaling Down the HZO Thickness

The ferroelectric phase in HfO_2 is not considered as stable phase. If bulk free energy is considered, no polar phases are present in phase diagram of neither HfO_2 nor ZrO_2 , figure I.7. Although, its stabilisation through surface energy effects was theoretically suggested by Materlik *et al.* in 2015 [35]. In 2019, Park *et al.* [197] proposed a kinetic model to complete the previously proposed and less accurate thermodynamic model. Over past years, several works have demonstrated ferroelectricity in HfO_2 -based alloys and especially in HZO, in a thickness range between ~ 8 nm to 25 nm. However, it becomes challenging to obtain robust ferroelectric properties when the HZO thickness is further scaled. Nevertheless, the synthesis of ultra-thin HZO layers is of great interest to satisfy the request of miniaturisation for various technological applications. For this reason, the research has extensively investigated how to fabricate ultra-thin HZO-based devices with robust ferroelectricity. Previous to presentation of our experimental results, it is worthy

to revise briefly the parameters that could influence the o-phase formation in HZO thin films. In the literature, several studies reported a dependence of the o-phase formation on fabrication conditions and on other physical parameters, as the material used for the electrodes, the concentration of oxygen vacancies (III.1.3), and the grain size. Park *et al.* [198] investigated the evolution of the o-phase fraction of HZO layer of different thicknesses grown on TiN or Ir bottom electrodes. They demonstrated that the o-phase formation depends on the grain size and a critical value of ~ 18 nm was found. Large grains favoured the formation of the m-phase, which was responsible for a degradation of the $2P_r$, above an HZO thickness of ~ 20 nm. The same group [199] observed a degradation of the $2P_r$ in HZO films below 8 nm, due to a lower surface energy of the t-phase compared to the o-phase. Lee *et al.* [144], in their study of the optimal fabrication conditions for an 11 nm-thick HZO-based structure, showed that a high deposition speed of HZO favoured the o-phase, thanks to the suppression of the grain growth. Furthermore, when HZO is few nm-thick, interface effects become non-negligible. Depolarising field generated by dead-layers becomes stronger and leads to a degradation of the ferroelectricity and a reduction of the coercive field. However, ferroelectricity has been demonstrated in ultra-thin films. For instance, Chernikova *et al.* [200] detected ferroelectric behaviour in a n^+ Si/HZO/TiN structure, where the HZO layer was 2.5 nm-thick. At this thickness, $2P_r$ is rather low, and, in order to obtain a satisfactory resistive switching, they concluded that the optimisation of interface properties was crucial. Other articles reported the existence of ferroelectricity in ultra-thin region in epitaxial HZO [68, 87, 162]. Nevertheless, the stabilisation of the o-phase at very low thickness is still under investigation, due to the multiple factors that take part to this process, such as the fabrication conditions, the surface energy effects, and the role of the electrodes.

III.7 Conclusion of the Chapter

The first part of this chapter gave an overview on the fabrication methods of HZO thin films and defects formed during the synthesis process, which can affect the device performances. The second section was dedicated to the state of art and the requisites for FTJs commercialisation. At last, the structure used as a reference for this work was presented, together with the structural and electrical charac-

terisations by means of XRR, GI-XRD, AFM, RBS, TEM, HR-TEM, PUND, I-V, and C-V measurements. Reference structures based on 12 nm-thick HZO layer showed robust ferroelectric behaviour. However, for synthesis of FTJs, the thickness of the HZO layer should be reduced to allow the electrons to tunnel between the electrodes. As mentioned in section III.6, this is a challenging task, which requires the control of several parameters. Chapters IV and V are dedicated to exploration of ways to stabilise the ferroelectric phase in ultra-thin HZO films and to enhance their ferroelectric performances. At first, we explored impact of different bottom electrodes (chapter IV), afterwards we focused on the use of interface engineering to optimise the FTJ stacks (chapter V).

Reduction of HZO Thickness and Impact of the Bottom Electrode

One of the challenges associated to the use of HZO as a ferroelectric material for the realisation of FTJs is related to obtaining robust ferroelectricity at a thickness of few nanometers. The structure presented in chapter III was characterised by good ferroelectric properties, but it was not suitable to serve as a FTJ, because of the HZO layer was too thick. Indeed, a 12 nm-thick ferroelectric film does not allow the tunnelling of electrons between the electrodes. The first part of this chapter is dedicated to the study of $n^+Si(100)/TiN/HZO/TiN/Ti/Pt$ heterostructures characterised by decreasing HZO thickness, from 12 nm to 6 nm. The second part is devoted to the presentation of different bottom electrode materials and their impact on the o-phase formation and stabilisation in the HZO layer. This in the frame of looking for solutions to improve the ferroelectric properties of ultra-thin HZO films for FTJ applications.

IV.1 Analysis of the Effect of Thickness Reduction

The reference structure of chapter III was considered as a starting point for the reduction of the HZO thickness. In this section, stacks based on 8 nm-thick, 7 nm-thick, and 6 nm-thick HZO are investigated with the purpose of understanding,

through structural and electrical characterisations, how ferroelectricity evolves with decreasing HZO thickness. The here presented samples were fabricated in the same conditions reported in table III.1 and annealed by RTA at 450 °C.

IV.1.1 Structural Characterisations: GI-XRD and HR-TEM

Figure IV.1 shows the GI-XRD patterns of four samples with 12 nm-thick, 8 nm-thick, 7 nm-thick, and 6 nm-thick HZO layer. It is clearly noticeable the evolution of the orthorhombic and monoclinic peaks when the thickness of HZO is thinned down. In figure IV.1a, the m-phase peaks at $\sim 28.4^\circ$ (m(11-1)), $\sim 31.6^\circ$ (m(111)), and $\sim 35.5^\circ$ (m(200)) are distinguishable and suggest a more significant component of m-phase crystallites. Figures IV.1b, c, and d show the GI-XRD patterns of the samples with 8 nm-thick, 7 nm-thick, and 6 nm-thick HZO layer. For the former case, the monoclinic contributions at $\sim 28.4^\circ$, $\sim 31.6^\circ$, and $\sim 35.5^\circ$ appear to be less important compared to the orthorhombic one at $\sim 30.5^\circ$. For the latter cases, they are almost non-existent (figure IV.1c and d), but only a small m-peak was detected at 35.5° .

The progressive disappearance of the m-phase with decreasing HZO thickness is also confirmed by the HR-TEM analysis. Figures IV.2a and b report the HR-TEM images of the n^+ Si/TiN/HZO/TiN/Ti/Pt heterostructure with a ~ 8 nm-thick and a magnified view of an o-phase crystallite. The FFT pattern in figure IV.2c was performed on the entire area represented in figure IV.2a and used to extract the reconstructed image of o-HZO crystallites of (111) orientation, in figure IV.2d. These findings revealed that, for a thin HZO layer, the amount of o-phase crystallites increases with respect to the reference structure described in section III.11.

The results of the fit of GI-XRD patterns of the four samples and the Sherrer equation III.7 were used to determine average out-of-plane o-phase crystallite size of the HZO layer. Figures IV.3a, b, c, and d show the GI-XRD experimental data, the fits, and difference between the two for the four considered structures. The FWHM of the yellow curve, which corresponds to result of the fit of only the o-HZO(111)-peak, was used to determine the crystallite size.

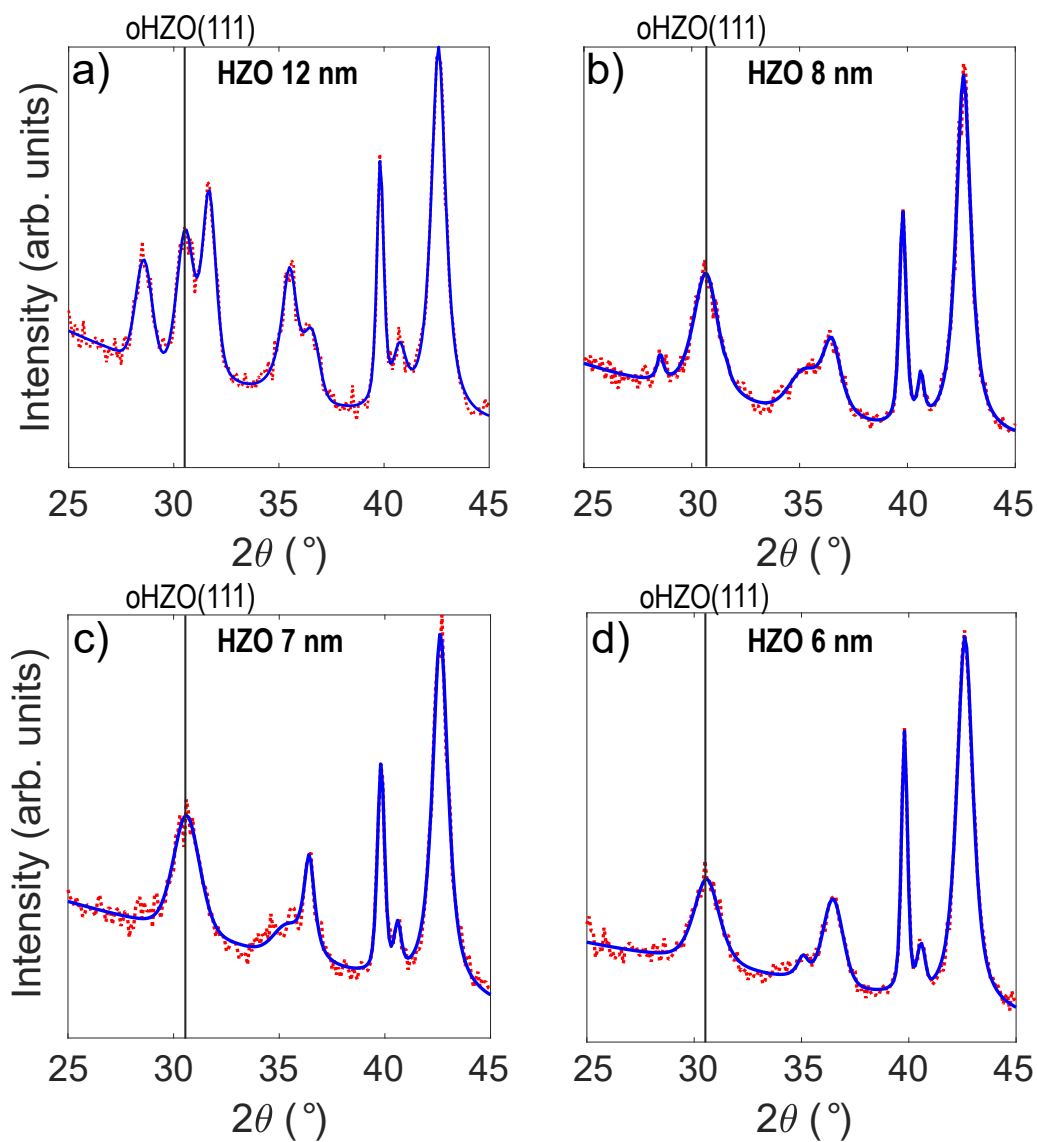


Figure IV.1: GI-XRD experimental data, dashed red line, and fit, straight blue line, of the structure $n^+Si(100)/TiN/HZO/TiN/Ti/Pt$ with: a) 12 nm-thick HZO layer. b) 8 nm-thick HZO layer. c) 7 nm-thick HZO layer. d) 6 nm-thick HZO layer.

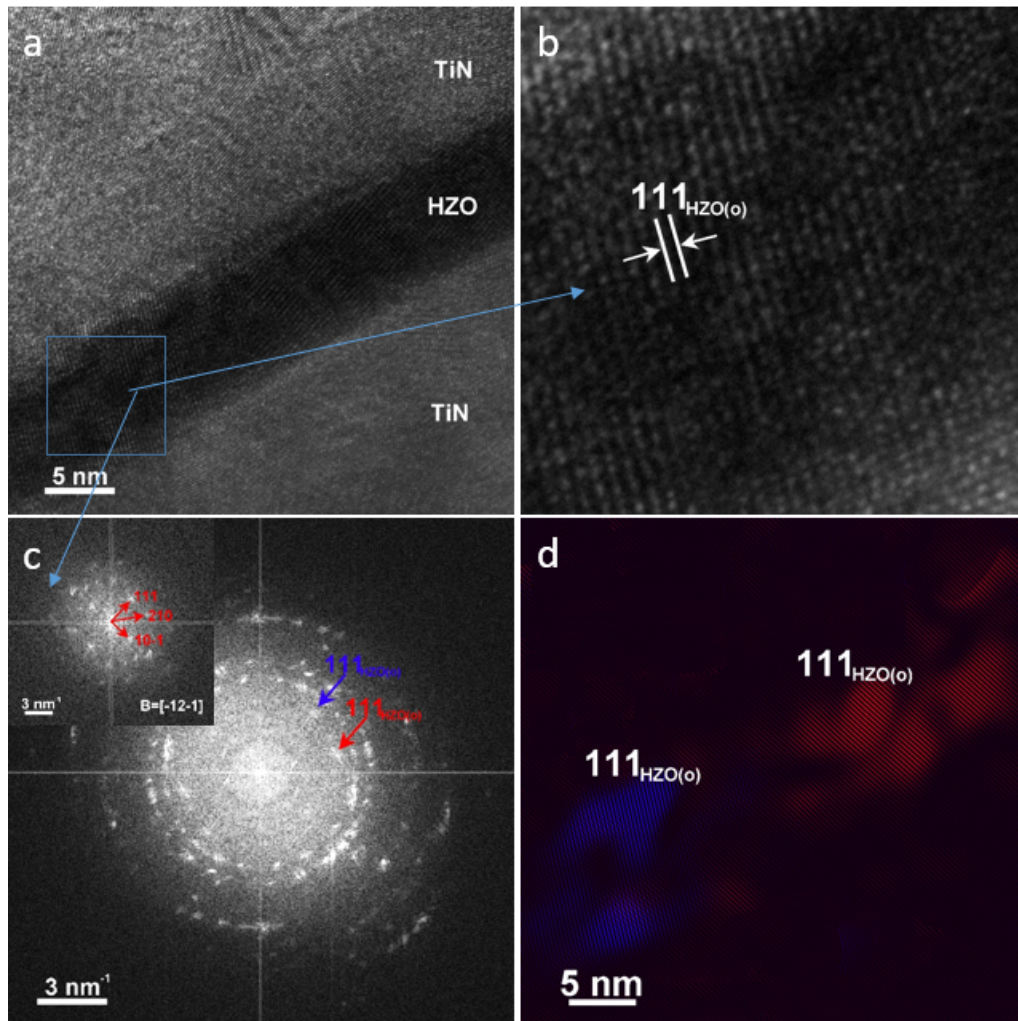


Figure IV.2: a) HR-TEM image of n^+ Si/TiN/HZO/TiN/Ti/Pt, HZO \sim 8 nm. b) Magnified view of a o-HZO crystallite from the area marked by the blue square in a). c) FFT pattern performed on a). d) Reconstructed image of the two HZO crystallites using the two spots marked in c).

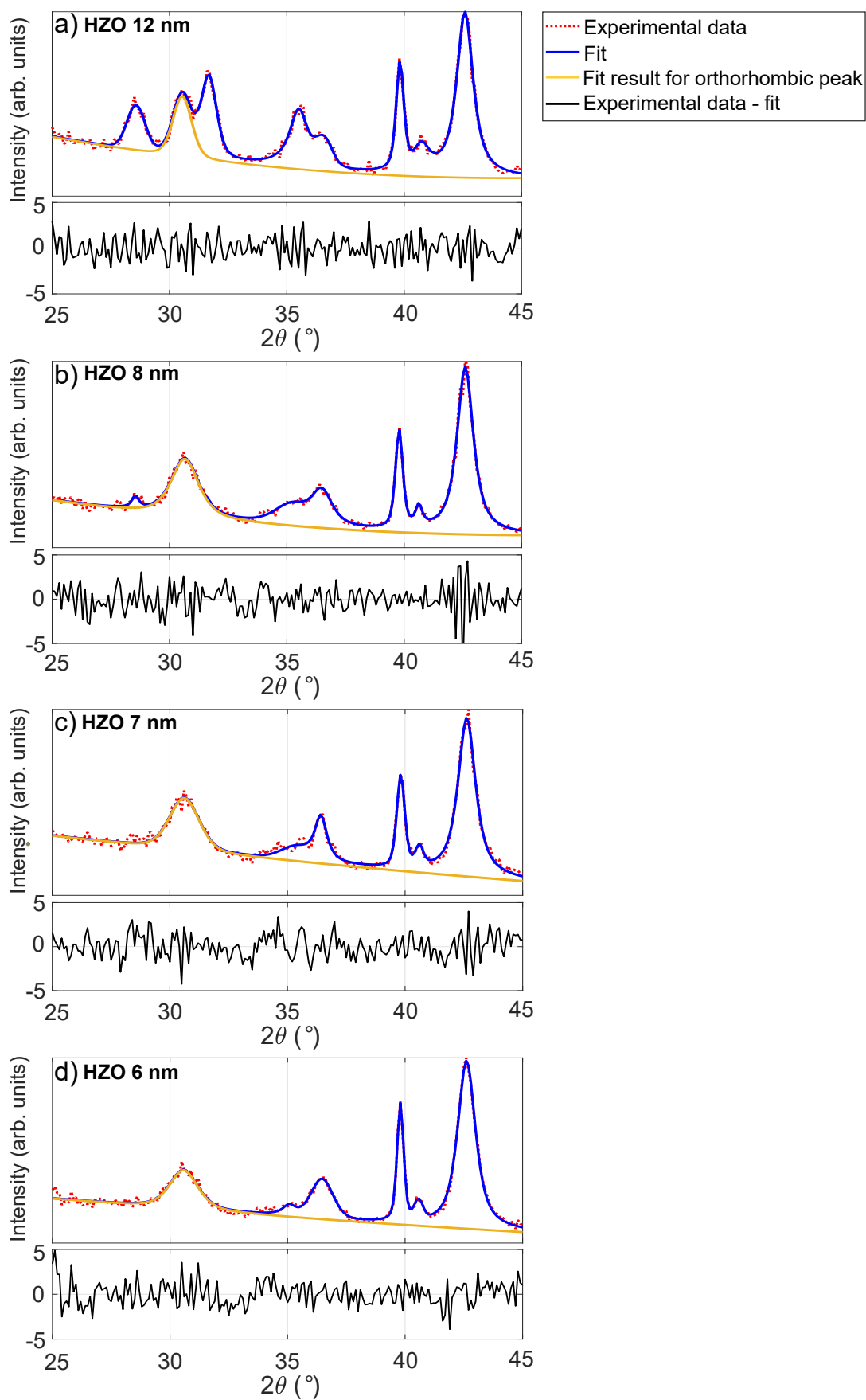


Figure IV.3: GI-XRD pattern, fit, and difference between experimental data and fit of the structure $n^+Si(100)/TiN/HZO/TiN/Ti/Pt$ with: a) HZO ~ 12 nm. b) HZO ~ 8 nm. c) HZO ~ 7 nm. d) HZO ~ 6 nm.

Table IV.1 reports the average out-of-plane o-phase crystallite size for different HZO thicknesses. The latter decreases proportionally with the thickness up to 7 nm, to increase again slightly for the 6 nm-thick HZO layer. This is characterised by the lowest HZO thickness/crystallite size ratio, while the 12 nm-thick HZO film by the highest. This suggests that as the thickness of the layer decreases the o-phase crystallites tend to increase in size, even though the values obtained for the 8 nm-thick, 7 nm-thick, and 6 nm-thick HZO layer are very similar. Figure IV.4 gives the trend of the value of the average crystallite size as a function of the HZO thickness.

Table IV.1: Average o-phase out-of-plane crystallite size for different HZO thicknesses.

HZO thickness (nm)	HZO crystallite size (nm)
12	8.6
8	5.8
7	5.5
6	5.7

IV.1.2 Electrical Characterisations

PUND

To validate existence of the ferroelectric phase in HZO, detected by GI-XRD, PUND was performed by means of the same protocol described in section III.4.1. Figures IV.5a, b, c, and d report the hysteresis cycles associated to the devices with 12 nm-thick, 8 nm-thick, 7 nm-thick, and 6 nm-thick HZO layer. The PUND measure to extract the hysteresis curves was performed after wake-up. At first glance, it is possible to confirm the presence of ferroelectricity for all the probed structures. A more detailed analysis of the P - V curves reveals that the highest $2P_r$ is reached with the 7 nm-thick HZO layer, $\sim 32 \mu C/cm^2$. Similar values are obtained for 12

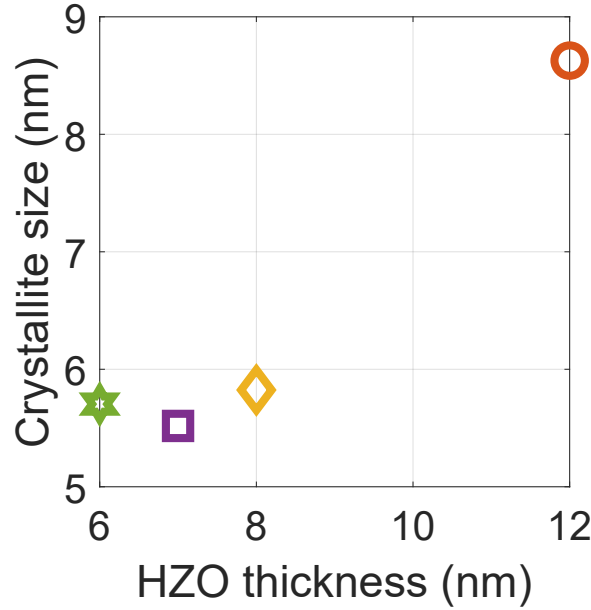


Figure IV.4: Crystallite size vs HZO thickness.

nm-thick, and 8 nm-thick HZO, for which it is $\sim 26 \mu\text{C}/\text{cm}^2$ and $31 \mu\text{C}/\text{cm}^2$, respectively. However, when the HZO thickness is scaled down to 6 nm, $2P_r$ notably decreases to $\sim 10 \mu\text{C}/\text{cm}^2$, in line with what was discussed in section III.6. This might indicate a threshold, in our case established to be ~ 6 nm, below which the ferroelectric performances of the devices steadily worsen. It is important to mention that this conclusion was drawn on the basis of the experimental findings related to this work, on used fabrication method, and conditions. Samples with a thickness ≤ 6 nm were often characterised by a degraded ferroelectricity and low endurance. The imprint is evident in the 12 nm-thick, 7 nm-thick, and 6 nm-thick HZO-based devices, while, it is more moderate in the 8 nm-thick one. Once again, for symmetric structures, the imprint is most probably linked to the presence of defects at the HZO/electrode interfaces that promotes the pinning of ferroelectric domains. As far as the coercive field (E_c) is concerned, the highest value is associated to the 12 nm-thick HZO film and the smallest to 6 nm-thick one. When E_c increases the amount of domains that contribute to the ferroelectric switching increases as well. For FTJs, a high coercive field is desirable in order to detect enough current before the switching of the polarisation.

A fundamental aspect to consider for the optimisation of ferroelectric HZO thin films is the endurance that corresponds to the change of $2P_r$ as a function of the voltage cycling. Figures IV.6a, b, c, and d show the endurance test of the structures

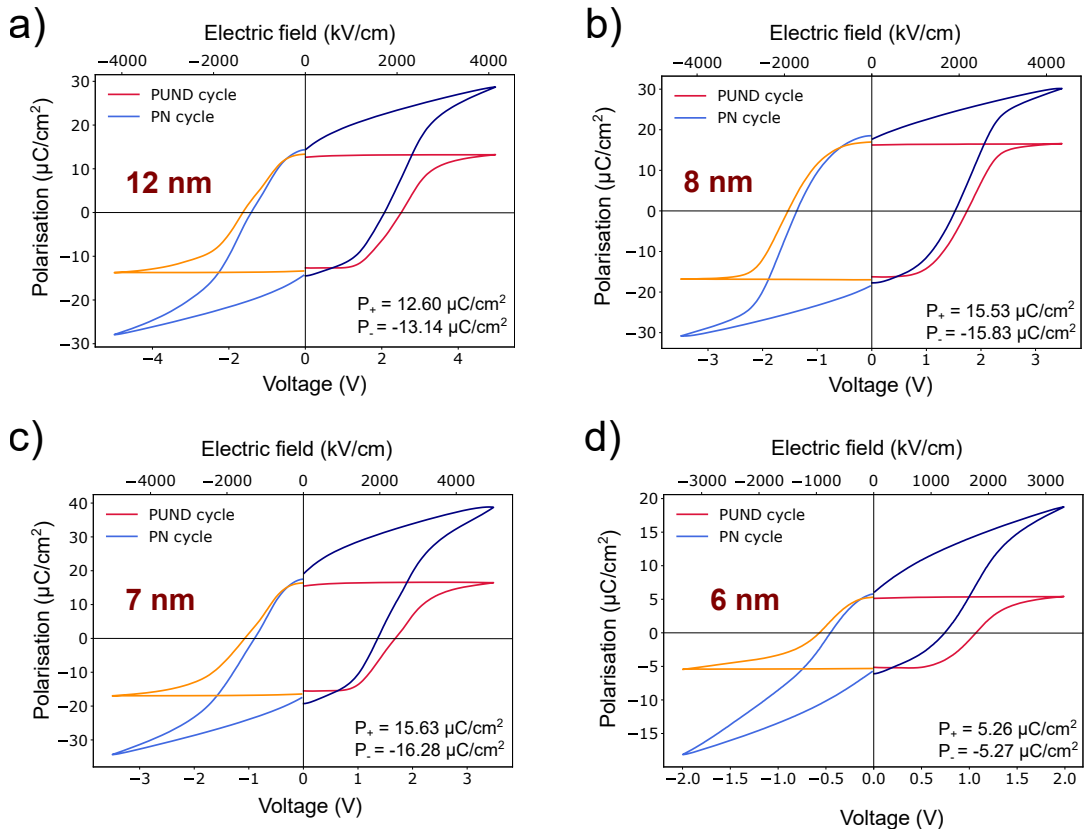


Figure IV.5: P - V curve of structure $n^+\text{Si}(100)/\text{TiN}/\text{HZO}/\text{TiN}/\text{Ti}/\text{Pt}$ with: a) ~ 12 nm-thick HZO layer, extracted after 5×10^2 cycles. b) ~ 8 nm-thick HZO layer, extracted after 5×10^3 cycles. c) ~ 7 nm-thick HZO layer, extracted after 5×10^2 cycles. d) ~ 6 nm-thick HZO layer, extracted after 5×10^4 cycles.

with 12 nm-thick, 8 nm-thick, 7 nm-thick, and 6 nm-thick HZO layer. If the wake-up is considered, samples with 12 nm-thick, 8 nm-thick, and 7 nm-thick HZO film are characterised by a less marked wake-up than the 6 nm-thick HZO one and they are ferroelectric in their pristine state. The 12 nm-thick and the 6 nm-thick HZO structures entered in a fatigue state before electrical breakdown that occurred at $\sim 5 \times 10^5$ cycles and 10^7 cycles, respectively. On the contrary, the samples with 8 nm-thick and 7 nm-thick HZO underwent electrical breakdown, at $\sim 10^4$ and at 10^5 cycles, before fatigue. The thinnest specimen presents the highest endurance, but also highest wake-up, while the specimen that has the lowest wake-up, in figure IV.6c, has also the lowest endurance. Ideally, wake-up should be minimised and endurance maximised. Consequently, in the frame of the optimisation process of the stack, it is important to fabricate a device that shows a good ferroelectric behaviour even in the pristine state.

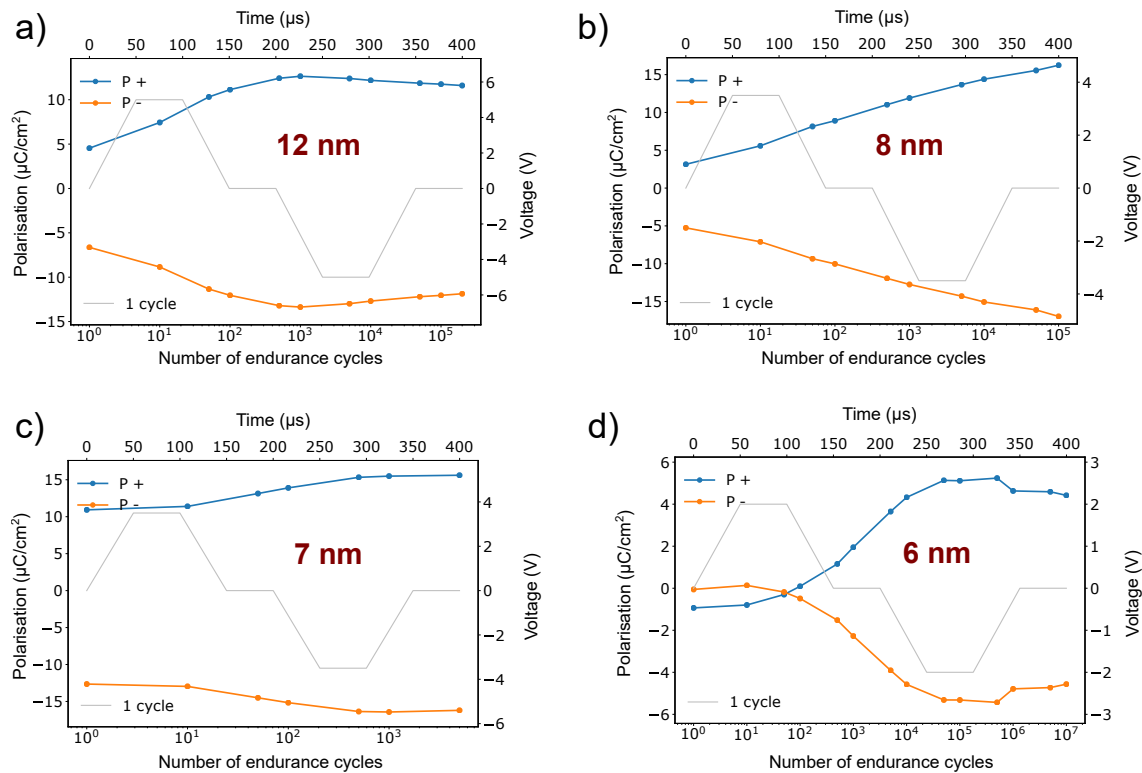


Figure IV.6: Endurance test of structure $n^+Si(100)/TiN/HZO/TiN/Ti/Pt$ with: a) ~ 12 nm-thick HZO layer. b) ~ 8 nm-thick HZO layer. c) ~ 7 nm-thick HZO layer. d) ~ 6 nm-thick HZO layer.

I-V measurements

Figure IV.7 reports the leakage current, represented in semi-logarithmic scale, measured for samples with different HZO thicknesses. The highest current corresponds to the 6 nm-thick HZO sample, for which it is of the order of μA when ± 1.5 V is applied. As the HZO thickness decreases, the leakage current increases and it reaches the minimum for the 12 nm-thick HZO specimen. For positive voltages, a slight difference between the current measured for the two polarisation states is noticeable only in the case of the 7 nm-thick HZO sample. A further reason for which the leakage current is higher for the thin samples might be related to the size of the crystallites in HZO. Small crystallites mean higher density of crystalline boundaries between nano-grains, which could favour a high leakage current.

C-V measurements

C-V curves of samples with different HZO thicknesses were performed on pristine capacitors and are shown in figure IV.8. As expected, the capacitance increases with decreasing ferroelectric thickness, because of their inverse proportionality,

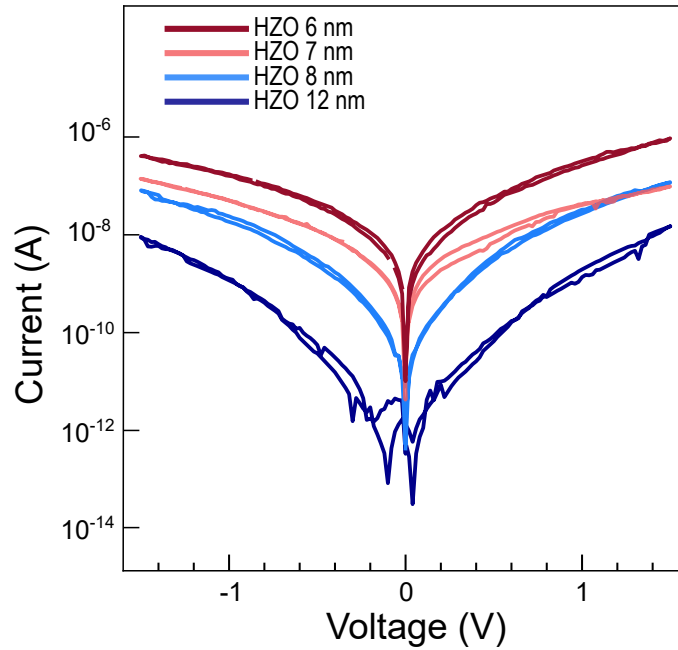


Figure IV.7: I - V curves in semi-log scale, for applied voltage ± 1.5 V, of samples $n^+\text{Si}(100)/\text{TiN}/\text{HZO}/\text{TiN}/\text{Ti}/\text{Pt}$ with: HZO ~ 12 nm, HZO ~ 8 nm, HZO ~ 7 nm, and HZO ~ 6 nm.

equation III.8. Its trend as a function of the voltage shows, for each sample, the butterfly shape typical of ferroelectric materials. The maximum value of C is ~ 7.5 pF for the 12 nm-thick HZO sample, ~ 9 pF for the 8 nm-thick and the 7 nm-thick ones, and ~ 10.5 pF in the case of the 6 nm-thick HZO structure. The irregular shape of the butterfly, specially for the 12 nm-thick and the 6 nm-thick HZO samples, and the slight asymmetry of the curves with respect to the 0 V can be attributed to defects at electrode/HZO interfaces and domain pinning [146, 201]. Table IV.2 reports the calculated values of the relative dielectric constant (ϵ_r) for the four samples, using the maximum value of C in reference to figure IV.8.

Table IV.2: Value of ϵ_r for different HZO thicknesses.

HZO thickness (nm)	Relative dielectric permittivity
12	~ 32.4
8	~ 26
7	~ 23
6	~ 23

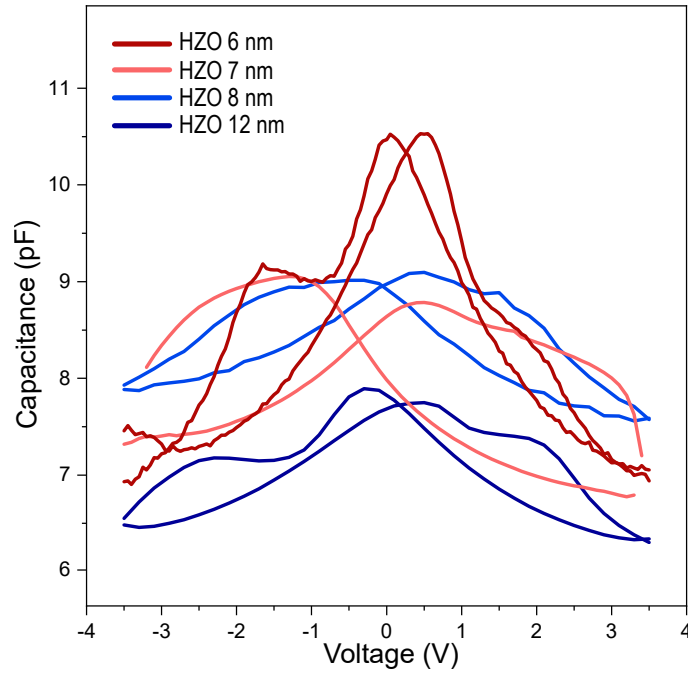


Figure IV.8: C - V measurements, for applied voltage of ± 3.5 V, of samples $n^+\text{Si}(100)/\text{TiN}/\text{HZO}/\text{TiN}/\text{Ti}/\text{Pt}$ with: HZO ~ 12 nm, HZO ~ 8 nm, HZO ~ 7 nm, and HZO ~ 6 nm.

IV.2 Bottom Electrode: State of the Art

The electrode material strongly impacts the physical, chemical, and electrical properties of the ferroelectric layer. For instance, the choice of the materials and the ferroelectric/electrode interface properties affect the leakage current density, the electric field characteristics across the ferroelectric, and the imprint that can be influenced by a top and bottom electrodes with different work functions. The bottom electrode plays a crucial role on initial state of the oxide growth and it serves as a nucleation layer. On the contrary, the top electrode does not affect the growth behaviour, but it applies a residual stress on the already formed oxide layer, impacting its ferroelectric properties as discussed in section III.2.3. This paragraph is dedicated to the investigation of various materials used as bottom electrode and their impact on the device performances. For fluorite-type ferroelectrics, several bottom electrode materials have been explored, such as elemental metals, metal nitrides, metal oxides, and semiconductors. This section gives an overview on the state of art of HZO-based and HfO_2 -based structure with different bottom electrodes. The most used material as electrode for fluorite-type structures is TiN, as it is a standard material in CMOS technology [202]. The use of TiN was initially reported by Böske *et al.* in 2011, in their first study on ferroelectricity in HfO_2 -

based thin films. Since then, TiN has been and it still remains widely used as a bottom electrode. Nevertheless, other metals and compounds have been explored and reported in the literature, few of them being very promising. In 2017, Ambriz-Vargas *et al.* [83] proposed a FTJ device, where HZO was sandwiched between Pt electrodes. Pt, as electrode material, could favour the deposition of highly oriented ferroelectric thin films [203]. In 2018, Goh *et al.* [84] studied effect of TiN, Si, SiGe, and Ge on HfO₂-based FTJs. They showed that devices with Ge bottom electrode exhibited high remanent polarisation and TER ratio. They attributed this result to the in-plane tensile strain exerted by the Ge bottom electrode on the HZO layer. In 2020, Chernikova *et al.* [204] compared the ferroelectric performances of capacitive structures using TiN and Ru bottom electrodes. They reported a more stable ferroelectric response using Ru bottom electrode rather than TiN, but an earlier breakdown. They attributed the first finding to the bottom interface properties and the second to a higher surface roughness of Ru bottom electrode with respect to TiN. Structures with Ru bottom electrode were demonstrated to guarantee a good ferroelectricity also by Cao *et al.* [205]. They showed high endurance, low leakage current, and high breakdown field. The obtained results were ascribed to a lower concentration of defects and oxygen vacancies in HZO with Ru electrodes. Ruthenium oxide (RuO₂) used as bottom electrode was shown to be very promising also for ferroelectric PZT, because it guarantees a very little inter-diffusion of PZT and a sharp interface [206]. Zacharacki *et al.* [207] reported a very large P_r in ferroelectric Hf_{1-x}Zr_xO₂ grown on Ge substrates. The o-phase formation was assigned to the residual thermal tensile strain applied by the Ge substrate and quality of ferroelectricity to the absence of an interfacial dead layer. The cited works are only few examples and other materials were explored as bottom electrode, such as TaN [45], Si [68, 187, 208], and Ir [198]. However, the film growth and the annealing conditions strongly affect the ferroelectric performances of HZO- and HfO₂-based devices, sometimes leading to very different results with respect to what is reported in the literature.

IV.3 Investigated Structures

The use of bottom electrodes other than TiN was pursued also in this work with the aim of finding a capacitive structure based on ultra-thin HZO with robust fer-

roelectric properties. As first, a reference thickness of 12 nm was employed to test the ferroelectricity of HZO grown on different bottom electrodes and the reproducibility of the results. Four bottom electrode materials were considered: n^+ Si, p^+ Ge, Pt, and TiN as reference for comparison. Figure IV.9 shows a schematic of samples that were analysed. The thickness of electrodes was 50 nm, except for n^+ Si, and p^+ Ge substrates. For each sample RTA annealing was performed at 450 °C. In the following paragraphs the structural and electrical characterisations are presented and, finally, a critical analysis of results is given.

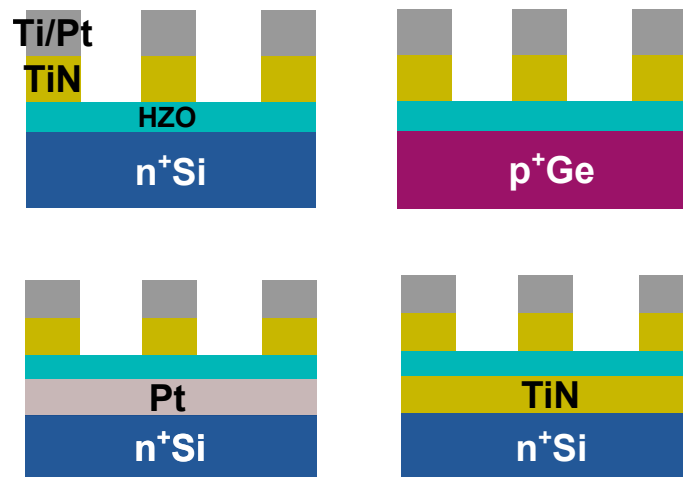


Figure IV.9: Schematics of the analysed samples with different bottom electrodes.

IV.3.1 Structural Characterisation: GI-XRD

The GI-XRD analysis was used to determine the presence of the o-peak at $\sim 30.5^\circ$ for structures with different bottom electrode materials. Figure IV.10 reports the superimposed GI-XRD patterns for the four probed samples. The o-phase peak was present in all the patterns, suggesting the existence of ferroelectric behaviour. In all cases, the m-peaks at $\sim 28.4^\circ$, $\sim 31.6^\circ$ $\sim 35.5^\circ$ were detected, confirming the presence of monoclinic crystallites in 12 nm-thick HZO layer deposited on electrodes other than TiN.

Figures IV.11a, b, c, and d show the fit for each pattern and, below, the difference with experimental data. Once again, Sherrer equation was used to determine the average out-of-plane o-phase crystallites size of HZO, reported in table IV.3.

Smallest crystallites correspond to HZO grown on a Pt bottom electrode, whilst largest to HZO grown on p^+ Ge. The difference in average crystallite size could be due to the fact that each electrode acts as a different nucleation layer for the

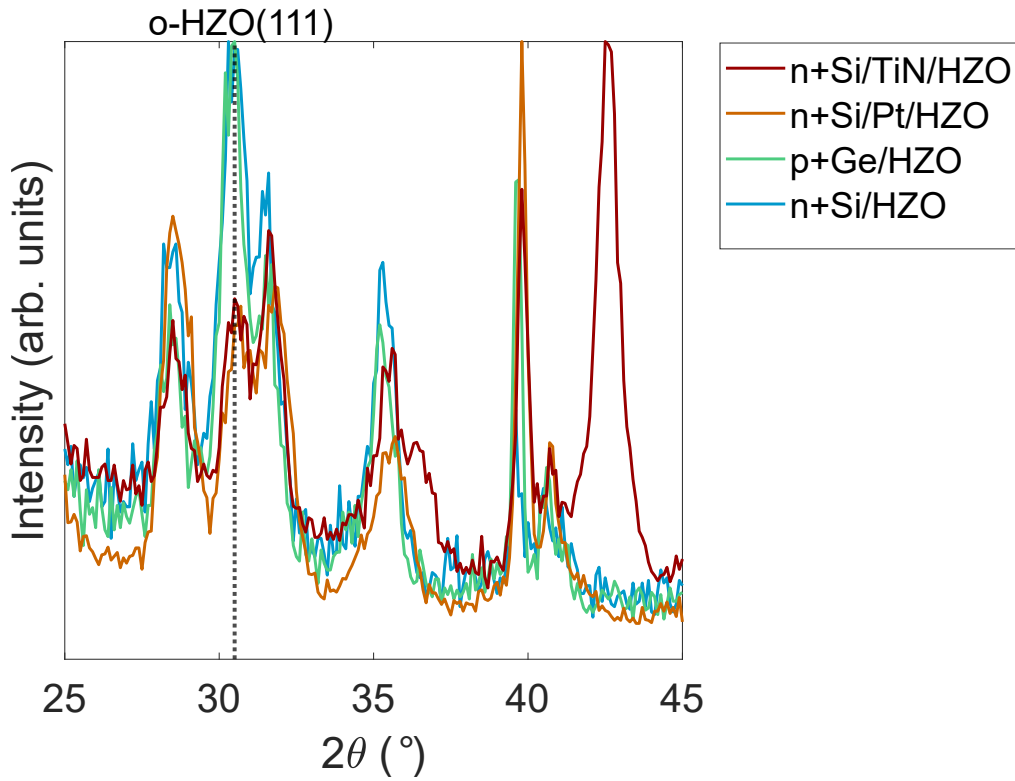


Figure IV.10: Superimposed experimental GI-XRD patterns of samples with different bottom electrodes: n^+ Si/TiN/HZO/TiN/Ti/Pt, n^+ Si/HZO/TiN/Ti/Pt, p^+ Ge/HZO/TiN/Ti/Pt, and n^+ Si/Pt/HZO/TiN/Ti/Pt.

Table IV.3: Average out-of-plane o-phase crystallite size of a 12 nm-thick HZO layer deposited on different bottom electrodes.

Bottom Electrode	HZO crystallite size (nm)
n^+ Si	8.4
p^+ Ge	9.4
n^+ Si/Pt	7.2
n^+ Si/TiN	8.6

HZO. Moreover, the mechanical stress due to lattice mismatch, thermal stress due to different thermal expansion coefficients (TECs), and electrode surface conditions significantly affect the ferroelectricity. Firstly, impact of lattice mismatch is considered. HZO is characterised by a lattice parameter of $\sim 5.12 \text{ \AA}$, close in value to the one of Si, which is $\sim 5.43 \text{ \AA}$. The lattice constant of Ge is $\sim 5.66 \text{ \AA}$, larger with respect to the HZO one. On the contrary, lattice parameters of TiN and Pt

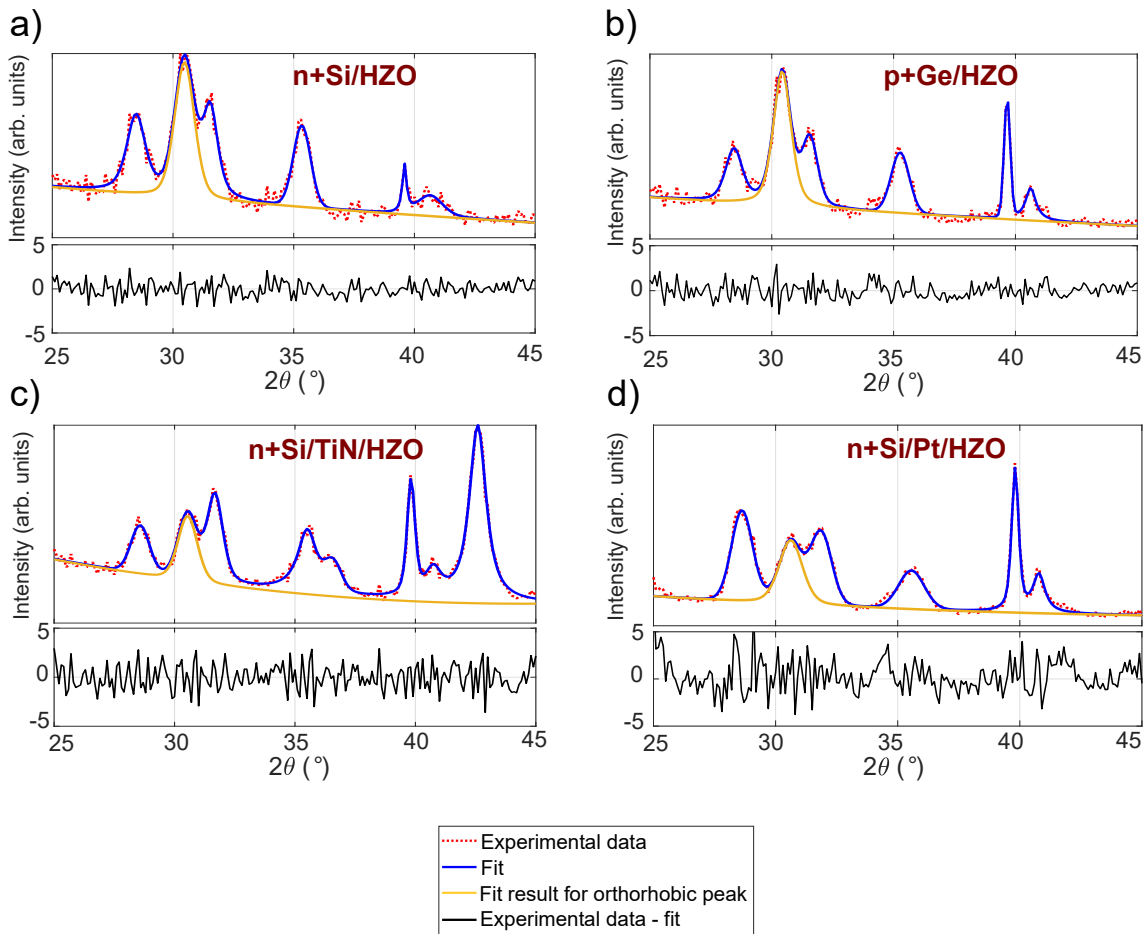


Figure IV.11: GI-XRD pattern, fit, and difference between experimental data and fit of: a) n⁺Si/HZO. b) of p⁺Ge/HZO. c) n⁺Si/TiN/HZO. d) n⁺Si/Pt/HZO.

are considerably smaller, ~ 4.24 Å, and ~ 3.94 Å, respectively. From these values, it is possible to hypothesise that TiN and Pt might influence the nucleation of HZO crystallites by exerting a mechanical compressive strain, while Si and Ge a tensile strain. Although, in a first approximation and without considering the crystal orientation of Si, the similarity between lattice constant of Si and the one of HZO could make this effect negligible. Secondly, the thermal strain can be considered as a possible contribution to the HZO ferroelectric properties. Table IV.4 reports the TECs of HZO and of the used bottom electrode materials. Pt should be responsible for the largest thermal tensile strain, while Si for the largest compressive strain. TECs of TiN and Ge are rather similar in value to HZO and so their effect is more attenuated with respect to the other bottom electrodes. The thermal strain exerted by the bottom electrode should have a more moderate impact on the ferroelectric properties of HZO than the one of the top electrode, which, post-annealing, acts as a capping layer. The evaluation of the HZO ferroelectricity by the electrical characterisation add more elements for a better understanding of

a possible effect of strain on HZO ferroelectric behaviour.

Table IV.4: Thermal expansion coefficients (TECs) of HZO and of different bottom electrodes.

Material	TEC (K^{-1})
HZO	7×10^{-6}
TiN	8×10^{-6}
Pt	27×10^{-6}
Ge	6.1×10^{-6}
Si	2.56×10^{-6}

IV.3.2 Electrical Characterisation: PUND

The electrical characterisation was performed by PUND. Figures IV.12a, b, and c report the P - V curves of HZO deposited on TiN, n^+ Si, and Pt bottom electrodes. The structure with the p^+ Ge bottom electrode did not show any ferroelectric behaviour, reason for which it is not here reported. Furthermore, the analysis of the latter sample was made difficult by the poor electrical conductivity of the p^+ Ge substrate, despite the high doping level. The highest $2P_r$ is associated to the reference sample (with TiN bottom electrode), $\sim 26 \mu C/cm^2$. When HZO was grown on n^+ Si, the $2P_r$ was $\sim 8 \mu C/cm^2$, while, for case of Pt bottom electrode, it was $\sim 18 \mu C/cm^2$. The imprint is evident in the structures with n^+ Si and Pt bottom electrodes, left and right shift with respect to the 0 V, respectively. In these cases, the imprint is generated by the different work function of the bottom and top electrodes. This phenomenon has already been described in the literature [209]. In the case of n^+ Si substrate, the asymmetric shape of the hysteresis curve for negative and positive applied voltages is related to a higher contribution of leakage current for a certain polarisation direction compared to the other, when a negative voltage is applied. Moreover, it is possible to notice that, for the Pt bottom electrode, the voltage used for the extraction of P - V characteristic was lower, $\pm 3V$, with respect to the other two cases, indicating a higher fragility.

The endurance test was performed on the different HZO-based structures and it

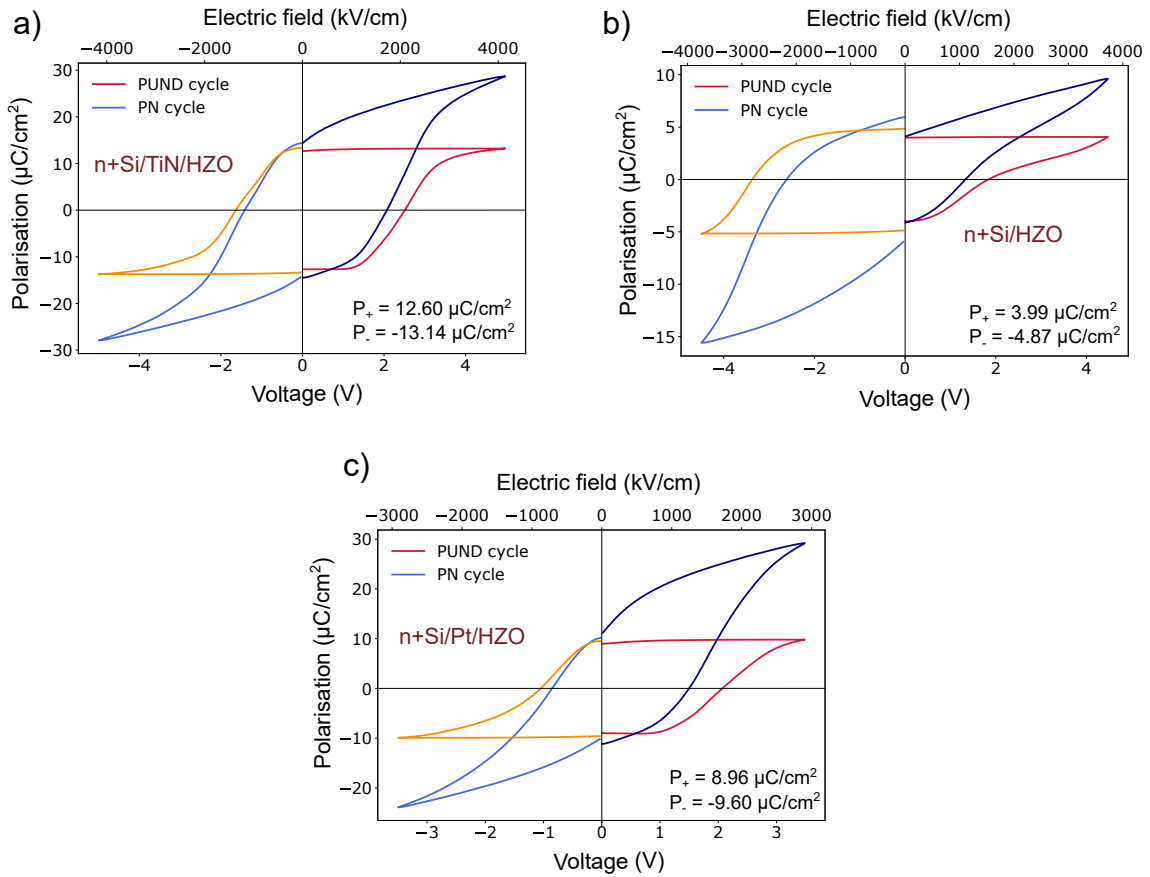


Figure IV.12: P - V curves of 12 nm-thick HZO-based devices with different bottom electrodes: a) n⁺Si/TiN, extracted after 5×10^2 cycles. b) n⁺Si, extracted after 5×10^2 cycles. c) n⁺Si/Pt/HZO, extracted after 10^4 cycles.

is reported in figure IV.13a, b, c. The obtained values of endurance are similar for the three cases, the highest being one of HZO grown on n⁺Si substrate, 10^6 cycles. For TiN/HZO and Pt/HZO samples, the endurance is 5×10^5 and 10^5 cycles, respectively. TiN/HZO is characterised by a moderate wake-up and its P_r reaches the maximum after 10^3 cycles and it enters in a fatigue state before the electrical breakdown. Pt/HZO is marked with a stronger wake-up. The P^r is $\sim 0 \mu\text{C}/\text{cm}^2$ in the pristine state, hits the maximum after 10^4 cycles, and slightly decreases before the electrical breakdown. N⁺Si/HZO presents an unusual trending for the P_r as function of cycling, indeed, the P_r oscillates before reaching breakdown, although, it is characterised by a rather low wake-up. This trend of P_r might be due to the defects redistribution and the domain pinning/unpinning during voltage cycling. From the previous analysis, we concluded that HZO deposited on TiN bottom electrode had the best ferroelectric performances. The reason why the results obtained for the other analysed electrodes were not satisfactory might be associated to the nature of the bottom electrode/HZO interface and to the state of the bottom elec-

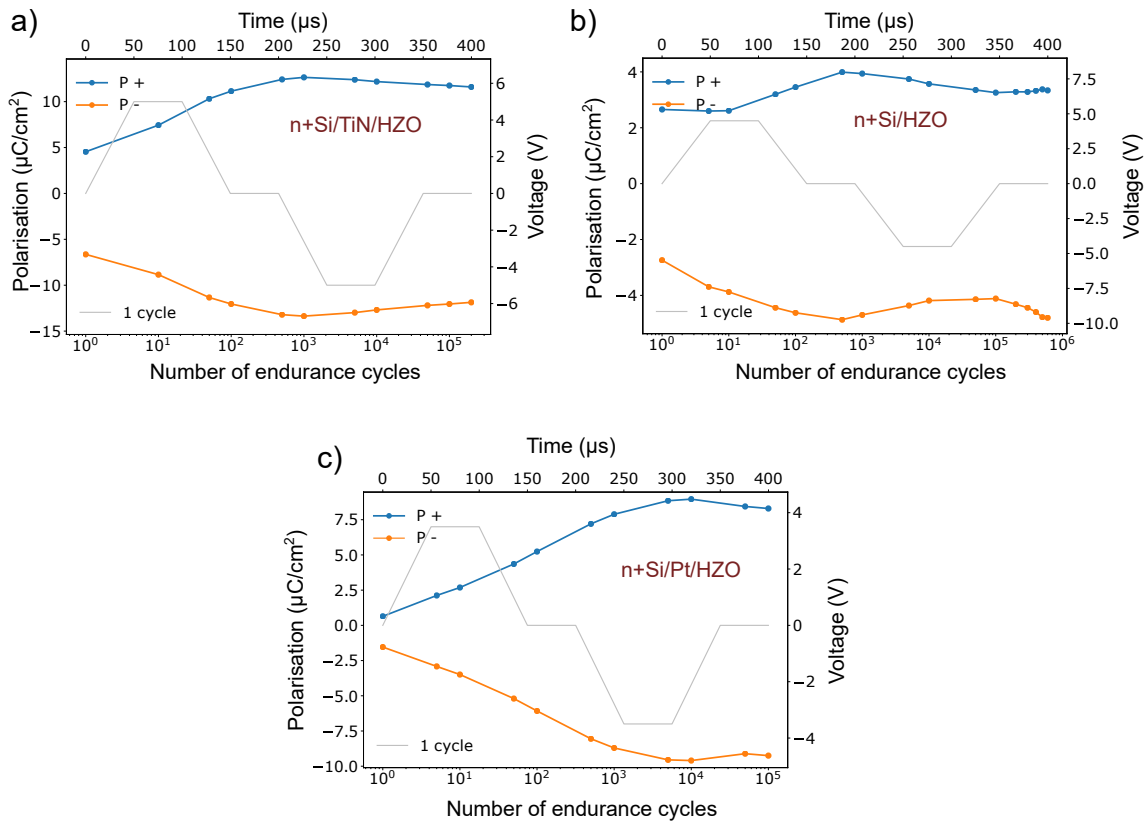


Figure IV.13: Endurance test of 12 nm-thick HZO-based devices with different bottom electrodes: a) of $n^+\text{Si}/\text{TiN}$. b) of $n^+\text{Si}$. c) $n^+\text{Si}/\text{Pt}/\text{HZO}$.

trode surface. For instance, Pt bottom electrode was previously investigated by our group and a possible explanation for which it does not favour a robust ferroelectricity in HZO was related to the metallic nature of the HZO/Pt interface rather than oxide one, as is the case of HZO/TiN interface [143]. In the literature it was shown that Pt has a negative impact also on the ferroelectric properties of PZT [210, 211]. Further causes could be linked to the recipes and the experimental conditions employed for the fabrication of samples.

IV.4 Thickness of TiN Bottom Electrode

The study of different bottom electrodes revealed that the HZO shows its best ferroelectricity when grown on TiN. In the frame of the optimisation of HZO ferroelectric performances, the influence of the thickness of TiN bottom electrode was studied. Its thickness was increased from 50 nm to 100 nm and structural and electrical characterisations were performed on a 12 nm-thick and a 6 nm-thick HZO-based structures. The obtained results were not satisfactory, a minor enhancement of the remanent polarisation and a higher wake-up were recorded.

Overall, a 100 nm-thick TiN bottom electrode had a better impact on a 6 nm-thick HZO sample compared to the 12 nm-thick one. In conclusion, it was decided to maintain a top and bottom electrode thickness of 50 nm. However, increasing the electrode thickness might still be a promising approach to improve the ferroelectric behaviour of HZO thin films and it requires further investigations. For instance, in the literature, few works claimed that thick TiN electrodes improve HZO ferroelectricity [212]. In particular, the strain induced by a thick top electrode promotes an enhanced stress-induced crystallisation of HZO o-phase.

IV.5 Conclusion of the Chapter

This chapter was dedicated to the study of $n^+Si/TiN/HZO/TiN/ti/Pt$ structures to evaluate the evolution of the HZO ferroelectric behaviour as a function of its thickness. The findings revealed a good ferroelectricity for a HZO thickness ≥ 7 nm. This allowed us to determine a threshold below which a degradation of ferroelectricity was obtained with the used fabrication conditions. However, one of the objectives of this thesis requires a thickness of HZO < 7 nm for FTJ applications. A first approach to improve ferroelectricity at low HZO thickness was the investigation of bottom electrode materials other than TiN. n^+Si , n^+Ge , and Pt were studied, but the results were not satisfactory for a 12 nm-thick HZO-based stack and consequently the HZO thickness was not further reduced. TiN bottom electrode was shown to be the best option with a thickness of 50 nm. It is clear that other ways to scale down the HZO thickness without compromise its ferroelectricity have to be explored. In chapter V, interface engineering was employed to this purpose and the effect of the insertion of Ti and Al interfacial layers was probed. Furthermore, tungsten (W) is presented in chapter V as an option for the synthesis of bottom and top electrode. The related results were not presented in this chapter, because they are part of a study of optimised HZO-based capacitors and FTJs with enhanced ferroelectricity.

Synthesis and Optimisation of Ultra-Thin HZO-based Ferroelectric Tunnel Junctions

This chapter is devoted to the exploration of two successful approaches for the development of 6 nm-thick HZO-based heterostructures with enhanced ferroelectricity. As it was seen in chapter IV, the use of n^+ Si, p^+ Ge, and n^+ Si/Pt as bottom electrodes was not a viable solution for the synthesis of ultra-thin HZO films with robust ferroelectricity. The first part of this chapter is dedicated to an analysis of the effect of interfacial layers inserted at the top electrode/HZO interface on the ferroelectric properties of HZO-based capacitors. The second part is focused on the study of stacks with tungsten (W) electrodes. W was used as bottom and top electrode, or as bottom or top electrode in combination with TiN. These two studies highlight the importance of the structural and compositional properties of HZO/electrode interfaces on the device ferroelectric behaviour.

V.1 Ultra-Thin Interfacial Layers: State of the Art

The insertion of ultra-thin dielectric layers at electrode/ferroelectric interfaces was proved to be beneficial to improve the ferroelectric performances of HZO-based capacitors and FTJs. Table V.1 provides an overview on the state of art of HZO-based heterostructures with the addition of an interfacial layer at the top or bottom

interface, together with some relevant parameters, such as remanent polarisation and endurance.

Table V.1: State of art: thin-HZO-based structure with the addition of the interfacial layers

Reference	HZO thickness (nm)	Interfacial Layer	Position Interface	$2P_r$ ($\mu\text{C}\cdot\text{cm}^{-2}$)	Endurance
[213]	10	TiO ₂ 1 nm	Top	16	10 ⁸
[214]	10	HfO ₂ 1 nm	Bottom	22.1	10 ¹⁰
			Top	19.6	10 ¹⁰
[215]	8.4	Al ₂ O ₃ 1 nm	Bottom	15	10 ⁵
		1.8		12	10 ⁵
		2.2		7	between 10 ⁵ and 10 ⁶
[216]	10	TiO ₂ 2 nm	Bottom and top	8 (as deposited and after wake-up)	NA
[187]	12	Al ₂ O ₃ 3 nm	Top	21	10 ⁶
[141]	12	Al ₂ O ₃ 2.5 nm	Top	NA	NA
[217]	20	Al ₂ O ₃ 1.6 nm	Top	30	NA
[218]	9.5	ZrO ₂ 2 nm	Bottom	32	NA

All the works reported here recorded a relevant improvement of HZO ferroelectric properties when an interfacial layer was added at the top, bottom, or both interfaces. In some cases, for metal-ferroelectric-insulator-metal (MFIM) FTJs, an ultra-thin dielectric layer was used to serve as tunnel barrier, while HZO provided the polarisation switching [141, 215, 219]. This approach allowed to measure an ON/OFF ratio for devices with HZO \sim 10 nm-thick, thus avoiding issues related to its scalability.

V.2 Ultra-Thin Interfacial Layers: Experimental Results

This section presents the experimental results obtained for HZO-based capacitors with the insertion of a Ti or Al metallic layers at the top electrode/HZO interface. Samples with a Ti interlayer at the top interface are characterised by a HZO thickness of 6 nm, suitable for FTJ applications. Both Ti and Al layers were grown at room temperature by RF sputtering of pure Ti and Al targets just prior to the top electrode deposition. Table V.2 reports the growth conditions of the interfacial layers.

Table V.2: Growth conditions of the interfacial layers.

Material	Target RF power (W)	Gas (sccm)	Working pressure (mbar)
Ti	100	50	5×10^{-2}
Al	100	50	5×10^{-2}

V.3 Titanium Interfacial Layer

The impact of the insertion of a Ti interfacial layer with a thickness of 1, 2, and 3 nm was explored. Figure V.1 reports a schematic of the two heterostructures, with (figure V.1a) and without (figure V.1b) the Ti interfacial layer, together with STEM-HAADF images of the bottom electrode/HZO/top electrode cross-section.

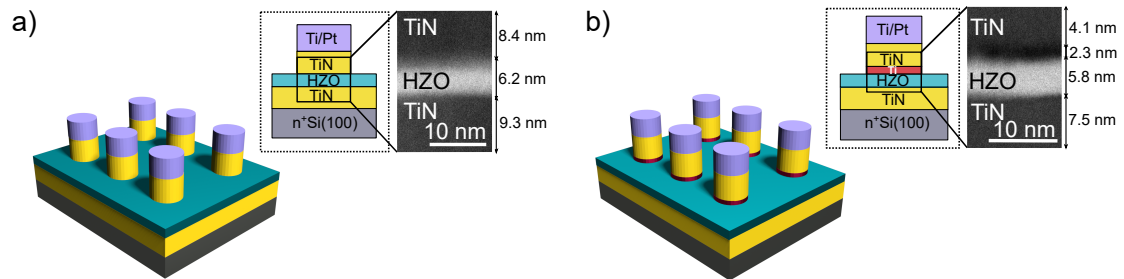


Figure V.1: Schematic of the samples. a) Without Ti interfacial layer, on the right the STEM-HAADF image of the TE/HZO/BE cross-section. b) With Ti interfacial layer, on the right the STEM-HAADF image of the TE/HZO/BE cross-section.

V.3.1 Structural Characterisations: GI-XRD, and EELS

GI-XRD Analysis

Four samples, labelled sample 0, 1, 2, and 3 for simplicity, were studied. For sample 0, the HZO layer was sandwiched between TiN bottom and top electrodes, while for samples 1, 2, and 3 an ultra-thin layer of Ti, of 1, 2, and 3 nm, respectively, was inserted at the top interface. The GI-XRD patterns obtained for the four samples are shown in figure V.2. Reference XRD patterns for TiN, HZO o-/t-phase, and HZO m-phase, respectively and are overlaid in figure V.2. The position of the o-/t- peak at $\sim 30.5^\circ$, which corresponds to the (111) planes, coincides with the expected value [157]. No m-phase components at $\sim 28.4^\circ$ (m-HZO (11-1)) and at $\sim 31.6^\circ$ (m-HZO(111)) were detected. The intensity of o-/t-peak, which was similar for the four cases, was not correlated to the presence of the Ti layer nor to

its thickness. This analysis validates the existence of the ferroelectric o-HZO phase for the analysed samples. The diffraction peak of o-HZO(111) family of planes, at $\sim 30.5^\circ$, was considered for evaluation of the out-of-plane average crystalline size of the HZO layer by means of the Scherrer equation, equation III.7. Overall, crystalline sizes around 5 nm were found for all samples. From a first analysis, the crystalline size was not correlated neither to the thickness of the Ti interfacial layer nor to its presence.

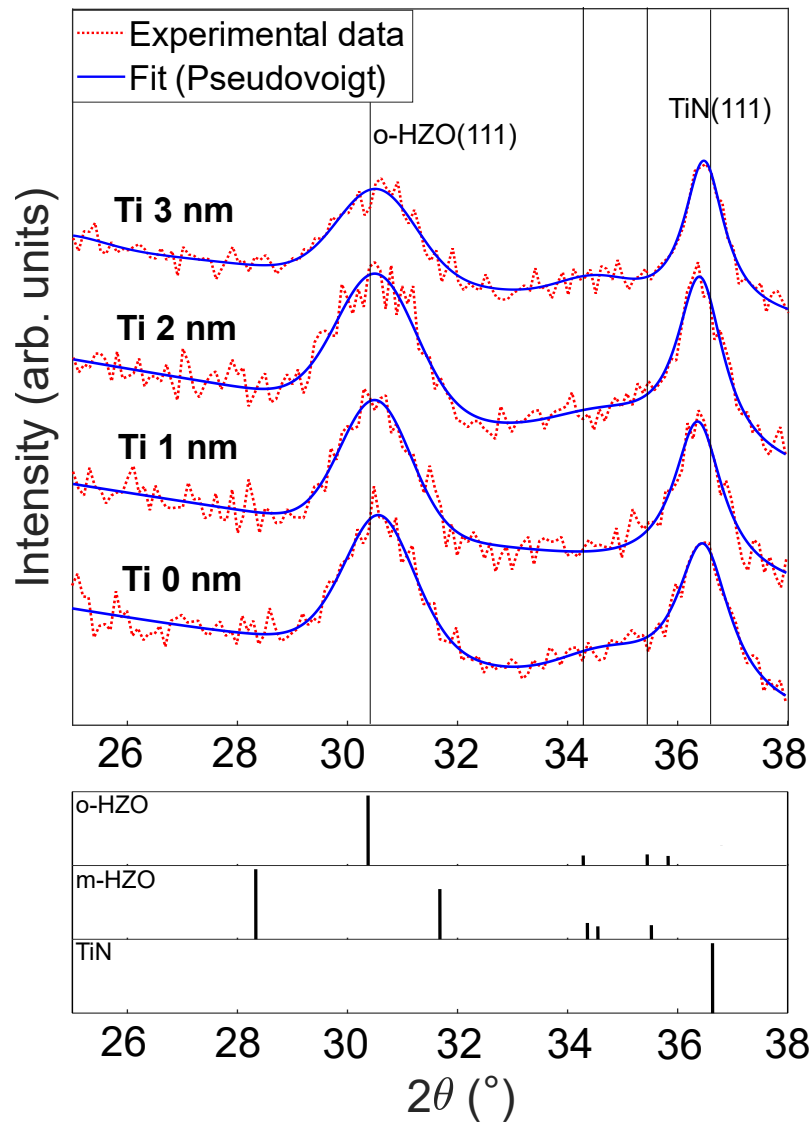


Figure V.2: GI-XRD patterns of the four considered samples. From the bottom: sample 0 with Ti 0 nm, sample 1 with Ti 1 nm, sample 2 with Ti 2 nm, sample 3 with Ti 3 nm. Below, the expected peak positions for orthorhombic HZO, monoclinic HZO, and TiN.

EELS Analysis

The structure and composition of the TiN/HZO top interface in sample 0 and the Ti/HZO top interface in sample 2 were investigated at nanoscale by STEM-EELS on pristine capacitors of 10 μm -diameter, as shown in figure V.3 and figure V.4, respectively. The spatial distribution of N (N-K edge at ~ 400 eV), Ti (Ti-L_{2,3} edges at ~ 455 eV), and O (O-K edge at ~ 530 eV) across TE/HZO interfaces are shown in figure V.3a and V.4a. For TiN/HZO top interface of sample 0, a TiN(O) layer is evidenced from the simultaneous presence of N-K, Ti-L_{2,3} and O-K edges, resulting from the oxidation of TiN layer. This oxidation is localised over ~ 2 nm, as indicated by O-K edge fine structures, which decreases remarkably from HZO to TiN and is accompanied with a shift of O-K edge onset to lower energy, as shown in figure V.3d. The TiN oxidation phenomenon is also described in a previous work by Bouaziz *et al.* [159], in a structure synthesised in the same experimental conditions as the ones considered here. The N-K edge fine structures in the TiN layer are similar to the ones reported in the literature [220], with some fine structure variations and an overall decrease of the N-K edge intensity in the TiN(O) layer, potentially resulting from oxidation [184] (figure V.3b). In addition, the constant energy and shape of Ti-L_{2,3} fine structures across the interface, shown in figure V.3c, suggest a low oxidation. For Ti/HZO top interface of sample 2, a TiO_z layer is evidenced over a couple of nanometers, from the simultaneous presence of O-K and Ti-L_{2,3} edges and the absence of N-K edge, as shown in figures V.4a and V.4b, thus indicating the oxidation of Ti layer. Specifically, Ti-L_{2,3} fine structures split (figure V.4c), as expected in TiO₂, where the L₃, and L₂ peaks split under influence of the crystal field [221]. L₃, and L₂ peaks also shift to higher energy compared to TiN. The O-K edge fine structures change across the HZO/TiO_z interface and the edge onset shifts to lower energy in the TiN(O) layer, as shown in figure V.4d. TiN layer deposited on top of Ti is thus partially oxidised over a very narrow range, as exemplified from simultaneous presence of N-K, Ti-L_{2,3}, and O-K edges. N-K edge fine structures at Ti/TiN interface are different from TiN, as a result of oxidation and subsequent chemical bonding between Ti *d* and O *p* states. Finally, O-K near edge structures of HZO are different in both samples. In sample 2 (figure V.4d), two distinct peaks are visible within 10 eV above edge onset, as expected in HZO polymorphs [222, 223], contrary to sample

0 (Figure V.3). Near-edge structures reflect local electronic structure around O atoms, which are covalently bonded to Hf and Zr atoms. Several parameters could be the cause of these spectral variations, such as local changes of crystal field [68], presence of oxygen vacancies [224–227], or local inhomogeneities in Hf *versus* Zr contents [228] integrated over the spectra displayed in figures V.3 and V.4. The EELS analysis demonstrates that the Ti layer is fully oxidised (sample 2), whereas in absence of Ti, TiN layer is only partially oxidised. The oxygen redistribution induced by Ti layer is meant to produce oxygen vacancies inside HZO film by pulling oxygen atoms towards the top interface. The oxidation phenomenon of the Ti layer explains the contrast difference at TE/HZO interface in the cross-section HAADF images in figures V.1a and b. In sample 2, TE/HZO interface appears dark from the presence of TiO_z interfacial layer.

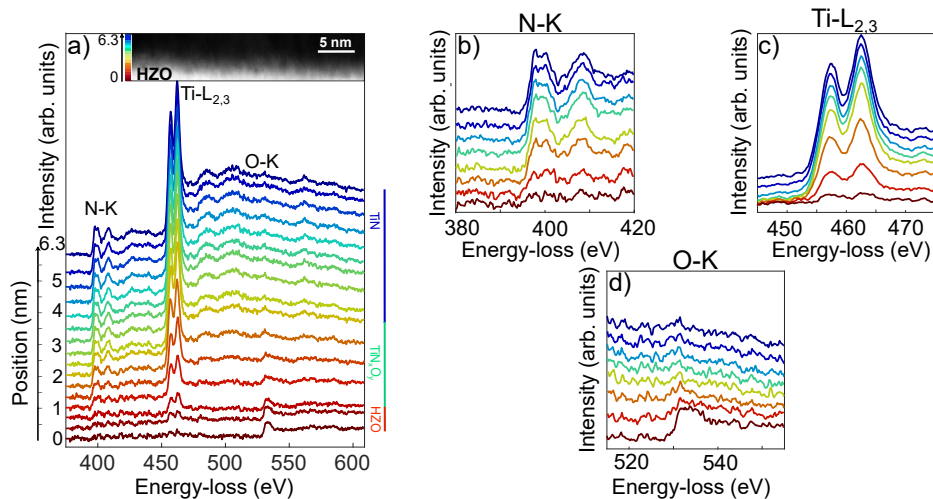


Figure V.3: STEM-EELS analysis of sample 0. a) EELS spectra acquired across the TE/HZO interface. Each spectrum is the average of 81 spectra projected horizontally along the interface, and is shifted vertically for clarity. The HAADF image acquired simultaneously is shown in inset. A spectrum image dataset of 16×81 pixels was acquired with a step size of 3.9 \AA , over an area of $\sim 6.3 \times 32 \text{ nm}^2$. b), c), d) Display over a narrower energy range of the N-K, Ti-L_{2,3}, and O-K edges, respectively.

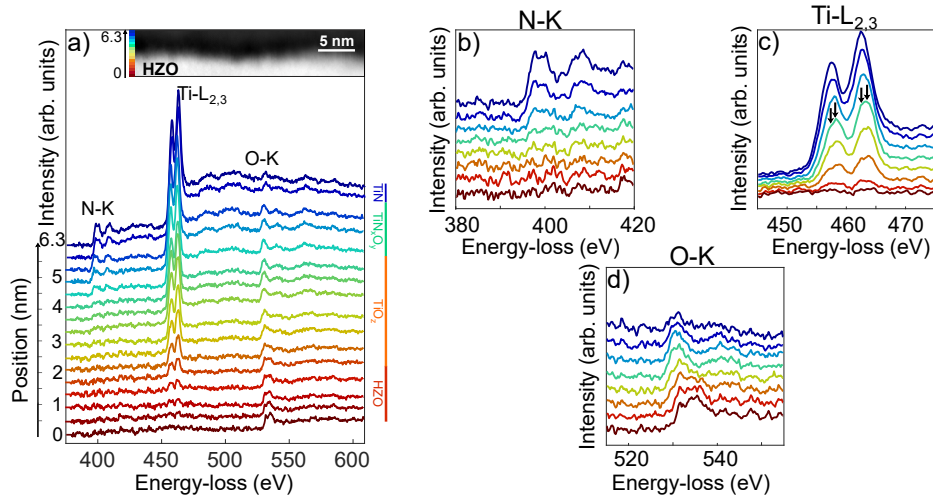


Figure V.4: STEM-EELS analysis of sample 2. a) EELS spectra acquired across the TE/HZO interface. Each spectrum is the average of 81 spectra projected horizontally along the interface, and is shifted vertically for clarity. The HAADF image acquired simultaneously is shown in inset. A spectrum image dataset of 16×81 pixels was acquired with a step size of 3.9 \AA , over an area of $\sim 6.3 \times 32 \text{ nm}^2$. b), c), d) Display over a narrower energy range of the N-K, Ti-L_{2,3}, and O-K edges, respectively.

V.3.2 Electrical Characterisation: PUND

P-V measurements were performed on the four samples. Figure V.5 shows the *P-V* curves extracted at $\sim 10^5$ cycles of samples 0, 1, 2, and 3. For an applied voltage of $\pm 2.5 \text{ V}$, the value of $2P_r$ ranges between $10 \mu\text{C}/\text{cm}^2$ for sample 0 and $25 \mu\text{C}/\text{cm}^2$ for sample 2. Samples 1 and 3 show a $2P_r$ of $23 \mu\text{C}/\text{cm}^2$ and $20 \mu\text{C}/\text{cm}^2$, respectively. The *P-V* curves indicate the presence of the ferroelectric imprint. For sample 0, it can be traced back to a different surface reconstruction at the top and bottom interfaces and to domain pinning by defects, as discussed in section III.4.1. In the case of sample 1, 2, and 3, the imprint could be induced by the Ti layer, which modifies the work function of the top electrode, as seen in section IV.3.2. This asymmetry between the two electrodes is responsible for a built-in field. The obtained results showed that presence of Ti clearly increases the value of $2P_r$. The highest $2P_r$ was obtained for sample 2 and lowest for sample 0. This could be attributed to two factors: I) The chemical properties of the Ti/HZO interface, which are different from the ones of interface TiN/HZO and promote the formation of o-phase grains. The TECs of Ti and TiN have close values, $9.410^{-6} \text{ K}^{-1}$ and 810^{-6} K^{-1} , respectively [229, 230]. Because of the similarity between the TECs of Ti and TiN, we proposed that the main cause of the ferroelectricity enhancement

in HZO for samples with Ti could arise from different chemical reconstructions of the top interface. II) The increased number of oxygen vacancies in HZO, which is induced by the Ti layer [231] and takes part in stabilisation of the o-phase in the HZO film [173, 174]. For a thicker interfacial layer, the polarisation inverts its positive trend, dropping to $20 \mu\text{C}/\text{cm}^2$ for sample 3. This behaviour can be explained by the increasing depolarising field produced at the interface by the TiO_z dielectric layer, which is responsible for the lower remanent polarisation of sample 3 [178, 232]. This tendency is also confirmed in the literature, Si *et al.* [233], Qu *et al.* [234], and Shekhawat *et al.* [215] reported a suppression of ferroelectricity when the thickness of the interfacial dielectric layer was increased. Furthermore, samples 1, 2, and 3 show a positive $2P_r$ in the pristine state, contrary to the null value of sample 0. This result was explained by the hypothesis that the interfacial properties of Ti/HZO promote the formation of o-phase crystallites, while the ones of TiN/HZO could be responsible for the stabilisation of a non-ferroelectric tetragonal phase, which might undergo a field-induced phase change during cycling [235]. The endurance curves in figure V.6 show that $2P_r$ increases for samples 1, 2, and 3 until breakdown occurs, while sample 0 enters in a fatigue state after $\sim 5 \times 10^5$ cycles, where $2P_r$ decreases to $\sim 9 \mu\text{C}/\text{cm}^2$. The increase of remanent polarisation is associated to the wake-up effect, which is partly due to the redistribution of defects, typically oxygen vacancies, during the cycling process [168, 236].

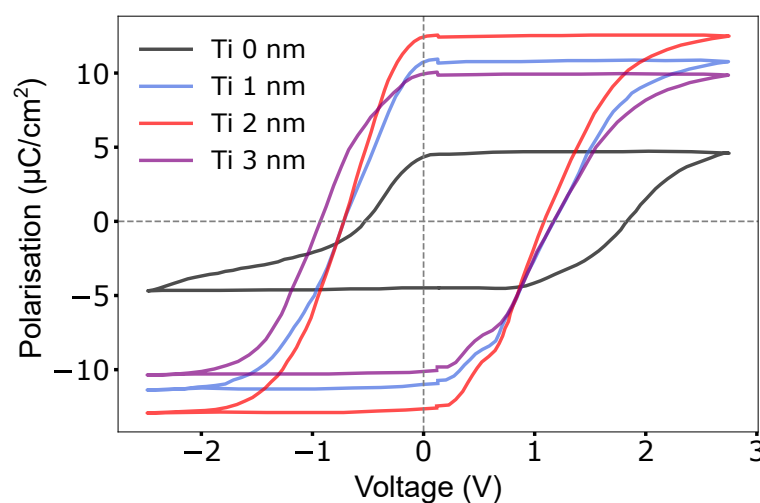


Figure V.5: Electrical characterisation of samples 0, 1, 2, and 3: P - V curves taken on woken up capacitors after $\sim 10^5$ cycles.

The endurance tests were performed on the four samples until the electrical break-

down. At 2.5 V, the value of $|P_+|$ and $|P_-|$ starts at $\sim 5 \mu\text{C}/\text{cm}^2$ for samples 1, 2, and 3, and at $\sim 0 \mu\text{C}/\text{cm}^2$ in the case of sample 0, for which it starts rising after 5×10^2 cycles. In sample 0, P_r reaches its maximum after 10^5 cycles. For samples 1, 2, and 3, P_r rises until electrical breakdown, which occurs after 10^6 , 10^5 , and 5×10^6 cycles, respectively. On average, these results indicated that the endurance value of the here tested devices is comparable to what is reported in the literature [141, 158].

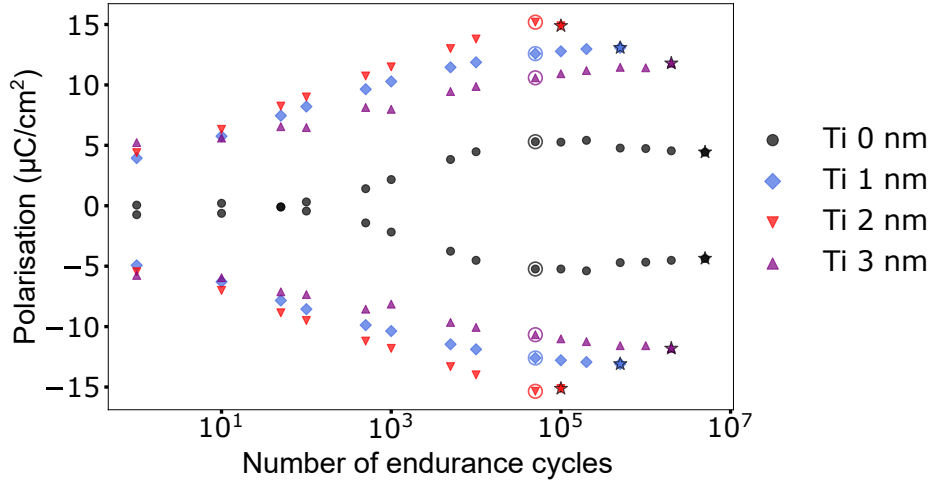


Figure V.6: Electrical characterisation of samples 0, 1, 2, and 3: endurance tests. Circles are drawn at the number of cycles at which the PUND measure was extracted, black stars indicate the breakdown point.

Table V.3 gives the values of endurance and $2P_r$ in pristine state, after $\sim 10^5$ cycles, and at electrical breakdown of samples 0, 1, 2, and 3.

Table V.3: Values of endurance, in number of cycles, and $2P_r$, in $\mu\text{C}\cdot\text{cm}^{-2}$, in pristine state, after $\sim 10^5$ cycles, and at breakdown of samples 0, 1, 2, and 3.

	$2P_r$ pristine state	$2P_r$ after 10^5 cycles	$2P_r$ at breakdown	Endurance
Sample 0 (Ti 0 nm)	0	10	9	$\sim 10^7$
Sample 1 (Ti 1 nm)	9	23	25	$\sim 10^6$
Sample 2 (Ti 2 nm)	10	25	30	10^5
Sample 3 (Ti 3 nm)	11	20	22	5×10^6

From the analysis of the presented results, we formulated an hypothesis that could explain the obtained trends for P_r and endurance as a function of the thickness of the Ti layer. A 2 or 3 nm-thick Ti interfacial layer is enough to ensure the bulk-like chemistry of titanium and titanium oxide, favouring o-phase formation through oxygen vacancy generation and providing a higher remanent polarisation. This is

true in the case of the pristine state as well. The decrease of P_r of sample 3 can be ascribed to the increased depolarising field that is induced by a thick dielectric layer. We can suppose that a 3 nm-thick Ti layer is not as beneficial as a 2 nm-thick one, as far as P_r is concerned. Furthermore, in sample 1, the Ti layer is too thin to provide the same interface conditions as in samples 2 and 3, and so to increase P_r at the value of sample 2. This might be due to the fact that a 1 nm-thick Ti layer is not enough to have the same chemical properties as bulk Ti. As mentioned, Ti scavenges oxygen from HZO, thus creating oxygen vacancies at top interface. Besides stabilising the ferroelectric phase at low HZO thickness, a high amount of oxygen vacancies is responsible for an increased leakage current that could make the specimen more fragile [172]. About the endurance, the highest value corresponds to sample 0, which can be considered satisfying for a 6-nm thick HZO film. For sample 1, we mentioned that 1 nm-thick Ti layer is not sufficient to increase P_r as for sample 2. However, it might produce more oxygen vacancies that can impact endurance, which decreases with respect to sample 0. In sample 3, a 3 nm-thick Ti layer is sufficient to efficiently scavenge oxygen from HZO film, but since the formed dielectric layer is thicker with respect of samples 1 and 2, it might result in a more resistant sample than samples 1 and 2. Eventually, for sample 2, the chemical properties of the Ti/HZO interface promote the o-phase formation and Ti layer is thin enough to limit effects of the depolarising field, compared to sample 3. Nevertheless, these benefits could be impacted by a low endurance of the sample, where an increased number of oxygen vacancies is responsible for an electrical breakdown after a low number of cycles [172].

In conclusion, these findings confirmed that the addition of a Ti interfacial layer is a very promising approach to obtain a robust ferroelectric phase in ultra-thin HZO films. However, its thickness is a crucial parameter to control, in order to avoid the degradation of the ferroelectric properties. *I-V* measurements, not here reported, were performed on these samples to test the leakage current, thus the FTJ behaviour. Despite their robust ferroelectric properties, a negligible ON/OFF ratio was measured on samples with the Ti interfacial layer. A study on structures with the addition of a Ti interlayer at the bottom electrode/HZO interface can be found in Annex VI.5.

V.4 Aluminium Interfacial Layer

The same analyses were performed using Al instead of Ti as interfacial layer. However, the results did not reveal an improvement of HZO ferroelectricity, but rather a degradation. Table V.4 lists the values of remanent polarisation of four samples with the structure $n^+Si/TiN/HZO/Al/TiN/Ti/Pt$, where the HZO was 6 nm-thick and the thickness of Al interlayer was 0, 1, 2, and 3 nm.

Table V.4: Values of the remanent polarisation and endurance for structures with Al interfacial layer.

Al thickness	$2P_r$ ($\mu C.cm^{-2}$)	Endurance (cycles)
Sample 0 (Al 0 nm)	10 (extracted after 5×10^4 cycles)	10^7
Sample 1 (Al 1 nm)	Not ferroelectric	NA
Sample 2 (Al 2 nm)	1.2 (extracted after 5×10^2 cycles)	10^3
Sample 3 (Al 3 nm)	6 (extracted after 5×10^2 cycles)	10^4

The findings showed that Al does not act as Ti to improve ferroelectricity of HZO thin films. This could be due to multiple factors that influence the the chemistry of Al/HZO interface. For instance, a less efficient redistribution of oxygen atoms and oxygen vacancies creation. A further reason could be associated to a milder mechanical strain exerted by the Al layer compared to a Ti one. The lattice parameters of Al and Ti are $\sim 4 \text{ \AA}$, and Ti $\sim 3 \text{ \AA}$, respectively. However, it was noticed that adding an Al interlayer at the top interface of a structure with an 11 nm-thick HZO layer promoted an enhancement of the $2P_r$, from $\sim 40 \mu C/cm^2$ to $\sim 44 \mu C/cm^2$, and a ON/OFF ratio of 2.4 was measured [237]. A possible conclusion could be that the Al interlayer is beneficial to the ferroelectricity of thick HZO films ($\sim 12 \text{ nm}$), while the Ti one improves the ferroelectric behaviour of thin HZO ($\sim 6 \text{ nm}$). This trend can be verified in the literature [217, 218].

To conclude on effect of Ti and Al interfacial layers, different thicknesses and configurations (top or bottom interface) were tested. A beneficial effect on HZO ferroelectric properties was recorded when the interlayer was inserted at the top interface.

V.5 Tungsten Electrodes

Very good results on ferroelectricity in ultra-thin HZO were obtained with tungsten (W) electrodes. In the literature, several groups reported exceptional ferroelectric properties of HZO-based structures with W electrodes [178, 238–241]. Tungsten, as top electrode, was proved to be a very effective capping layer, providing a strong in-plane tensile strain that favours the o-phase formation in HZO. Furthermore, the lower diffusion of W atoms into the HZO film inhibits the formation of dead layers at ferroelectric/electrode interfaces. Tungsten was investigated as bottom, top, and both electrodes. Figure V.7 shows the heterostructures that were studied. Tungsten was deposited at room temperature by RF sputtering at 200 W, at a pressure of 5×10^3 mbar, and using Ar as support gas with a flow of 50 sccm. Its thickness as electrode was 50 nm. A reference sample n^+ Si/TiN/HZO/TiN/Ti/Pt was considered for comparison. The thickness of HZO was 6 nm for all the structures. For simplicity, in the following the four specimens are called TiN/HZO/TiN, TiN/HZO/W, W/HZO/TiN, and W/HZO/W.

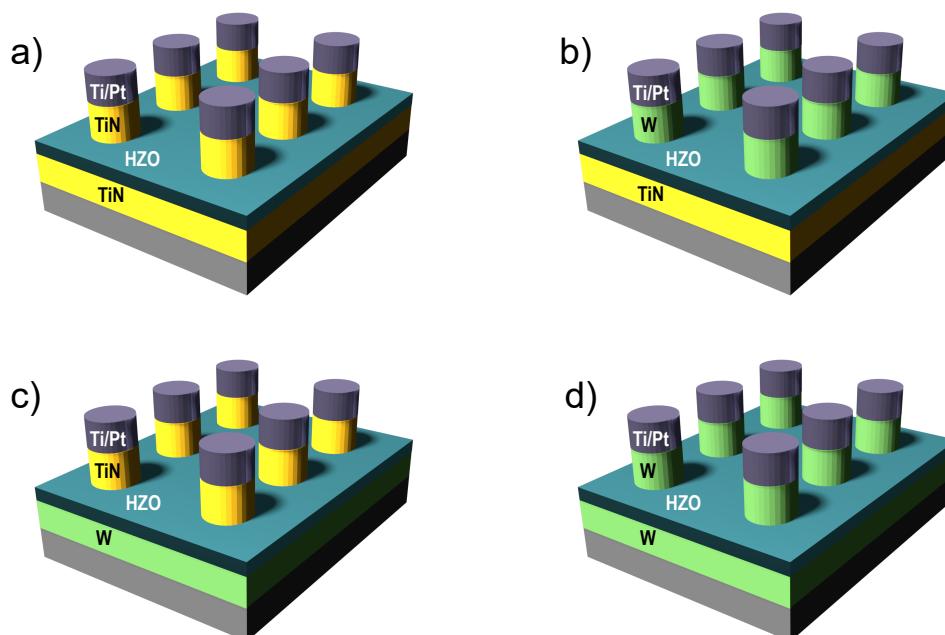


Figure V.7: Schematic of the studied samples.

V.5.1 Electrical Characterisations: PUND and I-V Measurements

PUND

The P - E curves of samples TiN/HZO/TiN, TiN/HZO/W, W/HZO/W, and W/HZO/TiN, are shown in figure V.8. The $2P_r$ of sample TiN/HZO/TiN is $\sim 4 \mu\text{C}/\text{cm}^2$. It is notably higher for samples TiN/HZO/W and W/HZO/W, for which it is $\sim 30 \mu\text{C}/\text{cm}^2$, and $\sim 40 \mu\text{C}/\text{cm}^2$ respectively. On the contrary, the $2P_r$ does not reach $1 \mu\text{C}/\text{cm}^2$ in the case of sample W/HZO/TiN. Sample TiN/HZO/TiN is characterised by the largest coercive field (E_c), $\sim \pm 1.5 \text{ MV}/\text{cm}$. E_c values of samples TiN/HZO/W and W/HZO/W are $\sim \pm 1 \text{ MV}/\text{cm}$ and $\sim \pm 0.8 \text{ MV}/\text{cm}$, respectively. An imprint was detected in TiN/HZO/TiN and TiN/HZO/W specimens. For the former, the imprint could be induced by structural and chemical differences between the bottom and top interfaces, such as different surface terminations and atomic arrangement (reference to section III.4.1). For the latter, a shift towards higher values of E_c of the P - E loop is most likely associated with different work functions of bottom and top electrodes (reference to sections IV.3.2 and V.3.2).

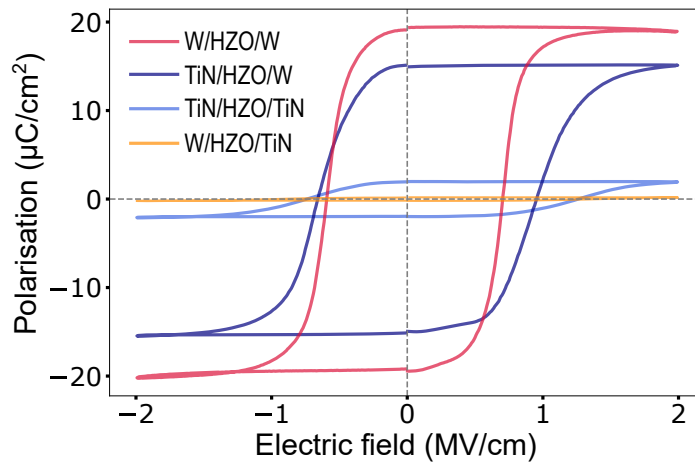


Figure V.8: P - E measurements of the four samples: TiN/HZO/TiN extracted at 10^5 cycles, TiN/HZO/W extracted at 10^4 cycles, W/HZO/TiN extracted at 10^5 cycles, and W/HZO/W extracted at 10^4 cycles.

The evolution of the polarisation as a function of the applied voltage cycles of samples TiN/HZO/TiN, TiN/HZO/W, W/HZO/W, and W/HZO/TiN is reported in figure V.9. Sample TiN/HZO/TiN is characterised by the highest value of endurance, 5×10^6 cycles. Instead, for samples TiN/HZO/W and W/HZO/W the electrical breakdown occurs at 5×10^5 and 10^4 cycles, respectively. Sample W/H-

ZO/TiN breaks down at $\sim 10^5$ cycles. Contrary to TiN/HZO/TiN, the TiN/HZO/W and W/HZO/W heterostructures show ferroelectricity in their pristine state. However, they are characterised by a significant wake-up compared to TiN/HZO/TiN sample. For TiN/HZO/W, P_r reaches its maximum after 10^4 cycles. Finally, sample W/HZO/TiN depicts an incipient ferroelectric behaviour with an undetectable wake-up before electrical breakdown occurs.

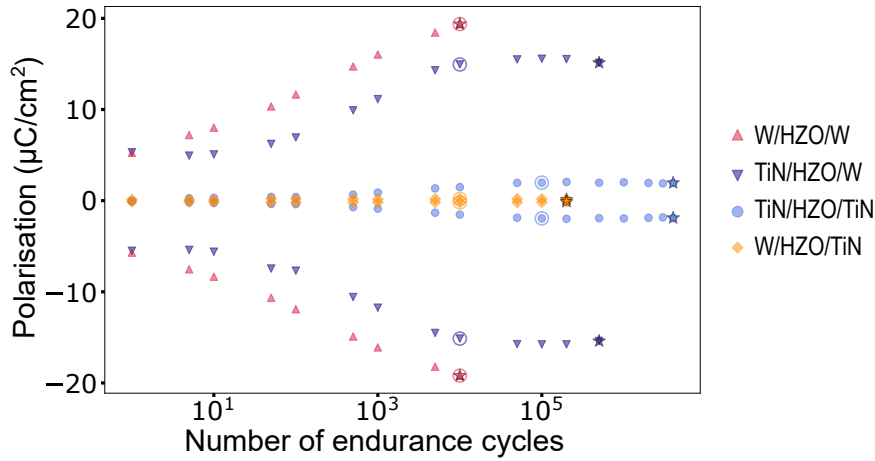


Figure V.9: Endurance tests performed on samples: TiN/HZO/TiN, TiN/HZO/W, W/HZO/TiN, and W/HZO/W. Circles are drawn at the number of cycles at which the PUND measure was extracted (where the P_r was at the maximum), black stars indicate the breakdown point.

I-V Measurements

For sample W/HZO/W, it was possible to measure an ON/OFF ratio and demonstrate the FTJ behaviour. Static I - V measurements were carried out on pristine capacitors according to the following protocol. A first I - V , back-forth, was performed from 0 V to -2 V to polarise the device. Afterwards, two I - V (back-forth) between 0 V to 2 V and other two between 0 V to -2 V were applied alternatively. The first segment, between 0 V and 2 V, was used to measure the conductance of the device in a polarisation state opposite with respect to the current one. The polarisation was then switched during the segment 2 V - 0 V. The second I - V was used to verify that the measured hysteresis did not depend on the previous state of the device. Figures V.10a and b show the two first I - V for positive and negative voltages. It is noticeable that in first segment (0 V to 2 V, in blue) in figure V.10b and a, the current is lower in the region below 1 V than in segment 2 V - 0 V. On the contrary, the second I - V (in red) does not show any hysteresis and superimposes to

the second segment (2 V - 0 V) of the first I - V . This trend, suggest that the device behaved as a FTJ and an ON/OFF ratio was calculated (inset in figures V.10a and V.10b)). For negative voltages, the ON/OFF ratio is maximum at -0.7 V, with a value of 2, and for positive voltages, it reaches a maximum of 2.5 at 0.5 V. Five alternate I - V measurements were performed for positive and negative voltages to test the reproducibility of the results. The extracted ON/OFF ratios are reported in figure V.10c and d, respectively. The ON/OFF ratio is better reproduced in the case of negative voltages, while for positive voltages it decreases, from red to blue curve, as the number of applied I - V tests increases. The values of the ON/OFF ratio could be limited by the endurance of the sample, which underwent electrical breakdown before a complete wake-up.

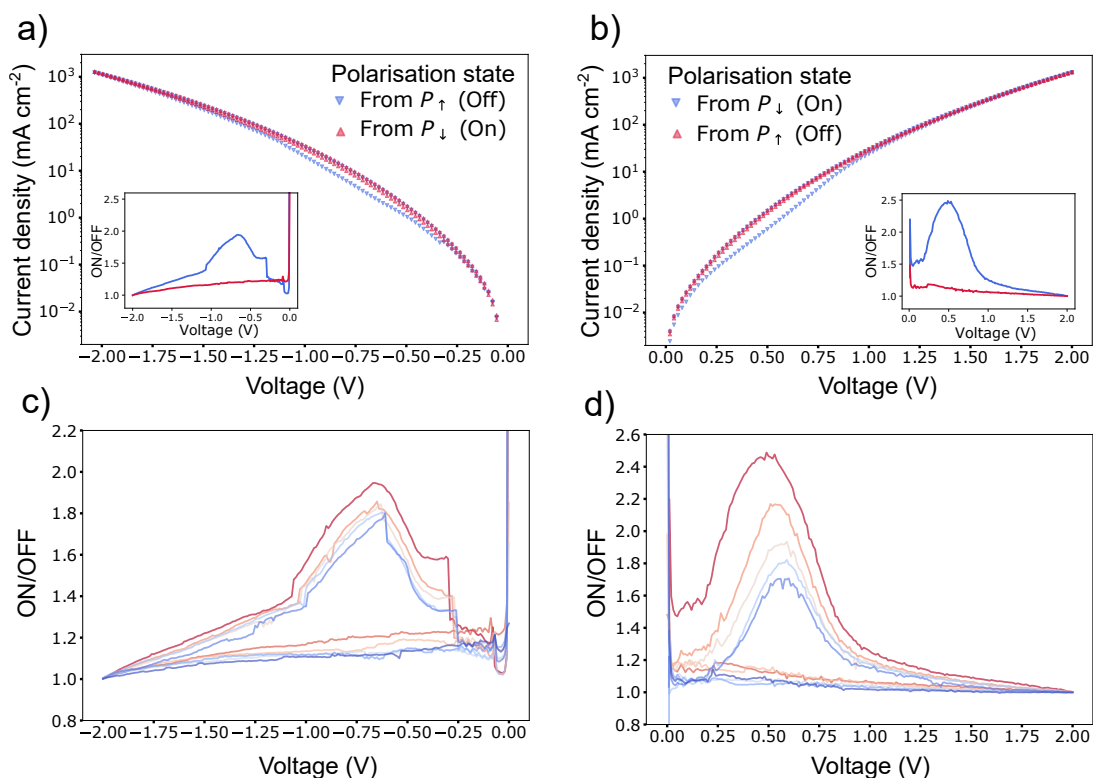


Figure V.10: a) I - V curves for negative applied voltage, inset shows the maximum value of ON/OFF ratio. b) I - V curves for positive voltage, inset shows the maximum value of ON/OFF ratio. c) Extracted ON/OFF ratio for I - V measures performed at negative applied voltage. d) Extracted ON/OFF ratio for I - V measures performed at positive applied voltage.

V.5.2 Structural Characterisations: GI-XRD, EELS, and HR-TEM

Structural and chemical analyses were performed at different lengthscales, using GI-XRD for the whole stack, STEM-EELS for individual interfaces, and HRTEM for

the HZO film. This multiscale approach was performed to study the HZO/electrode interfacial characteristics and the nanostructure of HZO.

GI-XRD

Figure V.11 shows the GI-XRD patterns and the fits of the four specimens. For samples TiN/HZO/TiN, TiN/HZO/W, and W/HZO/W, the position of o-peak at $\sim 30.5^\circ$, corresponding to o-HZO(111) planes, coincides with the expected value [144]. For the four structures a monoclinic component is detectable at $\sim 35.5^\circ$ (m-HZO(200)), while the reflections m-HZO(11-1) ($\sim 28.4^\circ$) and m-HZO(111) ($\sim 31.6^\circ$) are absent.

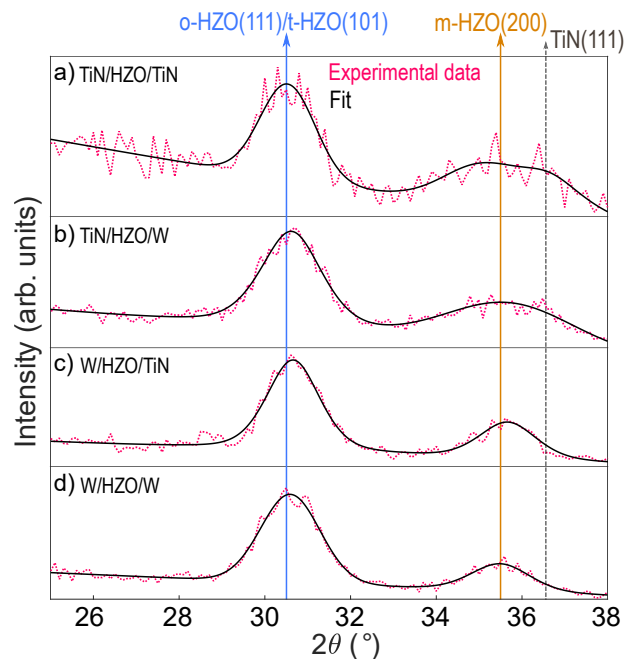


Figure V.11: GI-XRD pattern and fit of samples -from top- TiN/HZO/TiN, TiN/HZO/W, W/HZO/TiN, and W/HZO/W.

Finally, HZO o-/t-peak at $\sim 30.5^\circ$ was used to evaluate the average o-HZO out-of-plane crystallite size, reported in table V.5. Samples TiN/HZO/W and W/HZO/W are characterised by smaller crystallites of ~ 4.9 nm compared to samples W/TiN/HZO and TiN/HZO/TiN, for which the average crystallite size is ~ 5.7 nm and ~ 5.4 nm, respectively.

EELS

The microstructure and chemistry of the interfaces were investigated at high resolution using STEM-EELS on $10 \mu\text{m}$ -diameter pristine capacitors. Figure V.12

Table V.5: Average o-phase out-of-plane crystallite size of the studied structures.

Structure	o-HZO crystallite size (nm)
n ⁺ Si/TiN/HZO/TiN/Ti/Pt	5.4
n ⁺ Si/TiN/HZO/W/Ti/Pt	4.9
n ⁺ Si/W/HZO/TiN/Ti/Pt	5.7
n ⁺ Si/W/HZO/W/Ti/Pt	4.9

reports the evolution of the O-K edge along the cross-section bottom electrode (BE)/HZO/top electrode (TE), shown in the HAADF image, of the four studied structures. The O-K edges, in figures V.12a, c, e, and g, were extracted from the bottom interface, top interface, HZO, and from TiN for samples TiN/HZO/TiN, TiN/HZO/W, and W/HZO/TiN. Corresponding contour plots of the projected O-K edge intensity along interfaces are shown in figure V.12b, d, f, h. For the structure TiN/HZO/TiN (figure V.12a, b), the presence of an O-K pre-edge in HZO at bottom and top interfaces is in contrast with the center of the HZO film, where the edge onset is sharper and without pre-edge peaks. The similarity of the O-K near-edge fine structure (ELNES) at the bottom and top interfaces suggests that the chemistry is similar at both interfaces. The coexistence of N-K, Ti-L_{2,3}, and O-K edges over few nm at bottom and top interfaces indicates oxidation of TiN into TiN(O) [158, 242], which is in agreement with earlier reports that the O-K pre-edge features suggest the presence of defects, such as oxygen vacancies in HZO, HfO₂, or ZrO₂ [68, 224, 225, 227, 243]. The same O-K edge fine structure variations are observed at the TiN/HZO interfaces in samples W/HZO/TiN (figure V.12c, d) and TiN/HZO/W (figure V.12e, f). However, the difference between the W/HZO and TiN/HZO interfaces is remarkable, as highlighted in the extracted edges V.12c, e, and in the contour plots in figure V.12d, f. The O-K ELNES in HZO at W/HZO interface is comparable to the centre of the HZO film and fades once W is reached. This observation indicates that the creation of oxygen vacancies in HZO at the W/HZO interface is much less prominent than at the TiN/HZO interface. Similar conclusions are reached for the sample W/HZO/W. The fine structure of the O-K edge, which reflects the local electronic structure around oxygen atoms, of the HZO layer is characterised by two distinct peaks, lightblue line in figures V.12a, c,

e, g. These are due to metal e_g - t_{2g} splitting of the Hf $5d$ bands [224, 244]. The ratio between high-energy peak (~ 537 eV) and low-energy peak (~ 533 eV), and the peak splitting differs for each specimen. Samples TiN/HZO/W and W/HZO/W are characterised by a lower peak ratio and a distinct splitting. On the contrary, a higher peak ratio and less defined peak splitting mark structures TiN/HZO/TiN and W/HZO/TiN. The latter features can be associated with a oxygen-deficient HZO [152, 245]. In conclusion, TiN as a top electrode seems to be responsible for a more efficient oxygen scavenging from the HZO layer with respect to W to electrode. This result acts as a further explanation for the appearance of a TiN(O) interlayer at HZO/TiN (TE) interface.

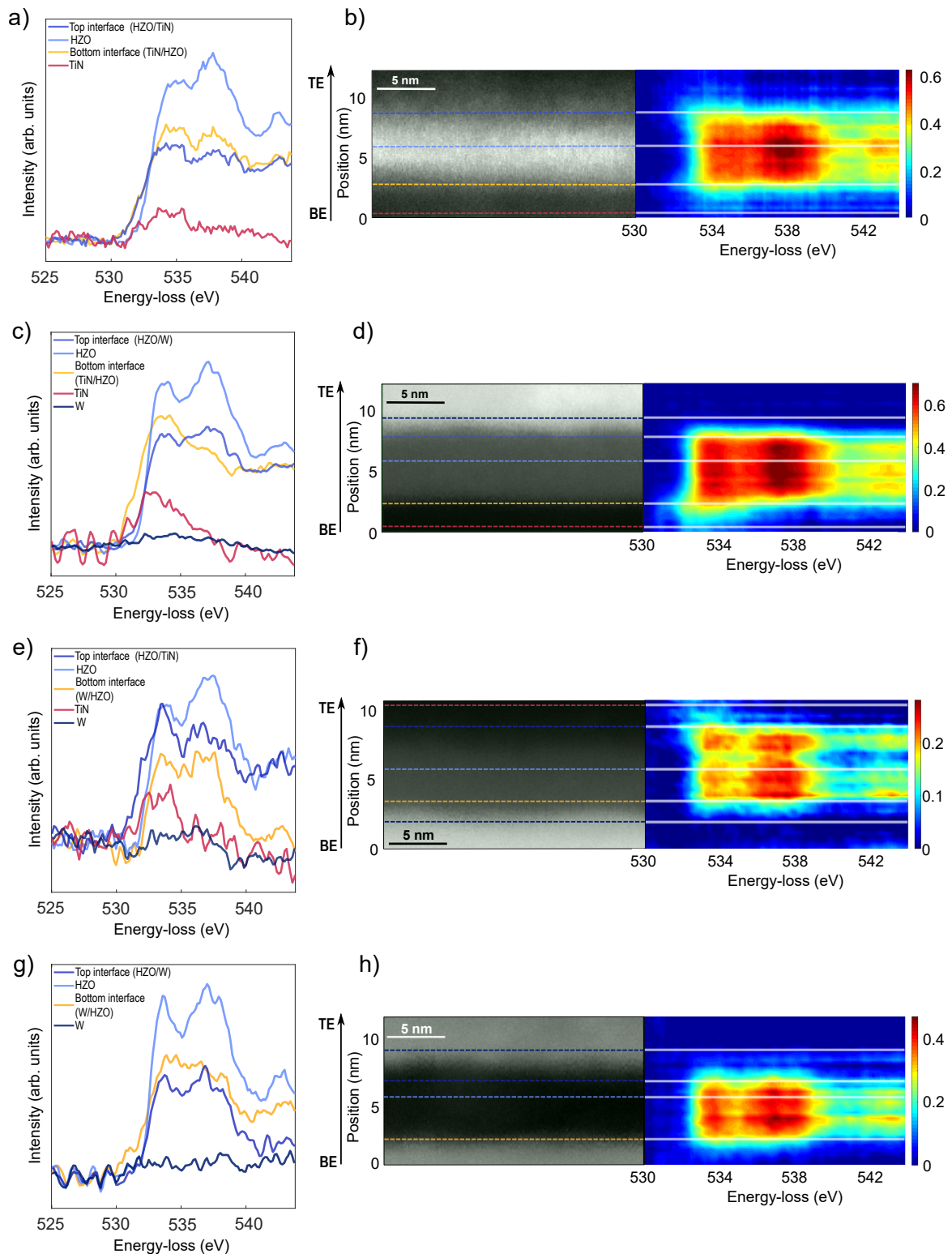


Figure V.12: EELS analysis: a) EELS O-K edge of sample TiN/HZO/TiN extracted in HZO, TiN electrode, at bottom interface, and top interface, b) On the left, STEM-HAADF image of the cross-section BE/HZO/TE, dashed color lines correspond to the positions where spectra in a) were extracted. On the right, EELS O-K edges represented as contour plot extracted along the cross-section BE/HZO/TE. c) and d) EELS analysis of sample TiN/HZO/W. e) and f) EELS analysis of sample W/HZO/TiN. g) and h) EELS analysis of sample W/HZO/W.

HR-TEM

HR-TEM was employed to investigate the nanostructure of the cross-section BE/HZO/TE and the local in-plane crystallite size of the HZO layer. HR-TEM images of structures TiN/HZO/TiN, TiN/HZO/W, W/HZO/TiN, and W/HZO/W are displayed in figures V.13, b, c, and d, respectively. Samples TiN/HZO/TiN, and W/HZO/TiN are characterised by larger in-plane crystallite size, figures V.13a, c, compared to samples TiN/HZO/W and W/HZO/W, figures V.13b, d. The contours of the crystallites are marked with dashed red boxes in figure V.13d. The latter samples are also characterised by a smaller out-of-plane average crystallite size with respect to the other two specimens, determined by GI-XRD and shown in table V.5. Large in-plane and out-of-plane crystallite sizes seem to be correlated with poor ferroelectric performances, which were discussed in section V.5.1. In the literature, it has been shown that large crystallites negatively impact the ferroelectricity in HZO-based structures [144]. Regarding the electrodes/HZO interfaces, the W/HZO interface appears sharper than the TiN/HZO interface, where the interfacial layer is more evident (see figure V.13b, c). This observation corroborates the evolution of the O-K edge fine structures (Figures V.12c, e), which confirms the low oxidation of the W electrode at the W/HZO interface.

This study revealed the importance of chemistry and structure of interfaces on the ferroelectric properties of ultra-thin HZO films. Tungsten as top electrode guarantees better ferroelectric performances compared to TiN top electrode, when ultra-thin HZO films (< 7 nm) are considered. This result confirms some reports in literature [178, 233, 239–241]. Several reasons exist to explain this behaviour. W is characterised by a smaller lattice parameter (~ 3.6 Å) than TiN (~ 4.24 Å), which might induce a larger mechanical strain. Furthermore, the lower thermal expansion coefficient (TEC) of W ($\sim 4.16 \times 10^{-6} K^{-1}$) compared to the one of HZO

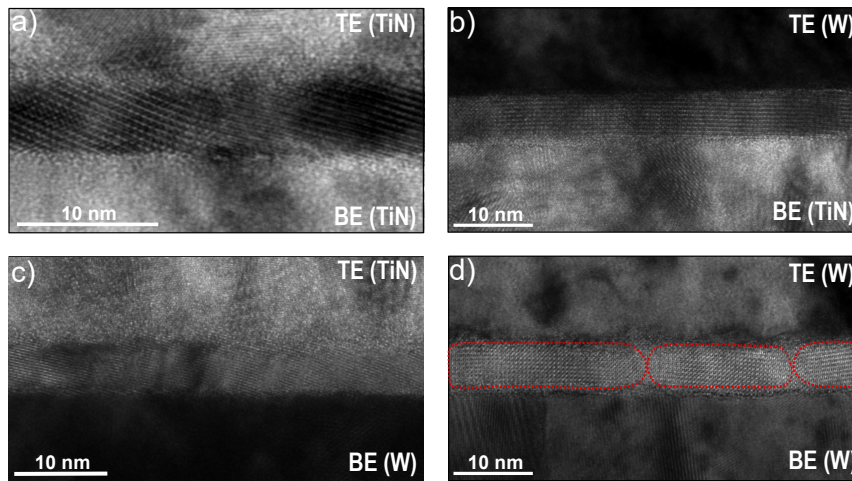


Figure V.13: HR-TEM images of samples: a) TiN/HZO/TiN. b) TiN/HZO/W. c) W/HZO/TiN. d) W/HZO/W, the red dashed boxes specifies the contours of the crystallites.

($\sim 7 \times 10^{-6} K^{-1}$) could generate a strong in-plane tensile strain on HZO layer during cooling [241]. The TEC of TiN is $\sim 8 \times 10^{-6} K^{-1}$, which is a much closer value to the TEC of HZO, hence suggesting lower induced in-plane tensile strain in HZO in the latter case. The strain components might facilitate the o-phase formation in HZO ultra-thin films [241]. An additional aspect that could contribute to the high $2P_r$ of samples TiN/HZO/W and W/HZO/W is the lower oxidation of HZO/W top interface compared to HZO/TiN one, as demonstrated by EELS. This implies a reduction of the dead-layer thickness, which is among the first causes of ferroelectricity degradation in HZO [178]. When W is used as bottom electrode, no ferroelectricity was detected. We hypothesised that W changes the nucleation of HZO o-phase from the point of view of the nanostructure. The two main reasons the could justify this hypothesis are the larger out-of-plane and in-plane crystallite size compared to the other samples, extracted from GIXRD and HR-TEM, and the small shift towards larger values of 2θ of the o-/t-peak in figure V.11. The latter aspect might indicate the predominance of HZO t-phase, since the position of the t-HZO(111) is expected at $\sim 30.8^\circ$ in the bulk [188]. Despite high value of remanent polarisation, the endurance of samples TiN/HZO/W and W/HZO/W was lower than that of TiN/HZO/TiN. This is supported by the smaller out-of-plane and in-plane average crystallite size in the TiN/HZO/W and W/HZO/W samples, extracted from GIXRD and HRTEM. Indeed, smaller crystallites suggest a higher density of crystalline boundaries between nano-grains, which could be responsible for high leakage current (figure V.10), thus enhanced fragility of samples.

V.6 Summary of the Ferroelectric Performances of the Analysed Samples

Table V.6: Summary of the ferroelectric performances of the analysed samples with a 6 nm-thick HZO layer.

Sample	Interlayer thickness (nm)	$2P_r$ ($\mu\text{C}\cdot\text{cm}^{-2}$)	Endurance (cycles)	ON/OFF ratio
TiN/HZO/TiN	NA	9 (at breakdown)	10^7	NA
TiN/HZO/Ti/TiN	1	25 (at breakdown)	10^6	NA
TiN/HZO/Ti/TiN	2	30 (at breakdown)	10^5	NA
TiN/HZO/Ti/TiN	3	22 (at breakdown)	5×10^6	NA
TiN/HZO/Al/TiN	1	NA	NA	NA
TiN/HZO/Al/TiN	2	1.2 (at 5×10^2)	10^3	NA
TiN/HZO/Al/TiN	3	6 (at 5×10^2)	10^4	NA
TiN/HZO/TiN	NA	4 (at 10^5 cycles)	5×10^6	NA
TiN/HZO/W	NA	30 (at 10^4 cycles)	5×10^5	NA
W/HZO/TiN	NA	1 (at 10^4 cycles)	10^5	NA
W/HZO/W	NA	40 (at 10^4 cycles)	10^4	2.5

V.7 Conclusion of the Chapter

Scaling down the HZO thickness without compromising its ferroelectricity is an extremely delicate task. In the previous sections two approaches were proposed. The insertion of a Ti interfacial layer and use of W electrodes were very promising to improve $2P_r$ of ultra-thin HZO films, however some issues have still to be faced. For both cases, the samples presented a non-negligible wake-up and the endurance did not match the value required by the industry, mentioned in table I.3. In this chapter, two effective ways to develop ultra-thin HZO-based devices with enhanced ferroelectric properties were shown and the FTJ-like behaviour demonstrated. The main focus of the analysis is on the extreme importance of the quality of electrode/HZO interfaces to obtain functioning devices. The structural properties of the interfaces greatly influence the HZO ferroelectricity, especially at very low thickness, where interface effects become dominant. An appropriate control over the interfacial properties is fundamental for achieving reliable HZO-based devices and for reducing the HZO thickness, for the synthesis of tunnelling

devices to be used in beyond-Von Neumann computing. In chapter VI in-memory and brain-inspired computing will be presented, together with the description of the crossbar architecture. The latter is a promising method for the integration of ferroelectric-based memristors in dense memory array for neuromorphic applications.

Advanced Applications of HZO-based Thin Films: Perspectives

This chapter gives an overview of the concept of in-memory and brain-inspired computing as solutions to overcome the limits of the Von-Neumann hardware architecture, in terms of the treatment of large amount of data. Here, preliminary results on the fabrication of crossbar matrices and protocol to demonstrate multi-state programming of devices developed throughout the thesis are presented. Finally, very first results of a study on HZO optical properties of different crystalline phases are shown. This could represent an interesting and promising perspective for the use of HZO for silicon-based optoelectronic applications.

VI.1 In-memory Computing

The recent exponential development of artificial intelligence (AI) technologies has massively increased demand of computing power for the implementation of machine learning algorithms. Simultaneously, Moore's law has significantly slowed down and classic Von-Neumann architecture is showing its inefficiency in terms of the process of large quantity of information. The latter aspects indicate that the scaling down of CMOS components is reaching its limits and novel hardware architectures beyond Von-Neumann have to be explored. The Von-Neumann ar-

chitecture physically dissociates the memory unit and process unit, consequently the data have to be transferred from one to another when the computational tasks occur. For certain applications, among which AI systems, this feature constitutes a constraint in terms of latency and energy cost. A solution is offered by in-memory computing, which allows to store data and perform certain computational tasks in the same physical site, thus entirely eliminating latency, figure VI.1. The computations are performed by exploiting the physical properties of memory components, i.e. non-volatile resistance states of memristors, their array-level organisation, logic control, and peripheral circuitry. This approach consistently improves also the time consumption and the efficiency of certain operations, by exploiting the parallelism offered by arrays of millions of nanoscale memory devices serving as computing units.

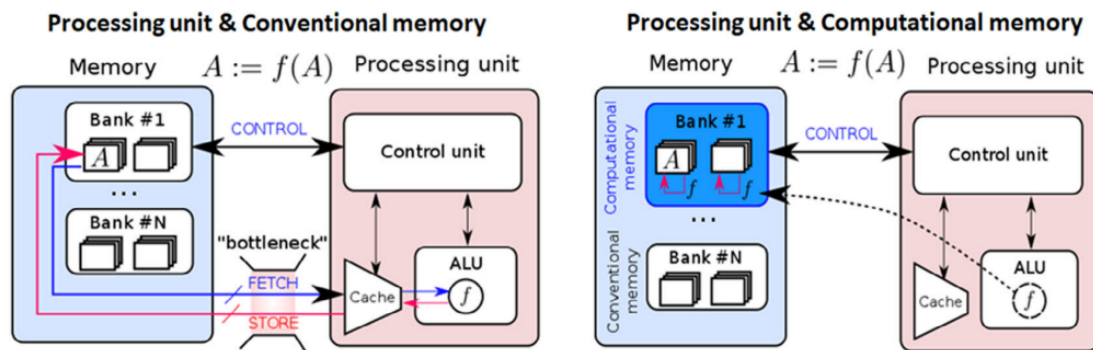


Figure VI.1: Schematic of the working principle of in-memory and conventional computing. In conventional computing if an operation f is performed on data D , D has to be moved into a processing unit. In in-memory computing, $f(D)$ is performed within the computational memory unit, through exploitation of physical properties of memory devices. *Reprinted from "Memristors: From In-Memory Computing, Deep Learning Acceleration, and Spiking Neural Networks to the Future of Neuromorphic and Bio-Inspired Computing", Mehonic et al., Advanced Intelligent Systems, 2020.*

The peculiar physical properties of memristors make them extremely promising as memory units for in-memory computing. The high resistance state (HRS) and low resistance state (LRS) could represent logic states "0" and "1", respectively. Moreover, certain memristive devices can be programmed in a continuum of states to allow analog storage. Memristors can be programmed into a desired resistance state upon the application of certain pulse schemes of a specific order and amplitude. This characteristic is fundamental for artificial neural networks (ANNs) training. Furthermore, in-memory computing can greatly reduce the complexity

of the matrix vector multiplications (MVM), briefly described in section VI.2, at the basis of ANNs working principle.

VI.1.1 Brain-inspired In-memory Computing

In-memory computing with memristors would be a turning point solution to reduce the power consumption requested by ANNs trainings in brain-inspired computing. ANNs significantly evolved over the past years and can be classified in three generations according to the characteristic neural transfer function, as it is schematised in figure VI.2 [246]. The first generation neurons, which are called perceptrons, had a step function response to the neuronal input. Deep neural networks (DNNs) are based on the second generation neurons, which rely on a continuous neuronal output with non-linear characteristic functions, such as the *Rectified Linear Unit* (ReLU). Finally, the third generation neurons, on which spike neural networks (SNNs) are based, are characterised by a bio-plausible neural behaviour [247] and communicate through discrete spikes.

Below a brief description of DNNs and SNNs is given, together with a simple explanation of their working principle. More details can be found in the review by Mehonic *et al.* [248].

- **Deep Neural Networks (DNN)**

Are made of parallel process units, neurons, connected by plastic synapses. The weight of synapses is tuned, i.e. programming the state of resistance, by millions of labelled examples. These kind of networks are trained by supervised learning algorithms and are demonstrated to perform extremely well certain supervised learning tasks. During the training, inputs are forward propagated throughout the neuron layers, meanwhile the synaptic networks perform multiply accumulate operations. The results of the final neuron layer are compared with the inputs and the errors are back propagated. The synaptic weight is then updated to reduce these errors. With modern hardware architectures, the movements of millions of synaptic weights from process to memory units is the cause of a performance bottleneck, thus in-memory computing is explored as solution to overcome this issue. The in-memory approach consists of mapping the neuron layers into a memory computing unit, where the memristive devices are organised according to a

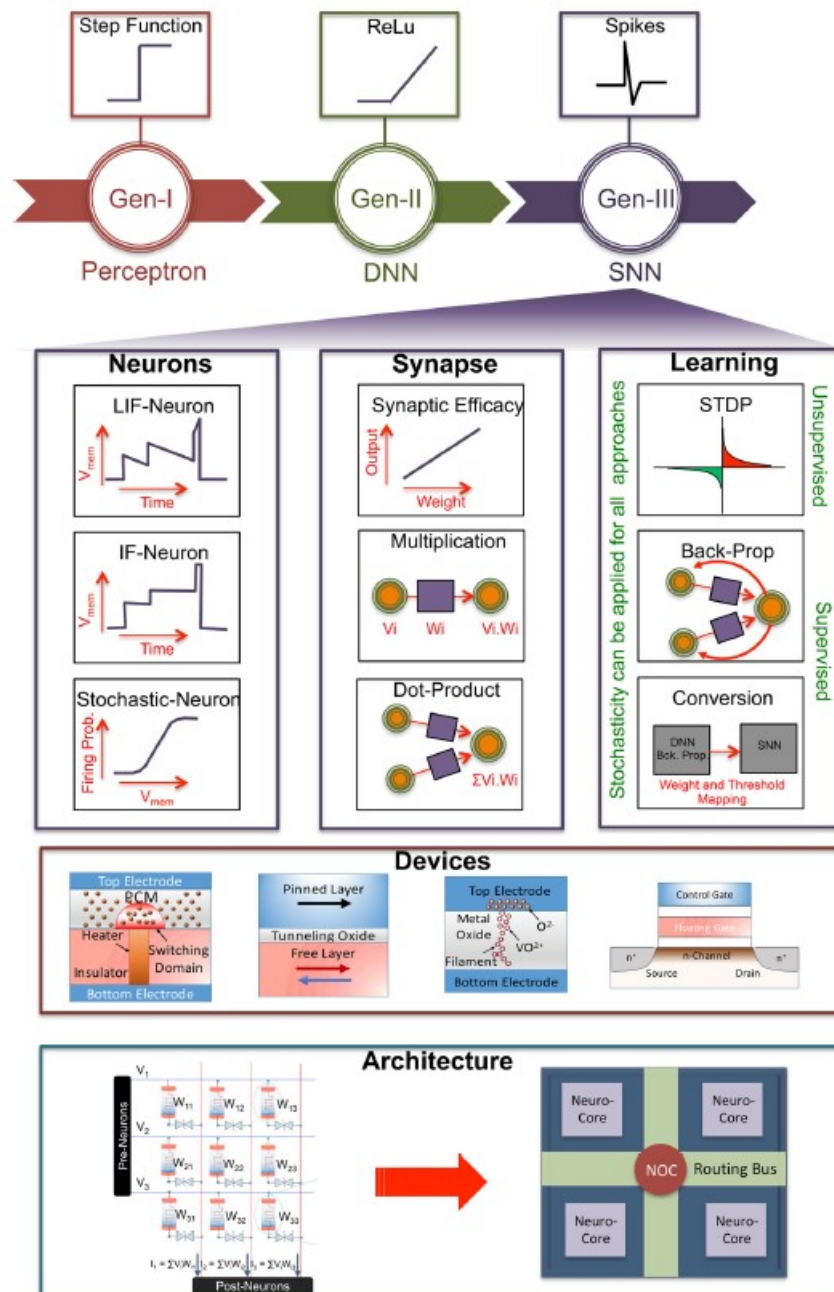


Figure VI.2: The three generation of neural networks. The first generation (Gen-I) uses a step transfer functions. The second generation (Gen-II) uses non-linear transfer functions such as ReLU. The third generation (Gen-III) uses the spiking behaviour of biological neurons. The three components of SNNs are neurons, synapses, and learning, which can be supervised or unsupervised. *Reprinted from "Pathways to efficient neuromorphic computing with non-volatile memory technologies", Chakraborty et al., Applied Physics Reviews, 2022.*

crossbar configuration, described in section VI.2. The synaptic weights are stored in the resistance state of the memristor, and data propagation is carried out by input the data to the crossbar array rows and deciphering the results at the columns through MVMs. However, challenges related to this approach are the inaccuracies linked to programming of memristors into a

certain synaptic weight, the drift, and the noise associated to the conductance values. Figure VI.3 shows a schematic of DNN working principle for image recognition.

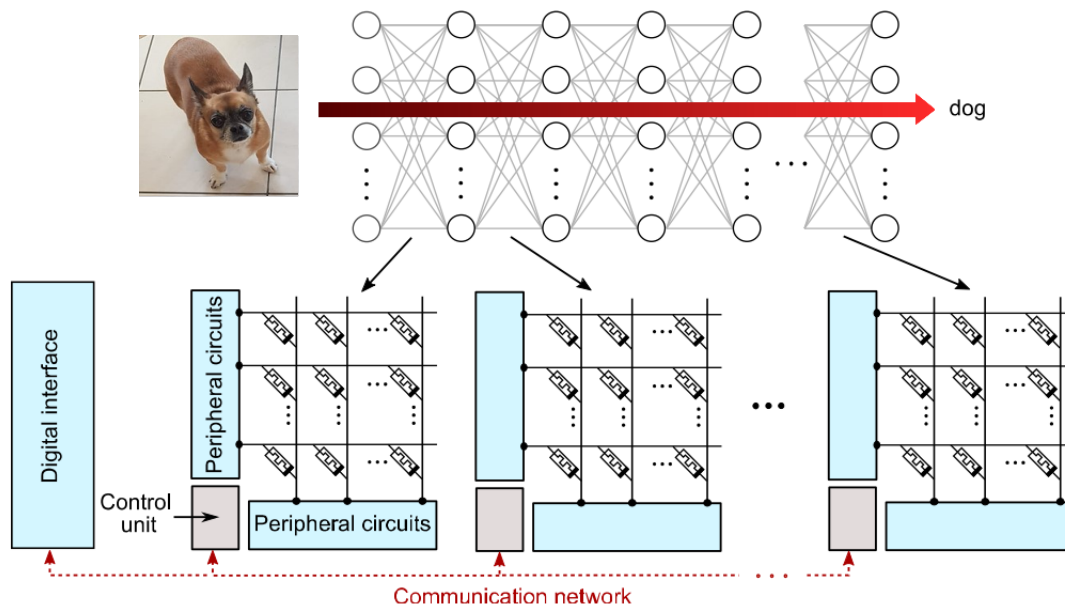


Figure VI.3: Example of DL based on in-memory computing. The various layers of a neural network are mapped into a computational memory unit where memristive devices are integrated in a crossbar structure. Synaptic weights are stored in the conductance state of the memristive devices. A common communication network is used to send data from one array to another. *Reprinted from "Memristors: From In-Memory Computing, Deep Learning Acceleration, and Spiking Neural Networks to the Future of Neuromorphic and Bio-Inspired Computing", Mehonic et al., Advanced Intelligent Systems, 2020.*

- **Spike Neural Networks (SNN)**

Are modelled on integrate-fire behaviour of neurons in the brain. According to this model, the neurons communicate between each others through binary signals or spikes. When a spike arrives to a synapse, it triggers a current flow into the post-synaptic neuron, with a magnitude of the current weighted by the effective conductance of the synapse. The latter current is integrated by the neuron to determine its membrane potential and a spike is issued when it exceeds a certain threshold. SNNs can be integrated into CMOS processes and the use of memristive devices could consistently increase the computational efficiency. Indeed, memristors that represent the synaptic weight can be organised in a crossbar configuration and the CMOS circuitry at the periphery can be designed to implement neuronal integration and learning

logic. Currently, several devices have been explored for the realisation of neuronal integration and firing characteristics, however there exists only a few proofs of concept all-memristor SNNs.

Despite memristors represent an highly promising approach for in-memory and brain-inspired computing, thanks to their stable non-volatile resistance state, fast resistance switching, and excellent energy efficiency, there are still some challenges related to their fabrication and integration that need to be faced. These are mainly related to device reliability, fabrication, uniformity, and scalability. One of the main issues of memristive technologies is non-linearity in current/voltage characteristic, due to the leakage currents. This non-linear dependence of output current from input voltage prevents accurate matrix-vector computations. A further issue concerns the device-to-device variability proper to nanoscale devices. For this aspect, it is crucial to improve the material engineering and optimisation of the device structure, including oxide/metal interfaces, and oxide microstructure that are the focus of this thesis. This would lead to a great improvements in the stability of operating characteristics. Finally, it is worthy to mention that, at the current state, most of non-idealities that characterise memristors are studied on the single devices or small arrays, and consequently a great work has still to be done for more extensive reliability studies for memristors to gain full maturity.

VI.1.2 Ferroelectric Memristors for Brain-inspired Computing

Ferroelectric-based memristors exploit partial polarisation switching of their domains to achieve multiple intermediate polarisation states and they can serve as synaptic weight cells for neural networks. The literature offers various examples of use of ferroelectric-based devices for the implementation of brain-inspired computing [133, 249, 250]. Here, few works are reported, with a special focus on FTJs. Berdan *et al.* [251] presented low-power linear computation using FTJs crossbar, where the tunnel barrier was made of 4 nm of Si:HfO₂. They demonstrated a linear vector multiplication at ultra-low current in a 5 × 5 crossbar array. Ultra-low current computations would open the possibility of integration of large arrays in hardware and enable neural networks operation in the range of hundred of tera-operations per second per watt. A further example of FTJ-based crossbar structure is given by Luo *et al.* [134]. They evaluated performances of a

1024 × 1024 array using as memory devices Al₂O₃/HZO-based FTJs, where Al₂O₃ tunnel barrier was modulated by the polarisation switching of HZO. Finally, Zhu *et al.* [135] fabricated a crossbar array of HZO-based capacitive synapses with ultra-low weight updating energy for the image reconstruction, highlighting the great potential of ferroelectric-based memristive arrays for high-efficiency neuromorphic systems. Contrary to the conventional linear memristors, tunnelling devices are characterised by a non-linear *I-V* behaviour, but they operate at very low current, offering possibility to further reduce the power consumption. Upon the linearisation of the *I-V* characteristic, FTJs provide ultra-low conductance and operating current and enable selectorless crossbar array. Indeed, in linear resistive memories arrays, the leakage current has to be blocked by a selector or a transistor in series to the memory device. In non-linear FTJs, the high difference between currents biased with a different voltage eliminates the need of selectors. This aspect further increases the interest for FTJs in this fast-developing field.

VI.2 Crossbar Architecture

This section is dedicated to the presentation of the crossbar architecture and of the fabrication procedure that was used to synthesised HZO-based crossbar arrays. Figure VI.4 shows an example of a crossbar configuration. At each cross point, the current is the product of the input voltage and conductance ($I=GV$) of the memristor, according to the Ohm's law for multiplication. At each column, the total current is the sum of the currents at each cross point according to Kirchhoff's current law. The latter operations implement a vector matrix multiplication that is the basis for computation in ANNs, but very resource-expensive for traditional computing systems.

In the frame of this thesis, the fabrication of crossbar matrices was carried out by sputtering, UV photolithography, and rapid thermal annealing by following a recipe developed at RMIT. Three lithography masks, optimised for a 3 inches wafer, were used for the synthesis of bottom electrode, HZO, top electrode, and protective conductive layer. The substrate used for the growth was i-Si(100)/SiO₂, the oxide being 200 nm-thick. The procedure followed for the fabrication of crossbar samples is illustrated below.

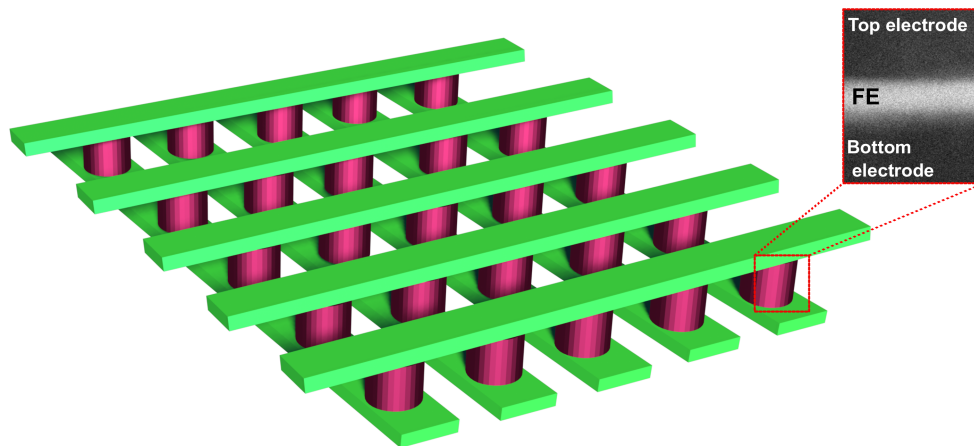


Figure VI.4: Schematic of the crossbar architecture.

1. Cleaning of the substrate in acetone and ethanol
2. Dehydration bake at 120 °C
3. Application of positive photoresist AZ5214
4. Soft bake at 90 °C
5. UV exposure
6. Post-exposure bake at 120 °C
7. UV flood exposure
8. Development to remove the photoresist
9. Deposition of TiN bottom electrode
10. Lift-off in acetone
11. Alignment of mask for the deposition of HZO
12. Repetition of procedure of steps 1-9
13. Alignment of mask for the deposition of TiN top electrode and Pt conductive layer
14. Repetition of procedure of steps 1-9

The TiN bottom and top electrodes were 50 nm-thick, the HZO layer was 12 nm-thick, and the Pt conductive layer was 100 nm-thick. The synthesis of crossbar

samples was carried out only at the end of the project, so to test the fabrication procedure a reference HZO thickness of 12 nm was chosen. Figure VI.5a shows the image taken by optical microscope of a series of memristors, where the squares represent the electrical contacts. The top electrode is characterised by the lighter color, given by the Pt layer deposited onto the TiN top electrode. Figure VI.5b reports a detail of a single memristor, where the HZO layer is distinguishable as the square in the middle of the cross made by the bottom and top electrodes, which are 5 μm in width. Finally, figure VI.5c shows the crossbar structure, where vertical lines represent the bottom electrodes and the horizontal lines the top ones. In this case, the bottom and top electrodes are 10 μm -wide. Figure VI.6 shows the image of a finished sample.

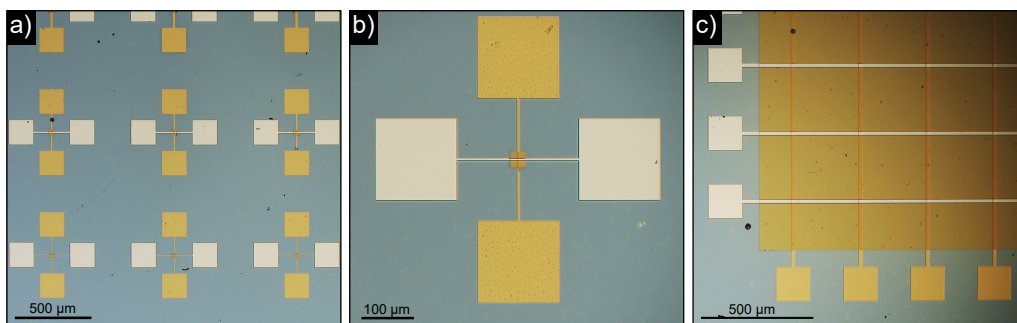


Figure VI.5: Images taken by optical microscope that show details of: a) a series of memristors. b) A single memristor. c) A Crossbar array.

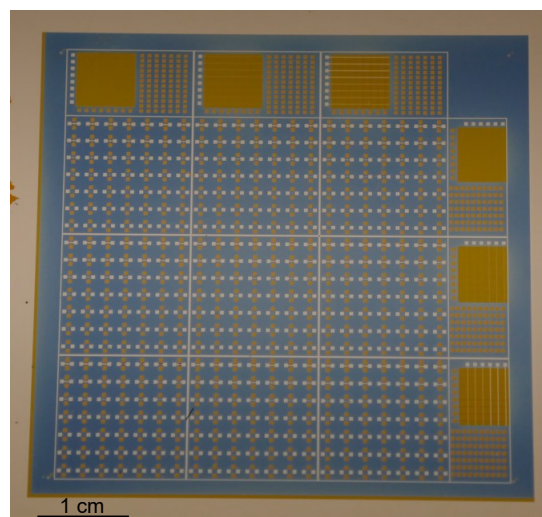


Figure VI.6: Image taken by optical microscope of a crossbar sample.

VI.3 Multi-state Programming

One of the objectives of this thesis was the demonstration of the usability of the here synthesised structures for the emulation of certain synaptic plasticity mechanisms. In this context, few introductory test protocols for the multi-state programming of the ferroelectric polarisation were developed. The measurements were carried out on a the reference structure with a 12 nm-thick HZO layer and on $10\mu\text{m}$ -diameter capacitors by means of the probe station described in section III.4.1. At first, the possibility to program at least ten states of polarisation was tested. The procedure consisted on the application of a single writing pulse at time and the aim was to switch the polarisation between 0 and 1, where 0 represents a null fraction of switched polarisation and 1 a full polarisation switching, with a step of 0.1. Figure VI.7a shows the fraction of switched polarisation as a function of the pulse duration, for a fixed positive voltage of 1.66 V (on the left) and a fixed negative voltage of -1.36 V (on the right). Figure VI.7b report the same measure performed by fixing the pulse duration at $10\mu\text{s}$ and varying the applied voltage between -4 V and 0 V (on the left) and 0 V and 4 V (on the right). The measurements were repeated five times to test the reproducibility of the results, which was confirmed by the superimposed and well distinguished coloured dots in figures VI.7a and b.

A second approach that was explored consisted on the application of multiple identical pulses with the aim of emulating the potentiation/depression characteristic of the synapses. In this case, the single pulse was replaced by a series of pulses, each one with a duration of 20 ns. Figures VI.8a and b represent the polarisation switching as a function of the number of applied pulses for different writing voltages. In the case of an applied voltage of 1.6 V, after the first pulse the fraction of the switched polarisation was 20 % and after 10^5 pulses it was ~ 80 %. On the contrary, when ~ 4 V were used, the fraction of switched polarisation after the first few pulses was > 80 %, while, for a voltage of ~ 1.5 V, it did not reach the 20 % after 10^5 pulses. It is clear that for a correct control of the polarisation switching, which includes the exploitation of the maximum number of polarisation states, the duration, the shape, and the number of pulses have to be optimised.

However, it was possible to give a very first demonstration of the potentiation/de-

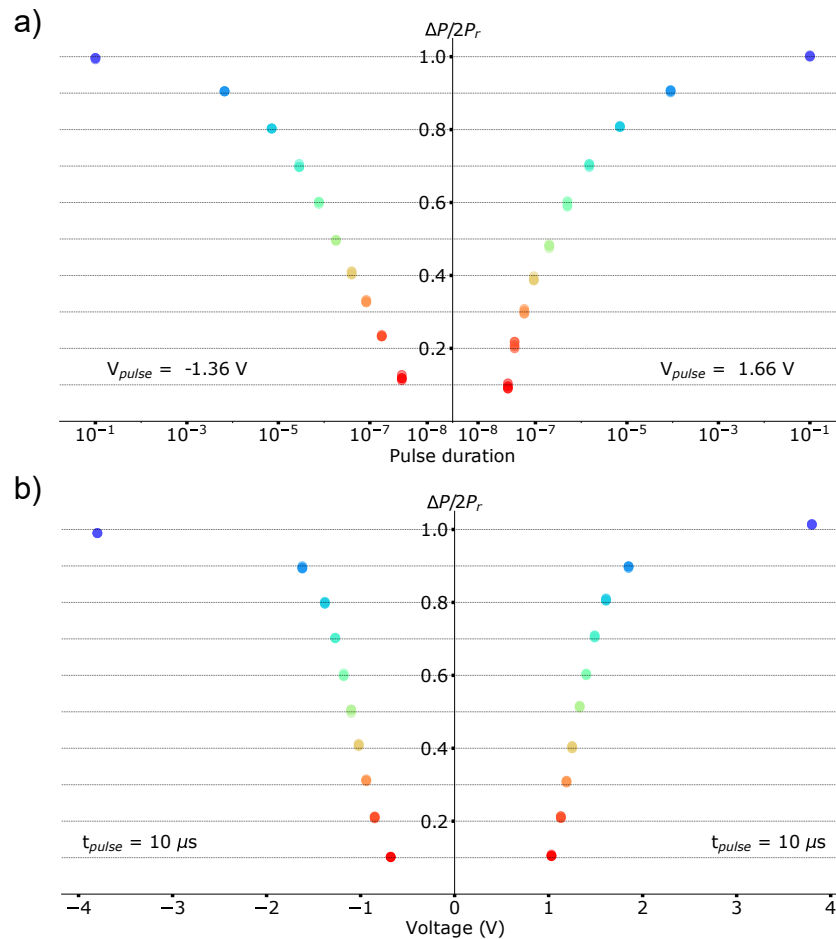


Figure VI.7: Demonstration of multi-state programming of the polarisation. a) Pulses with fixed writing voltage and variable duration. b) Pulses with fixed duration and variable writing voltage. The measurements were repeated five times.

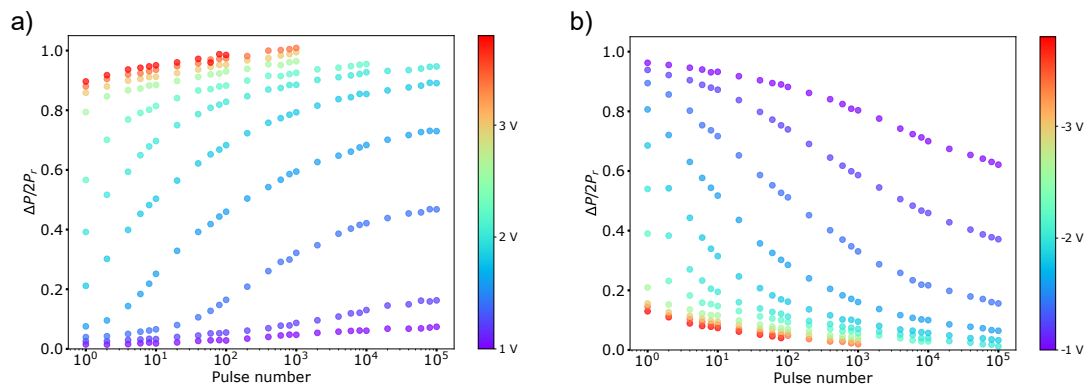


Figure VI.8: Switching of the polarisation as a function of the number of writing pulses and of the writing voltage. a) For a positive applied voltage. b) For a negative applied voltage.

pression behaviour in the here fabricated devices. Figure VI.9 shows the potentiation/depression characteristic as a function of the number of applied pulses. The curve was reconstructed from figure VI.8 by extracting the curves at 2 V and at -1.8 V.

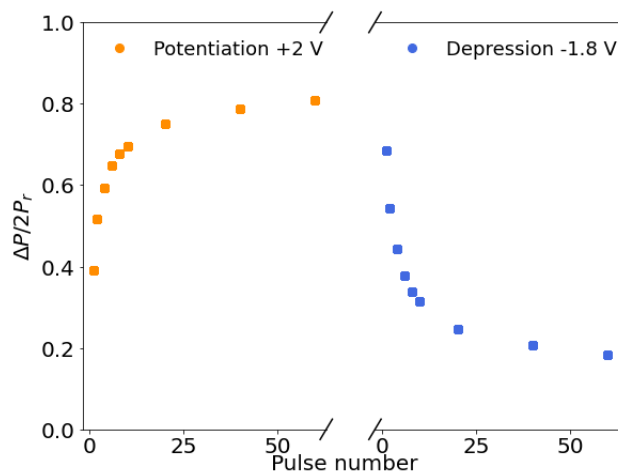


Figure VI.9: Demonstration of a potentiation/depression characteristic measured on one of the here synthesised devices.

The results presented here represent the last part of the thesis project and are only preliminary. To obtain a functioning device, further studies should be performed on optimised protocols for the implementation of synaptic plasticity mechanisms.

VI.4 Study of HZO Optical Properties for Optoelectronic Applications

Thanks to its compatibility with CMOS technology, HZO could be an interesting material also for optoelectronic applications. Probing the optical properties of HZO-based devices might open a path for the developing novel concepts to face the request of low energy consumption. In this section, preliminary experiments of the investigation of HZO optical properties are reported. The analysis is performed with the aim of studying differences in HZO optical response as a function of the crystalline phase and the orientation of the polarisation. This study, which is currently in progress, is conducted from an experimental and a theoretical point of view, in the framework of a collaboration with the University of Connecticut (UConn). The experiments are carried out by ellipsometry and valence electron energy-loss spectroscopy (V-EELS). Ab initio quantum mechanical calculations for monoclinic, orthorhombic, and tetragonal HZO phases are performed using VASP package at UConn. The density functional theory was used to calculate the refractive index, extinction coefficient, absorption coefficient, and low-energy-loss spectrum of the different HZO phases in the range 0 - 50 eV, in order to compare it

with experimental data. The ellipsometry was performed on two samples with the structure p^+Si/HZO , where HZO, synthesised by sputtering, was 27 nm-thick and 6 nm-thick, respectively. These two reference thicknesses were chosen based on the fact that, after annealing, the 27 nm-thick HZO layer shows mainly monoclinic phase, while the 6 nm-thick one is orthorhombic. The crystalline phase analysis was conducted by GI-XRD. Figure VI.10 shows the refractive index and the extinction coefficient as a function of the photon energy collected by ellipsometry on the monoclinic sample, in figure VI.10a, and on the orthorhombic one, in figure VI.10b. Preliminary DFT calculations, not reported here, showed a good match between experimental and theoretical values of the aforementioned quantities.

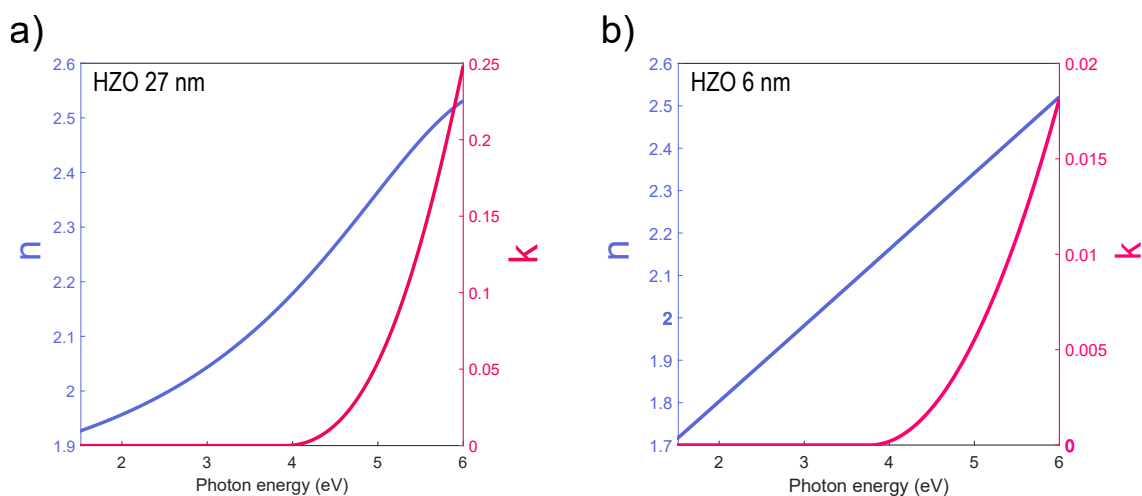


Figure VI.10: Refractive index and extinction coefficient obtained with ellipsometry on a p^+Si/HZO sample: a) HZO was 27 nm-thick, and showed a monoclinic crystal structure. b) HZO was 6 nm-thick, and showed an orthorhombic crystal structure.

Valence low-energy electron spectroscopy (V-EELS) was performed on the orthorhombic sample in the range 0 - 50 eV, in figure VI.11. From the low-loss region of the EEL spectrum, it is possible to acquire information on the electronic structure and optical properties of a material, by correlating the spatial intensity to the complex dielectric function ($\text{Im}(\epsilon)$). The obtained results are consistent to what has been reported in the literature by Guedj *et al.* and Hung *et al.* for HfO_2 [252, 253]. They simulated the low-absorption spectra of HfO_2 using time-dependent DFT. According to these works, the first shoulder at ~ 10 eV, in figure VI.11, corresponds to particle transitions between the highest valence band ($O2p$) and the lowest conduction band ($Hf5d$), like the peak at ~ 35 eV, which is ascribed to a single-particle transitions of $Hf5p$ electrons. The spectral features at ~ 13 eV

and at ~ 38 eV are representative of a bulk plasmon caused by the collective excitation of $O2p$, $Hf5d$, and $6s$ electrons, and of a local-field (LF)-damped plasmon, respectively. Finally, the features of the spectral region between 16 eV and 30 eV are attributed to the collective excitation of $Hf4f$ and $O2s$ electrons.

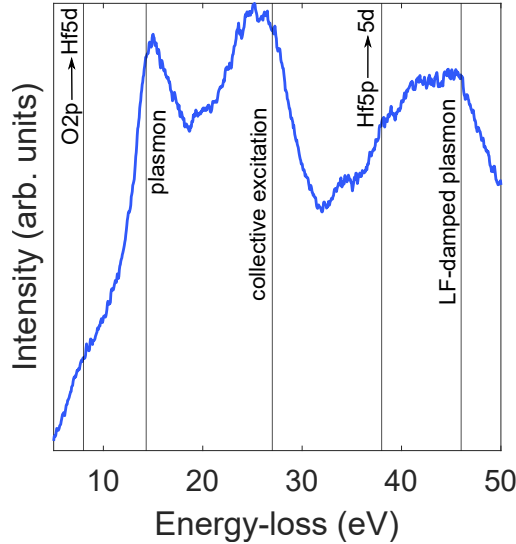


Figure VI.11: VEELS spectrum of orthorhombic HZO.

The here presented are only introductory results of a study that could be promising for opening new paths for the use of HZO as optoelectronic material, and further experiments and theoretical computations should be performed. Despite the presence of few theoretical and experimental works [254, 255], which studied the HZO optical properties, this topic has been scarcely investigated in the literature. However, the demonstration of a dependence of HZO optical response on its crystalline phase and polarisation orientation would unfold interesting ways for a fast and completely non-disruptive reading operation of HZO-based memory components.

VI.5 Conclusion of the Chapter

In-memory and brain-inspired computing were presented as solutions for the Von-Neumann memory bottleneck. For the implementation of the latter, specific hardware architectures are required in order to limit the power consumption for the process of large amount of information. This chapter gave an introduction to the fabrication of HZO-based crossbar arrays and to the multi-state programming of the devices realised in this work. The protocol used for the demonstration of

multi-state programming was described and a very first demonstration of synaptic potentiation/depression characteristic was reported. Despite the here presented results were only preliminary and not extensively developed throughout the thesis, they highlighted the possibility for the integration of HZO in crossbar structures synthesised by sputtering and the potential of these devices to mimic synaptic behaviour. Finally, an initial study of HZO optical properties was introduced as very promising for the realisation low-power optoelectronic devices, and for the use of HZO in other CMOS-compatible platforms.

Conclusion and Perspectives

To overcome the Von-Neumann memory bottleneck, new paradigms of computation and novel hardware architectures were proposed, and became object of an extensive research over the past few decades. In this context, brain-inspired computing has gain a considerable interest. The latter, which takes inspiration from the way biological networks of neuron and synapses perform computations, allows the treatment of massive amount of data at low energy cost. An extremely promising approach for the realisation of memory units in neuromorphic architectures is the memristor. In non-volatile memristors, the stable resistance corresponds to the stored information. Ferroelectric-based memristors allow non-volatile multi-level memory effect and analog storage of information, thanks to the continuum of resistance states into which they can be induced. However, one of the major challenges for the development of these kind of architectures concerns the realisation of high quality, reliable, and scalable layers of ferroelectric materials for the implementation of the single memory unit. The discovery of ferroelectricity in doped HfO_2 in 2011 opened the path for the development of a wide range of memory devices based on ferroelectric CMOS-compatible HfO_2 . Since then, HfO_2 has been used for the development of ferroelectric field-effect transistors, ferroelectric random access memory, negative capacitance field-effect transistors, and ferroelectric tunnel junctions. Different chemical substitutions and processing conditions have been explored to stabilise ferroelectric polymorphs, based on HfO_2 , in polycrystalline thin films. Among different strategies, which exploit compounds from the solid solution of the physically and chemically compatible ZrO_2 and HfO_2 ,

the Hf:Zr 1:1 substitution compound is of particular interest, due to its high polarisation value. $\text{Hf}_{0.5}\text{Zr}_{0.5}\text{O}_2$ shows robust ferroelectricity and low-temperature preparation, which is crucial for its transfer into the semiconductor-based industry. Among HfO_2/HZO -based non-volatile memory devices, ferroelectric tunnel junctions offer the possibility to perform low-current operations and to increase the device scalability for their integration into dense memory arrays. This work had as objectives the realisation, investigation, and optimisation of the structural, chemical, physical, and ferroelectric properties of ultra-thin HZO films for the synthesis of FTJs, which could be used as memory units for neuromorphic hardware architectures. In detail, we presented:

- The fabrication process by sputtering, the structural, and the electrical characterisations of $n^+\text{Si}(100)/\text{TiN}/\text{HZO}/\text{TiN}/\text{Ti}/\text{Pt}$ heterostructure, with 12 nm-thick HZO layer, that was used as a reference for this work. The structural characterisations were carried out by X-ray reflectometry, X-ray diffraction, transmission electron microscopy, and high-resolution transmission electron microscopy. The stoichiometry of the HZO was established by means of Rutherford backscattering spectrometry and the morphology of its surface was investigated by atomic force microscopy. The ferroelectricity was confirmed by positive-up-negative-down technique. Capacitance vs voltage and current vs voltage measurements were performed to evaluate the dielectric properties of the stack and the electronic conduction mechanisms through the ferroelectric layer. We demonstrated a robust ferroelectricity and the reproducibility of the results for the reference structure. Finally, the issues related to the scalability of the HZO thickness for the synthesis of FTJs were addressed.
- The study of HZO-based heterostructures characterised by decreasing HZO thickness. We showed how the ferroelectric properties evolved when HZO was scaled down to 6 nm and how they degraded when its thickness was <7 nm. For the realisation of FTJs, the synthesis of high-quality ultra-thin HZO films was crucial. For this reason, we studied different approaches in order to enhance the ferroelectric behaviour of ultra-thin HZO. As first, we studied the impact of different bottom electrode materials other than TiN, such as n-doped Si, p-doped Ge, and Pt on a 12 nm-thick HZO film. We concluded

that the best ferroelectric properties were obtained when TiN was used as bottom electrode, with a thickness of 50 nm.

- The presentation of two successful methods for the synthesis of high-quality 6 nm-thick HZO films. The first one consisted on the insertion of a Ti interfacial layer at the top electrode/HZO interface. This promoted an oxygen redistribution that contributed to a significant improvement of the HZO ferroelectricity. The second one involved the use of W as bottom and top electrode or in combination with TiN. Devices with W electrodes showed exceptional ferroelectric properties. For both studies, a particular focus was dedicated to the role played by the structural and compositional characteristics of the electrode/ferroelectric interfaces on the device performances. We underlined how crucial was the quality of the interfaces when the HZO thickness was few nm. We managed to synthesised by sputtering ultra-thin HZO layers with enhanced ferroelectricity competitive with the state of the art.
- The realisation of a FTJ based on a 6 nm-thick HZO layer with W bottom and top electrodes. We measured an ON/OFF ratio of 2.5 that was reproducible. For the optimisation of FTJs, work has still to be done to improve the endurance and minimise the wake-up effect. A future step in this direction is the further reduction of the thickness of the HZO layer, in order to enhance the tunnel contribution to the current, and thus the ON/OFF ratio.
- The description of the recipe for the fabrication of crossbar arrays and the presentation of a protocol for multi-state programming of HZO-based devices, with a very first demonstration of synaptic potentiation/depression behaviour. Finally, we presented new perspectives for a potential use of HZO in optoelectronic applications. We investigated the optical properties of HZO experimentally, by means of ellipsometry and valence electron energy-loss spectroscopy, and theoretically, by density functional theory. This study could open new ways towards the optical reading of HZO-based memory devices for a completely non disruptive and fast read-out operation.

An overview of the perspectives to continue the work presented in this thesis was given in chapter VI. The fabrication of crossbar arrays should be further investi-

gated and developed, in order to realise matrices where each HZO-based memory unit is characterised by robust ferroelectric properties. Here, we presented only one crossbar sample with TiN electrodes and a 12 nm-thick HZO layer. It would be interesting, to reduce the HZO thickness, for instance to 6 nm, and replace the TiN electrodes by W ones. However, the synthesis process of crossbar matrices requires the optimisation of various aspects, among which the crossbar size of the synaptic elements, in order to minimise non-idealities, such as device variations and non-ideal resistances. These are currently some of the main challenges related to the development crossbar architectures. A further aspect, which was only introduced in this work and which should be explored further, is the development of protocols for the demonstration of synaptic plasticity mechanisms. In section VI.3, we gave only a first evidence of the synaptic potentiation/depression behaviour of a 12 nm-thick HZO-based capacitor. A step forward could be the demonstration of the latter characteristic in FTJ devices, with a HZO thickness of 6 nm. In addition, the study of other pulse schemes for the implementation of synaptic plasticities, as spike-timing-dependent plasticity (STDP), should be investigated. Finally, the analysis of the HZO optical properties from a fundamental point of view could lead to novel platforms for the use of ferroelectric HZO in optoelectronic. Currently, this field is scarcely explored, although it should be object of further studies.

Annex A: Scientific Communications Throughout the Thesis

Articles

First Author

- Greta Segantini, Rabei Barhoumi, Benoît Manchon, Ingrid C. Infante, Pedro Rojo Romeo, Matthieu Bugnet, Nicolas Baboux, Shruti Nirantar, Damien Deleruyelle, Sharath Sriram, Bertrand Vilquin. *Phys. Status Solidi (RRL)* 2022, 16, 2100583.

Second Author

- Benoît Manchon, Greta Segantini, Nicolas Baboux, Pedro Rojo Romeo, Rabei Barhoumi, Ingrid C. Infante, Fabien Alibart, Dominique Drouin, Bertrand Vilquin, Damien Deleruyelle. *Phys. Status Solidi (RRL)* 2022, 16, 2100585.

Journal Front Page

- Special Issue: (Hf,Zr)O₂-based Ferroelectrics. *Phys. Status Solidi (RRL)*, 16, 10.

Conferences: Oral Presentations

- Greta Segantini, Pedro Rojo Romeo, Benoît Manchon, Nicolas Baboux, Rabei Barhoumi, Ingrid C. Infante, Damien Deleruyelle, Bertrand Vilquin, Sharath Sriram. *Effect of bottom electrodes on HZO thin films properties*. ISAF-ISIF-PFM 2021, IEEE International Symposium on Applications of Ferroelectrics, 2021.
- Greta Segantini, Pedro Rojo Romeo, Benoît Manchon, Nicolas Baboux, Rabei Barhoumi, Ingrid C. Infante, Damien Deleruyelle, Bertrand Vilquin, Sharath Sriram. *Impact of a dielectric layer at TiN/HfZrO₂ interface for ferroelectric tunnel junction applications*. Journée de la Matière Condensée JMC17, 2021.
- Greta Segantini, Benoît Manchon, Pedro Rojo Romeo, Nicolas Baboux, Rabei Barhoumi, Ingrid C. Infante, Damien Deleruyelle, Shruti Nirantar, Bertrand Vilquin, Sharath Sriram. *Role of ultra-thin Ti and Al interfacial layers in HfZrO₂ ferroelectric tunnel junctions*. E-MRS Fall Meeting, 2021.
- Greta Segantini, Benoît Manchon, Rabei Barhoumi, Pedro Rojo Romeo, Ingrid C. Infante, Nicolas Baboux, Shruti Nirantar, Matthieu Bugnet, Simon Jeannot, Damien Deleruyelle, Sharath Sriram, Bertrand Vilquin. *Fabrication Process for sub-8 nm HfZrO₂-based ferroelectric tunnel junctions with enhanced properties*. E-MRS Spring Meeting, 2022.
- Greta Segantini, Benoît Manchon, Rabei Barhoumi, Pedro Rojo Romeo, Ingrid C. Infante, Nicolas Baboux, Shruti Nirantar, Matthieu Bugnet, Simon Jeannot, Damien Deleruyelle, Sharath Sriram, Bertrand Vilquin. *Comparative study of sub-8 nm HZO-based ferroelectric tunnel junctions with enhanced ferroelectricity*. ISAF-PFM-ECAPD 2022, IEEE International Symposium on Applications of Ferroelectrics, 2022.

Conferences and Schools: Poster Presentations

- Greta Segantini, Pedro Rojo Romeo, Benoît Manchon, Nicolas Baboux, Rabei Barhoumi, Ingrid C. Infante, Damien Deleruyelle, Bertrand Vilquin, Sharath

Sriram. *Influence of bottom electrodes on HZO thin films features*. Material Challenges for Memory, APL Materials, 2021.

- Greta Segantini, Pedro Rojo Romeo, Benoît Manchon, Nicolas Baboux, Rabei Barhoumi, Ingrid C. Infante, Damien Deleruyelle, Bertrand Vilquin, Sharath Sriram. *Bottom electrode impact on $\text{Hf}_{0.5}\text{Zr}_{0.5}\text{O}_2$ ferroelectric tunnel junctions*. E-MRS Spring Meeting, 2021.
- Greta Segantini, Benoît Manchon, Rabei Barhoumi, Pedro Rojo Romeo, Ingrid C. Infante, Nicolas Baboux, Shruti Nirantar, Matthieu Bugnet, Damien Deleruyelle, Sharath Sriram, Bertrand Vilquin. *Comparative study of ultra-thin HZO-based capacitors with enhanced ferroelectricity*. 2022 UFFC Ferroelectrics School, 2022.

Annex B: GI-XRD Fitting Procedure

To evaluate the crystalline phase components of the materials that composed the heterostructures presented in this work, a fitting procedure was implemented in Matlab. The results obtained from the fit of X-ray diffraction patterns were useful to evaluate the average out-of-plane crystallite size for different HZO phases, to investigate their dependence on the electrode materials and on the presence of interfacial layers. The fitting function was the sum of two pseudovoigt functions accounting for the Cu Kalpha1 and Cu Kalpha2 radiations and is reported below:

$$\begin{aligned}
 PV(Cu(K\alpha_1 + 0.5K\alpha_2)) = & h(1 - \gamma) \exp \left(-\ln(2) \left(\frac{2(x - c)}{FWHM} \right)^2 \right) + \frac{\gamma}{1 + \left(\frac{2(x-c)}{FWHM} \right)^2} \\
 & + 0.5h(1 - \gamma) \exp \left(-\ln(2) \left(\frac{x - 2 \left(\frac{1}{\sin(\lambda \sin(c))} \right)}{FWHM} \right)^2 \right) + \frac{\gamma}{1 + \left(\frac{x - 2 \left(\frac{1}{\sin(\lambda \sin(c))} \right)}{FWHM} \right)^2}
 \end{aligned}
 \tag{B1}$$

Where h is the height of the peak, c is the center, $FWHM$ is the full width at half maximum of the considered peak, $\lambda = \frac{1.54433}{1.54056}$ is the ratio between the Cu Kalpha1 and Cu Kalpha2 radiations, and $\gamma = \frac{Gaussian}{Lorentzian}$ is the ratio between the Gaussian and Lorentzian profile that compose the pseudovoigt function, in this case it was half Gaussian, and half Lorentzian. In red, the pseudovoigt that represents the Kalpha1 radiation and, in blue, the one corresponding to the Cu Kalpha2 one. The function coded to fit all the peaks that appeared in the GI-XRD pattern was a sum

of pseudovoigt functions, each one corresponding to a certain peak. The fit was accounting only for the contribution of pseudovoigts corresponding to the peaks that were present in the XRD patter, otherwise it was put equal to zero.

Annex C: Samples with Ti Interfacial layer Inserted at the Top Interface and Different HZO Thickness

In this annex, other results obtained on insertion of Ti at the top electrode/HZO interface are presented. A study on the effect of Ti interlayer at different HZO thicknesses was performed. Figure C1 shows the GI-XRD patterns of 12 nm-thick, 8 nm-thick, and 7 nm-thick HZO samples with 2 nm-thick Ti layer inserted at top interface and table C1 reports the out-of-plane average o-phase crystallite size. Figures C2a, b, c, and C3a, b, c show the *P-V* measurements and the endurance tests.

The GI-XRD patterns in figure C1 resemble the ones reported in section III.3.2 for structures without interlayer. In the 12 nm-thick HZO sample, the monoclinic peaks at 28.7° , and at 31.6° are clearly distinguishable, while they fade as the HZO thickness decreases. M-peak at 35.5° is present in the three patterns, although it drops consistently for the 7 nm-thick HZO sample. O-phase out-of-plane average crystallite size of 12 nm-thick HZO sample is smaller compared to reference structure IV.1, on the contrary for 8 nm-thick and 7 nm-thick samples, it is slightly larger.

P-V curves show that the Ti layer is beneficial to the remanent polarisation for low HZO thickness, in particular to the 6 nm-thick HZO structure, studied in section V.3.2. For the 7 nm-thick and 8-nm thick samples, the Ti interlayer does not seem to have a particular influence on P_r , which degrades consistently in the case of the 12 nm-thick HZO sample. A slight imprint is present for the three structures. For

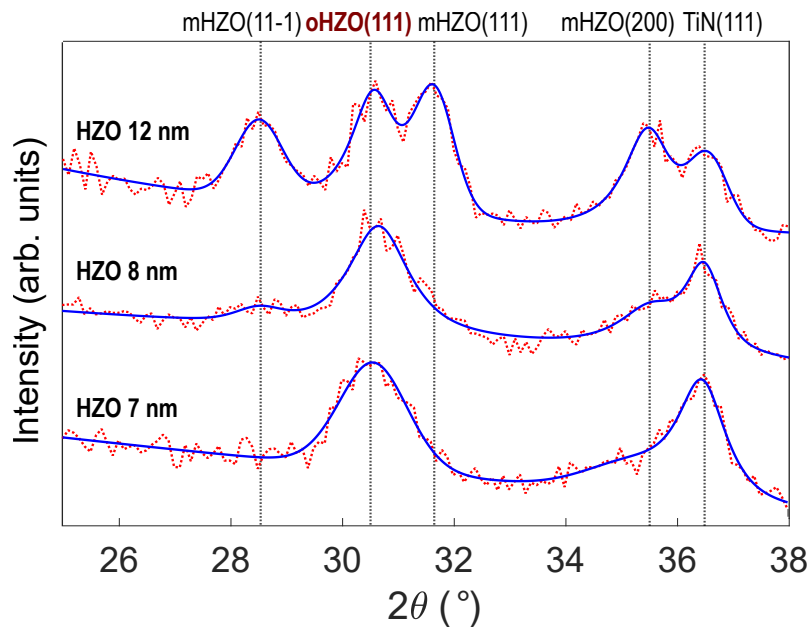


Figure C1: GI-XRD pattern and fit of the structure with Ti interfacial layer at the top interface $n^+Si(100)/TiN/Ti/HZO/TiN/Ti/Pt$, from top: 12 nm-thick HZO layer, 8 nm-thick HZO layer, and 7 nm-thick HZO layer.

Table C1: Average out-of-plane o-phase crystallite size of HZO for different thicknesses and Ti interfacial layer deposited at the top interface.

HZO thickness (nm)	o-HZO crystallite size (nm)
12	7.9
8	6.3
7	5.8

these samples, the endurance is not impacted by the presence of Ti. It is $\sim 10^5$ cycles, similar to the one of the samples without interlayer, in section IV.1.2.

Table C2 reports the values of $2P_r$ and endurance of samples with 3 nm-thick and 1 nm-thick Ti interlayer with different HZO thicknesses. The results related to the 6 nm-thick HZO samples with different thicknesses of Ti interfacial layer, deposited at top electrode/HZO interface, were presented in chapter V.

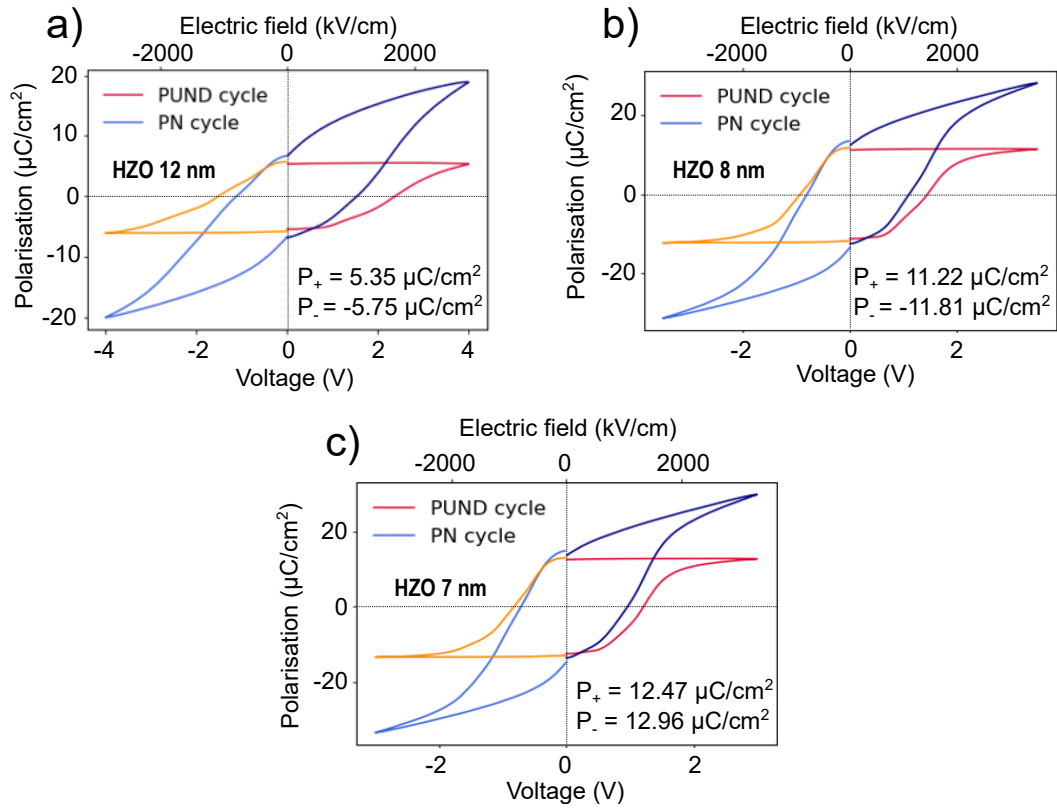


Figure C2: P - V measures of samples $n^+\text{Si}(100)/\text{TiN}/\text{HZO}/\text{Ti}/\text{TiN}/\text{Ti}/\text{Pt}$ with a) 12 nm-thick HZO layer, extracted after 5×10^2 cycles. b) 8 nm-thick HZO layer, extracted after 5×10^2 cycles. c) 7 nm-thick HZO layer, extracted after 5×10^2 cycles.

Table C2: Remanent polarisation and endurance of samples with different HZO thicknesses, and with a 3 nm- and 1 nm-thick Ti interfacial layer at the top interface.

Ti thickness (nm)	HZO thickness (nm)	$2P_r$ ($\mu\text{C}/\text{cm}^2$)	Endurance (cycles)
1	12	~ 8	5×10^5
1	8	~ 22	10^4
1	7	~ 9	5×10^5
3	12	~ 11	10^6
3	8	~ 26	10^4
3	7	~ 32	10^5

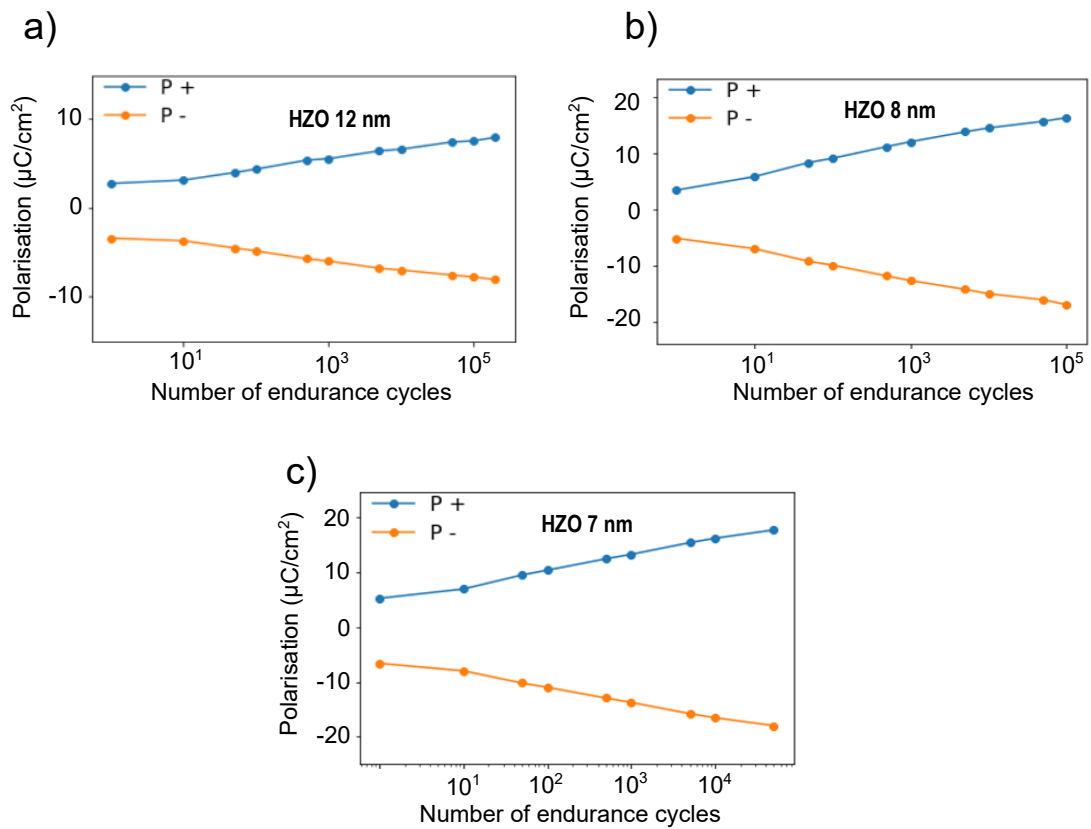


Figure C3: Endurance test of samples $n^+\text{Si}(100)/\text{TiN}/\text{HZO}/\text{Ti}/\text{TiN}/\text{Ti}/\text{Pt}$ with: a) 12 nm-thick HZO layer. b) 8 nm-thick HZO layer. c) 7 nm-thick HZO layer.

Annex D: Ti Interfacial Layer at the Bottom Electrode/HZO Interface

The effect of the Ti interfacial layer, presented in chapter V, was investigated also when it was deposited at the bottom electrode/HZO interface. The impact of the interlayer on the structural and electrical properties of HZO was studied on samples with different HZO thicknesses, ranging between 12 nm and 6 nm. The Ti layer was 2 nm-thick and was growth by RF sputtering after the deposition of the TiN bottom electrode, and prior to deposition of the HZO layer, without braking the vacuum. Figure D1 shows a schematic of the sample structure.

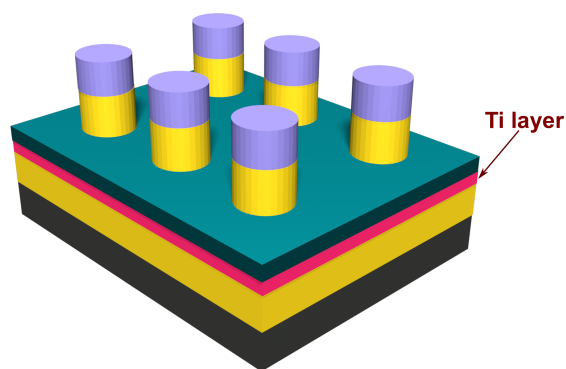


Figure D1: Schematic of the structure $n^+Si(100)/TiN/Ti/HZO/TiN/Ti/Pt$, with Ti interfacial layer deposited at the bottom interface.

The GI-XRD patterns, in figure D2, confirm the presence of the o-/t-peak at $\sim 30.5^\circ$. As it was the case for structures with different HZO thicknesses and with Ti interlayer at top electrode/HZO interface, described in section IV.1.1 and VI.5 respectively, the monoclinic components at $\sim 28.7^\circ$ and at 31.6° vanish as the

HZO thickness decreases. However, the average out-of-plane o-phase crystallite size of these samples, reported in table D1, is larger compared to the one measured for samples without the interfacial layer and with the 2 nm-thick Ti at top electrode/HZO interface, shown in table IV.1 and C1, respectively. In the case of the 6 nm-thick HZO sample, the crystallite size with the Ti at the bottom interface is also bigger compared to the case of Ti at the top interface, where it was ~ 4.8 nm.

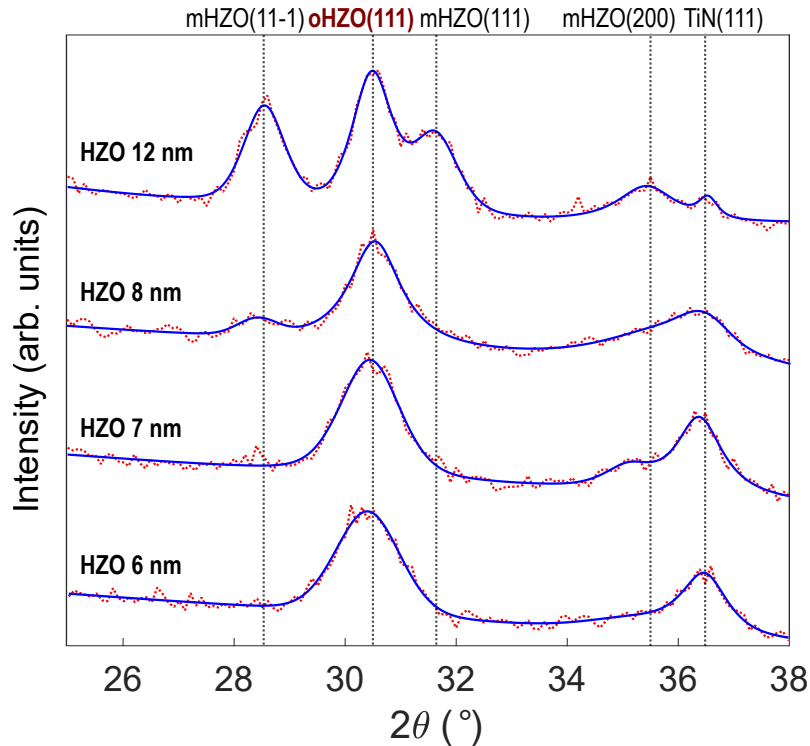


Figure D2: GI-XRD pattern and fit of the structure with Ti interfacial layer at the bottom interface $n^+Si(100)/TiN/Ti/HZO/TiN/Ti/Pt$, from top: 12 nm-thick HZO layer, 8 nm-thick HZO layer, 7 nm-thick HZO layer, 6 nm-thick HZO layer.

Table D1: Average out-of-plane o-phase crystallite size of HZO with different thicknesses and a Ti interfacial layer at the bottom interface.

HZO thickness (nm)	o-HZO crystallite size (nm)
12	9.5
8	7.2
7	6.5
6	6

The P - V curves and endurance tests are reported in figures D3a, b, c, and D4a, b,

c, respectively. In the case of the 12 nm-thick sample, the value of $2P_r$ is similar to the reference structure (section IV.1.2). On the contrary, the $2P_r$ of the 8 nm-thick and 7 nm-thick HZO samples is consistently lower. For the 6 nm-thick HZO structure, no ferroelectric behaviour was observed. For these samples, the imprint is more evident with respect to the structures without Ti and with Ti at the top interface.

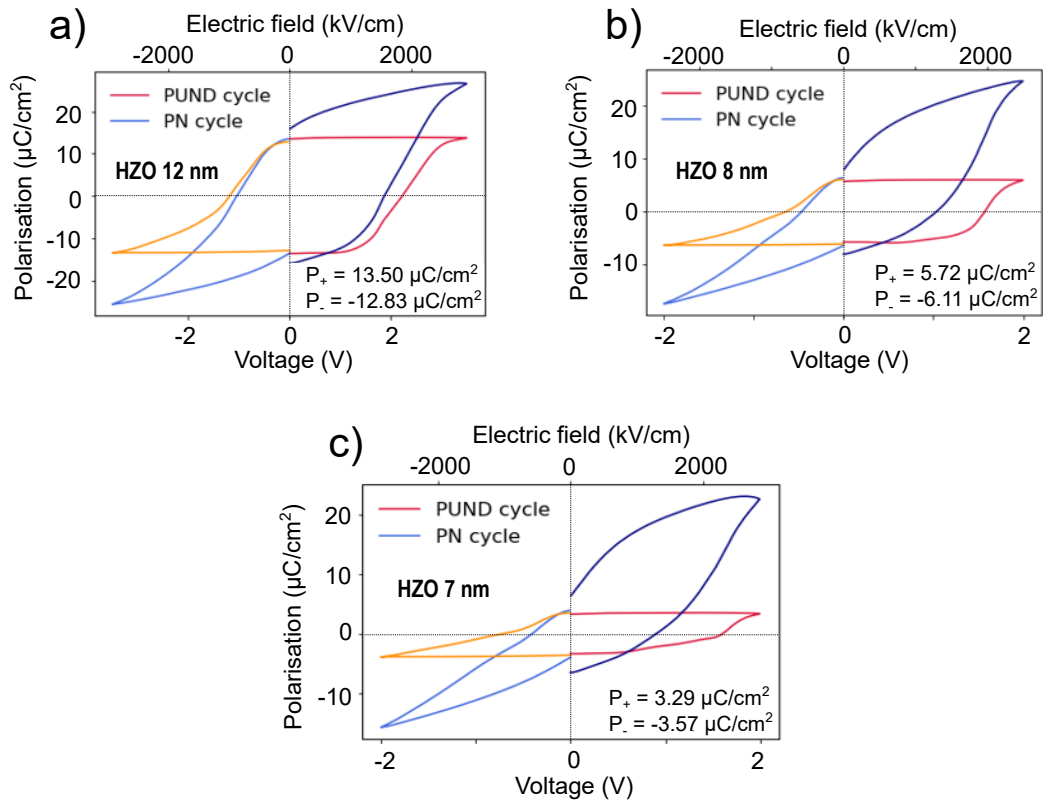


Figure D3: P - V measures of samples $n^+Si(100)/TiN/Ti/HZO/TiN/Ti/Pt$ with a) 12 nm-thick HZO layer, extracted after 5×10^2 cycles. b) 8 nm-thick HZO layer, extracted after 5×10^2 cycles. c) 7 nm-thick HZO layer, extracted after 5×10^2 cycles.

The 12 nm-thick HZO sample is characterised by an endurance of 10^5 cycles, while for samples with 8 nm-thick and 7 nm-thick HZO layer, it is 5×10^5 cycles. Ti inserted at the bottom interface seems to reduce the wake-up effect compared to cases without interfacial layer and with Ti at the top interface.

Indeed, the Ti layer might influence the nucleation of the HZO at growth stage. The absence of ferroelectricity in the 6 nm-thick HZO sample could be related to the presence of the non-ferroelectric tetragonal phase. Furthermore, the crystallite size was shown to have an impact on the nucleation of the t-phase at low HZO thickness [256]. In conclusion, from the obtained results, it seems that the Ti

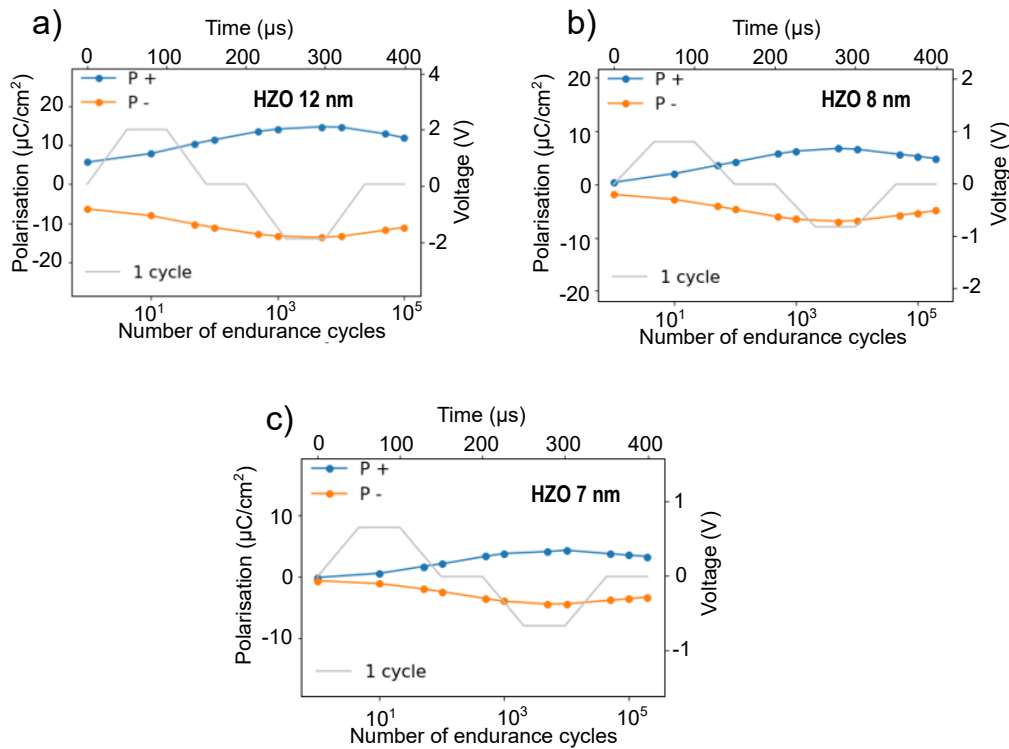


Figure D4: Endurance test of samples $n^+\text{Si}(100)/\text{TiN}/\text{Ti}/\text{HZO}/\text{TiN}/\text{Ti}/\text{Pt}$ with: a) 12 nm-thick HZO layer. b) 8 nm-thick HZO layer. c) 7 nm-thick HZO layer.

layer at the top interface promoted the stabilisation of the o-phase when the HZO thickness was reduced, while the Ti at the bottom interface helped to reduce the wake-up. Figure D5 shows the average out-of-plane o-phase crystallite size calculated for samples with different HZO thicknesses without interfacial layer, with a 2 nm-thick Ti layer at the top interface, and at the bottom interface.

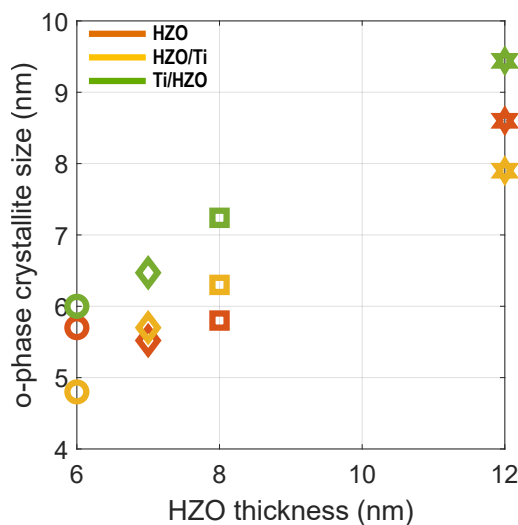


Figure D5: Average out-of-plane o-phase crystallite size vs HZO thickness for samples without Ti interlayer, with Ti at top interface, and with Ti at bottom interface.

Annex E: XPS Analysis of the HZO/Top Electrode Interface

To investigate the chemistry of the top electrode/HZO interface, X-ray photoelectron (XPS) spectroscopy was used as a complement to electron energy-loss spectroscopy (EELS) to study the effect of the Ti interfacial layer. In this annex XPS data of samples with and without Ti are presented, preceded by a brief description of the XPS technique and the set up used for the experiments.

X-ray Photoelectron Spectroscopy

XPS is a technique that belongs to the family of photoemission or photoelectron spectroscopies (PES). These techniques are used to investigate the energy distribution of electrons emitted from a sample by photoelectric effect (photoelectrons), according to the Einstein's equation $h\nu = |E_B| + \phi + E_{kin}$, where E_B is the binding energy of the electrons and E_{kin} is the kinetic energy of photoelectrons. XPS takes its name from the energy range of the impinging electrons that is between 100 and 2000 eV (X region). Since the X radiation is responsible for the excitation of the core electrons, XPS is mainly used to study core levels, the analysis of which allows the identification of the single chemical element. Figure E1 schematises the main components of a PES experiment, which are a monochromatic photon source, the sample to analyse, the electron energy analyser, and the detector. The sample is placed in a vacuum chamber.

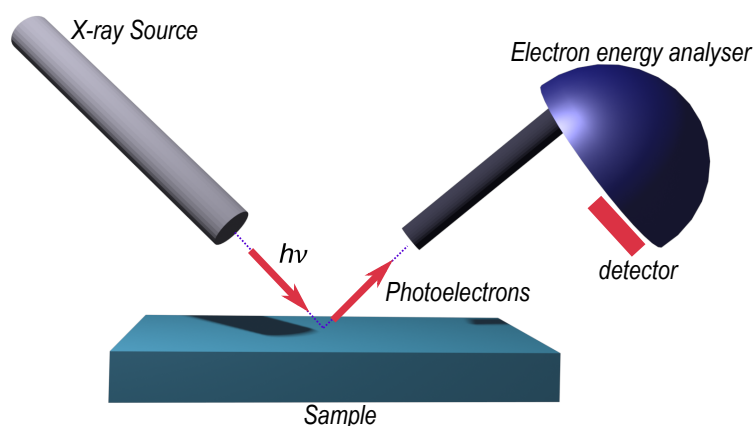


Figure E1: Scheme of an experiment of photoemission spectroscopy.

Physical Principle

The volume of the sample where photoelectrons are generated by the X-ray source is considerably larger compared to the number of photoelectrons that reach the detector. This is due, from an experimental point of view, by the fact that the area of the sample excited by the photon beam is generally larger compared to the one seen by the analyser, and, from a fundamental point of view, by the fact that the generation depth of photoelectrons is much higher than their escape depth. For instance, for 10^5 generated photoelectrons, only one is experimentally revealed by the detector, leading to a process efficiency of approximately 10^{-7} . The escape depth of photoelectrons depends on their kinetic energy, figure E2a reports the universal curve that describes the inelastic mean free path of electrons as a function of the kinetic energy and figure E2b the process of the generation of a photoelectron inside a metal.

Electron Energy Analyser

The electron energy analyser used for XPS is characterised by an hemispherical geometry, as it is depicted in figure E3. The pass energy E_0 is the kinetic energy that corresponds to an ideal trajectory inside the hemisphere, a voltage $V_D < 0$ is adjusted in order to make the energy of the analysed electrons equal to E_0 .

XPS data were collected at RMMF facility of RMIT, using a Kratos AXIS Supra XPS represented in figure E4.

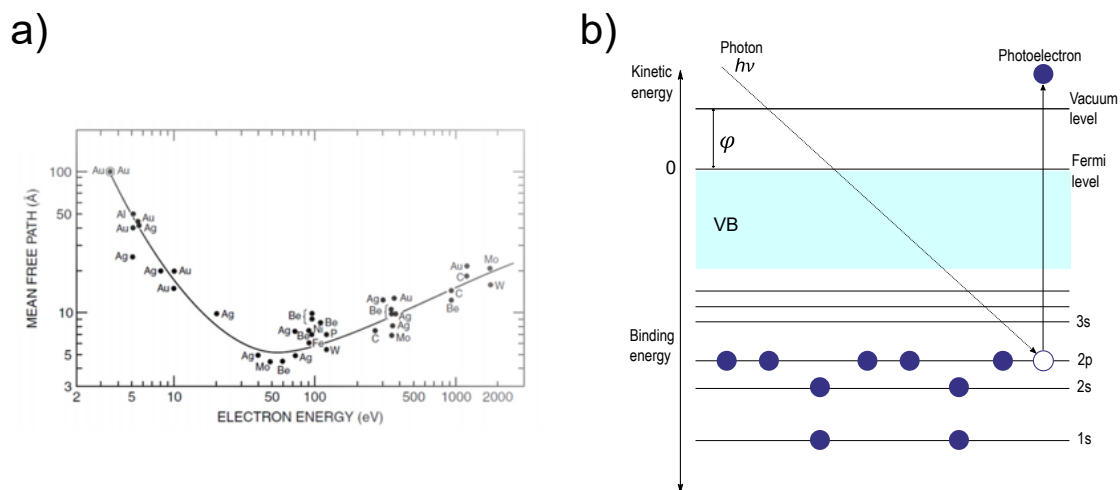


Figure E2: a) Inelastic mean free path as a function of the kinetic energy of electrons. Reprinted from: <https://www.kratos.com/applications/high-energy-xps>. b) Scheme of the generation process of a photoelectron.

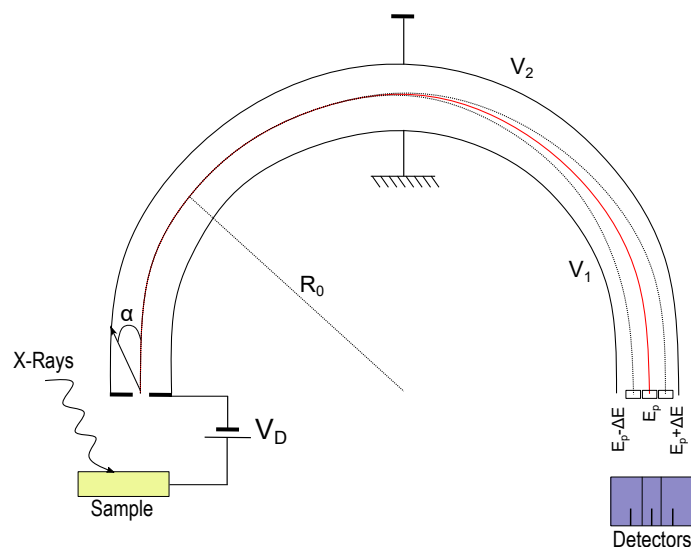


Figure E3: Scheme of a hemispherical electron energy analyser.

Experimental Results

The XPS analysis was performed on 6 nm-thick HZO samples with the Ti interfacial layer and without, for investigation of the top electrode/HZO interface. In order to probe the top interface, the TiN top electrode was 2 nm-thick and it covered the whole surface of the samples. The Ti interlayer, grown prior to the deposition of the top electrode, was also 2 nm-thick. Figure E5a shows the XPS Hf peaks of the sample without the Ti interlayer and figure E5b refers to the sample with the Ti. As it is possible to notice, the doublet that appears at ~ 16.2 eV, which corresponds to Hf 3^+ [257], is more evident in figure E5b than in figure E5a. This feature is attributed to an increase number of oxygen vacancies at the HZO/Ti interface

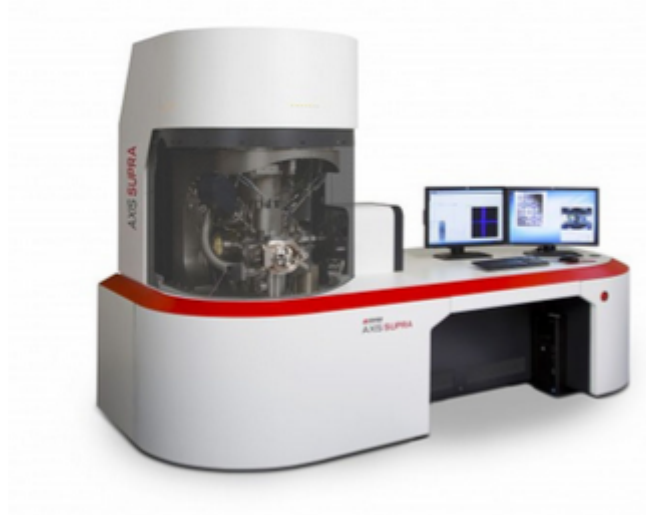


Figure E4: Kratos AXIS Supra XPS.

with respect to the HZO/TiN one. We could not conclude anything regarding the stoichiometry of the Ti(O). In the case of sample with Ti, the latter was deposited just below TiN and, by consequence, it was not possible to determine if the signal of Ti was actually corresponding to the Ti interlayer. The XPS study was a further confirmation of the oxygen scavenging of the Ti from the HZO layer underneath.

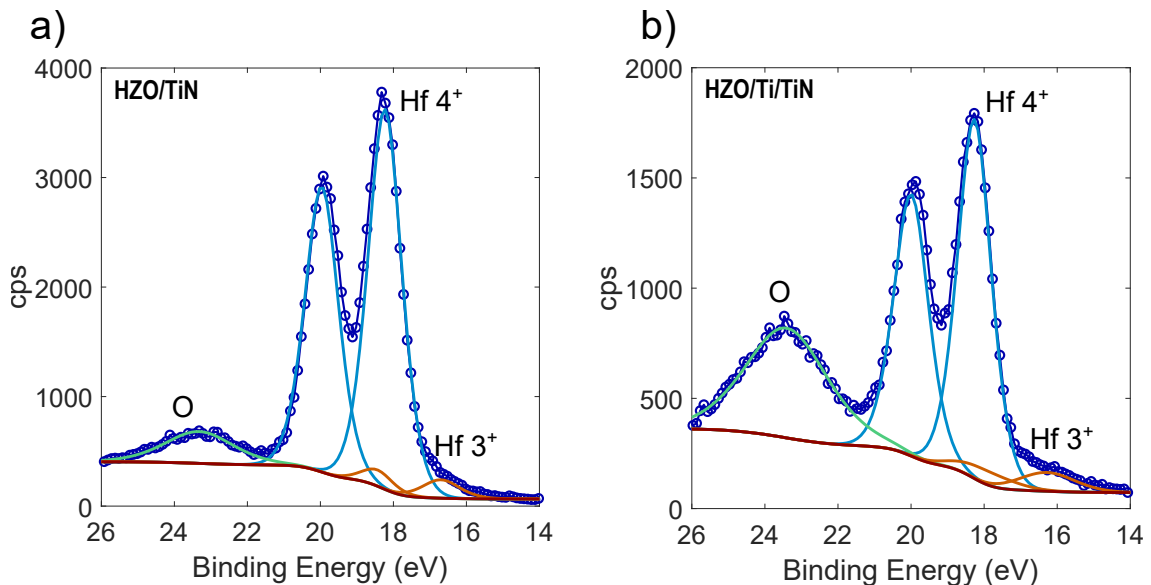


Figure E5: a) Hf XPS peaks of sample n^+ Si/TiN/HZO/TiN, with TiN top electrode ~ 2 nm, b) Hf XPS peaks of sample n^+ Si/TiN/HZO/TiN, with TiN top electrode ~ 2 nm, and Ti interlayer ~ 2 nm.

Bibliography

- [1] V. Y. Shur, “Fast polarization reversal process: evolution of ferroelectric domain structure in thin films,” *Ferroelectric Thin Films: Synthesis and Basic Properties*, vol. 10, pp. 153–192, 1996.
- [2] G. Shirane, E. Sawaguchi, and Y. Takagi, “Dielectric properties of lead zirconate,” *Physical Review*, vol. 84, no. 3, pp. 476–481, 1951.
- [3] E. Sawaguchi, G. Shirane, and Y. Takagi, “Phase Transition in Lead Zirconate,” 1951.
- [4] Z. Zhou, Q. Yang, M. Liu, Z. Zhang, X. Zhang, D. Sun, T. Nan, N. Sun, and X. Chen, “Antiferroelectric Materials, Applications and Recent Progress on Multiferroic Heterostructures,” *SPIN*, vol. 05, p. 1530001, mar 2015.
- [5] S.-H. Yi, H.-C. Lin, and M.-J. Chen, “Ultra-high energy storage density and scale-up of antiferroelectric TiO₂/ZrO₂/TiO₂ stacks for supercapacitors,” *Journal of Materials Chemistry A*, vol. 9, no. 14, pp. 9081–9091, 2021.
- [6] A. K. Tagantsev, K. Vaideeswaran, S. B. Vakhrushev, A. V. Filimonov, R. G. Burkovsky, A. Shaganov, D. Andronikova, A. I. Rudskoy, A. Q. Baron, H. Uchiyama, D. Chernyshov, A. Bosak, Z. Ujma, K. Roleder, A. Majchrowski, J. H. Ko, and N. Setter, “The origin of antiferroelectricity in PbZrO₃,” *Nature Communications*, vol. 4, 2013.
- [7] N. A. Spaldin, “Fundamental size limits in ferroelectricity,” *Science*, vol. 304, no. 5677, pp. 1606–1607, 2004.

- [8] J. F. Ihlefeld, A. M. Vodnick, S. P. Baker, W. J. Borland, and J. P. Maria, “Extrinsic scaling effects on the dielectric response of ferroelectric thin films,” *Journal of Applied Physics*, vol. 103, no. 7, 2008.
- [9] J. Junquera and P. Ghosez, “Critical thickness for ferroelectricity in perovskite ultrathin films,” *Nature*, vol. 422, no. 6931, pp. 506–509, 2003.
- [10] R. R. Mehta, B. D. Silverman, and J. T. Jacobs, “Depolarization fields in thin ferroelectric films,” *Journal of Applied Physics*, vol. 44, no. 8, pp. 3379–3385, 1973.
- [11] D. Damjanovic, “Ferroelectric, dielectric and piezoelectric properties of ferroelectric thin films and ceramics,” *Reports on Progress in Physics*, vol. 61, no. 11, pp. 1267–1324, 1998.
- [12] H. M. Duiker, P. D. Beale, J. F. Scott, C. A. Paz De Araujo, B. M. Melnick, J. D. Cuchiaro, and L. D. McMillan, “Fatigue and switching in ferroelectric memories: Theory and experiment,” *Journal of Applied Physics*, vol. 68, no. 11, pp. 5783–5791, 1990.
- [13] H. N. Al-Shareef, D. Dimos, W. L. Warren, and B. A. Tuttle, “A model for optical and electrical polarization fatigue in SrBi₂Ta₂O₉, and Pb(Zr,Ti)O₃,” *Integrated Ferroelectrics*, vol. 15, no. 1-4, pp. 53–67, 1997.
- [14] A. Q. Jiang, Y. Y. Lin, and T. A. Tang, “Charge injection and polarization fatigue in ferroelectric thin films,” *Journal of Applied Physics*, vol. 102, no. 7, pp. 0–9, 2007.
- [15] U. Robels and G. Arlt, “Domain wall clamping in ferroelectrics by orientation of defects,” *Journal of Applied Physics*, vol. 73, no. 7, pp. 3454–3460, 1993.
- [16] E. L. Colla, D. V. Taylor, A. K. Tagantsev, and N. Setter, “Discrimination between bulk and interface scenarios for the suppression of the switchable polarization (fatigue) in Pb(Zr,Ti)O₃ thin films capacitors with Pt electrodes,” *Applied Physics Letters*, vol. 72, no. 19, pp. 2478–2480, 1998.
- [17] D. J. Johnson, D. T. Amm, E. Griswold, K. Sreenivas, G. Yi, and M. Sayer,

- “Measuring Fatigue in PZT Thin Films,” *MRS Proceedings*, vol. 200, pp. 289–295, 1990.
- [18] J. F. Scott and M. Dawber, “Oxygen-vacancy ordering as a fatigue mechanism in perovskite ferroelectrics,” *Applied Physics Letters*, vol. 76, no. 25, pp. 3801–3803, 2000.
- [19] I. K. Yoo and S. B. Desu, “Mechanism of Fatigue in Ferroelectric Thin Films,” *Physica Status Solidi (a)*, vol. 133, no. 2, pp. 565–573, 1992.
- [20] C. K. Kwok and S. B. Desu, “Role of Oxygen Vacancies on the Ferroelectric Properties of Pzt Thin Films,” *MRS Proceedings*, vol. 243, pp. 393–398, 1991.
- [21] M. Grossmann, O. Lohse, D. Bolten, U. Boettger, R. Waser, W. Hartner, M. Kastner, and G. Schindler, “Lifetime estimation due to imprint failure in ferroelectric SrBi₂Ta₂O₉ thin films,” *Applied Physics Letters*, vol. 76, no. 3, pp. 363–365, 2000.
- [22] J. Bouaziz, P. Rojo Romeo, N. Baboux, and B. Vilquin, “Imprint issue during retention tests for HfO₂-based FRAM: An industrial challenge?,” *Applied Physics Letters*, vol. 118, no. 8, pp. 0–7, 2021.
- [23] R. E. Cohen, “Origin of ferroelectricity in perovskite oxides,” *Nature*, vol. 358, pp. 136–138, jul 1992.
- [24] T. Mikolajick, S. Slesazeck, H. Mulaosmanovic, M. H. Park, S. Fichtner, P. D. Lomenzo, M. Hoffmann, and U. Schroeder, “Next generation ferroelectric materials for semiconductor process integration and their applications,” *Journal of Applied Physics*, vol. 129, no. 10, 2021.
- [25] S. Sedky, A. Witvrouw, H. Bender, and K. Baert, “Experimental determination of the maximum post-process annealing temperature for standard CMOS wafers,” *IEEE Transactions on Electron Devices*, vol. 48, no. 2, pp. 377–385, 2001.
- [26] T. S. Böscke, J. Müller, D. Bräuhäus, U. Schröder, and U. Böttger, “Ferroelectricity in hafnium oxide thin films,” *Applied Physics Letters*, vol. 99, no. 10, 2011.

- [27] J. Müller, T. S. Böske, D. Bräuhaus, U. Schröder, U. Böttger, J. Sundqvist, P. Kcher, T. Mikolajick, and L. Frey, “Ferroelectric Zr_{0.5}Hf_{0.5}O₂ thin films for nonvolatile memory applications,” *Applied Physics Letters*, vol. 99, no. 11, pp. 0–3, 2011.
- [28] S. Kol and A. Oral, “Hf-Based High- κ Dielectrics: A Review,” *Acta Physica Polonica A*, vol. 136, pp. 873–881, dec 2019.
- [29] B. Johnson and J. L. Jones, “Chapter 2 - structures, phase equilibria, and properties of hfo₂,” in *Ferroelectricity in Doped Hafnium Oxide: Materials, Properties and Devices* (U. Schroeder, C. S. Hwang, and H. Funakubo, eds.), Woodhead Publishing Series in Electronic and Optical Materials, pp. 25–45, Woodhead Publishing, 2019.
- [30] J. Wang, H. P. Li, and R. Stevens, “Hafnia and hafnia-toughened ceramics,” *Journal of Materials Science*, vol. 27, no. 20, pp. 5397–5430, 1992.
- [31] T. D. Huan, V. Sharma, G. A. Rossetti, and R. Ramprasad, “Pathways towards ferroelectricity in hafnia,” *Physical Review B - Condensed Matter and Materials Physics*, vol. 90, no. 6, pp. 1–5, 2014.
- [32] D. Shin, R. Arróyave, and Z. K. Liu, “Thermodynamic modeling of the Hf-Si-O system,” *Calphad: Computer Coupling of Phase Diagrams and Thermochemistry*, vol. 30, no. 4, pp. 375–386, 2006.
- [33] Y. Al-Khatatbeh, K. K. Lee, and B. Kiefer, “Phase diagram up to 105 GPa and mechanical strength of HfO₂,” *Physical Review B - Condensed Matter and Materials Physics*, vol. 82, no. 14, pp. 1–9, 2010.
- [34] E. H. Kisi, “Influence of hydrostatic pressure on the t \rightarrow o transformation in Mg-PSZ studied by in situ neutron diffraction,” *Journal of the American Ceramic Society*, vol. 81, no. 3, pp. 741–745, 1998.
- [35] R. Materlik, C. Kuneth, and A. Kersch, “The origin of ferroelectricity in Hf_{1-x}Zr_xO₂: A computational investigation and a surface energy model,” *Journal of Applied Physics*, vol. 117, no. 13, pp. 0–15, 2015.
- [36] X. Zhao and D. Vanderbilt, “First-principles study of structural, vibrational,

- and lattice dielectric properties of hafnium oxide,” *Physical Review B - Condensed Matter and Materials Physics*, vol. 65, no. 23, pp. 1–4, 2002.
- [37] C. B. Carter and M. G. Norton, *Ceramic materials: science and engineering*. Springer Science & Business Media, 2007.
- [38] S. Starschich and U. Boettger, “An extensive study of the influence of dopants on the ferroelectric properties of HfO₂,” *Journal of Materials Chemistry C*, vol. 5, no. 2, pp. 333–338, 2017.
- [39] M. H. Park, T. Schenk, C. M. Fancher, E. D. Grimley, C. Zhou, C. Richter, J. M. Lebeau, J. L. Jones, T. Mikolajick, and U. Schroeder, “A comprehensive study on the structural evolution of HfO₂ thin films doped with various dopants,” *Journal of Materials Chemistry C*, vol. 5, no. 19, pp. 4677–4690, 2017.
- [40] R. Batra, T. D. Huan, G. A. Rossetti, and R. Ramprasad, “Dopants Promoting Ferroelectricity in Hafnia: Insights from a comprehensive Chemical Space Exploration,” *Chemistry of Materials*, vol. 29, no. 21, pp. 9102–9109, 2017.
- [41] J. Müller, U. Schröder, T. S. Böscke, I. Müller, U. Böttger, L. Wilde, J. Sundqvist, M. Lemberger, P. Kücher, T. Mikolajick, and L. Frey, “Ferroelectricity in yttrium-doped hafnium oxide,” *Journal of Applied Physics*, vol. 110, no. 11, pp. 1–6, 2011.
- [42] F. Huang, X. Chen, X. Liang, J. Qin, Y. Zhang, T. Huang, Z. Wang, B. Peng, P. Zhou, H. Lu, L. Zhang, L. Deng, M. Liu, Q. Liu, H. Tian, and L. Bi, “Fatigue mechanism of yttrium-doped hafnium oxide ferroelectric thin films fabricated by pulsed laser deposition,” *Physical Chemistry Chemical Physics*, vol. 19, no. 5, pp. 3486–3497, 2017.
- [43] S. Mueller, J. Mueller, A. Singh, S. Riedel, J. Sundqvist, U. Schroeder, and T. Mikolajick, “Incipient ferroelectricity in Al-doped HfO₂ thin films,” *Advanced Functional Materials*, vol. 22, no. 11, pp. 2412–2417, 2012.
- [44] S. Mueller, C. Adelman, A. Singh, S. Van Elshocht, U. Schroeder, and T. Mikolajick, “Ferroelectricity in gd-doped hfo₂ thin films,” *ECS Journal of Solid State Science and Technology*, vol. 1, no. 6, p. N123, 2012.

- [45] M. Hoffmann, U. Schroeder, T. Schenk, T. Shimizu, H. Funakubo, O. Sakata, D. Pohl, M. Drescher, C. Adelman, R. Materlik, A. Kersch, and T. Mikolajick, "Stabilizing the ferroelectric phase in doped hafnium oxide," *Journal of Applied Physics*, vol. 118, no. 7, pp. 0–9, 2015.
- [46] T. Schenk, S. Mueller, U. Schroeder, R. Materlik, A. Kersch, M. Popovici, C. Adelman, S. Van Elshocht, and T. Mikolajick, "Strontium doped hafnium oxide thin films: Wide process window for ferroelectric memories," *European Solid-State Device Research Conference*, pp. 260–263, 2013.
- [47] U. Schroeder, C. Richter, M. H. Park, T. Schenk, M. Pešić, M. Hoffmann, F. P. Fengler, D. Pohl, B. Rellinghaus, C. Zhou, C. C. Chung, J. L. Jones, and T. Mikolajick, "Lanthanum-Doped Hafnium Oxide: A Robust Ferroelectric Material," *Inorganic Chemistry*, vol. 57, no. 5, pp. 2752–2765, 2018.
- [48] Y. Sharma, D. Barrionuevo, R. Agarwal, S. P. Pavunny, and R. S. Katiyar, "Ferroelectricity in rare-earth modified Hafnia thin films deposited by sequential pulsed laser deposition," *ECS Solid State Letters*, vol. 4, no. 11, pp. N13–N16, 2015.
- [49] H. Chen, Y. Chen, L. Tang, H. Luo, K. Zhou, X. Yuan, and D. Zhang, "Obvious ferroelectricity in undoped HfO₂ films by chemical solution deposition," *Journal of Materials Chemistry C*, vol. 8, no. 8, pp. 2820–2826, 2020.
- [50] P. Polakowski and J. Müller, "Ferroelectricity in undoped hafnium oxide," *Applied Physics Letters*, vol. 106, no. 23, 2015.
- [51] R. Ruh, H. Garrett, R. Domagala, and N. Tallan, "The svstern zirconia-hafnia," *Journal of the American Ceramic Society*, vol. 51, no. 1, pp. 23–28, 1968.
- [52] R. RUH and P. W. CORFIELD, "Crystal Structure of Monoclinic Hafnia and Comparison with Monoclinic Zirconia," *Journal of the American Ceramic Society*, vol. 53, no. 3, pp. 126–129, 1970.
- [53] S. V. Ushakov, A. Navrotsky, Y. Yang, S. Stemmer, K. Kukli, M. Ritala, M. A. Leskelä, P. Fejes, A. Demkov, C. Wang, B. Y. Nguyen, D. Triyoso, and P. Tobin, "Crystallization in hafnia- and zirconia-based systems," *Physica Status Solidi (B) Basic Research*, vol. 241, no. 10, pp. 2268–2278, 2004.

- [54] J. Müller, T. S. Böske, U. Schröder, S. Mueller, D. Bräuhaus, U. Böttger, L. Frey, and T. Mikolajick, "Ferroelectricity in simple binary ZrO₂ and HfO₂," *Nano Letters*, vol. 12, no. 8, pp. 4318–4323, 2012.
- [55] M. H. Park, H. J. Kim, Y. J. Kim, Y. H. Lee, T. Moon, K. D. Kim, S. D. Hyun, F. Fengler, U. Schroeder, and C. S. Hwang, "Effect of Zr Content on the Wake-Up Effect in Hf_{1-x}Zr_xO₂ Films," *ACS Applied Materials and Interfaces*, vol. 8, no. 24, pp. 15466–15475, 2016.
- [56] Y. Wei, P. Nukala, M. Salverda, S. Matzen, H. J. Zhao, J. Momand, A. S. Everhardt, G. Agnus, G. R. Blake, P. Lecoeur, B. J. Kooi, J. Íñiguez, B. Dkhil, and B. Noheda, "A rhombohedral ferroelectric phase in epitaxially strained Hf_{0.5}Zr_{0.5}O₂ thin films," *Nature Materials*, vol. 17, no. 12, pp. 1095–1100, 2018.
- [57] D. A. Buck, "Ferroelectrics for digital information storage and switching.," tech. rep., MASSACHUSETTS INST OF TECH CAMBRIDGE DIGITAL COMPUTER LAB, 1952.
- [58] J. Rodriguez, K. Remack, K. Boku, K. R. Udayakumar, S. Aggarwal, S. Summerfelt, T. Moise, H. McAdams, J. McPherson, R. Bailey, M. Depner, and G. Fox, "Reliability properties of low voltage PZT ferroelectric capacitors and arrays," *Annual Proceedings - Reliability Physics (Symposium)*, vol. 4, no. 3, pp. 200–208, 2004.
- [59] J. M. Koo, B. K. Seo, S. Kim, S. Shin, J. H. Lee, H. Baik, J. H. Lee, J. H. Lee, B. J. Bae, J. E. Lim, D. C. Yoo, S. O. Park, H. S. Kim, H. Han, S. Baik, J. Y. Choi, Y. J. Park, and Y. Park, "Fabrication of 3D trench PZT capacitors for 256Mbit FRAM device application," *Technical Digest - International Electron Devices Meeting, IEDM*, vol. 2005, no. c, pp. 340–343, 2005.
- [60] J. Müller, E. Yurchuk, T. Schlösser, J. Paul, R. Hoffmann, S. Müller, D. Martin, S. Slesazek, P. Polakowski, J. Sundqvist, M. Czernohorsky, K. Seidel, P. Kücher, R. Boschke, M. Trentzsch, K. Gebauer, U. Schröder, and T. Mikolajick, "Ferroelectricity in HfO₂ enables nonvolatile data storage in 28 nm HKMG," *Digest of Technical Papers - Symposium on VLSI Technology*, pp. 25–26, 2012.

- [61] S. Dünkler, M. Trentzsch, R. Richter, P. Moll, C. Fuchs, O. Gehring, M. Majer, S. Wittek, B. Müller, T. Melde, H. Mulaosmanovic, S. Slesazeck, S. Müller, J. Ocker, M. Noack, D. A. Löhr, P. Polakowski, J. Müller, T. Mikolajick, J. Höntschel, B. Rice, J. Pellerin, and S. Beyer, “A FeFET based super-low-power ultra-fast embedded NVM technology for 22nm FDSOI and beyond,” *Technical Digest - International Electron Devices Meeting, IEDM*, pp. 19.7.1–19.7.4, 2018.
- [62] S. Salahuddin and S. Datta, “Use of negative capacitance to provide voltage amplification for low power nanoscale devices,” *Nano Letters*, vol. 8, no. 2, pp. 405–410, 2008.
- [63] V. V. Zhirnov and R. K. Cavin, “Negative capacitance to the rescue?,” *Nature Nanotechnology*, vol. 3, no. 2, pp. 77–78, 2008.
- [64] S. C. Chang, U. E. Avci, D. E. Nikonov, and I. A. Young, “A Thermodynamic Perspective of Negative-Capacitance Field-Effect Transistors,” *IEEE Journal on Exploratory Solid-State Computational Devices and Circuits*, vol. 3, no. September, pp. 56–64, 2017.
- [65] M. Hoffmann, M. Pešić, K. Chatterjee, A. I. Khan, S. Salahuddin, S. Slesazeck, U. Schroeder, and T. Mikolajick, “Direct Observation of Negative Capacitance in Polycrystalline Ferroelectric HfO₂,” *Advanced Functional Materials*, vol. 26, no. 47, pp. 8643–8649, 2016.
- [66] V. Garcia and M. Bibes, “Ferroelectric tunnel junctions for information storage and processing,” *Nature Communications*, vol. 5, 2014.
- [67] a. L. Esaki, R. Laibowitz, and P. Stiles, “Polar switch,” *IBM Tech. Discl. Bull*, vol. 13, no. 2161, p. 114, 1971.
- [68] S. S. Cheema, D. Kwon, N. Shanker, R. dos Reis, S.-L. Hsu, J. Xiao, H. Zhang, R. Wagner, A. Datar, M. R. McCarter, C. R. Serrao, A. K. Yadav, G. Karbasian, C.-H. Hsu, A. J. Tan, L.-C. Wang, V. Thakare, X. Zhang, A. Mehta, E. Karapetrova, R. V. Chopdekar, P. Shafer, E. Arenholz, C. Hu, R. Proksch, R. Ramesh, J. Ciston, and S. Salahuddin, “Enhanced ferroelectricity in ultrathin films grown directly on silicon,” *Nature*, vol. 580, pp. 478–482, apr 2020.

- [69] M. Stengel, D. Vanderbilt, and N. A. Spaldin, "Enhancement of ferroelectricity at metal-oxide interfaces," *Nature Materials*, vol. 8, no. 5, pp. 392–397, 2009.
- [70] J. Rodriguez Contreras, H. Kohlstedt, U. Poppe, R. Waser, C. Buchal, and N. A. Pertsev, "Resistive switching in metal-ferroelectric-metal junctions," *Applied Physics Letters*, vol. 83, no. 22, pp. 4595–4597, 2003.
- [71] H. Kohlstedt, A. Petraru, K. Szot, A. Rüdiger, P. Meuffels, H. Haselier, R. Waser, and V. Nagarajan, "Method to distinguish ferroelectric from non-ferroelectric origin in case of resistive switching in ferroelectric capacitors," *Applied Physics Letters*, vol. 92, p. 062907, feb 2008.
- [72] M. Gajek, M. Bibes, S. Fusil, K. Bouzehouane, J. Fontcuberta, A. Barthélémy, and A. Fert, "Tunnel junctions with multiferroic barriers," *Nature Materials*, vol. 6, no. 4, pp. 296–302, 2007.
- [73] V. Garcia, S. Fusil, K. Bouzehouane, S. Enouz-Vedrenne, N. D. Mathur, A. Barthélémy, and M. Bibes, "Giant tunnel electroresistance for non-destructive readout of ferroelectric states," *Nature*, vol. 460, no. 7251, pp. 81–84, 2009.
- [74] A. Gruverman, D. Wu, H. Lu, Y. Wang, H. W. Jang, C. M. Folkman, M. Y. Zhuravlev, D. Felker, M. Rzechowski, C. B. Eom, and E. Y. Tsybal, "Tunneling electroresistance effect in ferroelectric tunnel junctions at the nanoscale," *Nano Letters*, vol. 9, no. 10, pp. 3539–3543, 2009.
- [75] D. Pantel, S. Goetze, D. Hesse, and M. Alexe, "Room-temperature ferroelectric resistive switching in ultrathin $\text{Pb}(\text{Zr}_{0.2}\text{Ti}_{0.8})\text{O}_3$ films," *ACS Nano*, vol. 5, no. 7, pp. 6032–6038, 2011.
- [76] X. Wang, M. Wu, F. Wei, Y. Zhang, C. Zheng, X. Lou, S. J. Pennycook, and Z. Wen, "Electroresistance of $\text{Pt}/\text{BaTiO}_3/\text{LaNiO}_3$ ferroelectric tunnel junctions and its dependence on BaTiO_3 thickness," *Materials Research Express*, vol. 6, p. 046307, jan 2019.
- [77] Z. Xi, J. Ruan, C. Li, C. Zheng, Z. Wen, J. Dai, A. Li, and D. Wu, "Giant tunnelling electroresistance in metal/ferroelectric/semiconductor tunnel junctions," *Nature Materials*, vol. 18, no. 12, pp. 1255–1260, 2019.

- tions by engineering the Schottky barrier,” *Nature Communications*, vol. 8, p. 15217, aug 2017.
- [78] J. Li, N. Li, C. Ge, H. Huang, Y. Sun, P. Gao, M. He, C. Wang, G. Yang, and K. Jin, “Giant Electroresistance in Ferroionic Tunnel Junctions,” *iScience*, vol. 16, pp. 368–377, jun 2019.
- [79] A. Chanthbouala, V. Garcia, R. O. Cherifi, K. Bouzouane, S. Fusil, X. Moya, S. Xavier, H. Yamada, C. Deranlot, N. D. Mathur, M. Bibes, A. Barthélémy, and J. Grollier, “A ferroelectric memristor,” *Nature Materials*, vol. 11, pp. 860–864, oct 2012.
- [80] C. Yoon, J. H. Lee, S. Lee, J. H. Jeon, J. T. Jang, D. H. Kim, Y. H. Kim, and B. H. Park, “Synaptic Plasticity Selectively Activated by Polarization-Dependent Energy-Efficient Ion Migration in an Ultrathin Ferroelectric Tunnel Junction,” *Nano Letters*, vol. 17, pp. 1949–1955, mar 2017.
- [81] F. Y. Bruno, S. Boyn, S. Fusil, S. Girod, C. Carrétéro, M. Marinova, A. Gloter, S. Xavier, C. Deranlot, M. Bibes, A. Barthélémy, and V. Garcia, “Million-fold Resistance Change in Ferroelectric Tunnel Junctions Based on Nickelate Electrodes,” *Advanced Electronic Materials*, vol. 2, no. 3, pp. 1–7, 2016.
- [82] M. H. Park, Y. H. Lee, T. Mikolajick, U. Schroeder, and C. S. Hwang, “Review and perspective on ferroelectric HfO₂-based thin films for memory applications,” *MRS Communications*, vol. 8, pp. 795–808, sep 2018.
- [83] F. Ambriz-Vargas, G. Kolhatkar, R. Thomas, R. Nouar, A. Sarkissian, C. Gomez-Yáñez, M. A. Gauthier, and A. Ruediger, “Tunneling electroresistance effect in a Pt/Hf_{0.5}Zr_{0.5}O₂/Pt structure,” *Applied Physics Letters*, vol. 110, no. 9, pp. 1–6, 2017.
- [84] Y. Goh and S. Jeon, “The effect of the bottom electrode on ferroelectric tunnel junctions based on CMOS-compatible HfO₂,” *Nanotechnology*, vol. 29, no. 33, 2018.
- [85] J. Yoon, S. Hong, Y. W. Song, J. H. Ahn, and S. E. Ahn, “Understanding tunneling electroresistance effect through potential profile in Pt/Hf_{0.5}Zr_{0.5}O₂/TiN ferroelectric tunnel junction memory,” *Applied Physics Letters*, vol. 115, no. 15, pp. 0–5, 2019.

- [86] Y. Goh, J. Hwang, Y. Lee, M. Kim, and S. Jeon, “ Ultra-thin Hf 0.5 Zr 0.5 O 2 thin-film-based ferroelectric tunnel junction via stress induced crystallization ,” *Applied Physics Letters*, vol. 117, no. 24, p. 242901, 2020.
- [87] M. C. Sulzbach, S. Estandía, J. Gàzquez, F. Sánchez, I. Fina, and J. Fontcuberta, “Blocking of Conducting Channels Widens Window for Ferroelectric Resistive Switching in Interface-Engineered Hf0.5Zr0.5O2 Tunnel Devices,” *Advanced Functional Materials*, vol. 30, no. 32, 2020.
- [88] M. Cervo Sulzbach, H. Tan, S. Estandía, J. Gàzquez, F. Sánchez, I. Fina, and J. Fontcuberta, “Polarization and Resistive Switching in Epitaxial 2 nm Hf 0.5 Zr 0.5 O 2 Tunnel Junctions,” *ACS Applied Electronic Materials*, vol. 3, pp. 3657–3666, aug 2021.
- [89] P. Jiao, Z. Xi, X. Zhang, Y. Han, Y. Wu, and D. Wu, “ Electroresistance in metal/ferroelectric/semiconductor tunnel junctions based on a Hf 0.5 Zr 0.5 O 2 barrier ,” *Applied Physics Letters*, vol. 118, no. 25, p. 252901, 2021.
- [90] “Beyond von Neumann,” *Nature Nanotechnology*, vol. 15, pp. 507–507, jul 2020.
- [91] L. Chua, “Memristor-The missing circuit element,” *IEEE Transactions on Circuit Theory*, vol. 18, no. 5, pp. 507–519, 1971.
- [92] R. Berdan, E. Vasilaki, A. Khat, G. Indiveri, A. Serb, and T. Prodromakis, “Emulating short-term synaptic dynamics with memristive devices,” *Scientific Reports*, vol. 6, no. September 2015, pp. 1–9, 2016.
- [93] J. Zhu, T. Zhang, Y. Yang, and R. Huang, “A comprehensive review on emerging artificial neuromorphic devices,” *Applied Physics Reviews*, vol. 7, p. 011312, mar 2020.
- [94] M. J. Lee, C. B. Lee, D. Lee, S. R. Lee, M. Chang, J. H. Hur, Y. B. Kim, C. J. Kim, D. H. Seo, S. Seo, U. I. Chung, I. K. Yoo, and K. Kim, “A fast, high-endurance and scalable non-volatile memory device made from asymmetric Ta2O5-xx/TaO2-xbilayer structures,” *Nature Materials*, vol. 10, no. 8, pp. 625–630, 2011.

- [95] S. Gao, G. Liu, Q. Chen, W. Xue, H. Yang, J. Shang, B. Chen, F. Zeng, C. Song, F. Pan, and R. W. Li, "Improving Unipolar Resistive Switching Uniformity with Cone-Shaped Conducting Filaments and Its Logic-In-Memory Application," *ACS Applied Materials and Interfaces*, vol. 10, no. 7, pp. 6453–6462, 2018.
- [96] S. H. Lee, X. Zhu, and W. D. Lu, "Nanoscale resistive switching devices for memory and computing applications," *Nano Research*, vol. 13, no. 5, pp. 1228–1243, 2020.
- [97] S. Park, S. Jung, M. Siddik, M. Jo, J. Lee, J. Park, W. Lee, S. Kim, S. M. Sadaf, X. Liu, and H. Hwang, "Memristive switching behavior in Pr_{0.7}Ca_{0.3}MnO₃ by incorporating an oxygen-deficient layer," *Physica Status Solidi - Rapid Research Letters*, vol. 5, no. 10-11, pp. 409–411, 2011.
- [98] A. M. Van Der Zande, P. Y. Huang, D. A. Chenet, T. C. Berkelbach, Y. You, G. H. Lee, T. F. Heinz, D. R. Reichman, D. A. Muller, and J. C. Hone, "Grains and grain boundaries in highly crystalline monolayer molybdenum disulphide," *Nature Materials*, vol. 12, no. 6, pp. 554–561, 2013.
- [99] I. Valov, R. Waser, J. R. Jameson, and M. N. Kozicki, "Erratum: Electrochemical metallization memories - Fundamentals, applications, prospects (Nanotechnology (2011) 22 (254003))," *Nanotechnology*, vol. 22, no. 28, 2011.
- [100] Y. C. Chang and Y. H. Wang, "Solution-processed Al-chelated gelatin for highly transparent non-volatile memory applications," *Applied Physics Letters*, vol. 106, no. 12, pp. 23–26, 2015.
- [101] P. Junsangsri, F. Lombardi, and J. Han, "Macromodeling a phase change memory (pcm) cell by hspice," in *Proceedings of the 2012 IEEE/ACM International Symposium on Nanoscale Architectures*, pp. 77–84, 2012.
- [102] G. W. Burr, M. J. Breitwisch, M. Franceschini, D. Garetto, K. Gopalakrishnan, B. Jackson, B. Kurdi, C. Lam, L. A. Lastras, A. Padilla, *et al.*, "Phase change memory technology," *Journal of Vacuum Science & Technology B, Nanotechnology and Microelectronics: Materials, Processing, Measurement, and Phenomena*, vol. 28, no. 2, pp. 223–262, 2010.

- [103] M. Suri, O. Bichler, D. Querlioz, B. Traoré, O. Cueto, L. Perniola, V. Sousa, D. Vuillaume, C. Gamrat, and B. Desalvo, “Physical aspects of low power synapses based on phase change memory devices,” *Journal of Applied Physics*, vol. 112, no. 5, 2012.
- [104] T. Siegrist, P. Jost, H. Volker, M. Woda, P. Merkelbach, C. Schlockermann, and M. Wuttig, “Disorder-induced localization in crystalline phase-change materials,” *Nature Materials*, vol. 10, no. 3, pp. 202–208, 2011.
- [105] D. Kuzum, R. G. D. Jeyasingh, B. Lee, and H.-S. P. Wong, “Nanoelectronic Programmable Synapses Based on Phase Change Materials for Brain-Inspired Computing,” *Nano Letters*, vol. 12, pp. 2179–2186, may 2012.
- [106] S. Fukami and H. Ohno, “Perspective: Spintronic synapse for artificial neural network,” *Journal of Applied Physics*, vol. 124, no. 15, 2018.
- [107] J. Grollier, V. Cros, A. Hamzic, J. M. George, H. Jaffrès, A. Fert, G. Faini, J. Ben Youssef, and H. Legall, “Spin-polarized current induced switching in Co/Cu/Co pillars,” *Applied Physics Letters*, vol. 78, no. 23, pp. 3663–3665, 2001.
- [108] L. Berger, “Emission of spin waves by a magnetic multilayer traversed by a current,” *Physical Review B*, vol. 54, pp. 9353–9358, oct 1996.
- [109] A. Kurenkov, S. Fukami, and H. Ohno, “Neuromorphic computing with antiferromagnetic spintronics,” *Journal of Applied Physics*, vol. 128, no. 1, 2020.
- [110] S. Luo, K. Liao, P. Lei, T. Jiang, S. Chen, Q. Xie, W. Luo, W. Huang, S. Yuan, W. Jie, and J. Hao, “A synaptic memristor based on two-dimensional layered WSe₂nanosheets with short- And long-term plasticity,” *Nanoscale*, vol. 13, no. 13, pp. 6654–6660, 2021.
- [111] N. F. Mott, “Metal-insulator transitions,” *Pure and Applied Chemistry*, vol. 52, pp. 65–72, jan 1980.
- [112] H. T. Peng, M. A. Nahmias, T. F. De Lima, A. N. Tait, B. J. Shastri, and P. R. Prucnal, “Neuromorphic Photonic Integrated Circuits,” *IEEE Journal of Selected Topics in Quantum Electronics*, vol. 24, no. 6, 2018.

- [113] Z. Cheng, C. Ríos, W. H. P. Pernice, C. D. Wright, and H. Bhaskaran, “On-chip photonic synapse,” *Science Advances*, vol. 3, pp. 1–7, sep 2017.
- [114] Y. He, Y. Yang, S. Nie, R. Liu, and Q. Wan, “Electric-double-layer transistors for synaptic devices and neuromorphic systems,” *Journal of Materials Chemistry C*, vol. 6, no. 20, pp. 5336–5352, 2018.
- [115] H. Ling, D. A. Koutsouras, S. Kazemzadeh, Y. van de Burgt, F. Yan, and P. Gkoupidenis, “Electrolyte-gated transistors for synaptic electronics, neuromorphic computing, and adaptable biointerfacing,” *Applied Physics Reviews*, vol. 7, p. 011307, mar 2020.
- [116] X. Gu and S. S. Iyer, “Unsupervised Learning Using Charge-Trap Transistors,” *IEEE Electron Device Letters*, vol. 38, pp. 1204–1207, sep 2017.
- [117] P. Maier, F. Hartmann, T. Mauder, M. Emmerling, C. Schneider, M. Kamp, S. Höfling, and L. Worschech, “Memristive operation mode of a site-controlled quantum dot floating gate transistor,” *Applied Physics Letters*, vol. 106, p. 203501, may 2015.
- [118] M. Seo, M.-H. Kang, S.-B. Jeon, H. Bae, J. Hur, B. C. Jang, S. Yun, S. Cho, W.-K. Kim, M.-S. Kim, K.-M. Hwang, S. Hong, S.-Y. Choi, and Y.-K. Choi, “First Demonstration of a Logic-Process Compatible Junctionless Ferroelectric FinFET Synapse for Neuromorphic Applications,” *IEEE Electron Device Letters*, vol. 39, pp. 1445–1448, sep 2018.
- [119] C. Mohan, L. A. Camunas-Mesa, J. M. De La Rosa, E. Vianello, T. Serrano-Gotarredona, and B. Linares-Barranco, “Neuromorphic Low-Power Inference on Memristive Crossbars With On-Chip Offset Calibration,” *IEEE Access*, vol. 9, no. March, pp. 38043–38061, 2021.
- [120] A. Velichko, M. Belyaev, and P. Boriskov, “A model of an oscillatory neural network with multilevel neurons for pattern recognition and computing,” *Electronics (Switzerland)*, vol. 8, no. 1, 2019.
- [121] B. Baker, O. Gupta, N. Naik, and R. Raskar, “Designing neural network architectures using reinforcement learning,” *5th International Conference on Learning Representations, ICLR 2017 - Conference Track Proceedings*, pp. 1–18, 2017.

- [122] X. Wang, X. Lin, and X. Dang, "Supervised learning in spiking neural networks: A review of algorithms and evaluations," *Neural Networks*, vol. 125, pp. 258–280, 2020.
- [123] H. U. Dike, Y. Zhou, K. K. Deveerasetty, and Q. Wu, "Unsupervised Learning Based On Artificial Neural Network: A Review," *2018 IEEE International Conference on Cyborg and Bionic Systems, CBS 2018*, pp. 322–327, 2019.
- [124] B. Chen, F. Cai, J. Zhou, W. Ma, P. Sheridan, and W. D. Lu, "Efficient in-memory computing architecture based on crossbar arrays," *Technical Digest - International Electron Devices Meeting, IEDM*, vol. 2016-February, pp. 17.5.1–17.5.4, 2015.
- [125] S. Oh, H. Hwang, and I. K. Yoo, "Ferroelectric materials for neuromorphic computing," *APL Materials*, vol. 7, no. 9, 2019.
- [126] T. Y. Wu, T. S. Chang, H. Y. Lee, S. S. Sheu, W. C. Lo, T. H. Hou, H. H. Huang, Y. H. Chu, C. C. Chang, M. H. Wu, C. H. Hsu, C. T. Wu, M. C. Wu, and W. W. Wu, "Sub-nA Low-Current HZO Ferroelectric Tunnel Junction for High-Performance and Accurate Deep Learning Acceleration," *Technical Digest - International Electron Devices Meeting, IEDM*, vol. 2019-December, pp. 118–121, 2019.
- [127] C. Ma, Z. Luo, W. Huang, L. Zhao, Q. Chen, Y. Lin, X. Liu, Z. Chen, C. Liu, H. Sun, X. Jin, Y. Yin, and X. Li, "Sub-nanosecond memristor based on ferroelectric tunnel junction," *Nature Communications*, vol. 11, no. 1, pp. 1–9, 2020.
- [128] S. Slesazeck and T. Mikolajick, "Nanoscale resistive switching memory devices: A review," *Nanotechnology*, vol. 30, no. 35, 2019.
- [129] B. Max, M. Hoffmann, H. Mulaosmanovic, S. Slesazeck, and T. Mikolajick, "Hafnia-based double-layer ferroelectric tunnel junctions as artificial synapses for neuromorphic computing," *ACS Applied Electronic Materials*, vol. 2, no. 12, pp. 4023–4033, 2020.
- [130] Y. Yang, Z. Xi, Y. Dong, C. Zheng, H. Hu, X. Li, Z. Jiang, W. C. Lu, D. Wu, and Z. Wen, "Spin-Filtering Ferroelectric Tunnel Junctions as Multiferroic

Synapses for Neuromorphic Computing,” *ACS Applied Materials and Interfaces*, vol. 12, no. 50, pp. 56300–56309, 2020.

- [131] E. Covi, H. Mulaosmanovic, B. Max, S. Slesazek, and T. Mikolajick, “Ferroelectric-based synapses and neurons for neuromorphic computing,” *Neuromorphic Computing and Engineering*, vol. 2, no. 1, p. 012002, 2022.
- [132] P. Stoliar, H. Yamada, Y. Toyosaki, and A. Sawa, “Spike-shape dependence of the spike-timing dependent synaptic plasticity in ferroelectric-tunnel-junction synapses,” *Scientific Reports*, vol. 9, no. 1, pp. 1–10, 2019.
- [133] L. Chen, T.-Y. Wang, Y.-W. Dai, M.-Y. Cha, H. Zhu, Q.-Q. Sun, S.-J. Ding, P. Zhou, L. Chua, and D. W. Zhang, “Ultra-low power Hf_{0.5}Zr_{0.5}O₂ based ferroelectric tunnel junction synapses for hardware neural network applications,” *Nanoscale*, vol. 10, no. 33, pp. 15826–15833, 2018.
- [134] Y.-C. Luo, J. Hur, and S. Yu, “Ferroelectric Tunnel Junction Based Crossbar Array Design for Neuro-Inspired Computing,” *IEEE Transactions on Nanotechnology*, vol. 20, pp. 243–247, 2021.
- [135] Y. Zhu, Y. He, C. Chen, L. Zhu, H. Mao, Y. Zhu, X. Wang, Y. Yang, C. Wan, and Q. Wan, “HfZrO_x-based capacitive synapses with highly linear and symmetric multilevel characteristics for neuromorphic computing,” *Applied Physics Letters*, vol. 120, p. 113504, mar 2022.
- [136] D. Kuzum, S. Yu, and H. S. Philip Wong, “Synaptic electronics: Materials, devices and applications,” *Nanotechnology*, vol. 24, no. 38, 2013.
- [137] X. S. Gao, J. M. Liu, K. Au, and J. Y. Dai, “Nanoscale ferroelectric tunnel junctions based on ultrathin BaTiO₃ film and Ag nanoelectrodes,” *Applied Physics Letters*, vol. 101, no. 14, 2012.
- [138] A. Chanthbouala, A. Crassous, V. Garcia, K. Bouzehouane, S. Fusil, X. Moya, J. Allibe, B. Dlubak, J. Grollier, S. Xavier, C. Deranlot, A. Moshar, R. Proksch, N. D. Mathur, M. Bibes, and A. Barthélémy, “Solid-state memories based on ferroelectric tunnel junctions,” *Nature Nanotechnology*, vol. 7, no. 2, pp. 101–104, 2012.

- [139] S. S. Cheema, N. Shanker, C.-H. Hsu, A. Datar, J. Bae, D. Kwon, and S. Salahuddin, “One nanometer hfo₂-based ferroelectric tunnel junctions on silicon,” *Advanced Electronic Materials*, vol. 8, no. 6, p. 2100499, 2022.
- [140] S. Boyn, S. Girod, V. Garcia, S. Fusil, S. Xavier, C. Deranlot, H. Yamada, C. Carrétéro, E. Jacquet, M. Bibes, A. Barthélémy, and J. Grollier, “High-performance ferroelectric memory based on fully patterned tunnel junctions,” *Applied Physics Letters*, vol. 104, no. 5, pp. 7–10, 2014.
- [141] B. Max, M. Hoffmann, S. Slesazeck, and T. Mikolajick, “Ferroelectric Tunnel Junctions based on Ferroelectric-Dielectric Hf_{0.5}Zr_{0.5}O₂/Al₂O₃ Capacitor Stacks,” in *2018 48th European Solid-State Device Research Conference (ESS-DERC)*, pp. 142–145, IEEE, sep 2018.
- [142] Q. Liu, *Optimization of Epitaxial Ferroelectric Pb (Zr_{0.52}, Ti_{0.48}) O₃ Thin-Film Capacitor Properties*. PhD thesis, Ecully, Ecole centrale de Lyon, 2014.
- [143] J. Bouaziz, *Mémoires ferroélectriques non-volatiles à base de (Hf, Zr) O₂ pour la nanoélectronique basse consommation*. PhD thesis, Université de Lyon, 2020.
- [144] J. M. Lee, D. S. Park, S. C. Yew, S. H. Shin, J. Y. Noh, H. S. Kim, and B. D. Choi, “Novel Approach for the Reduction of Leakage Current Characteristics of 20 nm DRAM Capacitors with ZrO₂-Based High-k Dielectrics,” *IEEE Electron Device Letters*, vol. 38, no. 11, pp. 1524–1527, 2017.
- [145] C. Richter, T. Schenk, M. H. Park, F. A. Tschardtke, E. D. Grimley, J. M. LeBeau, C. Zhou, C. M. Fancher, J. L. Jones, T. Mikolajick, and U. Schroeder, “Si Doped Hafnium Oxide—A “Fragile” Ferroelectric System,” *Advanced Electronic Materials*, vol. 3, no. 10, pp. 1–12, 2017.
- [146] M. Pešić, F. P. G. Fengler, L. Larcher, A. Padovani, T. Schenk, E. D. Grimley, X. Sang, J. M. LeBeau, S. Slesazeck, U. Schroeder, and T. Mikolajick, “Physical Mechanisms behind the Field-Cycling Behavior of HfO₂-Based Ferroelectric Capacitors,” *Advanced Functional Materials*, vol. 26, no. 25, pp. 4601–4612, 2016.

- [147] C. J. Brennan, "Characterization and modelling of thin-film ferroelectric capacitors using c-v analysis," *Integrated Ferroelectrics*, vol. 2, no. 1-4, pp. 73–82, 1992.
- [148] A. Erbil, Y. Kim, and R. A. Gerhardt, "Giant permittivity in epitaxial ferroelectric heterostructures," *Physical Review Letters*, vol. 77, no. 8, pp. 1628–1631, 1996.
- [149] A. A. SAIF, Z. A. ZAHID JAMAL, Z. SAULI, and P. POOPALAN, "Frequency Dependent Electrical Properties of Ferroelectric Ba_{0.8}Sr_{0.2}TiO₃ Thin Film," *Materials Science*, vol. 17, pp. 186–190, jan 2011.
- [150] G. Walters, A. Shekhawat, N. G. Rudawski, S. Moghaddam, and T. Nishida, "Tiered deposition of sub-5 nm ferroelectric Hf_{1-x}Zr_xO₂ films on metal and semiconductor substrates," *Applied Physics Letters*, vol. 112, no. 19, 2018.
- [151] A. G. Chernikova and A. M. Markeev, "Dynamic imprint recovery as an origin of the pulse width dependence of retention in Hf_{0.5}Zr_{0.5}O₂-based capacitors," *Applied Physics Letters*, vol. 119, no. 3, pp. 0–7, 2021.
- [152] Y. Lee, H. Alex Hsain, S. S. Fields, S. T. Jaszewski, M. D. Horgan, P. G. Edgington, J. F. Ihlefeld, G. N. Parsons, and J. L. Jones, "Unexpectedly large remanent polarization of Hf_{0.5}Zr_{0.5}O₂metal-ferroelectric-metal capacitor fabricated without breaking vacuum," *Applied Physics Letters*, vol. 118, no. 1, pp. 0–6, 2021.
- [153] T. Onaya, T. Nabatame, N. Sawamoto, A. Ohi, N. Ikeda, T. Nagata, and A. Ogura, "Ferroelectricity of hfxzr_{1-x}o₂ thin films fabricated by 300 c low temperature process with plasma-enhanced atomic layer deposition," *Microelectronic Engineering*, vol. 215, p. 111013, 2019.
- [154] H.-G. Kim, D.-H. Hong, J.-H. Yoo, and H.-C. Lee, "Effect of Process Temperature on Density and Electrical Characteristics of Hf_{0.5}Zr_{0.5}O₂ Thin Films Prepared by Plasma-Enhanced Atomic Layer Deposition," *Nanomaterials*, vol. 12, p. 548, feb 2022.
- [155] T. H. Ryu, D. H. Min, and S. M. Yoon, "Comparative studies on ferroelectric switching kinetics of sputtered Hf_{0.5}Zr_{0.5}O₂thin films with variations in

- film thickness and crystallinity,” *Journal of Applied Physics*, vol. 128, no. 7, pp. 0–12, 2020.
- [156] Z. Fan, J. Xiao, J. Wang, L. Zhang, J. Deng, Z. Liu, Z. Dong, J. Wang, and J. Chen, “Ferroelectricity and ferroelectric resistive switching in sputtered Hf_{0.5}Zr_{0.5}O₂ thin films,” *Applied Physics Letters*, vol. 108, no. 23, 2016.
- [157] Y. H. Lee, H. J. Kim, T. Moon, K. D. Kim, S. D. Hyun, H. W. Park, Y. B. Lee, M. H. Park, and C. S. Hwang, “Preparation and characterization of ferroelectric Hf_{0.5}Zr_{0.5}O₂ thin films grown by reactive sputtering,” *Nanotechnology*, vol. 28, p. 305703, jul 2017.
- [158] J. Bouaziz, P. Rojo Romeo, N. Baboux, and B. Vilquin, “Characterization of ferroelectric hafnium/zirconium oxide solid solutions deposited by reactive magnetron sputtering,” *Journal of Vacuum Science and Technology B*, vol. 37, no. 2, p. 021203, 2019.
- [159] J. Bouaziz, P. Rojo Romeo, N. Baboux, R. Negrea, L. Pintilie, and B. Vilquin, “Dramatic impact of pressure and annealing temperature on the properties of sputtered ferroelectric HZO layers,” *APL Materials*, vol. 7, no. 8, 2019.
- [160] J. Bouaziz, P. R. Romeo, N. Baboux, and B. Vilquin, “Huge Reduction of the Wake-Up Effect in Ferroelectric HZO Thin Films,” *ACS Applied Electronic Materials*, vol. 1, no. 9, pp. 1740–1745, 2019.
- [161] J. Lyu, I. Fina, and F. Sánchez, “Fatigue and retention in the growth window of ferroelectric Hf_{0.5}Zr_{0.5}O₂ thin films,” *Applied Physics Letters*, vol. 117, p. 072901, aug 2020.
- [162] M. C. Sulzbach, S. Estandía, X. Long, J. Lyu, N. Dix, J. Gàzquez, M. F. Chisholm, F. Sánchez, I. Fina, and J. Fontcuberta, “Unraveling ferroelectric polarization and ionic contributions to electroresistance in epitaxial Hf_{0.5}Zr_{0.5}O₂ tunnel junctions,” *arXiv*, pp. 1–33, 2020.
- [163] P. Nukala, J. Antoja-Lleonart, Y. Wei, L. Yedra, B. Dkhil, and B. Noheda, “Direct Epitaxial Growth of Polar (1 – x)HfO₂ – (x)ZrO₂ Ultrathin Films on Silicon ,” *ACS Applied Electronic Materials*, vol. 1, no. 12, pp. 2585–2593, 2019.

- [164] P. Nukala, Y. Wei, V. de Haas, Q. Guo, J. Antoja-Lleonart, and B. Noheda, “Guidelines for the stabilization of a polar rhombohedral phase in epitaxial $\text{Hf}_{0.5}\text{Zr}_{0.5}\text{O}_2$ thin films,” *Ferroelectrics*, vol. 569, no. 1, pp. 148–163, 2020.
- [165] L. Bégon-Lours, M. Mulder, P. Nukala, S. De Graaf, Y. A. Birkhölzer, B. Kooi, B. Noheda, G. Koster, and G. Rijnders, “Stabilization of phase-pure rhombohedral HfZrO_4 in pulsed laser deposited thin films,” *Physical Review Materials*, vol. 4, no. 4, pp. 1–6, 2020.
- [166] Y. Kim, J. Woo, S. Im, Y. Lee, J. H. Kim, J.-P. Im, D. Suh, S. M. Yang, S.-M. Yoon, and S. E. Moon, “Optimized annealing conditions to enhance stability of polarization in sputtered HfZrO_x layers for non-volatile memory applications,” *Current Applied Physics*, vol. 20, pp. 1441–1446, dec 2020.
- [167] S. Jeon, D. Das, and V. Gaddam, “Effect of High Pressure Annealing Temperature on the Ferroelectric Properties of $\text{TiN}/\text{Hf}_{0.25}\text{Zr}_{0.75}\text{O}_2/\text{TiN}$ Capacitors,” *4th Electron Devices Technology and Manufacturing Conference, EDTM 2020 - Proceedings*, pp. 2020–2022, 2020.
- [168] Y. J. Lin, C. Y. Teng, S. J. Chang, Y. F. Liao, C. Hu, C. J. Su, and Y. C. Tseng, “Role of electrode-induced oxygen vacancies in regulating polarization wake-up in ferroelectric capacitors,” *Applied Surface Science*, vol. 528, no. June, p. 147014, 2020.
- [169] A. Chouprik, M. Spiridonov, S. Zarubin, R. Kirtaev, V. Mikheev, Y. Lebedinskii, S. Zakharchenko, and D. Negrov, “Wake-up in a $\text{Hf}_{0.5}\text{Zr}_{0.5}\text{O}_2$ film: A Cycle-by-cycle emergence of the remnant polarization via the domain depinning and the vanishing of the anomalous polarization switching,” *ACS Applied Electronic Materials*, vol. 1, no. 3, pp. 275–287, 2019.
- [170] B. Max, M. Pešić, S. Slesazek, and T. Mikolajick, “Interplay between ferroelectric and resistive switching in doped crystalline HfO_2 ,” *Journal of Applied Physics*, vol. 123, no. 13, 2018.
- [171] Z. Dong, X. Cao, T. Wu, and J. Guo, “Tunneling current in HfO_2 and $\text{Hf}_{0.5}\text{Zr}_{0.5}\text{O}_2$ -based ferroelectric tunnel junction,” *Journal of Applied Physics*, vol. 123, no. 9, 2018.

- [172] D. R. Islamov, V. A. Gritsenko, T. V. Perevalov, V. A. Pustovarov, O. M. Orlov, A. G. Chernikova, A. M. Markeev, S. Slesazek, U. Schroeder, T. Mikolajick, and G. Y. Krasnikov, "Identification of the nature of traps involved in the field cycling of Hf_{0.5}Zr_{0.5}O₂-based ferroelectric thin films," *Acta Materialia*, vol. 166, pp. 47–55, 2019.
- [173] T. Mittmann, M. Materano, S. C. Chang, I. Karpov, T. Mikolajick, and U. Schroeder, "Impact of oxygen vacancy content in ferroelectric HZO films on the device performance," *Technical Digest - International Electron Devices Meeting, IEDM*, vol. 2020-Decem, pp. 18.4.1–18.4.4, 2020.
- [174] T. Mittmann, M. Michailow, P. D. Lomenzo, J. Gärtner, M. Falkowski, A. Kersch, T. Mikolajick, and U. Schroeder, "Stabilizing the ferroelectric phase in HfO₂-based films sputtered from ceramic targets under ambient oxygen," *Nanoscale*, vol. 13, no. 2, pp. 912–921, 2021.
- [175] A. S. Sokolov, Y.-R. Jeon, S. Kim, B. Ku, D. Lim, H. Han, M. G. Chae, J. Lee, B. G. Ha, and C. Choi, "Influence of oxygen vacancies in ALD HfO_{2-x} thin films on non-volatile resistive switching phenomena with a Ti/HfO_{2-x}/Pt structure," *Applied Surface Science*, vol. 434, pp. 822–830, mar 2018.
- [176] Q. Luo, H. Ma, H. Su, K.-H. Xue, R. Cao, Z. Gao, J. Yu, T. Gong, X. Xu, J. Yin, *et al.*, "Composition-dependent ferroelectric properties in sputtered hf x zr 1- x o 2 thin films," *IEEE Electron Device Letters*, vol. 40, no. 4, pp. 570–573, 2019.
- [177] M. Stengel and N. A. Spaldin, "Origin of the dielectric dead layer in nanoscale capacitors," *Nature*, vol. 443, pp. 679–682, oct 2006.
- [178] S. Oh, H. Kim, A. Kashir, and H. Hwang, "Effect of dead layers on the ferroelectric property of ultrathin HfZrO_xfilm," *Applied Physics Letters*, vol. 117, no. 25, 2020.
- [179] Q. Yang, J. Cao, Y. Zhou, L. Sun, and X. Lou, "Dead layer effect and its elimination in ferroelectric thin film with oxide electrodes," *Acta Materialia*, vol. 112, pp. 216–223, 2016.

- [180] E. H. Kisi and C. J. Howard, "Crystal structures of zirconia phases and their inter-relation," *Key Engineering Materials*, vol. 154, no. 153-154, pp. 1–36, 1998.
- [181] R. Cao, Y. Wang, S. Zhao, Y. Yang, X. Zhao, W. Wang, X. Zhang, H. Lv, Q. Liu, and M. Liu, "Effects of Capping Electrode on Ferroelectric Properties of Hf_{0.5}Zr_{0.5}O₂ Thin Films," *IEEE Electron Device Letters*, vol. 39, no. 8, pp. 1207–1210, 2018.
- [182] Y. H. Lee, S. D. Hyun, H. J. Kim, J. S. Kim, C. Yoo, T. Moon, K. D. Kim, H. W. Park, Y. B. Lee, B. S. Kim, J. Roh, M. H. Park, and C. S. Hwang, "Nucleation-Limited Ferroelectric Orthorhombic Phase Formation in Hf_{0.5}Zr_{0.5}O₂ Thin Films," *Advanced Electronic Materials*, vol. 5, p. 1800436, feb 2019.
- [183] R. Athle, A. E. O. Persson, A. Irish, H. Menon, R. Timm, and M. Borg, "Effects of TiN Top Electrode Texturing on Ferroelectricity in Hf_{1-x}Zr_xO₂," *ACS Applied Materials and Interfaces*, vol. 13, pp. 11089–11095, mar 2021.
- [184] F. Esaka, K. Furuya, H. Shimada, M. Imamura, N. Matsubayashi, H. Sato, A. Nishijima, A. Kawana, H. Ichimura, and T. Kikuchi, "Comparison of surface oxidation of titanium nitride and chromium nitride films studied by x-ray absorption and photoelectron spectroscopy," *Journal of Vacuum Science and Technology A: Vacuum, Surfaces, and Films*, vol. 15, pp. 2521–2528, sep 1997.
- [185] K. He, N. Chen, C. Wang, L. Wei, and J. Chen, "Method for Determining Crystal Grain Size by X-Ray Diffraction," *Crystal Research and Technology*, vol. 53, no. 2, pp. 1–6, 2018.
- [186] V. Deshpande, K. S. Nair, M. Holzer, S. Banerjee, and C. Dubourdieu, "CMOS back-end-of-line compatible ferroelectric tunnel junction devices," *Solid-State Electronics*, vol. 186, no. April, p. 108054, 2021.
- [187] H. Ryu, H. Wu, F. Rao, and W. Zhu, "Ferroelectric Tunneling Junctions Based on Aluminum Oxide/ Zirconium-Doped Hafnium Oxide for Neuro-morphic Computing," *Scientific Reports*, vol. 9, no. 1, pp. 1–8, 2019.
- [188] M. Hyuk Park, H. Joon Kim, Y. Jin Kim, W. Lee, T. Moon, and C. Seong Hwang, "Evolution of phases and ferroelectric properties of thin Hf

- 0.5Zr0.5O₂ films according to the thickness and annealing temperature,” *Applied Physics Letters*, vol. 102, no. 24, pp. 0–5, 2013.
- [189] Y. Z. Wu, “Pinned interface dipole-induced tunneling electroresistance in ferroelectric tunnel junctions: A theoretical investigation,” *Journal of Applied Physics*, vol. 112, no. 5, 2012.
- [190] J. P. Veev, C. G. Duan, J. D. Burton, A. Smogunov, M. K. Niranjana, E. Tosatti, S. S. Jaswal, and E. Y. Tsymbal, “Magnetic tunnel junctions with ferroelectric barriers: Prediction of four resistance states from first principles,” *Nano Letters*, vol. 9, no. 1, pp. 427–432, 2009.
- [191] P. Sun, Y. Z. Wu, S. H. Zhu, T. Y. Cai, and S. Ju, “Interfacial dead layer effects on current-voltage characteristics in asymmetric ferroelectric tunnel junctions,” *Journal of Applied Physics*, vol. 113, no. 17, 2013.
- [192] P. Yuan, G. Q. Mao, Y. Cheng, K. H. Xue, Y. Zheng, Y. Yang, P. Jiang, Y. Xu, Y. Wang, Y. Wang, Y. Ding, Y. Chen, Z. Dang, L. Tai, T. Gong, Q. Luo, X. Miao, and Q. Liu, “Microscopic mechanism of imprint in hafnium oxide-based ferroelectrics,” *Nano Research*, vol. 15, no. 4, pp. 3667–3674, 2022.
- [193] D. Wang, J. Wang, Q. Li, W. He, M. Guo, A. Zhang, Z. Fan, D. Chen, M. Qin, M. Zeng, X. Gao, G. Zhou, X. Lu, and J. Liu, “Stable ferroelectric properties of Hf_{0.5}Zr_{0.5}O₂ thin films within a broad working temperature range,” *Japanese Journal of Applied Physics*, vol. 58, p. 090910, sep 2019.
- [194] S. J. Kim, J. Mohan, S. R. Summerfelt, and J. Kim, “Ferroelectric Hf_{0.5}Zr_{0.5}O₂ Thin Films: A Review of Recent Advances,” *Jom*, vol. 71, no. 1, pp. 246–255, 2019.
- [195] D. R. Islamov, A. G. Chernikova, M. G. Kozodaev, A. M. Markeev, T. V. Perevalov, V. A. Gritsenko, and O. M. Orlov, “Charge transport mechanism in thin films of amorphous and ferroelectric Hf_{0.5}Zr_{0.5}O₂,” *JETP Letters*, vol. 102, no. 8, pp. 544–547, 2015.
- [196] W. Shin, K. K. Min, J. H. Bae, J. Yim, D. Kwon, Y. Kim, J. Yu, J. Hwang, B. G. Park, D. Kwon, and J. H. Lee, “Comprehensive and accurate analysis of the working principle in ferroelectric tunnel junctions using low-frequency noise spectroscopy,” *Nanoscale*, vol. 14, no. 6, pp. 2177–2185, 2022.

- [197] M. H. Park, Y. H. Lee, T. Mikolajick, U. Schroeder, and C. S. Hwang, “Thermodynamic and Kinetic Origins of Ferroelectricity in Fluorite Structure Oxides,” *Advanced Electronic Materials*, vol. 5, no. 3, pp. 1–11, 2019.
- [198] M. H. Park, H. J. Kim, Y. J. Kim, W. Lee, T. Moon, K. D. Kim, and C. S. Hwang, “Study on the degradation mechanism of the ferroelectric properties of thin Hf_{0.5}Zr_{0.5}O₂ films on TiN and Ir electrodes,” *Applied Physics Letters*, vol. 105, no. 7, pp. 0–5, 2014.
- [199] M. H. Park, H. J. Kim, Y. J. Kim, Y. H. Lee, T. Moon, K. D. Kim, S. D. Hyun, and C. S. Hwang, “Study on the size effect in Hf_{0.5}Zr_{0.5}O₂ films thinner than 8 nm before and after wake-up field cycling,” *Applied Physics Letters*, vol. 107, p. 192907, nov 2015.
- [200] A. Chernikova, M. Kozodaev, A. Markeev, D. Negrov, M. Spiridonov, S. Zharubin, O. Bak, P. Buragohain, H. Lu, E. Suvorova, A. Gruverman, and A. Zenkevich, “Ultrathin Hf_{0.5}Zr_{0.5}O₂ Ferroelectric Films on Si,” *ACS Applied Materials and Interfaces*, vol. 8, no. 11, pp. 7232–7237, 2016.
- [201] F. P. Fengler, M. Pešić, S. Starschich, T. Schneller, C. Künneth, U. Böttger, H. Mulaosmanovic, T. Schenk, M. H. Park, R. Nigon, P. Muralt, T. Mikolajick, and U. Schroeder, “Domain Pinning: Comparison of Hafnia and PZT Based Ferroelectrics,” *Advanced Electronic Materials*, vol. 3, no. 4, 2017.
- [202] G. He and Z. Sun, *High-k gate dielectrics for CMOS technology*. John Wiley & Sons, 2012.
- [203] B. T. Lin, Y. W. Lu, J. Shieh, and M. J. Chen, “Induction of ferroelectricity in nanoscale ZrO₂ thin films on Pt electrode without post-annealing,” *Journal of the European Ceramic Society*, vol. 37, no. 3, pp. 1135–1139, 2017.
- [204] A. G. Chernikova, M. G. Kozodaev, R. R. Khakimov, S. N. Polyakov, and A. M. Markeev, “Influence of ALD Ru bottom electrode on ferroelectric properties of Hf_{0.5}Zr_{0.5}O₂-based capacitors,” *Applied Physics Letters*, vol. 117, p. 192902, nov 2020.
- [205] R. Cao, Q. Liu, M. Liu, B. Song, D. Shang, Y. Yang, Q. Luo, S. Wu, Y. Li, Y. Wang, and H. Lv, “Improvement of Endurance in HZO-Based Ferroelec-

- tric Capacitor Using Ru Electrode,” *IEEE Electron Device Letters*, vol. 40, pp. 1744–1747, nov 2019.
- [206] H. N. Al-Shareef, K. D. Gifford, S. H. Rou, P. D. Hren, O. Auciello, and A. I. Kingon, “Electrodes for ferroelectric thin films,” *Integrated Ferroelectrics*, vol. 3, pp. 321–332, dec 1993.
- [207] C. Zacharaki, P. Tsipas, S. Chaitoglou, S. Fragkos, M. Axiotis, A. Lagoyianis, R. Negrea, L. Pintilie, and A. Dimoulas, “Very large remanent polarization in ferroelectric Hf_{1-x}Zr_xO₂ grown on Ge substrates by plasma assisted atomic oxygen deposition,” *Applied Physics Letters*, vol. 114, no. 11, 2019.
- [208] P. D. Lomenzo, Q. Takmeel, C. M. Fancher, C. Zhou, N. G. Rudawski, S. Moghaddam, J. L. Jones, and T. Nishida, “Ferroelectric Si-Doped HfO₂ Device Properties on Highly Doped Germanium,” *IEEE Electron Device Letters*, vol. 36, no. 8, pp. 766–768, 2015.
- [209] J. Wang, M. D. Nguyen, N. Gauquelin, J. Verbeeck, M. T. Do, G. Koster, G. Rijnders, and E. Houwman, “On the Importance of the Work Function and Electron Carrier Density of Oxide Electrodes for the Functional Properties of Ferroelectric Capacitors,” *Physica Status Solidi - Rapid Research Letters*, vol. 14, no. 3, 2020.
- [210] T. V. Pham, T. N. Q. Bui, T. T. Phan, T. Miyasako, E. Tokumitsu, and T. Shimoda, “Analysis on interface layer between Pt electrode and ferroelectric layer of solution-processed PZT capacitor,” *MRS Proceedings*, vol. 1368, pp. mrss11–1368–ww08–11, jul 2011.
- [211] N. Sama, C. Soyer, D. Remiens, C. Verrue, and R. Bouregba, “Bottom and top electrodes nature and PZT film thickness influence on electrical properties,” *Sensors and Actuators A: Physical*, vol. 158, pp. 99–105, mar 2010.
- [212] S. J. Kim, J. Mohan, H. S. Kim, S. M. Hwang, N. Kim, Y. C. Jung, A. Sahota, K. Kim, H. Y. Yu, P. R. Cha, C. D. Young, R. Choi, J. Ahn, and J. Kim, “A comprehensive study on the effect of tin top and bottom electrodes on atomic layer deposited ferroelectric Hf_{0.5}Zr_{0.5}O₂ thin films,” *Materials*, vol. 13, no. 13, pp. 1–8, 2020.

- [213] V. Gaddam, D. Das, and S. Member, “based Tri-layer Capacitors at Low-Temperature (350 ° C) Annealing Process,” pp. 0–4, 2020.
- [214] V. Gaddam, D. Das, and S. Jeon, “Insertion of HfO₂ seed/dielectric layer to the ferroelectric HZO films for heightened remanent polarization in MFM capacitors,” *IEEE Transactions on Electron Devices*, vol. 67, no. 2, pp. 745–750, 2020.
- [215] A. Shekhawat, G. Walters, N. Yang, J. Guo, T. Nishida, and S. Moghaddam, “Data retention and low voltage operation of Al₂O₃/Hf_{0.5}Zr_{0.5}O₂ based ferroelectric tunnel junctions,” *Nanotechnology*, vol. 31, p. 39LT01, sep 2020.
- [216] Y. Qi, X. Xu, I. Krylov, and M. Eizenberg, “Ferroelectricity of as-deposited HZO fabricated by plasma-enhanced atomic layer deposition at 300 °C by inserting TiO₂ interlayers,” *Applied Physics Letters*, vol. 118, p. 032906, jan 2021.
- [217] H. Chen, L. Tang, L. Liu, Y. Chen, H. Luo, X. Yuan, and D. Zhang, “Significant improvement of ferroelectricity and reliability in Hf_{0.5}Zr_{0.5}O₂ films by inserting an ultrathin Al₂O₃ buffer layer,” *Applied Surface Science*, vol. 542, no. December 2020, p. 148737, 2021.
- [218] S. J. Lee, M. J. Kim, T. Y. Lee, T. I. Lee, J. H. Bong, S. W. Shin, S. H. Kim, W. S. Hwang, and B. J. Cho, “Effect of ZrO₂ interfacial layer on forming ferroelectric HfxZryOz on Si substrate,” *AIP Advances*, vol. 9, no. 12, 2019.
- [219] A. Shekhawat, H. A. Hsain, Y. Lee, J. L. Jones, and S. Moghaddam, “Effect of ferroelectric and interface films on the tunneling electroresistance of the Al₂O₃/Hf_{0.5}Zr_{0.5}O₂ based ferroelectric tunnel junctions,” *Nanotechnology*, vol. 32, p. 485204, nov 2021.
- [220] Y. Kihn, C. Mirguet, and L. Calmels, “EELS studies of Ti-bearing materials and ab initio calculations,” *Journal of Electron Spectroscopy and Related Phenomena*, vol. 143, no. 2-3 SPEC. ISS., pp. 117–127, 2005.
- [221] F. M. F. de Groot, J. C. Fuggle, B. T. Thole, and G. A. Sawatzky, “L_{2,3} x-ray-absorption edges of d⁰ compounds: K⁺, Ca²⁺, Sc³⁺, and Ti⁴⁺ in o_h (octahedral) symmetry,” *Physical Review B*, vol. 41, pp. 928–937, jan 1990.

- [222] T. Mizoguchi, M. Saitoh, and Y. Ikuhara, “First-principles calculation of oxygen K-electron energy loss near edge structure of HfO₂,” *Journal of Physics Condensed Matter*, vol. 21, no. 10, 2009.
- [223] D. W. McComb, “Bonding and electronic structure in zirconia pseudopolymorphs investigated by electron energy-loss spectroscopy,” *Physical Review B - Condensed Matter and Materials Physics*, vol. 54, no. 10, pp. 7094–7102, 1996.
- [224] G. D. Wilk and D. A. Muller, “Correlation of annealing effects on local electronic structure and macroscopic electrical properties for HfO₂ deposited by atomic layer deposition,” *Applied Physics Letters*, vol. 83, no. 19, pp. 3984–3986, 2003.
- [225] S. Ramanathan, D. A. Muller, G. D. Wilk, C. M. Park, and P. C. McIntyre, “Effect of oxygen stoichiometry on the electrical properties of zirconia gate dielectrics,” *Applied Physics Letters*, vol. 79, no. 20, pp. 3311–3313, 2001.
- [226] J. H. Jang, H. S. Jung, J. H. Kim, S. Y. Lee, C. S. Hwang, and M. Kim, “Investigation of oxygen-related defects and the electrical properties of atomic layer deposited HfO₂ films using electron energy-loss spectroscopy,” *Journal of Applied Physics*, vol. 109, no. 2, 2011.
- [227] S. Ostanin, A. J. Craven, D. W. McComb, D. Vlachos, A. Alavi, M. W. Finnis, and A. T. Paxton, “Effect of relaxation on the oxygen K-edge electron energy-loss near-edge structure in yttria-stabilized zirconia,” *Physical Review B - Condensed Matter and Materials Physics*, vol. 62, no. 22, pp. 14728–14735, 2000.
- [228] D. Y. Cho, H. S. Jung, and C. S. Hwang, “Structural properties and electronic structure of HfO₂-ZrO₂ composite films,” *Physical Review B - Condensed Matter and Materials Physics*, vol. 82, no. 9, pp. 1–7, 2010.
- [229] P. Hidnert, “Thermal expansion of titanium,” *J. Res. Natl. Bur. Stand.*, vol. 30, no. 1934, p. 101, 1943.
- [230] E. Mohammadpour, M. Altarawneh, J. Al-Nu’airat, Z. T. Jiang, N. Mondinos, and B. Z. Dlugogorski, “Thermo-mechanical properties of cubic titanium nitride,” *Molecular Simulation*, vol. 44, no. 5, pp. 415–423, 2018.

- [231] D. Walczyk, T. Bertaud, M. Sowinska, M. Lukosius, M. A. Schubert, A. Fox, D. Wolansky, A. Scheit, M. Fraschke, G. Schoof, C. Wolf, R. Kraemer, B. Tillack, R. Korolevych, V. Stikanov, C. Wenger, T. Schroeder, and C. Walczyk, "Resistive switching behavior in TiN/HfO₂/Ti/TiN devices," in *2012 International Semiconductor Conference Dresden-Grenoble (ISCDG)*, pp. 143–146, IEEE, sep 2012.
- [232] P. D. Lomenzo, S. Slesazeck, M. Hoffmann, T. Mikolajick, U. Schroeder, B. Max, and T. Mikolajick, "Ferroelectric Hf_{1-x}Zr_xO₂ memories: device reliability and depolarization fields," in *2019 19th Non-Volatile Memory Technology Symposium (NVMTS)*, pp. 1–8, IEEE, oct 2019.
- [233] M. Si, X. Lyu, and P. D. Ye, "Ferroelectric Polarization Switching of Hafnium Zirconium Oxide in a Ferroelectric/Dielectric Stack," *ACS Applied Electronic Materials*, vol. 1, no. 5, pp. 745–751, 2019.
- [234] Y. Qu, J. Li, M. Si, X. Lyu, and P. D. Ye, "Quantitative Characterization of Interface Traps in Ferroelectric/Dielectric Stack Using Conductance Method," *IEEE Transactions on Electron Devices*, vol. 67, no. 12, pp. 5315–5321, 2020.
- [235] R. Batra, T. D. Huan, J. L. Jones, G. Rossetti, and R. Ramprasad, "Factors Favoring Ferroelectricity in Hafnia: A First-Principles Computational Study," *The Journal of Physical Chemistry C*, vol. 121, pp. 4139–4145, mar 2017.
- [236] H. J. Kim, M. H. Park, Y. J. Kim, Y. H. Lee, T. Moon, K. D. Kim, S. D. Hyun, and C. S. Hwang, "A study on the wake-up effect of ferroelectric Hf_{0.5}Zr_{0.5}O₂ films by pulse-switching measurement," *Nanoscale*, vol. 8, no. 3, pp. 1383–1389, 2016.
- [237] B. Manchon, G. Segantini, N. Baboux, P. Rojo Romeo, R. Barhoumi, I. C. Infante, F. Alibart, D. Drouin, B. Vilquin, and D. Deleruyelle, "Insertion of an Ultrathin Interfacial Aluminum Layer for the Realization of a Hf_{0.5}Zr_{0.5}O₂ Ferroelectric Tunnel Junction," *Physica Status Solidi - Rapid Research Letters*, vol. 2100585, pp. 1–6, 2022.
- [238] M. Si, X. Lyu, P. R. Shrestha, X. Sun, H. Wang, K. P. Cheung, and P. D. Ye, "Ultrafast measurements of polarization switching dynamics on ferroelec-

- tric and anti-ferroelectric hafnium zirconium oxide,” *Applied Physics Letters*, vol. 115, p. 072107, aug 2019.
- [239] X. Lyu, M. Si, X. Sun, M. A. Capano, H. Wang, and P. Ye, “Ferroelectric and Anti-Ferroelectric Hafnium Zirconium Oxide: Scaling Limit, Switching Speed and Record High Polarization Density,” in *2019 Symposium on VLSI Technology*, vol. 2019-June, pp. T44–T45, IEEE, jun 2019.
- [240] G. Karbasian, R. dos Reis, A. K. Yadav, A. J. Tan, C. Hu, and S. Salahuddin, “Stabilization of ferroelectric phase in tungsten capped Hf 0.8 Zr 0.2 O 2,” *Applied Physics Letters*, vol. 111, p. 022907, jul 2017.
- [241] A. Kashir, H. Kim, S. Oh, and H. Hwang, “Large Remnant Polarization in a Wake-Up Free Hf 0.5 Zr 0.5 O 2 Ferroelectric Film through Bulk and Interface Engineering,” *ACS Applied Electronic Materials*, vol. 3, pp. 629–638, feb 2021.
- [242] G. Segantini, R. Barhoumi, B. Manchon, I. Cañero Infante, P. Rojo Romeo, M. Bugnet, N. Baboux, S. Nirantar, D. Deleruyelle, S. Sriram, and B. Vilquin, “Ferroelectricity Improvement in Ultra-Thin Hf0.5Zr0.5O2 Capacitors by the Insertion of a Ti Interfacial Layer,” *physica status solidi (RRL) – Rapid Research Letters*, p. 2100583, mar 2022.
- [243] B. J. Murdoch, D. G. McCulloch, R. Ganesan, D. R. McKenzie, M. M. Bilek, and J. G. Partridge, “Memristor and selector devices fabricated from HfO₂-xNx,” *Applied Physics Letters*, vol. 108, no. 14, 2016.
- [244] S. Stemmer, Z. Q. Chen, W. J. Zhu, and T. P. Ma, “Electron energy-loss spectroscopy study of thin film hafnium aluminates for novel gate dielectrics,” *Journal of Microscopy*, vol. 210, pp. 74–79, apr 2003.
- [245] J. Lee, M. S. Song, W. S. Jang, J. Byun, H. Lee, M. H. Park, J. Lee, Y. M. Kim, S. C. Chae, and T. Choi, “Modulating the Ferroelectricity of Hafnium Zirconium Oxide Ultrathin Films via Interface Engineering to Control the Oxygen Vacancy Distribution,” *Advanced Materials Interfaces*, vol. 9, no. 7, pp. 1–11, 2022.

- [246] I. Chakraborty, A. Jaiswal, A. K. Saha, S. K. Gupta, and K. Roy, “Pathways to efficient neuromorphic computing with non-volatile memory technologies,” *Applied Physics Reviews*, vol. 7, no. 2, 2020.
- [247] Y. Yang and P. Li, “BioLeaF: A Bio-plausible Learning Framework for Training of Spiking Neural Networks,” pp. 1–16, 2021.
- [248] A. Mehonic, A. Sebastian, B. Rajendran, O. Simeone, E. Vasilaki, and A. J. Kenyon, “Memristors—From In-Memory Computing, Deep Learning Acceleration, and Spiking Neural Networks to the Future of Neuromorphic and Bio-Inspired Computing,” *Advanced Intelligent Systems*, vol. 2, p. 2000085, nov 2020.
- [249] S. Thomann, H. L. G. Nguyen, P. R. Genssler, and H. Amrouch, “All-in-Memory Brain-Inspired Computing Using FeFET Synapses,” *Frontiers in Electronics*, vol. 3, pp. 1–18, feb 2022.
- [250] G. Zhong, M. Zi, C. Ren, Q. Xiao, M. Tang, L. Wei, F. An, S. Xie, J. Wang, X. Zhong, M. Huang, and J. Li, “Flexible electronic synapse enabled by ferroelectric field effect transistor for robust neuromorphic computing,” *Applied Physics Letters*, vol. 117, p. 092903, aug 2020.
- [251] R. Berdan, T. Marukame, K. Ota, M. Yamaguchi, M. Saitoh, S. Fujii, J. Deguchi, and Y. Nishi, “Low-power linear computation using nonlinear ferroelectric tunnel junction memristors,” *Nature Electronics*, vol. 3, no. 5, pp. 259–266, 2020.
- [252] L. Hung, C. Guedj, N. Bernier, P. Blaise, V. Olevano, and F. Sottile, “Interpretation of monoclinic hafnia valence electron energy-loss spectra by time-dependent density functional theory,” *Physical Review B*, vol. 93, no. 16, pp. 1–8, 2016.
- [253] C. Guedj, L. Hung, A. Zobelli, P. Blaise, F. Sottile, and V. Olevano, “Evidence for anisotropic dielectric properties of monoclinic hafnia using valence electron energy-loss spectroscopy in high-resolution transmission electron microscopy and ab initio time-dependent density-functional theory,” *Applied Physics Letters*, vol. 105, p. 222904, dec 2014.

- [254] J. F. Ihlefeld, T. S. Luk, S. W. Smith, S. S. Fields, S. T. Jaszewski, D. M. Hirt, W. T. Riffe, S. Bender, C. Constantin, M. V. Ayyasamy, P. V. Balachandran, P. Lu, M. David Henry, and P. S. Davids, "Compositional dependence of linear and nonlinear optical response in crystalline hafnium zirconium oxide thin films," *Journal of Applied Physics*, vol. 128, no. 3, 2020.
- [255] S. Muhammady, Y. Kurniawan, Suryana, and Y. Darma, "Local-symmetry distortion, optical properties, and plasmonic states of monoclinic Hf 0.5 Zr 0.5 O 2 system: a density-functional study," *Materials Research Express*, vol. 5, p. 096303, aug 2018.
- [256] M. H. Park, Y. H. Lee, H. J. Kim, T. Schenk, W. Lee, K. D. Kim, F. P. Fengler, T. Mikolajick, U. Schroeder, and C. S. Hwang, "Surface and grain boundary energy as the key enabler of ferroelectricity in nanoscale hafnia-zirconia: A comparison of model and experiment," *Nanoscale*, vol. 9, no. 28, pp. 9973–9986, 2017.
- [257] W. Hamouda, A. Pancotti, C. Lubin, L. Tortech, C. Richter, T. Mikolajick, U. Schroeder, and N. Barrett, "Physical chemistry of the TiN/Hf0.5Zr0.5O2 interface," *Journal of Applied Physics*, vol. 127, no. 6, pp. 0–9, 2020.